Final Report

FDOT Contract No.: BDK75 977-24
UF Contract No.: 00083423

Embedded Data Collector (EDC) Evaluation Phase II – Comparison with Instrumented Static Load Tests

Principal Investigators: Michael C. McVay
David Bloomquist
Primary Researcher: Khiem T. Tran

Department of Civil and Coastal Engineering
Engineering School of Sustainable Infrastructure and Environment
University of Florida
P.O. Box 116580
Gainesville, Florida 32611-6580

Developed for the

Florida Department of Transportation

Project Manager; Rodrigo Herrera, P.E.,

Co-Project Manager; Peter Lai (Retired)

December 2013

DISCLAIMER

Prepared in cooperation with the State of Florida Department of Transportation and the U.S. Department of Transportation.

SI (MODERN METRIC) CONVERSION FACTORS (from FHWA)

APPROXIMATE CONVERSIONS TO SI UNITS

SYMBOL	WHEN YOU KNOW	MULTIPLY BY	TO FIND	SYMBOL
LENGTH				
in	inches	25.4	millimeters	mm
ft	feet	0.305	meters	m
yd	yards	0.914	meters	m
mi	miles	1.61	kilometers	km

SYMBOL	WHEN YOU KNOW	MULTIPLY BY	TO FIND	SYMBOL
AREA				
in^2	square inches	645.2	square millimeters	mm^2
ft^2	square feet	0.093	square meters	m^2
yd^2	square yard	0.836	square meters	m^2
ac	acres	0.405	hectares	ha
mi^2	square miles	2.59	square kilometers	km^2

SYMBOL	WHEN YOU KNOW	MULTIPLY BY	TO FIND	SYMBOL
VOLUME				
fl oz	fluid ounces	29.57	milliliters	mL
gal	gallons	3.785	liters	L
ft^3	cubic feet	0.028	cubic meters	m^3
yd^3	cubic yards	0.765	cubic meters	m^3
NOTE: volumes greater than 1000 L shall be shown in m^3				

SYMBOL	WHEN YOU KNOW	MULTIPLY BY	TO FIND	SYMBOL
MASS				
oz	ounces	28.35	grams	g
lb	pounds	0.454	kilograms	kg
T	short tons (2000 lb)	0.907	megagrams (or "metric ton")	Mg (or "t")

SYMBOL	WHEN YOU KNOW	MULTIPLY BY	TO FIND	SYMBOL
TEMPERATURE (exact degrees)				
°F	Fahrenheit	5 (F-32)/9 or (F-32)/1.8	Celsius	°C

SYMBOL	WHEN YOU KNOW	MULTIPLY BY	TO FIND	SYMBOL
ILLUMINATION				
fc	foot-candles	10.76	lux	lx
fl	foot-Lamberts	3.426	candela/m^2	cd/m^2

SYMBOL	WHEN YOU KNOW	MULTIPLY BY	TO FIND	SYMBOL
FORCE and PRESSURE or STRESS				
Lbf*	poundforce	4.45	newtons	N
kip	kip force	1000	pounds	lbf
lbf/in^2	poundforce per square inch	6.89	kilopascals	kPa

APPROXIMATE CONVERSIONS TO SI UNITS

SYMBOL	WHEN YOU KNOW	MULTIPLY BY	TO FIND	SYMBOL
LENGTH				
mm	millimeters	0.039	inches	in
m	meters	3.28	feet	ft
m	meters	1.09	yards	yd
km	kilometers	0.621	miles	mi

SYMBOL	WHEN YOU KNOW	MULTIPLY BY	TO FIND	SYMBOL
AREA				
mm^2	square millimeters	0.0016	square inches	in^2
m^2	square meters	10.764	square feet	ft^2
m^2	square meters	1.195	square yards	yd^2
ha	hectares	2.47	acres	ac
km^2	square kilometers	0.386	square miles	mi^2

SYMBOL	WHEN YOU KNOW	MULTIPLY BY	TO FIND	SYMBOL
VOLUME				
mL	milliliters	0.034	fluid ounces	fl oz
L	liters	0.264	gallons	gal
m^3	cubic meters	35.314	cubic feet	ft^3
m^3	cubic meters	1.307	cubic yards	yd^3

SYMBOL	WHEN YOU KNOW	MULTIPLY BY	TO FIND	SYMBOL
MASS				
g	grams	0.035	ounces	oz
kg	kilograms	2.202	pounds	lb
Mg (or "t")	megagrams (or "metric ton")	1.103	short tons (2000 lb)	T

SYMBOL	WHEN YOU KNOW	MULTIPLY BY	TO FIND	SYMBOL
TEMPERATURE (exact degrees)				
°C	Celsius	1.8C+32	Fahrenheit	°F

SYMBOL	WHEN YOU KNOW	MULTIPLY BY	TO FIND	SYMBOL
ILLUMINATION				
lx	lux	0.0929	foot-candles	fc
cd/m^2	candela/m^2	0.2919	foot-Lamberts	fl

SYMBOL	WHEN YOU KNOW	MULTIPLY BY	TO FIND	SYMBOL
FORCE and PRESSURE or STRESS				
N	newtons	0.225	poundforce	lbf
kPa	kilopascals	0.145	poundforce per square inch	lbf/in^2

*SI is the symbol for International System of Units. Appropriate rounding should be made to comply with Section 4 of ASTM E380.
(Revised March 2003)

TECHNICAL REPORT DOCUMENTATION PAGE

1. Report No.	2. Government Accession No.	3. Recipient's Catalog No.

4. Title and Subtitle Embedded Data Collector (EDC) Evaluation Phase II – Comparison with Instrumented Static Load Tests	5. Report Date December 2013 6. Performing Organization Code
7. Author(s) Michael C. McVay, David Bloomquist, and Khiem Tran	8. Performing Organization Report No.
9. Performing Organization Name and Address University of Florida – Dept. of Civil and Coastal Engineering Engineering School of Sustainable Infrastructure and Environment 365 Weil Hall – P.O. Box 116580 Gainesville, FL 32611-6580	10. Work Unit No. (TRAIS) 11. Contract or Grant No. BDK75 977-24
12. Sponsoring Agency Name and Address Florida Department of Transportation 605 Suwannee Street, MS 30 Tallahassee, FL 32399	13. Type of Report and Period Covered Final Report 9/1/09 – 12/31/13 14. Sponsoring Agency Code

15. Supplementary Notes

16. Abstract

A total of 139 piles and 213,000 hammer blows were compared between the Embedded Data Collector (EDC), and the Pile Driving Analyzer (PDA) along with SmartPile Review versions (3.6, 3.72, 3.73, 3.76 and 3.76.1): Several of the blows were analyzed with Case Pile Wave Analysis Program (CAPWAP).

- Fixed method EDC/PDA ratio was consistent (0.89 to 0.97) for all version numbers, with little variability (max coefficient of variation (CV) = 0.17);
- UF method EDC/PDA ratio was slightly unconservative (1.12) for earlier versions (3.6), but conservative (0.89 to 0.93) for later releases, with little variability (max CV = 0.18);
- Top pile compressive stresses, CSX (EDC/PDA), were consistent (0.91 to 0.93) for all versions, with little variability (max CV = 0.09);
- Bottom pile compressive stresses, CSB (EDC/PDA), ranged from 0.77 for earlier version (3.6), but quickly stabilized at 0.74 for all subsequent versions (3.72-3.761), with maximum variability (CV = 0.25);
- Pile tension stress, TSX (EDC/PDA), was slightly unconservative (1.2) for earlier versions (3.6), but was conservative (0.87 to 0.90) for all later releases, with max variability (CV = 0.29);
- UF EDC/CAPWAP total capacity ratio varied from 1.0 (ver 3.6) to 0.89 (ver 3.761), with $R^2 = 0.89$;
- UF EDC/CAPWAP skin friction ratio varied from 0.78 to 1.04, with $R^2 = 0.57$;
- UF EDC/CAPWAP tip resistance ratio varied from 0.85 to 0.93, with $R^2 = 0.76$.

A total of 12 static pile test were collected in Florida and Louisiana. From the 12 piles, a total of 17 independent measurements (i.e., total, skin, and tip capacities) were recorded. EDC and SmartPile had a bias or λ (ratio of measured/predicted) of 0.96, CV_R, of 0.258 for combined (total, tip and skin) resistances. Using AASHTO, 2012, the Load and Resistance Factor Design (LRFD) Φ was determined to be 0.65, for a reliability, β, of 2.33. CAPWAP had a bias, λ, of 0.91, $CV_R = 0.311$, and LRFD $\Phi = 0.54$ for $\beta=2.33$ with inclusion of side friction and tip resistance.

17. Key Words Deep Foundations, LRFD ϕ, Embedded Data Collectors (EDC), PDA, CAPWAP, Prestressed Concrete Piles, Skin, Tip, and Total Resistance and Case Studies	18. Distribution Statement No restrictions.

19. Security Classif. (of this report) Unclassified	20. Security Classif. (of this page) Unclassified	21. No. of Pages 190	22. Price

Form DOT F 1700.7 (8-72) Reproduction of completed page authorized

ACKNOWLEDGMENTS

The researchers would like to thank the Florida Department of Transportation (FDOT) for the financial support to carry out this research, as well as the input of the central office geotechnical engineers in the collection of site data. They would also like to thank the Louisiana Department of Transportation (LaDOT) for providing data on four piles.

EXECUTIVE SUMMARY

Monitoring the installation of driven pile foundations is of critical importance for ensuring adequate safety of Florida Department of Transportation (FDOT)-maintained structures (e.g., bridges) with piles. Dynamic load testing of driven test piles is currently the preferred alternative used by industry, on the grounds that it is a cost effective and a reliable method for assessing static capacity. Until 2008, the only method used for estimating pile resistance was the Pile Driving Analyzer (PDA)/CAse Pile Wave Analysis Program (CAPWAP) which involves external gauges attached to the top of the pile, from which stresses and capacity vs. depth were computed/displayed using Case capacity equation with J_{cL} assessed from CAPWAP analysis of test piles.

With the development of the Embedded Data Collector (EDC) system (Smart Structures Inc, 2008) strain and accelerometer gauges were placed at both the top and bottom of the pile, from which stresses at top and bottom of pile, total pile capacity, and end bearing were displayed for every blow of the hammer. Also since the instrumentation was cast into the piles at the casting yard, there was no need to climb the driving leads to attach gauges, speeding up the driving process.

In an effort to evaluate the effectiveness of the EDC system, the FDOT engaged in an evaluation program (Phase I) to compare the *dynamic load testing methods* and wave matching software (i.e., CAPWAP), which is used by industry. Phase I yielded promising results, prompting the Central Office's geotechnical team to pursue the implementation of EDC as well as evaluating its reliability by comparing the recorded results with static load tests, i.e., Phase II. This included further comparison of predicted stresses (e.g., top and bottom compression: CSX and CSB; tension, TSX), energy (EMX), damage (Beta), as well as capacity comparisons (Fixed

EDC/PDA, UF EDC/PDA, and UF EDC vs. CAPWAP). In addition, to adopt the EDC technology as an alternative to current pile driving monitoring practice, the FDOT required the Load and Resistance Factor Design (LRFD) resistance factors (Φ) be established for the new technology based on instrumented *static load test* results.

Also of interest was a separate comparison of skin friction and tip resistance predicted by the new technology. For instance NCHRP synthesis report 418 suggests that tip resistance at end of initial drive (EOID) may be added to skin friction from beginning of restrike (BOR) to give a better assessment of total pile capacity. Similarly, in the case of uplift pile design, only skin friction is considered and checked in the field. Therefore of great interest are methods to improve static skin friction and tip resistance assessment from dynamic data, as well the development LRFD resistance factors for skin, tip, and total pile capacity.

For the dynamic load testing comparisons, a total of 139 instrumented piles, including EDC, PDA, and CAPWAP at EOID, and BOR, were considered. The monitored piles were located in all FDOT districts, as well as the Florida Turnpike. A total of 213,000 hammer blows were monitored and evaluated. Results from five progressive versions of SmartPile Review software (3.6, 3.72, 3.73, 3.76 and 3.76.1) were compared, yielding the following observations:

- Fixed method EDC/PDA ratio was consistent (0.89 to 0.97) for all version numbers, with little variability (max coefficient of variation (CV) = 0.17);
- UF method EDC/PDA ratio was slightly unconservative (1.12) for earlier versions (3.6), but conservative (0.89 to 0.93) for later releases, with little variability (max CV = 0.18);
- Top pile compressive stresses, CSX (EDC/PDA), were consistent (0.91 to 0.93) for all versions, with little variability (max CV = 0.09);
- Bottom pile compressive stresses, CSB (EDC/PDA), ranged from 0.77 for earlier version (3.6), but quickly stabilized at 0.74 for all subsequent versions (3.72-3.761), with maximum variability (CV = 0.25);
- Pile tension stress, TSX (EDC/PDA), was slightly unconservative (1.2) for earlier versions (3.6), but was conservative (0.87 to 0.90) for all later releases, with max variability (CV = 0.29);
- UF EDC/CAPWAP total capacity ratio varied from 1.0 (ver 3.6) to 0.89 (ver 3.761), with $R^2 = 0.89$;

- UF EDC/CAPWAP skin friction ratio varied from 0.78 to 1.04, with $R^2 = 0.57$;
- UF EDC/CAPWAP tip resistance ratio varied from 0.85 to 0.93, with $R^2 = 0.76$.

To improve or provide alternative assessment of skin friction, tip damping, etc. with the EDC gauges (top and bottom), further research was performed and evaluated on the piles for which static load testing was available. In the case of tip resistance, it was found that both force and energy equilibrium may be conserved at the bottom of pile through a single viscous damping value and a conventional static tip resistance vs. displacement. The tip force/energy approach gave reasonable static tip predictions for all top-down static load tests with tip instrumentation. The new method is available in SmartPile Review (version 3.761 and later) as an alternative to Middendorp et al. (1992) unloading point method used in the tip capacity section. It should be noted that the default method of analysis is currently the unloading point. For side friction, Tran et al. (2011a) showed that there exists a unique solution for skin friction alongside the pile, if measured strain and acceleration data at the top and bottom of the pile is used; however, this method has not been implemented in SmartPile Review. Moreover, side damping was shown to be proportional to the static skin friction, and multiple bilinear representation of skin friction (i.e., layers) may be uniquely recovered (Tran et al., 2011b) from the dynamic top and bottom gauge data. The latter offers a unique alternative for assessing pile skin friction instead of subtracting tip resistance from estimated total resistance, as used in current versions of SmartPile Review.

For SmartPile Review's LRFD Φ assessment, a total of 12 static pile test results were collected along with EDC, PDA, and CAPWAP results. Eight piles were from Florida, and four were from Louisiana. From the 12 piles, a total of 17 independent measurements (i.e,. total, skin, and tip capacities) were recorded. Note, independent values were identified as total and tip capacities for top-down tests and as skin friction for uplift tests. Given the number of piles and independent measurements, it was decided to assess one LRFD Φ for combined total, tip, and skin (uplift) (i.e., NCHRP 418 recommendation) for the EDC SmartPile Review. Based on the data set, the bias, or λ (ratio of measured/predicted), was 0.96, standard deviation, σ, was 0.248, and their ratio, the coefficient of variation, CV_R, was 0.258. Using AASHTO Bridge Design Specifications (2012), the LRFD Φ was determined to be 0.65, for a reliability, β, of 2.33. For the same data (skin, tip, and total minus one site), CAPWAP had a bias, λ, of 0.91, $CV_R = 0.311$, and LRFD $\Phi = 0.54$ for $\beta=2.33$. It is believed that the CAPWAP Φ was lower than the suggested NCHRP 507 value (0.65) as result of the inclusion of skin and tip resistance in the assessment. Due to the limited test data (17), a range in LRFD Φ (0.6 to 0.7) was estimated for the case of SmartPile Review. It is recommended that an additional 10 to 15 (skin, tip and total capacities) measurements would reduce the uncertainty in LRFD Φ by 25%.

TABLE OF CONTENTS

page

CHAPTERS

APPENDIX

LIST OF TABLES

LIST OF FIGURES

CHAPTER 1
INTRODUCTION

1.1 Background

Monitoring the installation of driven pile foundations is of critical importance for ensuring adequate safety of Florida Department of Transportation (FDOT) maintained structures (e.g., bridges) with piles. Dynamic load testing of driven test piles is currently the preferred alternative used by industry on the grounds that it is a cost effective and a reliable method for assessing total capacity. Until 2008, the method used was the Pile Driving Analyzer (PDA)/CAse Pile Wave Analysis Program (CAPWAP), which involved external gauges attached to the top of the pile, from which stresses and capacity vs. depth were computed/displayed using Case capacity equation with J_{cL} assessed from CAPWAP analysis of test piles.

With the development of Embedded Data Collector (EDC) system (Smart Structures Inc, 2008) strain and accelerometer gauges were placed at both the top and bottom of the pile, from which stresses at top and bottom of pile, total pile capacity, and end bearing were displayed for every blow of the hammer. Also since the instrumentation was cast into the piles at the casting yard, there was no need to climb the driving leads to attach gauges, speeding up the driving process.

In an effort to evaluate the effectiveness of the EDC system, the FDOT engaged in an evaluation program (Phase I) of comparison with *dynamic load testing methods* and wave matching software (i.e., CAPWAP), which is used by industry. Phase I yielded promising results, prompting the Central Office’s geotechnical team to pursue the implementation of EDC as well as evaluating its reliability by comparing the recorded results with static load tests, i.e., Phase II. To adopt the EDC technology as an alternatve to current pile driving monitoring practice, the FDOT requires Load and Resistance Factor Design (LRFD) resistance factors (Φ) for the technology, which should be established from a sufficiently large database of instrumented *static load test* results. The FDOT estimates approximately 20 static load tests will suffice for phase II LRFD Φ assessment. The FDOT recommends that the static load tests be incorporated into the construction phase of bridge construction. This effort is to collect the static load tests, along with EDC and CAPWAP data for developing resistance factors for LRFD design. Since the EDC gauges are located at both the top and bottom of the pile, each load test will identify skin friction, end bearing and total static pile capacity. LRFD resistance factors will be established for skin friction, end bearing and total static capacity.

1.2 Objective and Supporting Tasks

In the case of the PDA each blow of the hammer, dynamic strains and particle motions would be monitored (PDA) at the top of the pile and dynamic forces/stresses would be predicted along the pile, as well as static total capacity using an assumed Case lumped damping parameter, J_{cL}. Also, using a few of the blow data at the End of Drive (EOD) and Beginning of Restrike (BOR), the Construction Engineering Inspector (CEI) obtains improved estimates of damping as well as distribution of skin friction and end bearing using the finite difference code (CAPWAP). Because of the non-unique nature of CAPWAP, the process involves varying static resistance, quake and damping along the length of the pile until an acceptable match quality between the measured and predicted wave up force at the top of the pile is obtained. Due to cost associated with the equipment, monitoring (PDA) and office analyses (i.e., CAPWAP), FDOT typically monitors approximately 10% of their installed piles. Due to the high variability of Florida soil and rock stratigraphy/properties (i.e., coefficient of variation, $CV \approx 0.5$), LRFD resistance factors for assessment of static axial design loads are 0.55 for the PDA and 0.65 when both PDA and CAPWAP analyses are performed (FDOT Structures Design Guidelines).

EDC uses wireless technology which eliminates the need for personnel to climb (safety) the leads (in some instances > 80 ft) in order to attach gauges to the pile. Next the gauge packs (strain and acceleration instruments) are placed within the body of the pile (top and bottom) prior to concreting. The dual location of the instrumentation improves the assessment of tip stresses, static tip resistance (end bearing piles), as well as separation of side from tip resistance (dynamically and statically). Also, with improvements in laptop processing, real time assessment of results (stresses, static tip, skin and total resistance) for every blow are available. It should be noted that with current approach of pile monitoring (i.e., monitoring 10% of piles), much of the uncertainty associated with pile capacity is due to soil/rock variability which can be greatly reduced by increased pile monitoring. However, the accurate assessment of EDC's bias and variance with static resistance is required.

For EDC technology, LRFD resistance factors must be determined for FDOT practice. The assessment will require approximately 20 to 30 high quality static pile load tests obtained from either top down compression testing, or bottom-up Osterberg Testing for the various soil/rock conditions throughout the state. Since the technology is capable of separating skin from tip resistance, the resistance factor may be determined from independent measurements, e.g., total, tip or skin in the case of pullout tests.

FDOT engineers have also been comparing EDC with existing PDA and CAPWAP data: 1) top gauges measured stresses (PDA and EDC); 2) bottom stresses (EDC measured, PDA predicted); and 3) skin, tip and total pile capacity predictions (EDC vs. PDA and CAPWAP). This comparison has been performed on over 100 piles with similar results (e.g., capacity: EDC (Fixed Method)/PDA – mean = 0.97 and CV = 0.17) and some variability (e.g., tip stresses, EDC/PDA = 0.75, CV = 0.25). There is a need to continue this comparison for other sites with different soil/rock conditions and pile driving equipment.

Finally, the recent NCHRP Synthesis Report 418, "Developing Production Pile Driving Criteria from Test Pile Data," has suggested the use of tip resistance at end of initial drive (EOID) with the skin friction assessed from beginning of restrike (BOR) blows to better assess the total capacity of piles. The reasoning being that at EOID the pile generally mobilizes the full tip resistance (i.e., tip movements 15-25 mm), but not the full skin friction due to changes in stress (e.g., excess pore pressure) along the pile. However after sufficient time, the beginning of the BOR restrike blows, full skin friction of the pile is developed (i.e., "pile freeze"), but the tip resistance may not be fully mobilized due to limited tip movement (e.g., 5-10 mm). Consequently, NCHRP 418 suggests that the total capacity of the pile be assessed as the sum of EOID tip resistance with the BOR skin friction. Of interest to the FDOT is the prediction of changes in both tip and skin resistance of piles between EOID and BOR for Florida soil/rock conditions. Also in the case of EDC system (gauges at top and bottom of pile), what is the predicted skin and tip variability between EOID and BOR and how does it compare with static load tests. Also, are their improvements to current EDC prediction of tip resistance (i.e., Middendorp, 1992 – Unloading Point), skin friction (i.e., total – tip), i.e., direct assessment using top and bottom gauges.

The anticipated outcomes of EDC Phase II research are 1) evaluation of EDC estimates of static resistance (i.e., total, skin friction and tip resistance) when compared to static load tests; 2) development of LRFD resistance factors for EDC pile monitoring (i.e., skin friction, end bearing, etc.; 3) establishment of high quality static skin friction and end bearing database, which is useful for multitude of other research (i.e., LRFD Φ, spatial variability, pile freeze, etc.); 4) evaluate EDC estimation of pile stresses and damping; and 5) using EDC data in combination with load tests and in situ testing to improve pile freeze predictions. The original plan to accomplish the work is outlined in the Tasks listed below. Most of the goals were accomplished, however in order to obtain a more statistically significant database additional load test results will be incorporated into the analysis, and the results will be presented under a separate report.

1.2.1 Task 1 - Static Load Testing of EDC Monitored Piles

It is anticipated that approximately 20 to 30 static load tests will be performed on 18” to 30” prestressed concrete piles. Each pile will have had EDC systems and a set of sister bars installed in the casting yard (i.e., top and bottom) and monitored during driving. In addition, the pile will be dynamically monitored at EOID, BOR, as well as after the load test. The latter will require that the driving equipment (i.e., hammer, leads, crane, etc.) be repositioned over the test pile and struck multiple times (i.e., ensure hammer is operating). The load test will be performed either top down (i.e., nearby piles as reaction) or bottom-up with Osterberg cell. The EDC and sister bar strain gauges will be monitored under loading (i.e., top down or bottom-up Osterberg) to separate tip resistance from skin friction along the length of the pile. If the load test is only to be performed once on the pile, the test will be conducted after dissipation of pore pressure (i.e., freeze). However, in the case of multiple repetitions of the load test (e.g., Osterberg testing) in high freeze soil, the testing will occur right after driving, as well as one other time to quantify changes in static skin friction and end bearing with time. The static load testing plan (i.e., project, numbers, etc.), use of Osterberg cell (i.e., bottom-up testing) or reaction frame (i.e., top down testing) will be established by district and central office personnel and be identified in the contract plans. As part of this effort, research personnel will be on site for all the load tests, recording the data and subsequently separating out skin and tip resistance for each test. In addition, the data will be uploaded along with driving data (i.e., EDC) into the FDOT on-line database for later use.

To further increase the value of the load tests for design, in situ testing will be performed in the footprint, as well as in the vicinity of the EDC/load tested pile. The test could be either SPT or CPT. In the case of CPT testing, the State Materials Office (SMO) equipment and personnel is setup to perform the testing. The data from the in situ tests, EDC monitoring and static load tests will provide important data for the later tasks (e.g., LRFD resistance factors), but other ongoing research as well. For instance, the CPT/SPT testing in the footprint and vicinity of the EDC/load tested pile should be used in the study of spatial variability effects on LRFD resistance values for axial pile design.

1.2.2 Task 2 - Assessment of LRFD Resistance Factors for EDC Monitored Piles

As identified earlier, FDOT has engaged in an evaluation program (Phase I) of *EDC estimation of static pile resistance (skin and tip)* along with dynamic stresses (i.e., compression and tension) with current technology (PDA and CAPWAP) used by industry. Phase I has yielded promising results, prompting Central Office's Geotechnical team to pursue the implementation of EDC, i.e., Phase II investigation, which requires establishment of LRFD resistance factors for the EDC technology based sufficiently large database of instrumented *static load test* results. Note the current pile monitoring technology may not be used to assess the resistance factors since their static values are estimated using instrumentation located only at the top of the pile. The EDC system with instrumentation at the top and bottom of the pile assess stresses/capacities, etc., quite differently than the current technology. For instance, static tip resistance estimate from the EDC uses the unloading point method for single degree of system model (tip) with damping and inertia forces back calculated from the strain and velocity at the pile tip. The PDA estimates tip resistance from the ratio returning tip stress to total stresses at the pile top. The

CAPWAP software estimates the tip resistance from single degree of freedom tip model by matching the return wave at the top of the pile.

As a minimum for task 2, it is expected that LRFD resistance factors for EDC be established for total pile capacity estimation. However, to increase the data set size, as well include all FDOT pile load scenarios (e.g., uplift resistance), skin friction (uplift load tests), and end bearing (vs. measured static tip) should be considered.

1.2.3 Task 3 - Evaluation of EDC Pile Stresses, Damping, and Static Resistances

Systems with instrumentation at the top and bottom of the pile can readily separate out both dynamic and static forces alongside (i.e., skin) from the pile tip response. The latter is significant, since pile behavior (i.e., compression and tension driving stresses, damping, static resistance, freeze, etc.) is different alongside the pile than at its tip. For instance, peak compressive stresses (i.e., hard driving) or peak wave up tension stresses (i.e., no tip resistance) will initiate from the bottom or tip of the pile which may be directly monitored with the EDC system.

Also of great interest is development of ways to validate pile gauge (strain and accelerometer) response for both the top and bottom set of gauges. For instance, it is believed that most hammer impacts excite the resonant frequencies of the pile (e.g., wavelength, λ, equal to multiples of the pile's length). For any wavelength, the damping, c, may be assessed directly from the decay of F_{down} at the top and bottom gauges for multiple peaks ($t > 2L/c + 4L/c$, etc.) which requires the gauges exhibit periodic decay (i.e., logarithmic decrement after hammer separates from pile). The latter may be checked from both set of gauges and compared. Similarly, double integration of the acceleration trace gives displacements at the top and bottom of the pile resulting in a net shortening or lengthening of the pile which may be compared to changes in residual stresses at tip of pile (i.e., compression or tension). Other ways of validating or checking the gauges and their responses can be implemented.

The 200 pile data set with over 300,000 blows for piles throughout Florida that the FDOT has collected having both EDC and PDA/CAPWAP data will be used for Task 3 activities. It is expected that this task will begin at the start of the project and last its full length.

1.2.4 Task 4 - Improvements in Estimation of Pile Freeze and Estimates of Pile Axial Capacities

Currently, the PDA and Smartpile use the Case Static Total Pile capacity approach which uses the dynamic force measurements only the top of the pile to assess total static pile resistance. Even though Smartpile uses the top and bottom gauges to estimate the case lumped damping parameter, FDOT project: **BD545-87** has shown that side damping and static skin friction along a pile may be assessed directly using the top and bottom gauges in the pile which may be added to the static tip for improved estimate of total static pile capacity. The new approach may prove quite useful in quantifying pile side friction freeze from tip freeze, since the former has been shown to vary much more than the latter in freeze susceptible soils which supports NCHRP 418. Also of interest, is if the long term static resistance of a pile can be assessed from the EOID, eight to 15 minute as well as 24 hour restrike measurements on a pile. How does total pile capacity vary with time vs. skin and tip resistance.

1.2.5 Task 5 - Report and Database Preparation

Task 5 concerns the recovery and storage of all the static load test results, in situ and EDC pile monitoring data in the FDOT database for futures use of FDOT. In addition, task 5 involves the summarization/recommendation of 1) LRFD resistance factors for EDC monitored piles based on soil/rock type; 2) evaluation of pile driving stresses, damping, static skin and tip resistance using EDC pile monitoring system; 3) evaluate and improve LRFD resistance factors

EDC; and finally 4) evaluate EDC tip sensor for assessing long-term static response of piles founded in high freeze soils.

CHAPTER 2
STATIC LOAD TESTS OF EDC MONITORED PILES

2.1 Introduction

The EDC evaluation program in Phase I showed promising results, which prompted the FDOT to evaluate its reliability through comparison with static load tests on piles monitored with the EDC system. Furthermore, complete adoption of the EDC system required established LRFD resistance factors. To determine these, typically 30 tests guarantee a sufficient set of values for accurately assessing the mean and CV. A total of 17 load test results were collected during Phase II. Of these, five had load tests that were pullout tests giving only measured side friction. The limited tests with measured side and tip from load tests (12) were grouped with the measurements from the five pullout tests to determine the bias and CV for use in determining a total pile capacity resistance factor for EDC. This chapter presents the results from the EDC systems and load test measurements collected from the 17 tests and their summary statistics.

2.2 Static Load Tests at Sample Sites

2.2.1 Site 1 (Dixie Highway)

The site is on SR 810, Dixie Highway at Hillsboro Canal in Broward County, Florida. The site consists of upper layers of approximately 15 m of medium dense sand with cemented sand zones underlain by limestone (bearing layer). The first pile analyzed (pile 1) was a 0.61 m-square by 15.2 m-long prestressed concrete pile, driven to a depth 14 m below the ground surface by a single-acting diesel hammer. One week after installation, restrikes were conducted to investigate whether the skin friction had changed (discussed in later chapter). Then the pile was load tested to failure in accordance to ASTM D1143 (quick test) three days after the restrike. The compression loads were applied using two 500-ton hydraulic jacks.

The results of static compression load test for pile 1 is shown in Figure 2-1. Based on the load test, the ultimate skin friction (75 – 80 tons) was achieved at a small displacement of about 5 mm.

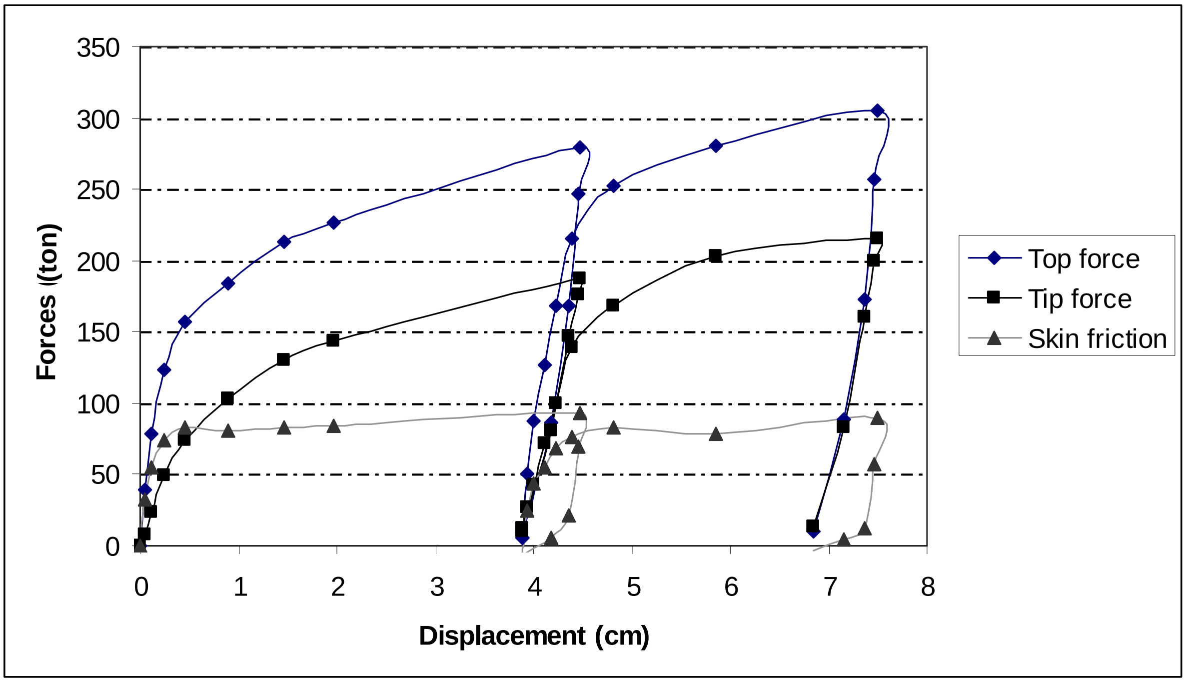

Figure 2-1 Static compression load test of Dixie Highway, End Bent 1

The second pile of this site also was a 0.61-m-square prestressed precast pile also installed approximately 15 m below the ground surface, at Pier 8. Restrikes were conducted 4 days after installation, and the static compression load test was conducted two days after the restrikes.

Figure 2-2 presents the result of the static compression load test for pile 2, which occurred two days after the restrike. The ultimate static skin friction (90 tons) is mobilized at small displacement, approximately 5 mm.

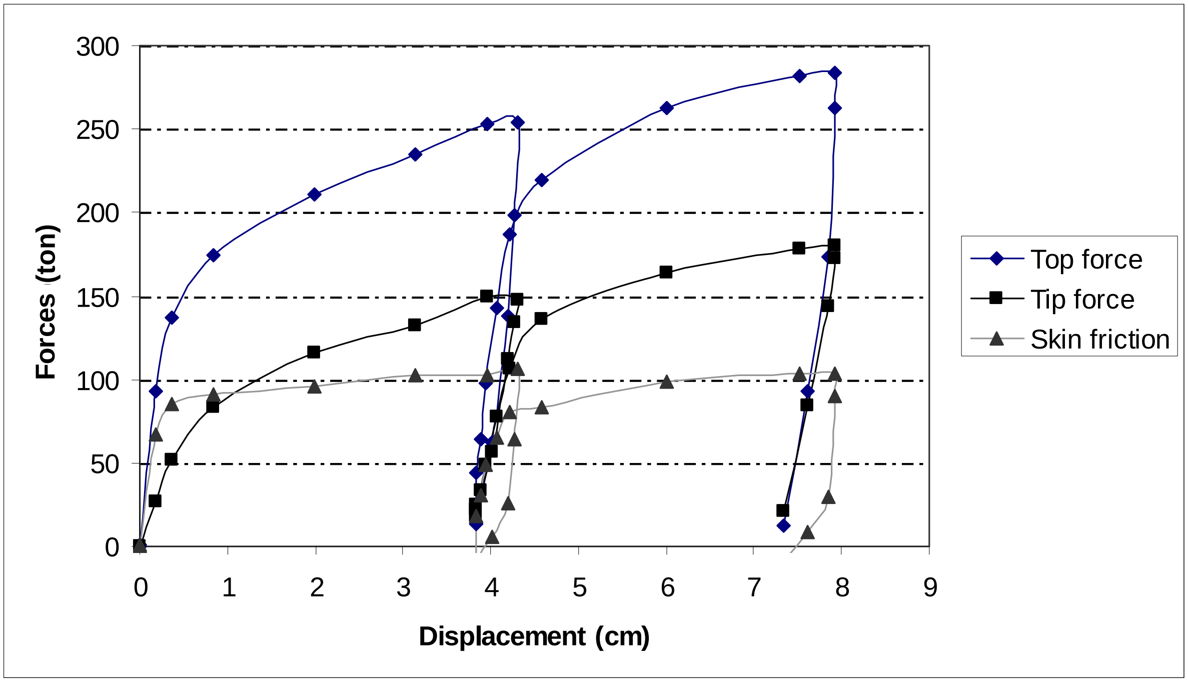

Figure 2-2 Static compression load test of Dixie Highway, Pier 8

Figure 2-3 presents the result of the load test on the third pile located at pier 4, which occurred 3 days after the restrike. The test was a pullout test and the ultimate static skin friction (106 tons) is mobilized at small displacement, approximately 5 mm.

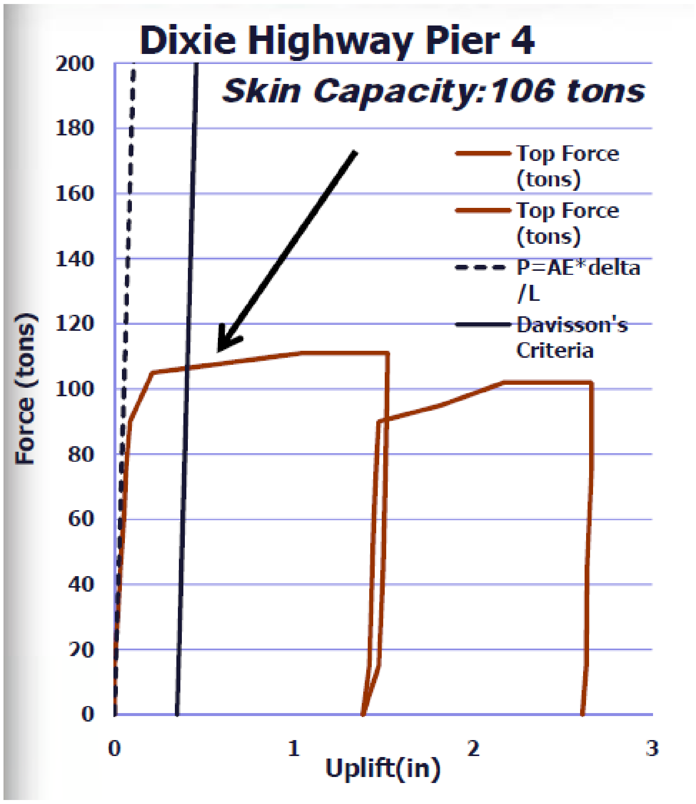

Figure 2-3 Load test of Dixie Highway, Pier 4

2.2.2 Site 2 (Caminada Bay)

Site 2 is at Caminada Bay, Louisiana, 70 km south of New Orleans. The site consists of 2 uppers layers: 1) 10 m of silty fine sand with clay (SPT N ~ 14) and, 2) 10 m of fine sand with silt (SPT N ~ 24); underlain by a high plasticity (40 < PI < 70) clay. The first pile (pile 1) presented is a 0.76-m-square precast prestressed concrete pile installed 21 m below the ground surface using a single acting diesel hammer. Restrikes were conducted 7 days after installation, and the static compression load test was conducted 2 days after the restrikes.

A top down load test was performed on this pile. Shown in Figure 2-4 is the measured top force, as well as skin and tip resistance as a function of displacement. The skin friction was separated from the tip resistance based on strain gauges cast at the tip of the pile. From the load test, the ultimate skin friction (80 Tons) was found at a displacement of approximately 10 mm.

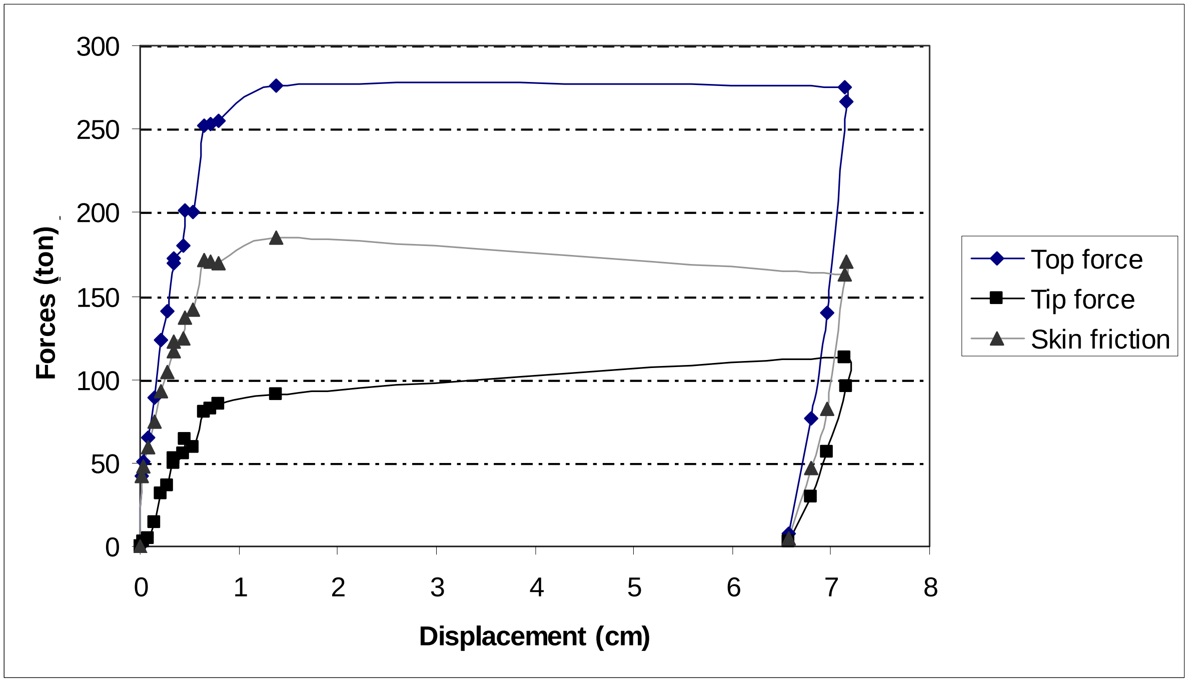

Figure 2-4 Static compression load test of Caminada Bay Pile 1

The second pile at the Caminada Bay site (pile 2) was also a 0.76-m-square precast prestressed concrete pile installed about 21 m below the ground surface. Restrikes were conducted one month after installation, and the static compression load test was conducted 2 days after the restrikes.

The results of a compression load test on pile 2 are shown in Figure 2-5. As with measurements of pile 1, skin friction was separated from the tip resistance based on strain gauges cast at the tip of the pile. From the load test, the ultimate skin friction (240 Tons) was found at a displacement of approximately 20 mm.

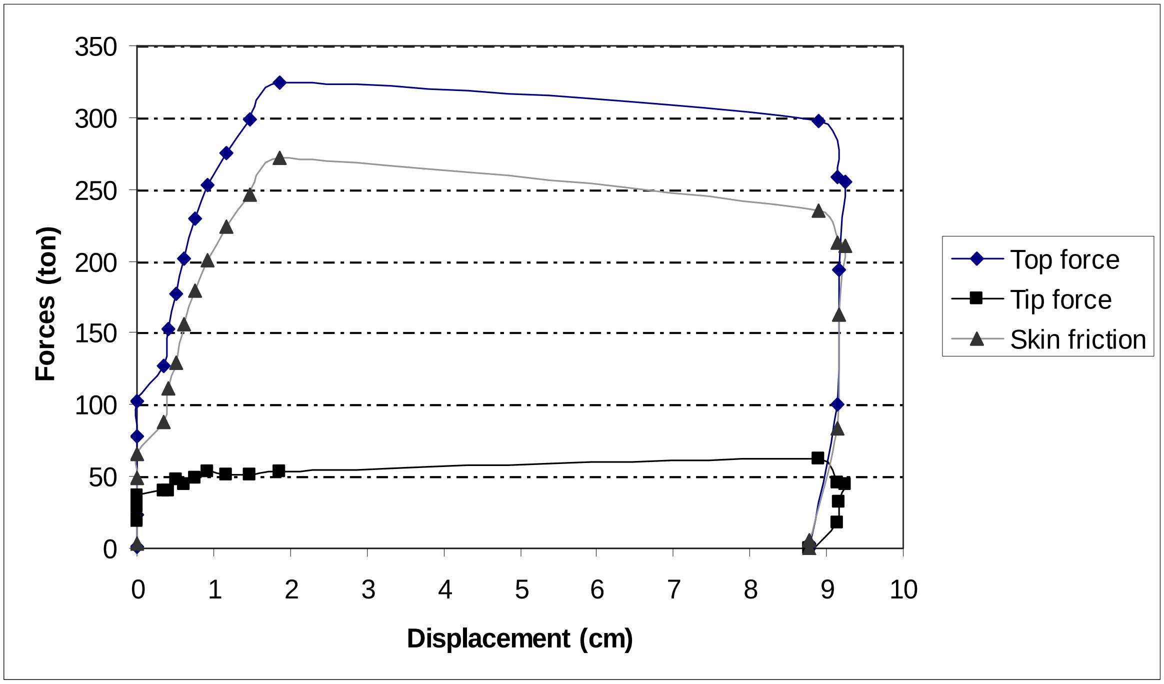

Figure 2-5 Static compression load test of Caminada Bay Pile 2

2.2.3 Site 3 (Bayou Lacassine)

Site 3 is at Jefferson Davis Parish, Louisiana. The site consists of interbedded layers of sandy-silt overlying clay. Both piles were driven with an ICE I-62 diesel hammer with a rated energy of 165 kip-ft. Both piles had Smart-Structure's EDC gauges at the top and bottom of the pile. Applied Foundation Testing monitored both piles.

The first pile (Bent 1, Pile 3) presented was 30" x 75 ft and driven on 9/18/2012 with ICE I-62 hammer with recorded stroke and energy given in Figure 2-6. Evident, little energy was used to drive the pile until elevation -64 ft. Figure 2-7 shows the recorded blow count vs. pile depth with driving stopped at pile depth 70.5 ft.

Shown in Figure 2-8 is the static load response for Bent 1, Pile 1. Evident, the Davisson and ultimate capacities are quite similar. Unfortunately, the EDC tip gauges were not monitored during the static top down test (i.e., no tip load vs. displacement)

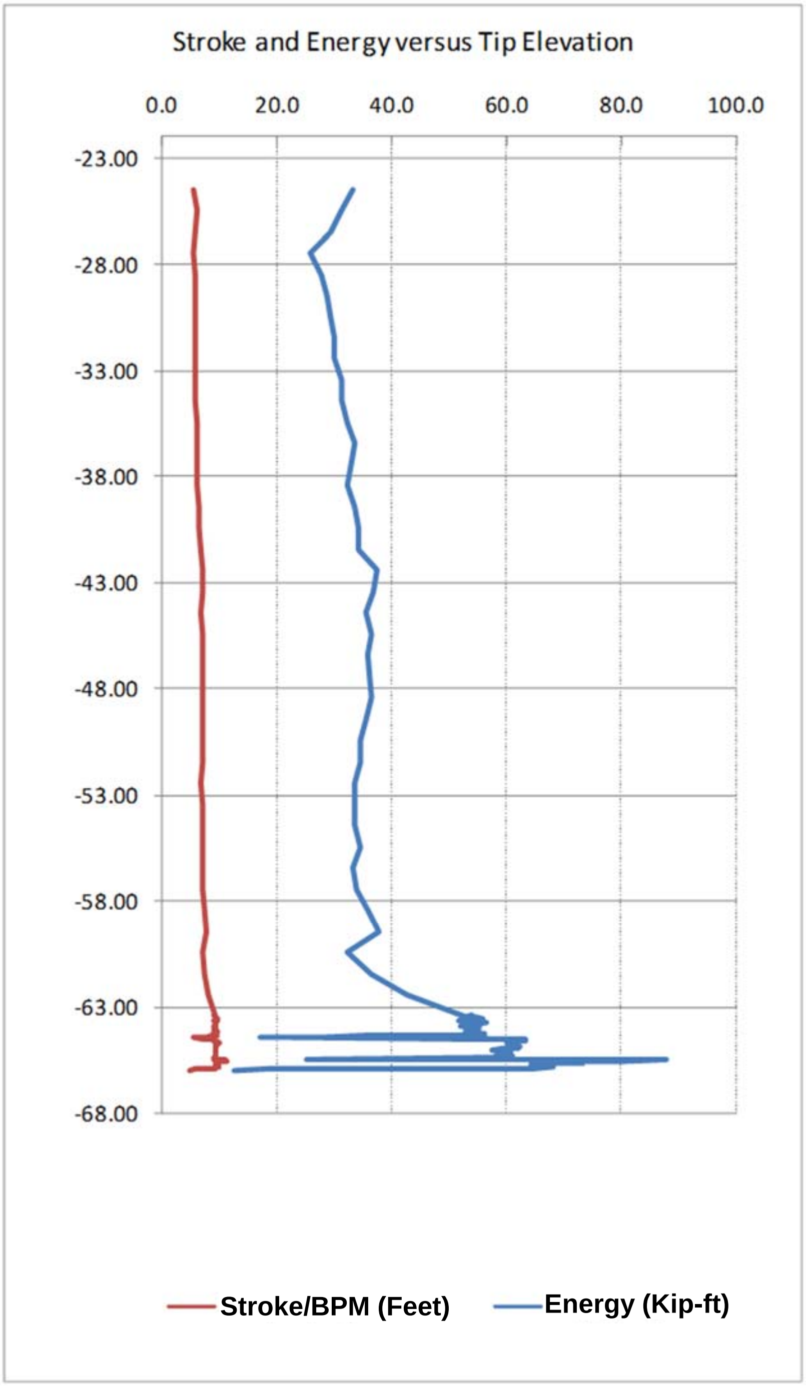

Figure 2-6 Recorded stroke and energy of Bent 1 Pile 3 with ICE I-62

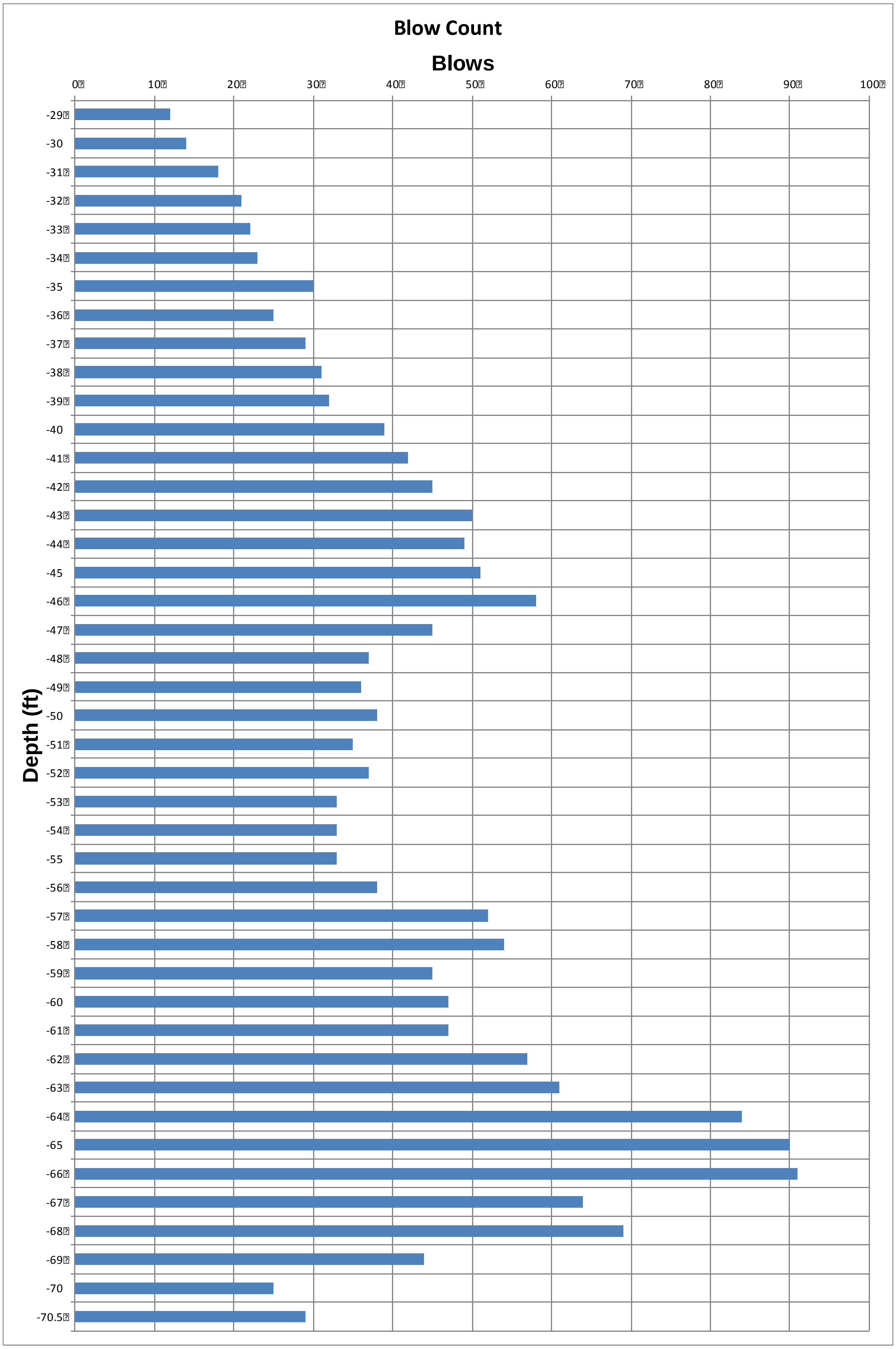

Figure 2-7 Recorded driving record for Bent 1 Pile 3

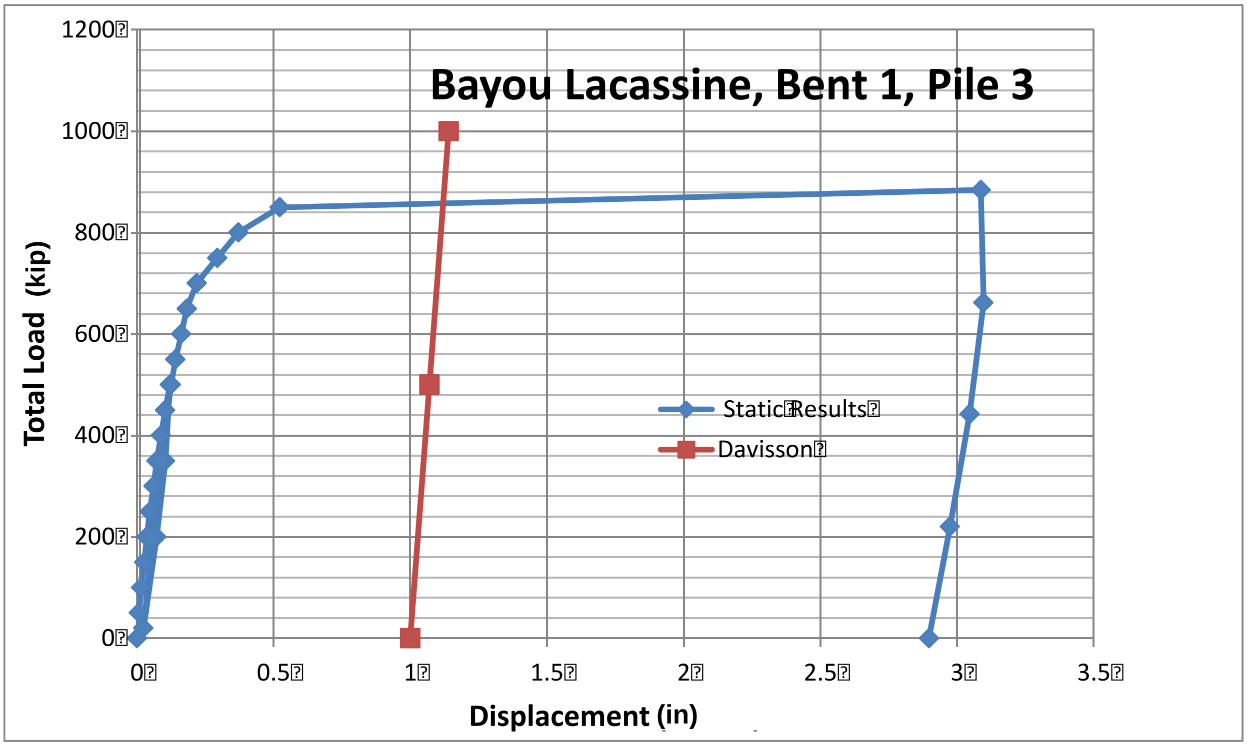

Figure 2-8 Static load test results and Davisson capacity for Bayou Lacassine, Bent 1 Pile 3

The second EDC pile driven at Bayou Lacassine was also a 30” x 75 ft pile. The pile was driven on 10/04/2012 with ICE I-62 hammer and restruck the following day to assess pile freeze. Figure 2-9 shows the recorded blow count vs. pile depth. Driving stopped at a depth of 69.33 ft.

Shown in Figure 2-10 is the static load response for Bent 1, Pile 3. As with Pile 1, the Davisson and ultimate capacities are similar. Note, the Louisiana Department of Transportation (LaDOT) did not report static tip response of pile 3. It was not known if LaDOT instrumented the tip of either piles; however, even though EDC packs were placed at the tip of the piles, SmartStructure’s personnel were not present at time of load tests to monitor tip response.

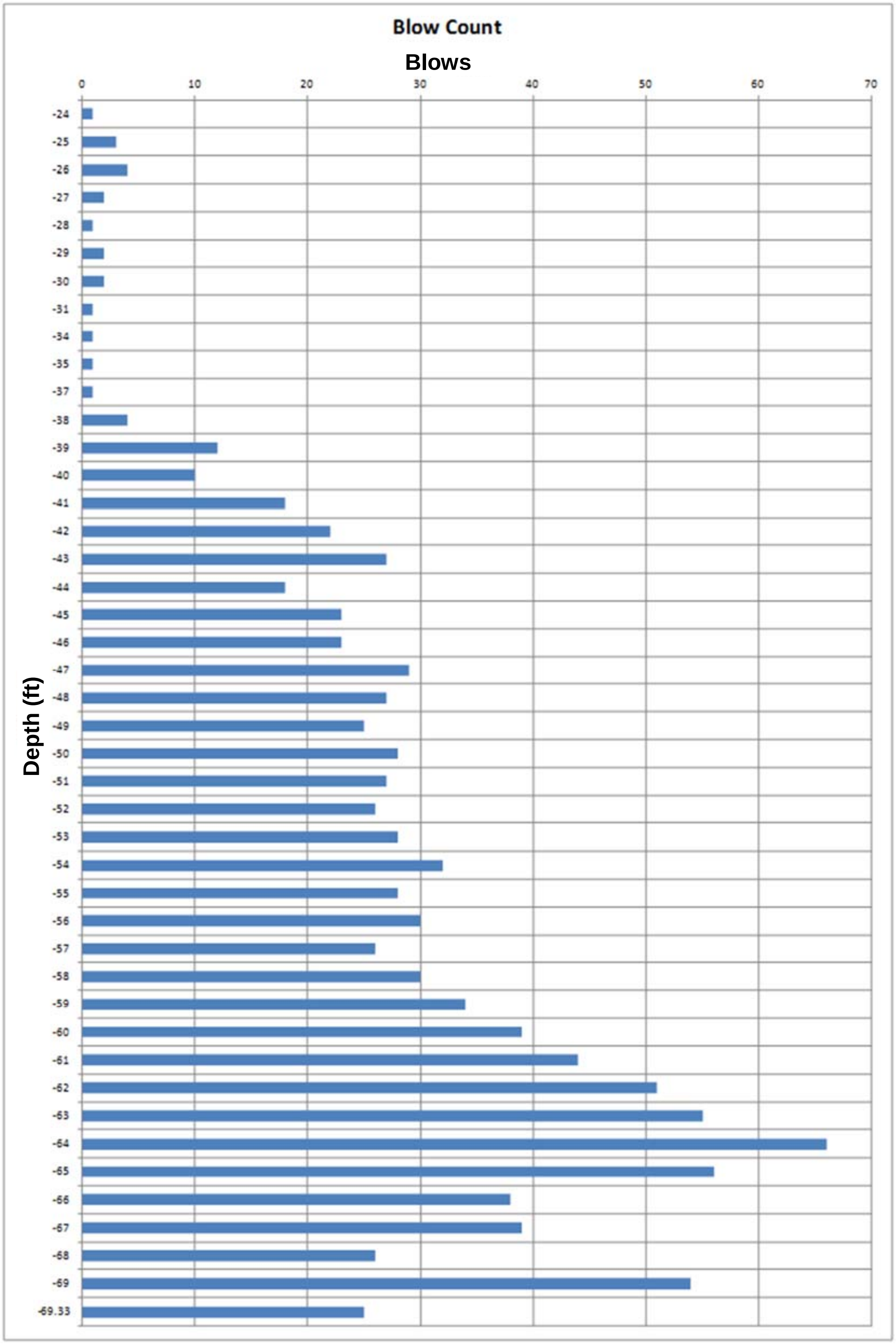

Figure 2-9 Recorded driving record for Bent 1 Pile 1

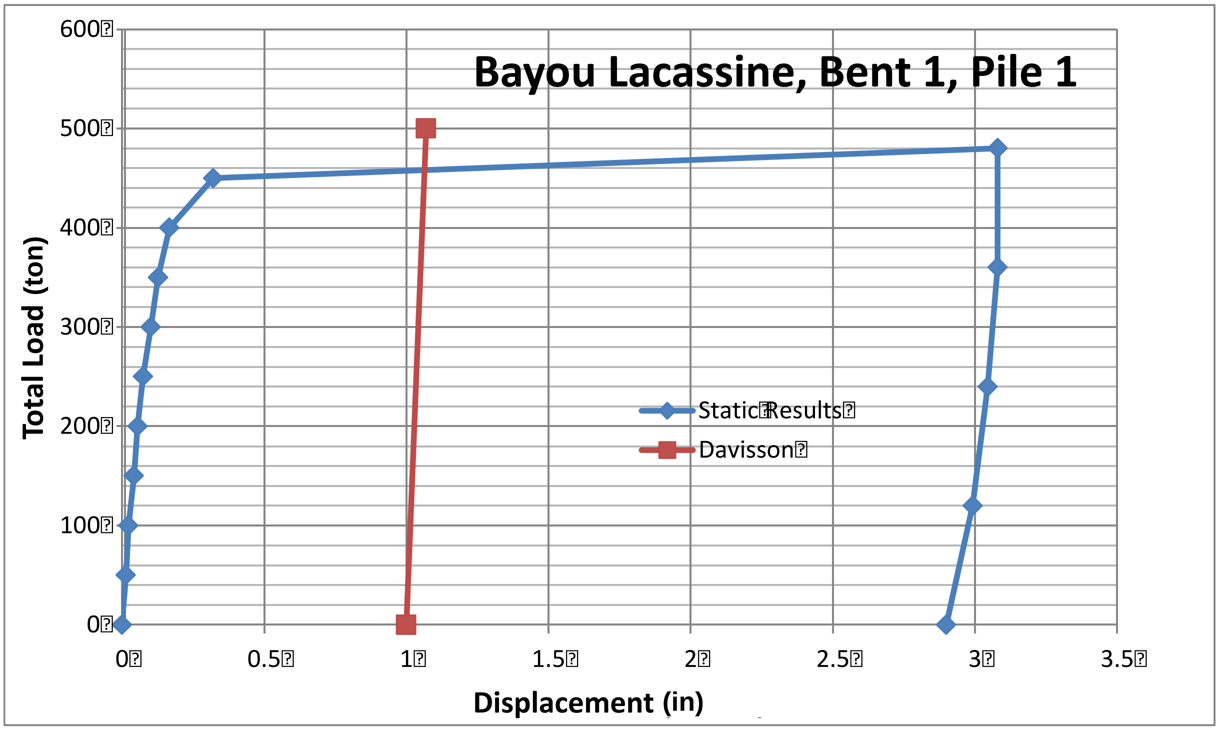

Figure 2-10 Static load test results and Davisson capacity for Bayou Lacassine, Bent 1, Pile 1

2.2.4 Site 4 (I-95 Eau Gallie Bridge)

Site 4 is at Eau Gallie Bridge over I-95. The pile analyzed is a 0.45-m-square precast prestressed concrete pile driven 24 m below the ground surface using a single acting diesel hammer. Restrikes were conducted 16 days after installation. Figure 2-11 shows the ultimate tip capacity (200 kips), side friction capacity (180 Kips) and the Davisson's capacity which is 380 kips.

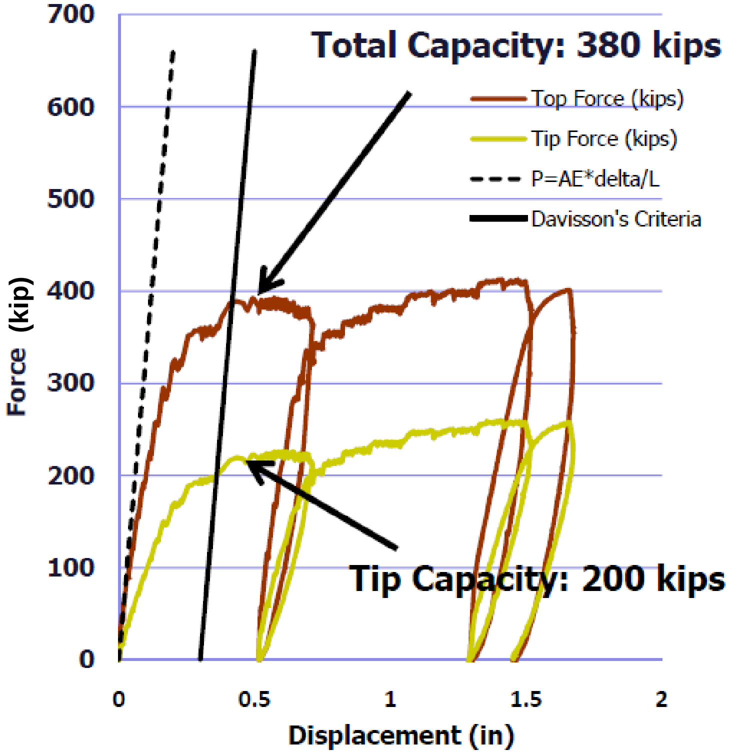

Figure 2-11 Static load test results and Davisson capacity for I-95 Eau Gallie Bridge, Bent 1, Pile 1

2.2.5 Site 5 (5th Street Bascule)

Piles 37 and 52 within Pier 2 were 0.61-m-square pre-stressed concrete piles, driven to a depth of approximately 29 m below the ground surface. Piles 42 and 9 were in Pier 3 and were also 0.61-m-square pre-stressed concrete piles, driven to a depth of, approximately, 29 m below the ground surface.

Figure 2-12 shows the skin friction from the initial pull for each pile. At Pier 3, pile 42 showed a skin friction of 76 tons while Pile 9 showed 36 tons. At Pier 2, Pile 53 showed 90 tons while Pile 37 showed 93 tons. Note, these load tests are uplift tests only, i.e., skin friction; since no tip or static top down is mobilized. The measured and predicted (presented in a later chapter) is only for skin friction.

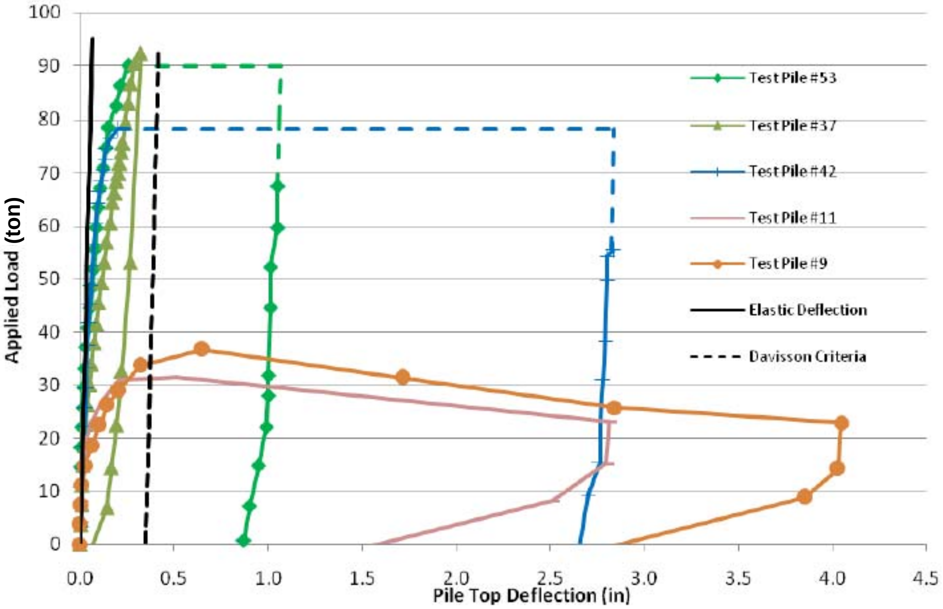

Figure 2-12 Initial tension pile load tests and Davisson capacity for Piles 53, 37, 42, and 9

2.3 Summary of Static Load Tests at Sample Sites

Shown in Table 1 is the all of the collected data which have load tests. The database consists of 12 piles (8-Florida, and 4-Louisiana), eight are top-down compression and four are uplift or tension piles. The values presented in the table will be used to analyze measured versus predicted (EDC/SmartPile) skin, tip and total resistance and calculate an associated LRFD resistance factor.

Table 2-1 Collected measured pile response

	MEASURED		
Site & Pile	Davisson Capacity	Tip Capacity	Skin Resistance
	(Kip)	(Kip)	(Kip)
Dixie Highway End Bent 1	430	296	134
Dixie Highway Pier 8	380	200	180
Caminida Bay Bent 1, LADOT	540	144.8	395.2
Caminida Bay Bent 7 LADOT	625	80	545
Bayou Lacassine LADOT, Bent 1 Pile 1	460		
Bayou Lacassine LADOT, Bent 1 Pile 3	845		
I-95 Jax	380	200	180
Dixie Highway Pier 4			212
5th St Bascule Pier2 Pile 37			185
5th St Bascule Pier2 Pile 53			180
5th St Bascule Pier 3 Pile 9			68
5th St Bascule Pier 3 Pile 42			153

CHAPTER 3
COMPARISON OF EDC TO PDA AND CAPWAP RESULTS

3.1 Introduction

An important component of this research was the comparison of EDC to PDA and CAPWAP results. This includes top and bottom compression stresses (CSX and CSB), tension stresses (TSX), hammer energy transfer to pile (EMX), pile damage (Beta), Case Fixed Static Pile Capacity from EDC to PDA (Fixed/PDA), and Variable UF Static Pile Capacity from EDC to PDA (UF/PDA). In the case of the Variable UF Static Pile Capacity from EDC to PDA (UF/PDA), the case fixed damping ratio, J_{cL}, used in the PDA static capacity estimates was from CAPWAP, whereas for the EDC it was obtained from the ratio of top and toe velocities.

A total of 150 piles and 235,000 blows were considered in the analysis. All piles and associated EDC zip files (BDF) were located on SmartStructure's portal and were downloaded for this effort. Also available were PDA and CAPWAP results provided by the CEI for each site. The analysis started with EDC's SmartPile Review version 3.6 and progressed with time to version 3.761. The comparison were carried out by blow, as well as average pile response. For the comparison, a number of Excel sheets were developed to obtain summary statistics (mean, median, standard deviation) for both pile and blow response. Finally, individual comparisons (plots) of EDC response vs. CAPWAP for total, side and tip resistance are presented. A discussion of each follows.

3.2 Development of Excel Spreadsheets for EDC/PDA/CAPWAP Comparisons

The work initiated with automation of statistical comparisons for versions 3.6 and 3.72 of EDC, PDA and CAPWAP results. To automate the comparison process, it was important to have uniformity of naming convention of the session reports. To achieve uniformity in file names and their content, various procedures were tried and tested. First, all the files are placed in one directory with different folders according to their versions. Figure 3-1 shows and explains the Directory in details. This will be the standard directory for further access and comparison. To access all the files without confusion, each file is given an index number, Figure 3-2.

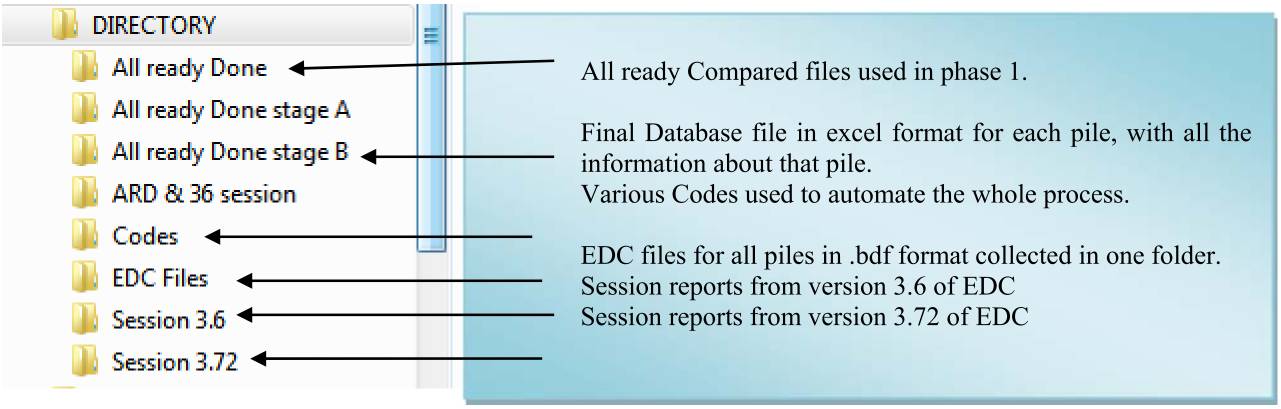

All ready Compared files used in phase 1.

Final Database file in excel format for each pile, with all the information about that pile.
Various Codes used to automate the whole process.

EDC files for all piles in .bdf format collected in one folder.
Session reports from version 3.6 of EDC
Session reports from version 3.72 of EDC

Figure 3-1 Default directory

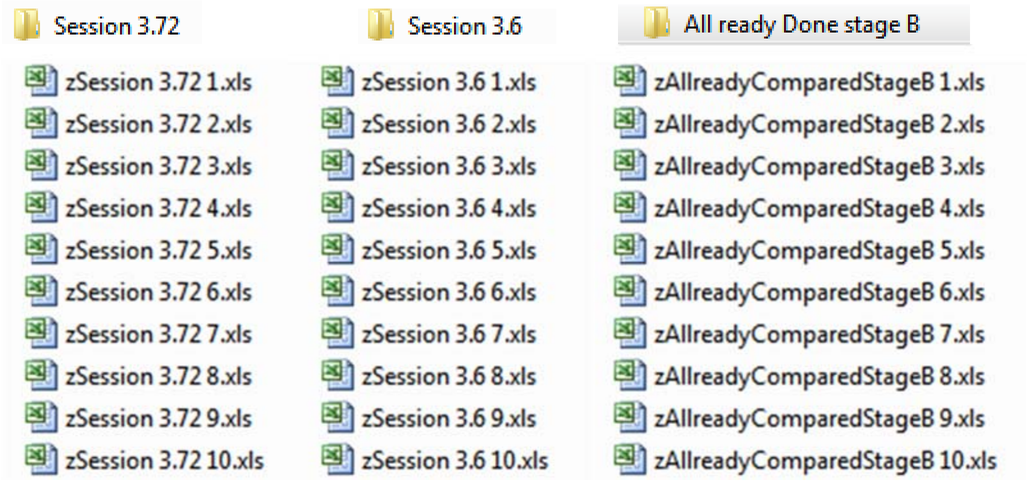

Session reports for 3.72   Session reports for 3.6   Final Database file for Pile 1 to 10

Figure 3-2 Folder contents

The codes used for the automation process can be separated into three separate stages:

- Stage 1. Running all the piles through the different version of Smart Pile Review (e.g., Ver 3.6, 3.72, etc.) and generating session reports;

- Stage 2. Creating database files for each pile with EDC/PDA comparisons for each version: Using Excel macro named “All_IN_One_Beta”
- Stage 3. Collecting all the statistical results from each pile in final database file using Excel macro named “Get_Data”.

Note, “All_IN_One_Beta” (e.g., Figure 3-3) and “Get_Data” macros are embedded in a file named as “All In One Beta 4.xlsm”. This file also collects statistical results from each pile. These codes and their function are explained next.

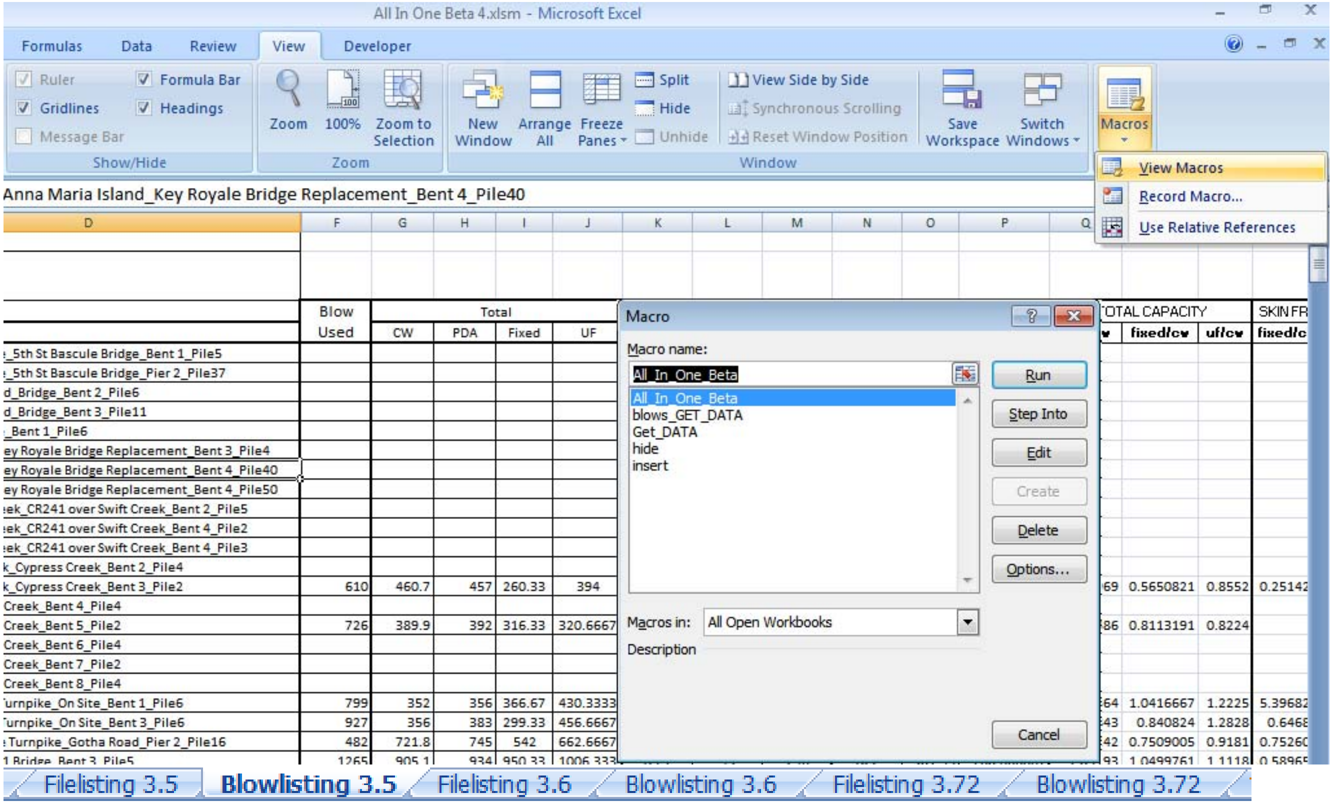

Anna Maria Island_Key Royale Bridge Replacement_Bent 4_Pile40

D	Blow Used	Total CW	Total PDA	Total Fixed	Total UF
_5th St Bascule Bridge_Bent 1_Pile5					
_5th St Bascule Bridge_Pier 2_Pile37					
d_Bridge_Bent 2_Pile6					
d_Bridge_Bent 3_Pile11					
_Bent 1_Pile6					
ey Royale Bridge Replacement_Bent 3_Pile4					
ey Royale Bridge Replacement_Bent 4_Pile40					
ey Royale Bridge Replacement_Bent 4_Pile50					
ek_CR241 over Swift Creek_Bent 2_Pile5					
ek_CR241 over Swift Creek_Bent 4_Pile2					
ek_CR241 over Swift Creek_Bent 4_Pile3					
k_Cypress Creek_Bent 2_Pile4					
k_Cypress Creek_Bent 3_Pile2	610	460.7	457	260.33	394
Creek_Bent 4_Pile4					
Creek_Bent 5_Pile2	726	389.9	392	316.33	320.6667
Creek_Bent 6_Pile4					
Creek_Bent 7_Pile2					
Creek_Bent 8_Pile4					
urnpike_On Site_Bent 1_Pile6	799	352	356	366.67	430.3333
urnpike_On Site_Bent 3_Pile6	927	356	383	299.33	456.6667
Turnpike_Gotha Road_Pier 2_Pile16	482	721.8	745	542	662.6667
1 Bridge_Bent 3_Pile5	1265	905.1	934	950.33	1006.333

TOTAL CAPACITY fixed/cw	TOTAL CAPACITY uf/cw	SKIN FR fixed/c
0.5650821	0.8552	0.25142
0.8113191	0.8224	
1.0416667	1.2225	5.39682
0.840824	1.2828	0.6468
0.7509005	0.9181	0.75260
1.0499761	1.1118	0.58965

Macro name: All_In_One_Beta

All_In_One_Beta
blows_GET_DATA
Get_DATA
hide
insert

Macros in: All Open Workbooks

Description

Figure 3-3 All-in-one Beta 4.xlsm file

It should be noted that, all these embedded codes were developed in Microsoft Excel 2007, are macro enabled, and require the user to have Microsoft’s Excel 2007 for proper operation. Also each code will ask the user to enable the macro to run these codes (Figures 3-4 and 3-5). Also a ‘Read Me’ file was created to assist user for using the embedded codes. A discussion of each follows.

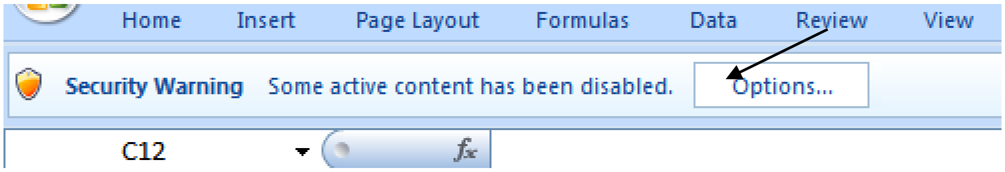

Security Warning Some active content has been disabled.

Figure 3-4 Security warning at the opening of file

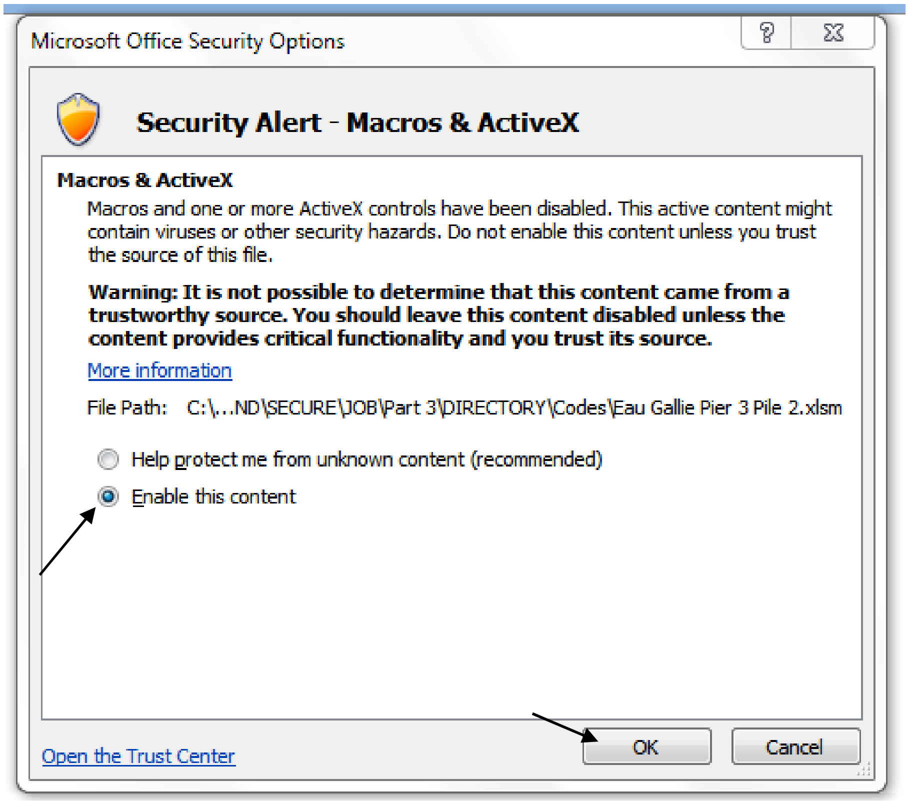

Microsoft Office Security Options

Security Alert - Macros & ActiveX

Macros & ActiveX

Macros and one or more ActiveX controls have been disabled. This active content might contain viruses or other security hazards. Do not enable this content unless you trust the source of this file.

Warning: It is not possible to determine that this content came from a trustworthy source. You should leave this content disabled unless the content provides critical functionality and you trust its source.

More information

File Path: C:\...ND\SECURE\JOB\Part 3\DIRECTORY\Codes\Eau Gallie Pier 3 Pile 2.xlsm

○ Help protect me from unknown content (recommended)

● Enable this content

Open the Trust Center

Figure 3-5 Enable the macros for activating and running Macro

3.2.1 Stage 2 All_In_One_Beta

This Excel sheet generates the database sheet for each pile that will have all the information about a specific pile. Creating one file for each pile with all the information (EDC, PDA, etc.) is important for subsequent stage activities. Each pile has one ‘All ready compared file’, which contains various graphs, Session details, Drive calculations and Blow distributions of previous versions and PDA Data for that particular pile. To compare any new version of EDC with PDA or CAPWAP, each pile has to be run through a version of Smart Pile Review to get session report. For this effort initially, all piles were run through version 3.6 and version 3.72 of EDC generating respective session reports. Next, these session reports are saved in the directory with a sequential name, e.g., session report for version 3.6 of EDC for pile number 29 in the database will be renamed as zSession 3.6 29.xls. This way, uniformity in naming the files is achieved which will enable any other Excel sheets to access all files one after the other without human interaction.

'All_In_One_Beta' is a code that copies Drive calculations, Session Details and Blow Distribution from session report for all available versions, (e.g., version 3.6 and version 3.72) and pastes it in 'All ready compared files'. These new sheets are named as per their version number. e.g., Drive Calculation sheet for 3.6 version is renamed as "Drive Calculations 3.6", Session Details as "Session Details 3.6" and so on. All the previous sheets in All ready done files are renamed as "Drive Calculations 3.5", "Session Details 3.5" and so on as can be seen in figure 3-6.

Figure 3-6 New database sheet for each pile

It should be noted that "All_In_One_Beta" also realigns the blow distribution for all versions with PDA blows. That is, it checks the alignment and blow distribution according to Column B of Excel sheet, which may skip or deletes unnecessary blows from the latest session report. This is particularly important to achieve uniformity in all versions and to make sure that corresponding blows of EDC and PDA align.

After aligning the data, the code computes EDC/PDA ratios in Column BA to BE for each blow. Next, the average, standard deviation and coefficient of variation are generated in columns CA4 to CN4 for all the blows. In the case of restrikes, columns CA5 to CN5 and CA6 to CN6 hold the EDC/PDA ratios. The code also searches the blows to see if CAPWAP result were available and collects that blow data in columns CA11 to DN11. Subsequent blows with CAPWAP data follow one another. Finally, the file is saved in the default directory "All ready compare stage B" folder. Figure 3-7 represents one such file and contents. All this information is generated first for previous versions, e.g., version 3.6 and then later versions, i.e., 3.72.

3.2.2 Stage 3 "Get_Data"

After generating all the blow comparisons for each pile, all the blow data must be collected into one Excel file so that all the results can be used to find summary statistics. This is achieved using another macro which is accessed from "All In One Beta 4" file (Figure 3-3). The code, "Get_Data" collects the Average, Standard deviation and Covariance from each file along with restrikes and arranges them in "All In One Beta 4.xlsm". The code also collects blow data for comparison of EDC with CAPWAP for plotting purposes. All this information is stored in "Blowlisting" sheet in the "All in One Beta 4" spreadsheet by SmartPile version number, e.g., Figure 3-9.

Also stored in "All In One Beta 4.xlm" under sheet "Filelisting" (Figure 3-8) sheet is the general EDC pile information: index #, name, Radio ID, CAPWAP blow, number of restrikes, restrike Blow etc. along with statistical results for all concurrent blows from column X onwards. Blow listing sheet has the same information in it but statistical results are for blows for which CAPWAPs are available. These blow numbers are represented in column H to K of each sheet.

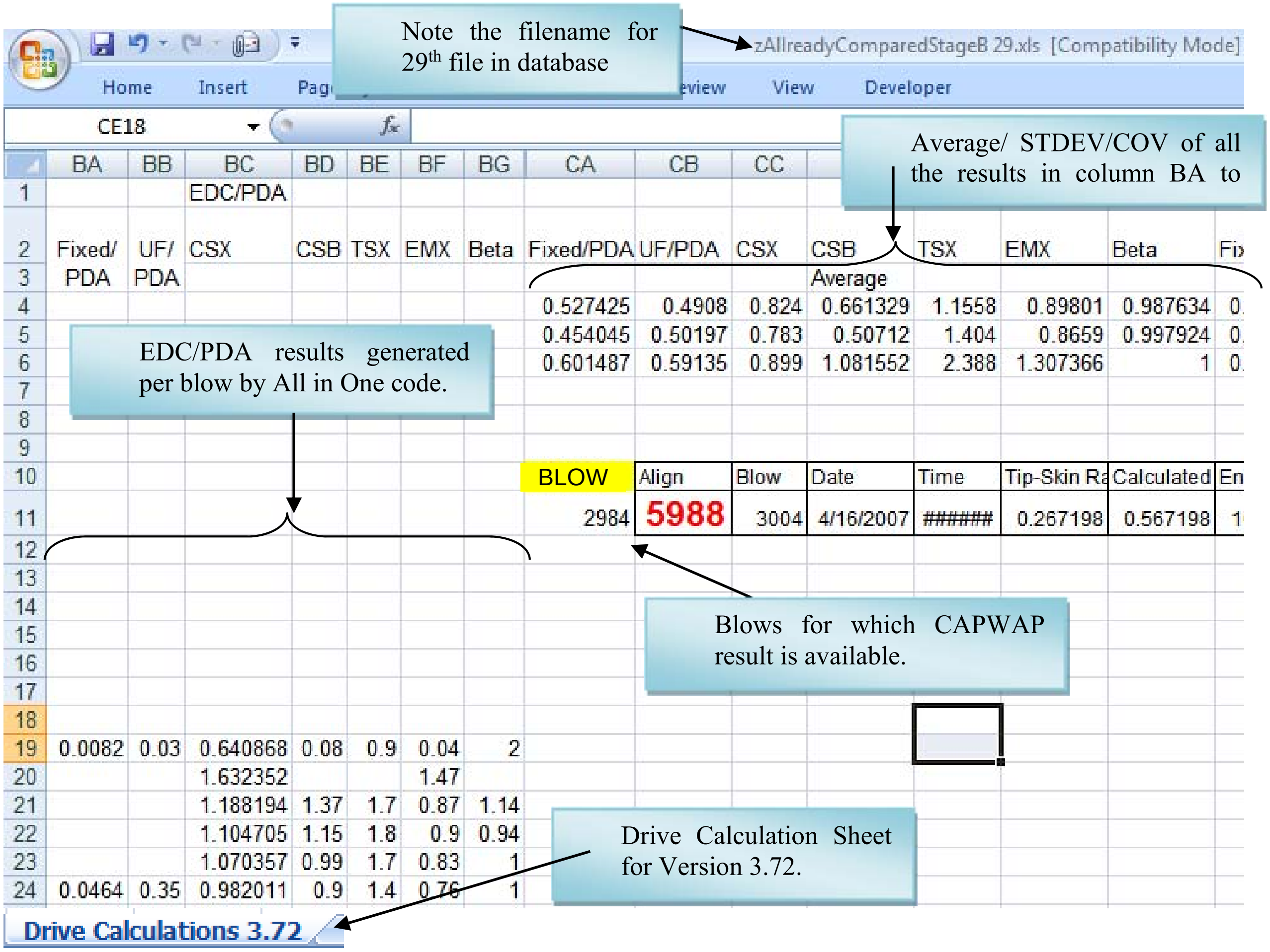

Note the filename for 29th file in database

Average/ STDEV/COV of all the results in column BA to

EDC/PDA results generated per blow by All in One code.

Blows for which CAPWAP result is available.

Drive Calculation Sheet for Version 3.72.

	BA	BB	BC	BD	BE	BF	BG	CA	CB	CC					
1			EDC/PDA												
2	Fixed/	UF/	CSX	CSB	TSX	EMX	Beta	Fixed/PDA	UF/PDA	CSX	CSB	TSX	EMX	Beta	Fi
3	PDA	PDA									Average				
4								0.527425	0.4908	0.824	0.661329	1.1558	0.89801	0.987634	0.
5								0.454045	0.50197	0.783	0.50712	1.404	0.8659	0.997924	0.
6								0.601487	0.59135	0.899	1.081552	2.388	1.307366	1	0.
7															
8															
9															
10								BLOW	Align	Blow	Date	Time	Tip-Skin Ra	Calculated	En
11								2984	5988	3004	4/16/2007	######	0.267198	0.567198	1
12															
13															
14															
15															
16															
17															
18															
19	0.0082	0.03	0.640868	0.08	0.9	0.04	2								
20			1.632352			1.47									
21			1.188194	1.37	1.7	0.87	1.14								
22			1.104705	1.15	1.8	0.9	0.94								
23			1.070357	0.99	1.7	0.83	1								
24	0.0464	0.35	0.982011	0.9	1.4	0.76	1								

Figure 3-7 Sample database file for each pile

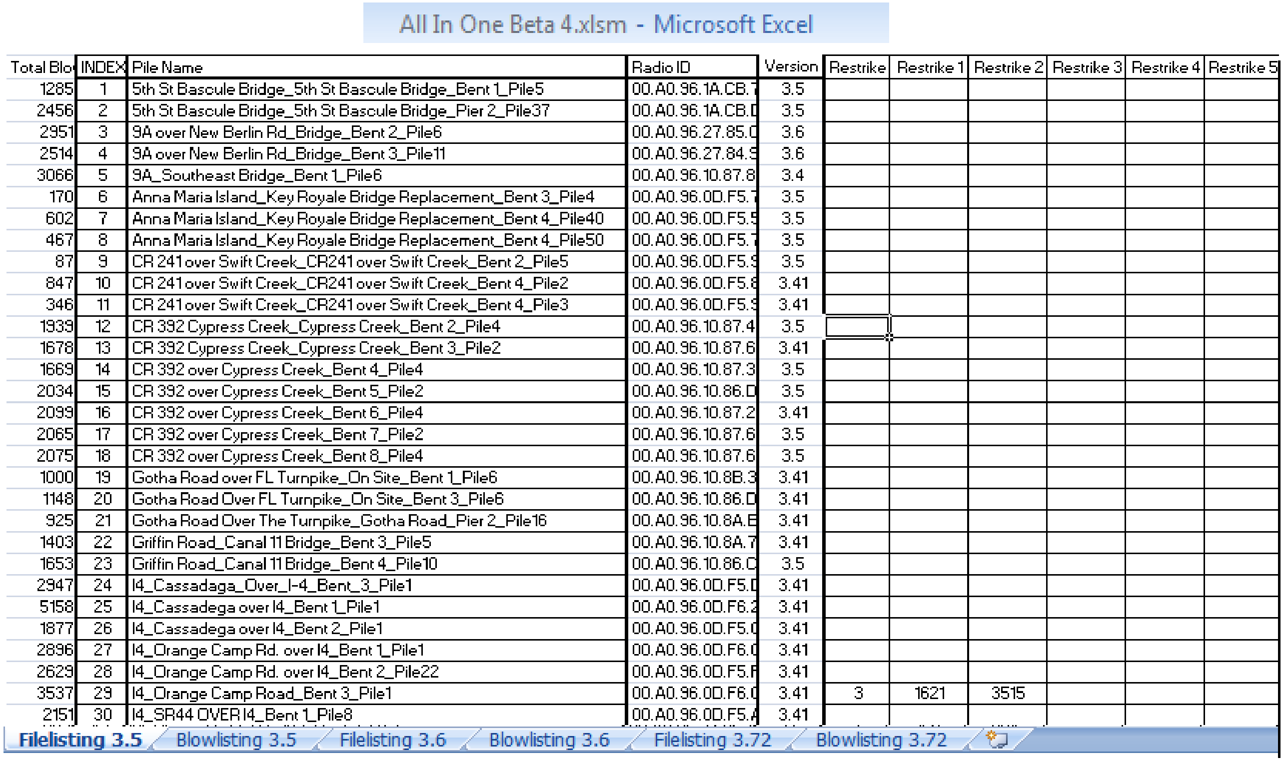

Total Blo	INDEX	Pile Name	Radio ID	Version	Restrike	Restrike 1	Restrike 2	Restrike 3	Restrike 4	Restrike 5
1285	1	5th St Bascule Bridge_5th St Bascule Bridge_Bent 1_Pile5	00.A0.96.1A.CB.7	3.5						
2456	2	5th St Bascule Bridge_5th St Bascule Bridge_Pier 2_Pile37	00.A0.96.1A.CB.D	3.5						
2951	3	9A over New Berlin Rd_Bridge_Bent 2_Pile6	00.A0.96.27.85.0	3.6						
2514	4	9A over New Berlin Rd_Bridge_Bent 3_Pile11	00.A0.96.27.84.9	3.6						
3066	5	9A_Southeast Bridge_Bent 1_Pile6	00.A0.96.10.87.8	3.4						
170	6	Anna Maria Island_Key Royale Bridge Replacement_Bent 3_Pile4	00.A0.96.0D.F5.7	3.5						
602	7	Anna Maria Island_Key Royale Bridge Replacement_Bent 4_Pile40	00.A0.96.0D.F5.5	3.5						
467	8	Anna Maria Island_Key Royale Bridge Replacement_Bent 4_Pile50	00.A0.96.0D.F5.7	3.5						
87	9	CR 241 over Swift Creek_CR241 over Swift Creek_Bent 2_Pile5	00.A0.96.0D.F5.9	3.5						
847	10	CR 241 over Swift Creek_CR241 over Swift Creek_Bent 4_Pile2	00.A0.96.0D.F5.8	3.41						
346	11	CR 241 over Swift Creek_CR241 over Swift Creek_Bent 4_Pile3	00.A0.96.0D.F5.9	3.41						
1939	12	CR 392 Cypress Creek_Cypress Creek_Bent 2_Pile4	00.A0.96.10.87.4	3.5						
1678	13	CR 392 Cypress Creek_Cypress Creek_Bent 3_Pile2	00.A0.96.10.87.6	3.41						
1669	14	CR 392 over Cypress Creek_Bent 4_Pile4	00.A0.96.10.87.3	3.5						
2034	15	CR 392 over Cypress Creek_Bent 5_Pile2	00.A0.96.10.86.D	3.5						
2099	16	CR 392 over Cypress Creek_Bent 6_Pile4	00.A0.96.10.87.2	3.41						
2065	17	CR 392 over Cypress Creek_Bent 7_Pile2	00.A0.96.10.87.6	3.5						
2075	18	CR 392 over Cypress Creek_Bent 8_Pile4	00.A0.96.10.87.6	3.5						
1000	19	Gotha Road over FL Turnpike_On Site_Bent 1_Pile6	00.A0.96.10.8B.3	3.41						
1148	20	Gotha Road Over FL Turnpike_On Site_Bent 3_Pile6	00.A0.96.10.86.D	3.41						
925	21	Gotha Road Over The Turnpike_Gotha Road_Pier 2_Pile16	00.A0.96.10.8A.E	3.41						
1403	22	Griffin Road_Canal 11 Bridge_Bent 3_Pile5	00.A0.96.10.8A.7	3.41						
1653	23	Griffin Road_Canal 11 Bridge_Bent 4_Pile10	00.A0.96.10.86.C	3.5						
2947	24	I4_Cassadaga_Over_I-4_Bent_3_Pile1	00.A0.96.0D.F5.D	3.41						
5158	25	I4_Cassadega over I4_Bent 1_Pile1	00.A0.96.0D.F6.2	3.41						
1877	26	I4_Cassadega over I4_Bent 2_Pile1	00.A0.96.0D.F5.0	3.41						
2896	27	I4_Orange Camp Rd. over I4_Bent 1_Pile1	00.A0.96.0D.F6.0	3.41						
2629	28	I4_Orange Camp Rd. over I4_Bent 2_Pile22	00.A0.96.0D.F5.F	3.41						
3537	29	I4_Orange Camp Road_Bent 3_Pile1	00.A0.96.0D.F6.0	3.41	3	1621	3515			
2151	30	I4_SR44 OVER I4_Bent 1_Pile8	00.A0.96.0D.F5.A	3.41						

Figure 3-8 Different sheets on all-in-one Beta 4 file (File listing 3.5)

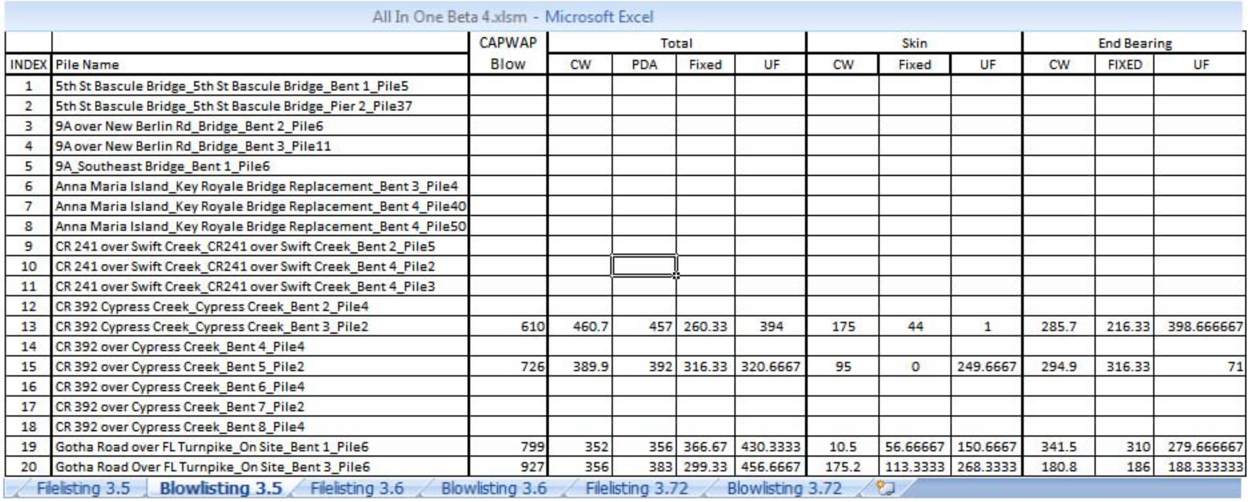

		CAPWAP	Total				Skin			End Bearing		
INDEX	Pile Name	Blow	CW	PDA	Fixed	UF	CW	Fixed	UF	CW	FIXED	UF
1	5th St Bascule Bridge_5th St Bascule Bridge_Bent 1_Pile5											
2	5th St Bascule Bridge_5th St Bascule Bridge_Pier 2_Pile37											
3	9A over New Berlin Rd_Bridge_Bent 2_Pile6											
4	9A over New Berlin Rd_Bridge_Bent 3_Pile11											
5	9A_Southeast Bridge_Bent 1_Pile6											
6	Anna Maria Island_Key Royale Bridge Replacement_Bent 3_Pile4											
7	Anna Maria Island_Key Royale Bridge Replacement_Bent 4_Pile40											
8	Anna Maria Island_Key Royale Bridge Replacement_Bent 4_Pile50											
9	CR 241 over Swift Creek_CR241 over Swift Creek_Bent 2_Pile5											
10	CR 241 over Swift Creek_CR241 over Swift Creek_Bent 4_Pile2											
11	CR 241 over Swift Creek_CR241 over Swift Creek_Bent 4_Pile3											
12	CR 392 Cypress Creek_Cypress Creek_Bent 2_Pile4											
13	CR 392 Cypress Creek_Cypress Creek_Bent 3_Pile2	610	460.7	457	260.33	394	175	44	1	285.7	216.33	398.666667
14	CR 392 over Cypress Creek_Bent 4_Pile4											
15	CR 392 over Cypress Creek_Bent 5_Pile2	726	389.9	392	316.33	320.6667	95	0	249.6667	294.9	316.33	71
16	CR 392 over Cypress Creek_Bent 6_Pile4											
17	CR 392 over Cypress Creek_Bent 7_Pile2											
18	CR 392 over Cypress Creek_Bent 8_Pile4											
19	Gotha Road over FL Turnpike_On Site_Bent 1_Pile6	799	352	356	366.67	430.3333	10.5	56.66667	150.6667	341.5	310	279.666667
20	Gotha Road Over FL Turnpike_On Site_Bent 3_Pile6	927	356	383	299.33	456.6667	175.2	113.3333	268.3333	180.8	186	188.333333

Figure 3-9 Different sheets on all-in-one Beta 4 file (Blow listing 3.5)

3.3 Comparison of PDA/CAPWAP to Earlier Versions (up to 3.72) of EDC SmartPile Review

The following tables show the statistical results obtained using macros to perform comparisons of PDA with various EDC versions. Table 3-1 represents all the earlier version of SmartPile Review (e.g., version 3.5) irrespective of their version number. Tables 3-2 and 3-3 are for version 3.6 and 3.72 statistical results, respectively. Restrikes are not included in these tables.

In Tables 3-2 and 3-3, count implies total number of piles that were involved in the comparison. Each pile has one average EDC/PDA comparison for each of the quantities like CSX, CSB, etc. All average values were obtained from "All In One Beta 4.xlsm" spreadsheet. Piles included in the "Count" have average values that are within ±3 standard deviation of the mean. The average of all the pile (137) averages, e.g., EDC fixed/PDA was **0.967**, are presented in Table 3-1. The same procedure is adapted for each version and for each EDC/PDA ratio, i.e., for quantities like CSX, CSB etc.

A comparison of the results in Tables 3-1 through 3-3, suggest the assessment of capacities, stresses, energies, etc. increased from the earlier versions to version 3.6. However, from version 3.6 to 3.72, the ratio of capacities (fixed/PDA, UF/PDA), bottom compression stress, CSB, tension stress, TSX, and energy, EMX diminished. Interestingly, version 3.72 shows both Fixed and UF EDC/PDA with similar mean capacity ratios (0.898) and similar COV (0.18 – 0.19). Compression stress ratios, CSX, are similar for all versions, but tip compression stresses, CSB, diminished from 0.764 to 0.761 to 0.714. The results are for 137 piles which were available at the time for comparison in the FDOT database.

Table 3-1 Summary pile results all earlier versions

	All Version earlier 3.6						
	Fixed/PDA	UF/PDA	CSX	CSB	TSX	EMX	Beta
Count	137	136	135	136	129	135	131
Average	**0.967**	1.084	0.926	0.764	1.192	1.009	0.982
Standard Deviation	0.189	0.205	0.086	0.238	0.294	0.214	0.036
COV	0.195	0.189	0.093	0.311	0.247	0.212	0.037
%n	0.985	0.978	0.978	0.985	0.977	0.985	0.970
Median	0.954	1.076	0.930	0.803	1.204	1.003	0.979

Table 3-2 Summary pile results version 3.6

	Version 3.6						
	Fixed/PDA	UF/PDA	CSX	CSB	**TSX**	EMX	Beta
Count	133	134	132	128	127	134	130
Average	0.992	1.126	0.924	0.761	1.206	1.010	0.977
Standard Deviation	0.200	0.241	0.089	0.191	0.302	0.264	0.051
COV	0.201	0.214	0.097	0.250	0.250	0.259	0.052
%n	0.970	0.978	0.970	0.962	0.976	0.992	0.977
Median	0.988	1.102	0.924	0.775	1.206	1.004	0.974

Table 3-3 Summary pile results version 3.72

	Version 3.72						
	Fixed/PDA	UF/PDA	CSX	CSB	**TSX**	EMX	Beta
Count	137	137	135	135	129	136	130
Average	0.898	0.897	0.923	0.714	0.848	0.980	0.963
Standard Deviation	0.168	0.172	0.091	0.224	0.268	0.275	0.104
COV	0.187	0.192	0.099	0.313	0.316	0.280	0.108
%n	0.992	0.985	0.978	0.985	0.984	0.992	0.962
Median	0.929	0.912	0.930	0.744	0.886	0.939	0.995

Instead of analyzing the results based on pile by pile basis, the analysis was performed on all concurrent blows. Presented in Tables 3-4 through 3-6 are the results for EDC earlier versions, and individual Versions 3.6 and 3.72. Again the number of piles are the same, but the average is based on the total number of concurrent blows in each analysis (>200,000 blows). Evident from a comparison Tables 3-1 and 3-4, the ratios went up and down only slightly for all versions, suggesting that the size of database is representative (# of piles or current blows).

Next, graphical comparisons of EDC capacities vs. CAPWAP were undertaken. Figures 3-10 to 3-21 represent various capacity comparison between CAPWAP, and EDC's Fixed and UF method. Each comparison series starts with EDC Fixed total capacity vs. CAPWAP and then EDC UF vs. CAPWAP total capacity, followed by skin resistance and finally end bearing comparisons based on version number. Also given in each plot is the least square linear regression fit, as well the goodness of fit, correlation coefficient, R^2.

An evaluation of the figures reveals the same trends observed in the Tables 3-1 to 3-6, with a few exceptions. For instance the linear trend ratio for total capacity by Fixed and UF method for version 3.6 are 0.927 and 1.016 vs. 0.992 and 1.126 from Table 3-2. Also the total capacity of EDC vs. CAPWAP trend line (EDC/CAPWAP) and the end bearing trend line match for version 3.72.

It should be noted that as the numbers of piles increases in the database with newer SmartPile radios, the analysis of blow output files with older versions of SmartPile Review (e.g., ver 3.6) are not possible (compatibility issues). However, newer versions of SmartPile Review (e.g., 3.76) are backward compatible, i.e., capable of reading and analyzing earlier recorded data (i.e., BDF files).

Table 3-4 Summary concurrent blow results – all earlier versions

Based on Concurrent blows, Earlier version of Smart Pile							
	Fixed/PDA	UF/PDA	CSX	CSB	TSX	EMX	Beta
Count	137	136	135	136	129	135	131
Total Number of Concurrent blows	212067	210889	207414	208295	202966	210379	204994
Sum	207527.9	230888.8	191307.9	160209.9	242643.4	205196.3	201809.2
Average	0.978	1.094	0.922	0.769	1.195	0.975	0.984
Stddev	0.189	0.205	0.086	0.238	0.294	0.214	0.036
COV	0.193	0.187	0.093	0.309	0.245	0.219	0.036
%n	0.950	1.057	0.876	0.734	1.111	0.940	0.924
Median	0.954	1.076	0.930	0.803	1.204	1.003	0.978

Table 3-5 Summary concurrent blow results – version 3.6

Based on Concurrent blows, Smart Pile version 3.6							
	Fixed/PDA	UF/PDA	CSX	CSB	TSX	EMX	Beta
Count	133	134	132	128	127	134	130
Total Number of Concurrent blows	206262	208104	203655	199165	200358	207150	202789
Sum	200760.3	230900.5	187500.1	154956.1	244020.4	208219.3	198844.6
Average	0.973	1.109	0.920	0.778	1.217	1.005	0.980
Stddev	0.200	0.241	0.089	0.191	0.302	0.264	0.051
COV	0.205	0.218	0.097	0.245	0.247	0.262	0.052
%n	0.919	1.057	0.859	0.709	1.118	0.953	0.911
Median	0.988	1.102	0.924	0.775	1.206	1.004	0.974

Table 3-6 Summary concurrent blow results – version 3.72

Based on Concurrent blows, Smart Pile version 3.72							
	Fixed/PDA	UF/PDA	CSX	CSB	TSX	EMX	Beta
Count	137	137	135	135	129	136	130
Total Number of Concurrent blows	211481	211902	207414	207865	204826	210644	202658
Sum	190005.8	192979.1	190073.3	150806.1	178354.5	198859.6	194522.4
Average	0.898	0.910	0.916	0.725	0.870	0.944	0.959
Stddev	0.168	0.172	0.091	0.224	0.268	0.275	0.104
COV	0.187	0.189	0.099	0.308	0.308	0.291	0.108
%n	0.870	0.884	0.870	0.690	0.817	0.911	0.891
Median	0.929	0.912	0.930	0.744	0.886	0.939	0.995

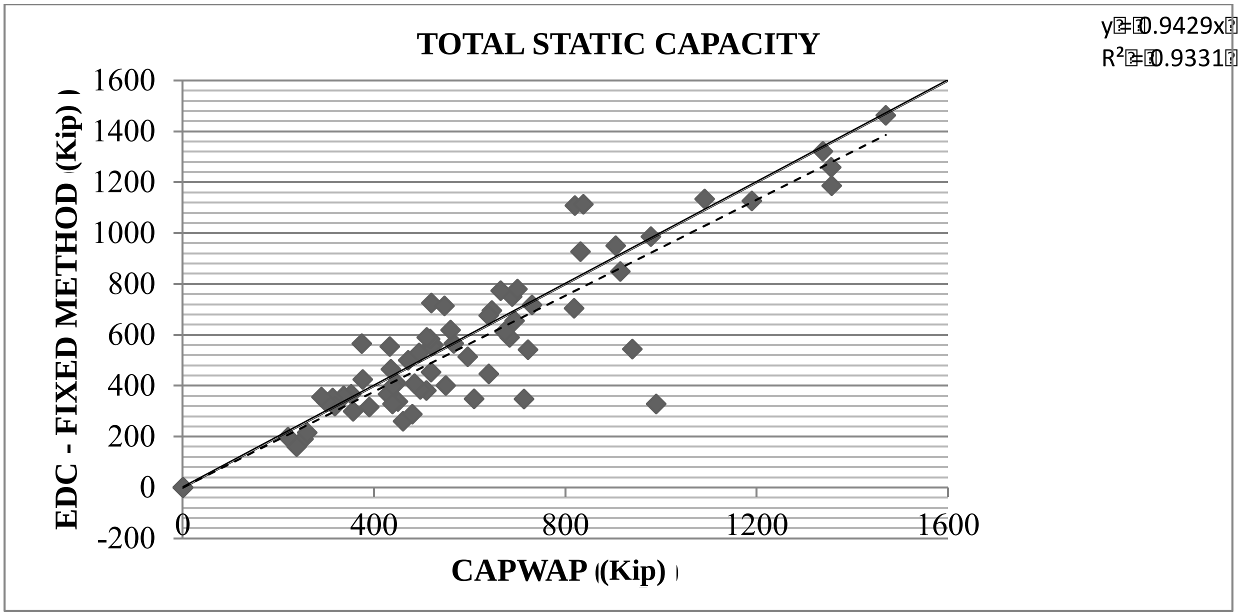

Figure 3-10 Total static capacity comparison, fixed method Vs. CAPWAP for previous SmartPile Review versions

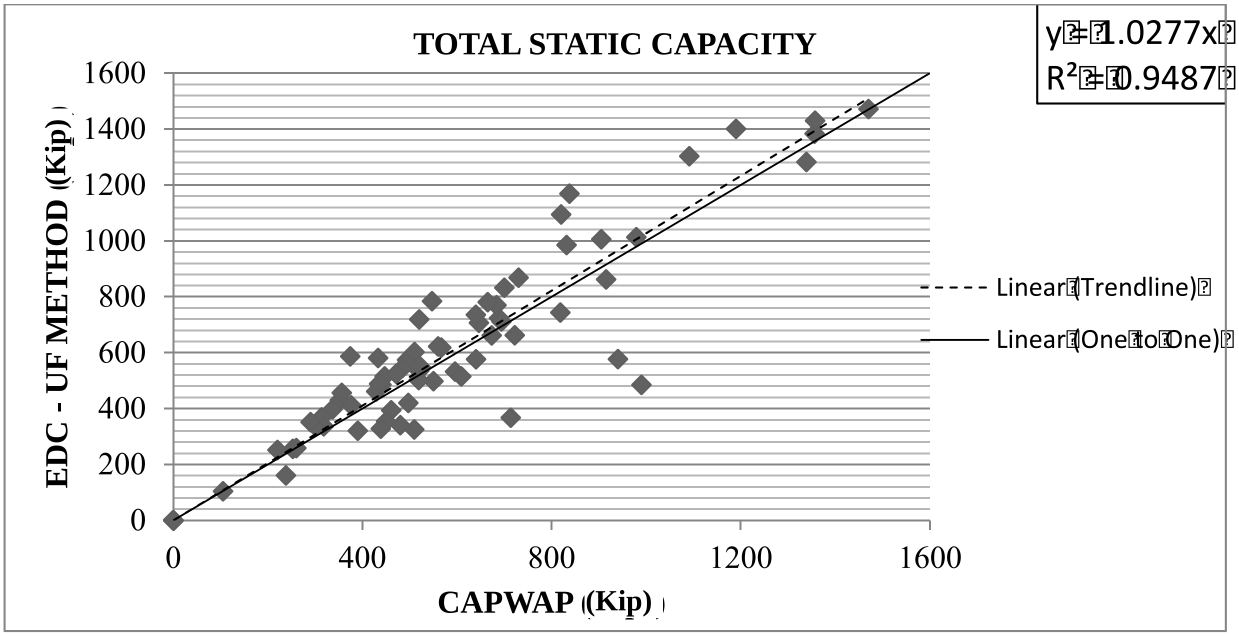

Figure 3-11 Total static capacity comparison, UF method Vs. CAPWAP for previous SmartPile Review versions

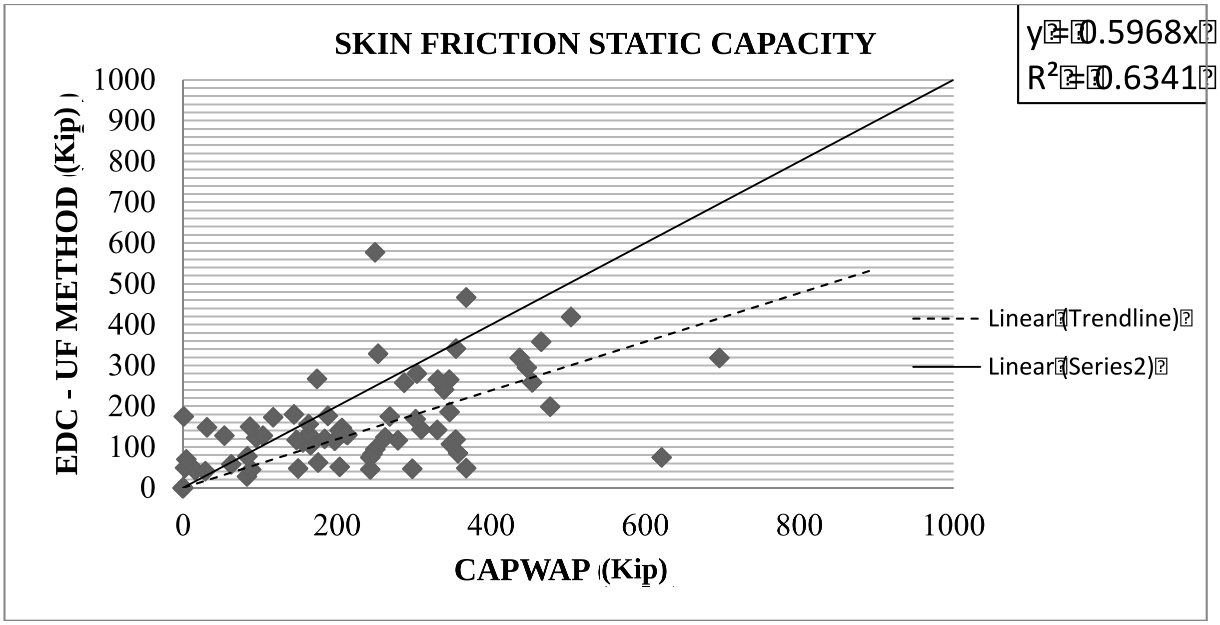

Figure 3-12 Skin friction static capacity comparison, UF method Vs. CAPWAP for previous SmartPile Review versions

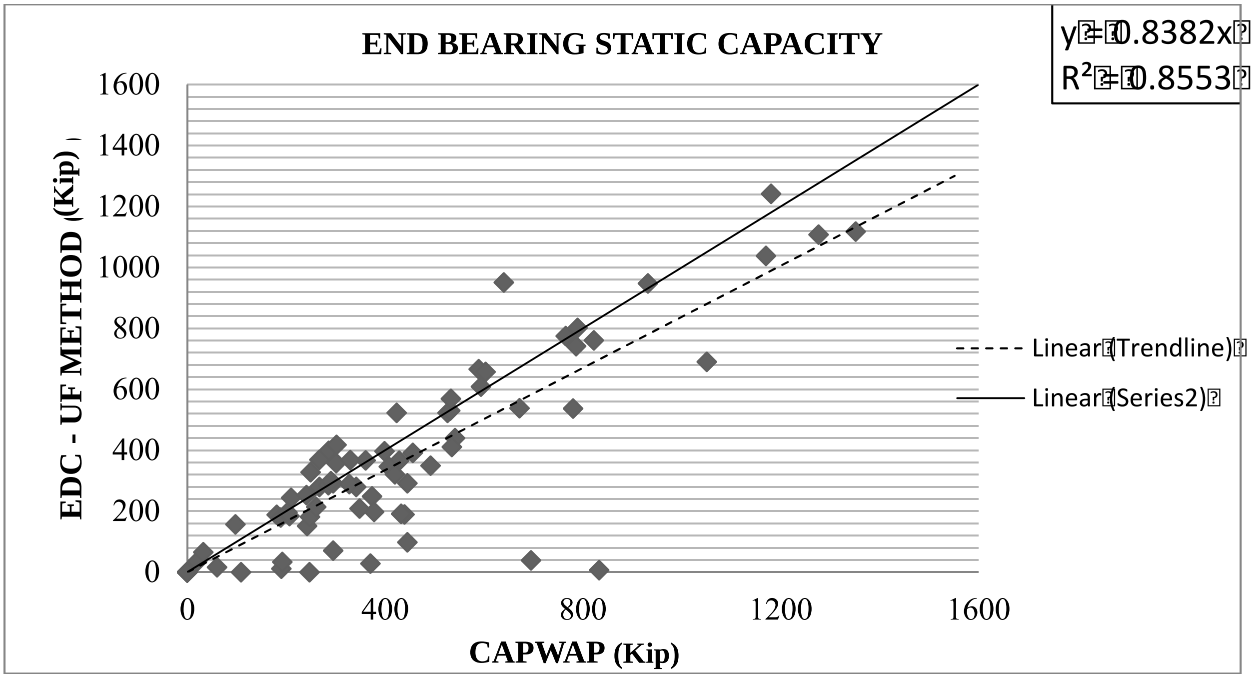

Figure 3-13 End bearing static capacity comparison, UF method Vs. CAPWAP for previous SmartPile Review versions

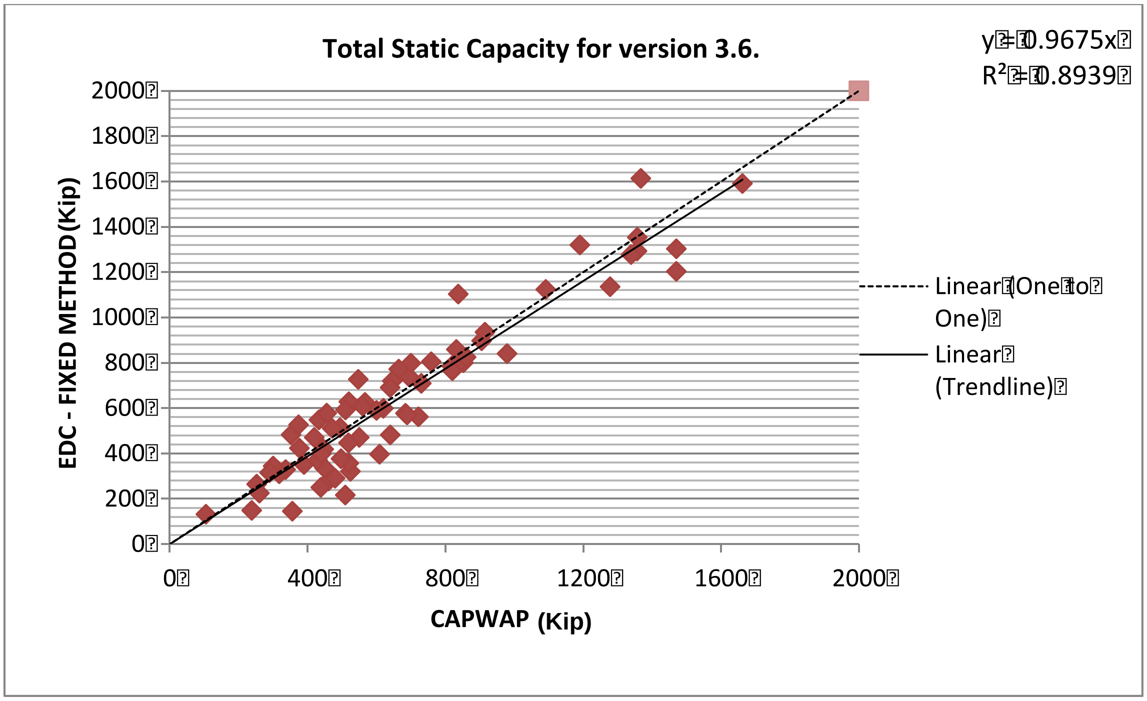

Figure 3-14 Total static capacity comparison, Fixed method Vs. CAPWAP for ver. 3.6

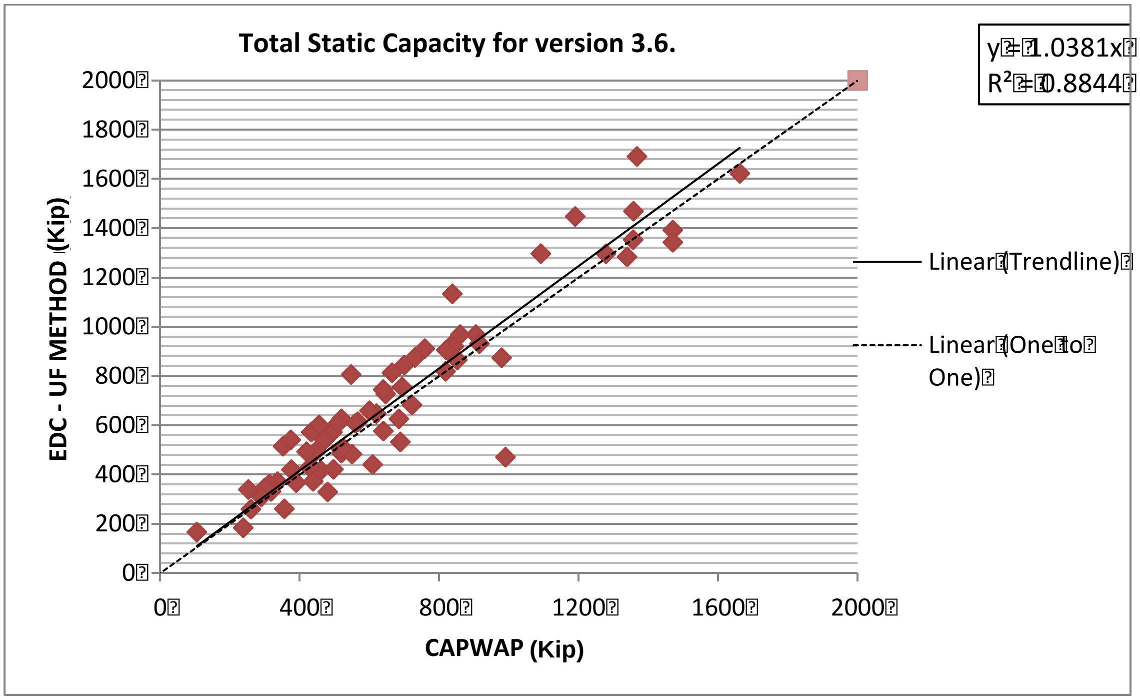

Figure 3-15 Total static capacity comparison, UF method Vs. CAPWAP for ver. 3.6

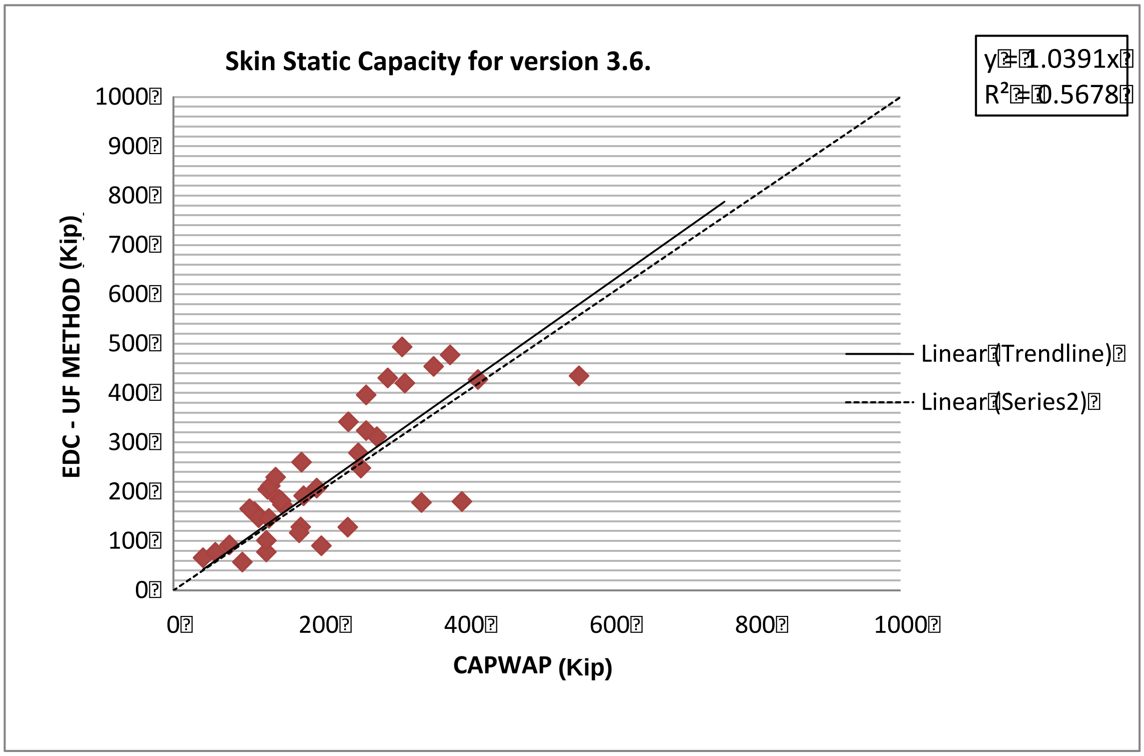

Figure 3-16 Skin friction static capacity comparison, UF method Vs. CAPWAP for ver. 3.6

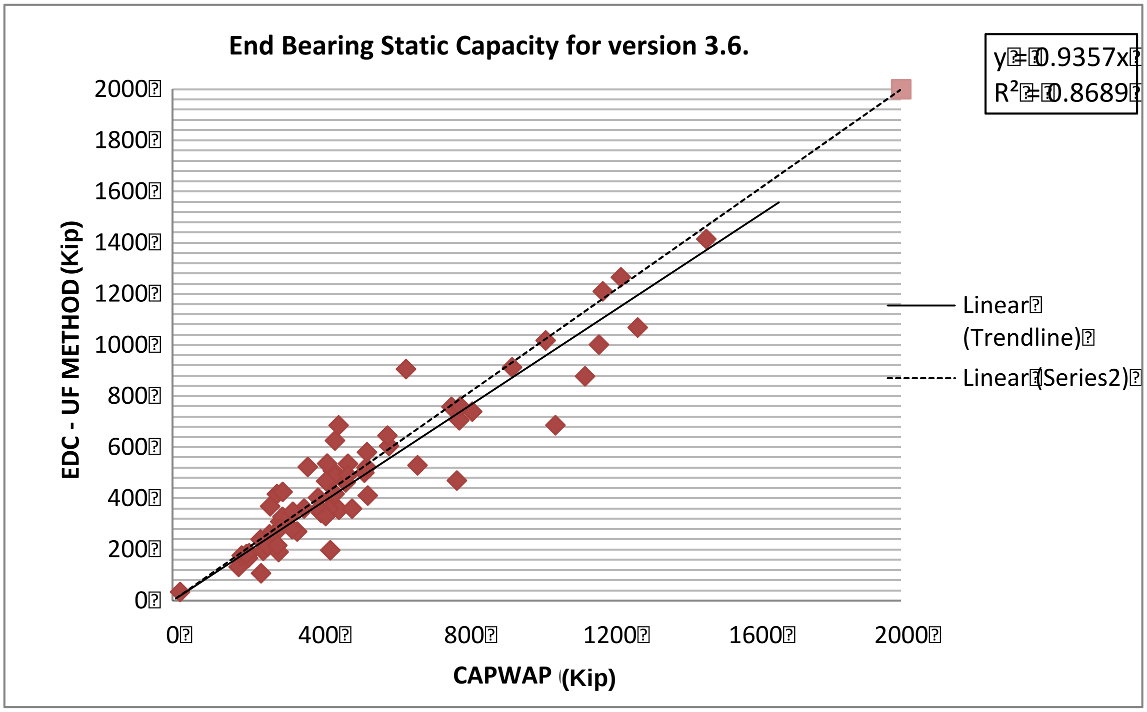

Figure 3-17 End bearing static capacity comparison, UF method Vs. CAPWAP for ver. 3.6

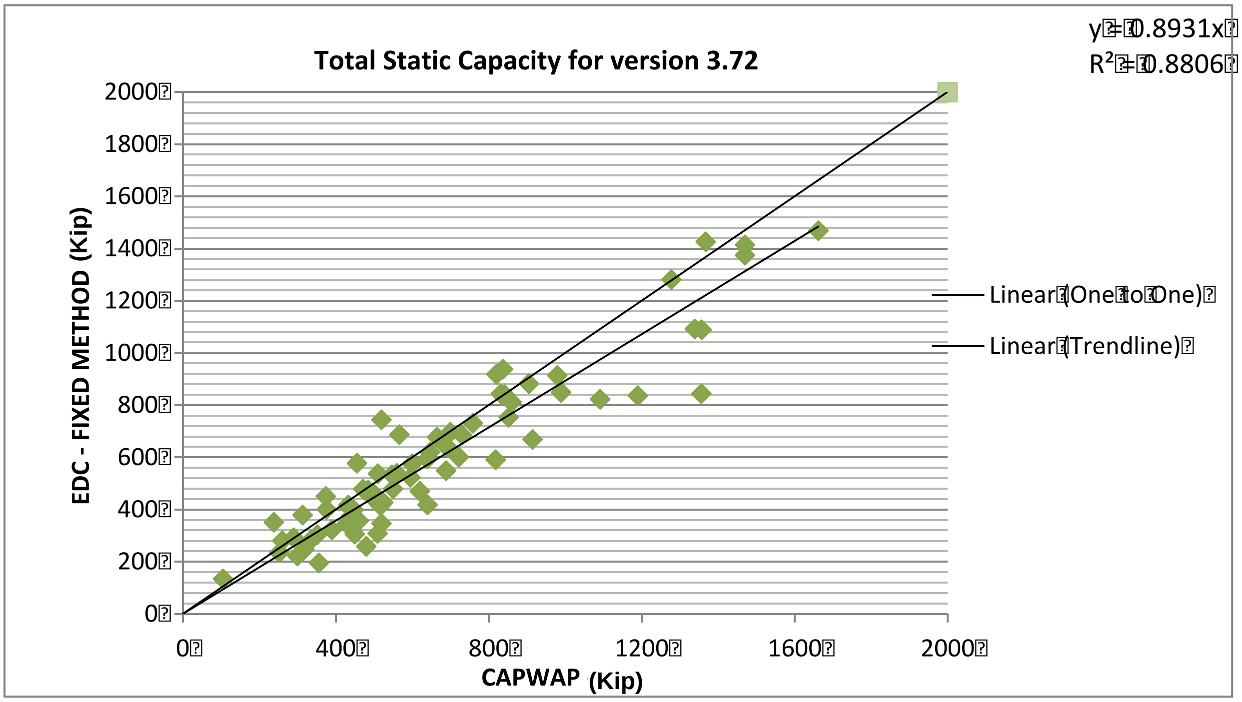

Figure 3-18 Total static capacity comparison, Fixed method Vs. CAPWAP for ver. 3.72

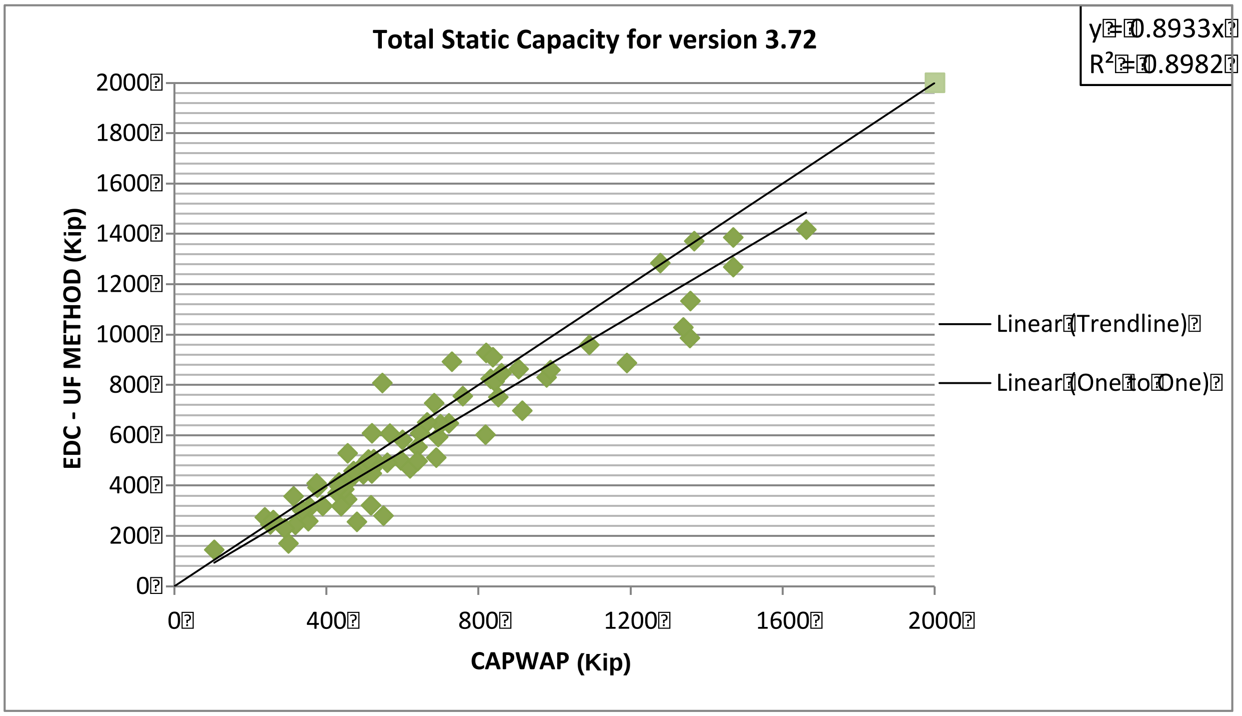

Figure 3-19 Total static capacity comparison, UF method Vs. CAPWAP for ver. 3.72

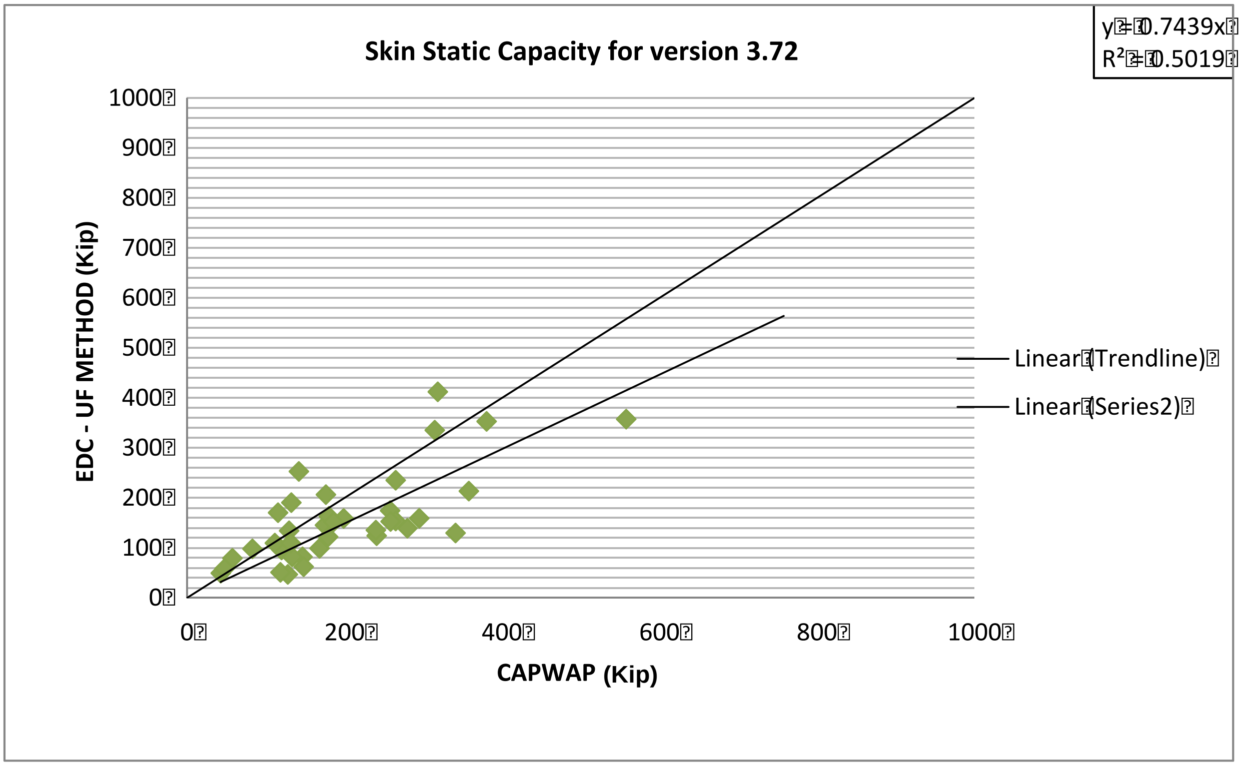

Figure 3-20 Skin friction static capacity comparison, UF method Vs. CAPWAP for ver. 3.72

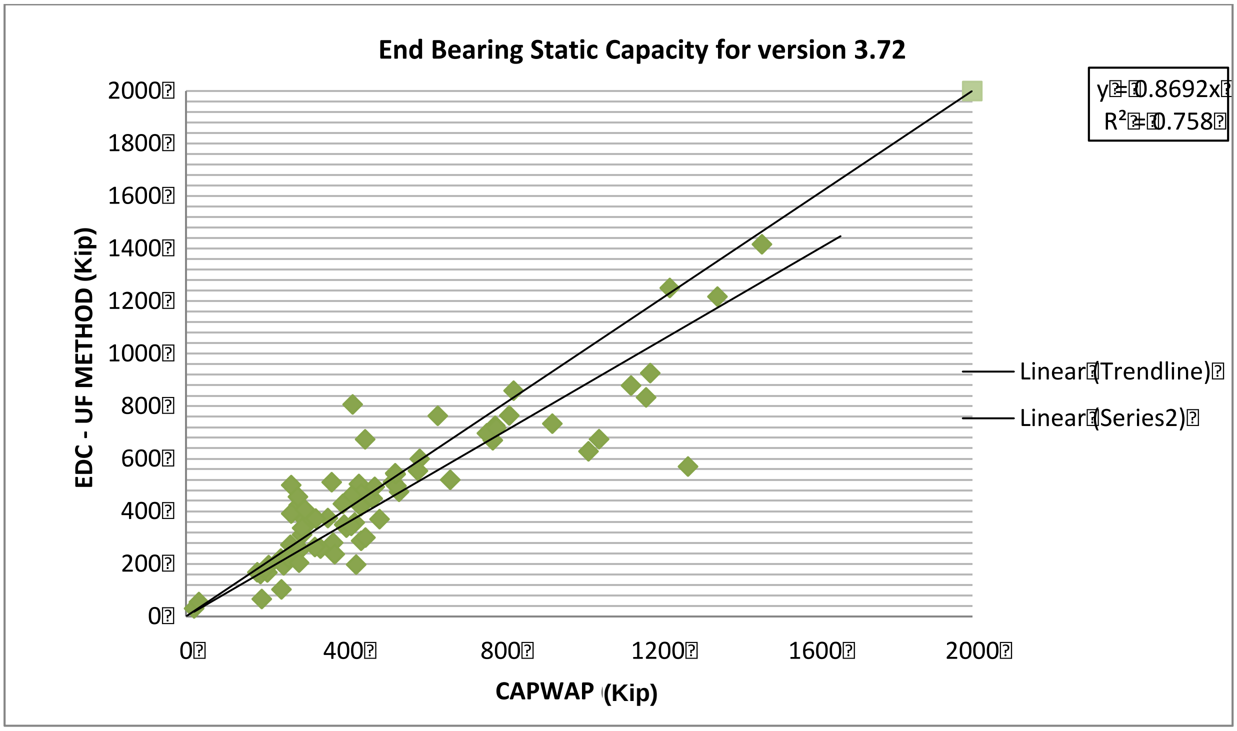

Figure 3-21 End bearing static capacity comparison, UF method Vs. CAPWAP for ver. 3.72

3.4 Comparisons of Later EDC SmartPile Review Versions to PDA/CAPWAP Results

With the addition of more pile data to the FDOT database for the comparison of EDC vs. SmartPile review, the Visual Basic code in the Excel spreadsheets (e.g., “All-In-One, etc.) was modified to include additional sites, piles, and newer SmartPile Review versions (3.73, 3.76 and 3.761). Subsequently, analyses were performed on the updated database, and histograms (e.g., CSX, TSX, CSB etc.) and plots (EDC vs. CAPWAP) were developed for each version.

The following tables show the statistical results of comparisons between PDA and various EDC versions. Table 3-7 presents comparisons of PDA vs. SmartPile versions up to 3.72; Table 3-8 presents comparisons of PDA vs. SmartPile versions 3.73 to 3.761. The left side of each table is results based on pile statistics, i.e., averages are found based on individual piles (i.e., Fixed/EDC, CSB, etc.) and then averaged over the database (137 to 139 piles, depending on radio version). Instead of developing summary statistics in terms of individual piles, the right side of Tables 3-7 and 3-8 were developed in terms of concurrent blows. This gives equal weight to any blow for any pile, whereas, the pile approach weighs piles equally.

In the comparisons for version 3.76, all the restrike blows were not considered based on correspondence with Smart Structures, Inc [restrike bug and subsequent fix (3.761)]. Also, for versions 3.76 and higher, tip override based on preload delta (i.e., pile damage) was invoked to ensure prediction of all piles in the database. Note, for some of the piles (approximately 20 – 15%), the change in preload delta strain was sufficient to automatically shut down the prediction unless the manual override was selected.

Table 3-7 EDC/PDA comparison for all earlier versions of EDC up to 3.72

SMART PILE VERSION - 3.72

Based on per pile, Smart Pile version 3.72

	Fixed/PDA	UF/PDA	CSX	CSB	TSX	EMX	Beta
Count	137	138	137	132	130	136	132
Average	0.896	0.894	0.922	0.741	0.851	0.968	0.963
Stddev	0.149	0.171	0.091	0.176	0.266	0.256	0.104
COV	0.166	0.191	0.099	0.238	0.312	0.264	0.108
%n	0.985	0.985	0.985	0.956	0.984	0.985	0.963
Median	0.927	0.911	0.930	0.749	0.893	0.933	0.995

Based on Concurrent blows, Smart Pile version version 3.72

	Fixed/PDA	UF/PDA	CSX	CSB	TSX	EMX	Beta
Count	137	138	137	132	130	136	132
#Blows	212463	212904	209253	204094	205828	212123	204497
Sum	192408.9	193703.4	191708.1	152097.6	179718.2	200074.4	196167.8
Average	0.905	0.909	0.916	0.745	0.873	0.943	0.959
Stddev	0.149	0.171	0.091	0.176	0.266	0.256	0.104
COV	0.164	0.188	0.099	0.237	0.305	0.271	0.109
%n	0.881	0.887	0.878	0.696	0.823	0.916	0.898
Median	0.927	0.911	0.930	0.749	0.893	0.933	0.995

SMART PILE VERSION - 3.6

Based on per pile, Smart Pile version 3.6

	Fixed/PDA	UF/PDA	CSX	CSB	TSX	EMX	Beta
Count	137	138	137	132	131	136	134
Average	0.984	1.121	0.924	0.767	1.204	1.015	0.975
Stddev	0.173	0.241	0.088	0.178	0.293	0.226	0.042
COV	0.176	0.215	0.096	0.232	0.243	0.222	0.044
%n	0.978	0.985	0.985	0.970	0.984	0.985	0.978
Median	0.987	1.105	0.924	0.779	1.202	1.008	0.973

Based on Concurrent blows, Smart Pile version version 3.6

	Fixed/PDA	UF/PDA	CSX	CSB	TSX	EMX	Beta
Count	137	138	137	132	131	136	134
#Blows	212014	212865	209253	204498	205119	210158	207098
Sum	207787.0	235262.9	192798.4	159467.6	249399.4	209675.1	202700.6
Average	0.980	1.105	0.921	0.779	1.215	0.997	0.978
Stddev	0.173	0.241	0.088	0.178	0.293	0.226	0.042
COV	0.177	0.218	0.096	0.229	0.241	0.226	0.043
%n	0.952	1.077	0.883	0.730	1.142	0.960	0.928
Median	0.987	1.105	0.924	0.779	1.202	1.008	0.973

SMART PILE (EARLIER VERSION)

Based on per pile, Earlier version of Smart Pile

	Fixed/PDA	UF/PDA	CSX	CSB	TSX	EMX	Beta
Count	137	136	136	132	129	136	132
Average	0.964	1.081	0.926	0.797	1.198	1.010	0.981
Stddev	0.185	0.198	0.086	0.186	0.289	0.216	0.036
COV	0.191	0.183	0.093	0.234	0.241	0.213	0.036
%n	0.985	0.978	0.985	0.956	0.977	0.992	0.970
Median	0.954	1.080	0.930	0.816	1.207	1.001	0.979

Based on Concurrent blows, Earlier version of Smart Pile

	Fixed/PDA	UF/PDA	CSX	CSB	TSX	EMX	Beta
Count	137	136	136	132	129	136	132
#Blows	209683	208505	205867	201138	200582	208832	203447
Sum	204202.7	227738.7	190065.2	160121.4	240833.1	204175.1	200358.4
Average	0.973	1.092	0.923	0.796	1.200	0.977	0.984
Stddev	0.185	0.198	0.086	0.186	0.289	0.216	0.036
COV	0.190	0.181	0.093	0.234	0.241	0.221	0.036
%n	0.935	1.043	0.870	0.733	1.103	0.935	0.917
Median	0.954	1.080	0.930	0.816	1.207	1.001	0.979

Table 3-8 EDC/PDA comparison for all earlier version of EDC from 3.73 to 3.761

SMART PILE VERSION - 3.761

Based on per pile, Smart Pile version 3.761

	Fixed/PDA	UF/PDA	CSX	CSB	TSX	EMX	Beta
Count	139	139	140	134	131	138	139
Average	0.890	0.905	0.924	0.740	0.875	0.965	0.963
Stddev	0.152	0.161	0.091	0.177	0.258	0.241	0.116
COV	0.170	0.177	0.099	0.239	0.295	0.250	0.121
%n	0.985	0.985	0.992	0.957	0.984	0.978	0.985
Median	0.925	0.910	0.931	0.749	0.900	0.934	0.995

Based on Concurrent blows, Smart Pile version version 3.761

	Fixed/PDA	UF/PDA	CSX	CSB	TSX	EMX	Beta
Count	139	139	140	134	131	138	139
#Blows	213885	213734	213905	205516	206199	213157	213631
Sum	190755.8	194432.4	196359.3	153196.6	183982.0	201992.4	204898.3
Average	0.891	0.909	0.917	0.745	0.892	0.947	0.959
Stddev	0.152	0.161	0.091	0.177	0.258	0.241	0.116
COV	0.170	0.177	0.100	0.237	0.290	0.255	0.121
%n	0.873	0.890	0.899	0.701	0.842	0.925	0.938
Median	0.925	0.910	0.931	0.749	0.900	0.934	0.995

SMART PILE VERSION - 3.76

Based on per pile, Smart Pile version 3.76

	Fixed/PDA	UF/PDA	CSX	CSB	TSX	EMX	Beta
Count	139	139	140	134	131	138	139
Average	0.889	0.905	0.924	0.740	0.875	0.965	0.963
Stddev	0.152	0.160	0.091	0.177	0.258	0.241	0.117
COV	0.170	0.177	0.099	0.239	0.295	0.250	0.121
%n	0.985	0.985	0.992	0.957	0.984	0.978	0.985
Median	0.925	0.910	0.931	0.749	0.900	0.934	0.995

Based on Concurrent blows, Smart Pile version version 3.76

	Fixed/PDA	UF/PDA	CSX	CSB	TSX	EMX	Beta
Count	139	139	140	134	131	138	139
#Blows	213885	213734	213905	205516	206199	213157	213631
Sum	190710.6	194347.2	196359.3	153196.6	183988.1	201986.4	204897.3
Average	0.891	0.909	0.917	0.745	0.892	0.947	0.959
Stddev	0.152	0.160	0.091	0.177	0.258	0.241	0.117
COV	0.170	0.176	0.100	0.237	0.290	0.255	0.121
%n	0.873	0.890	0.899	0.701	0.842	0.925	0.938
Median	0.925	0.910	0.931	0.749	0.900	0.934	0.995

SMART PILE VERSION - 3.73

Based on per pile, Smart Pile version 3.73

	Fixed/PDA	UF/PDA	CSX	CSB	TSX	EMX	Beta
Count	138	139	140	135	131	138	138
Average	0.913	0.928	0.925	0.735	0.880	0.985	0.965
Stddev	0.151	0.188	0.093	0.185	0.274	0.240	0.111
COV	0.166	0.202	0.100	0.251	0.311	0.243	0.115
%n	0.978	0.985	0.992	0.964	0.984	0.978	0.978
Median	0.930	0.926	0.933	0.745	0.898	0.966	0.996

Based on Concurrent blows, Smart Pile version version 3.73

	Fixed/PDA	UF/PDA	CSX	CSB	TSX	EMX	Beta
Count	138	139	140	135	131	138	138
#Blows	210440	211291	213905	205946	205899	213157	210994
Sum	191857.3	196321.1	196542.9	152533.3	185593.8	206344.2	203346.5
Average	0.911	0.929	0.918	0.740	0.901	0.968	0.963
Stddev	0.151	0.188	0.093	0.185	0.274	0.240	0.111
COV	0.166	0.202	0.101	0.249	0.304	0.248	0.115
%n	0.879	0.899	0.900	0.698	0.850	0.945	0.931
Median	0.930	0.926	0.933	0.745	0.898	0.966	0.996

A comparison of the tables, suggest that the UF capacity predicted by versions 3.76 and 3.761 of SmartPile are conservative to PDA versus earlier version of SmartPile (3.6). Also of interest, the COV of the UF/PDA has dropped to 0.178 which is close to the Fixed/PDA of 0.171.

For better visualization of these variations, plots of means for each EDC version were plotted in histogram form. Figure 3-22 shows the variation in capacities based on mean pile results, whereas Figure 3-23 presents the mean concurrent blow results. Evident from a comparison of Figure 3-22 and 3-23, the results are quite comparable, suggesting size of database or piles considered are representative.

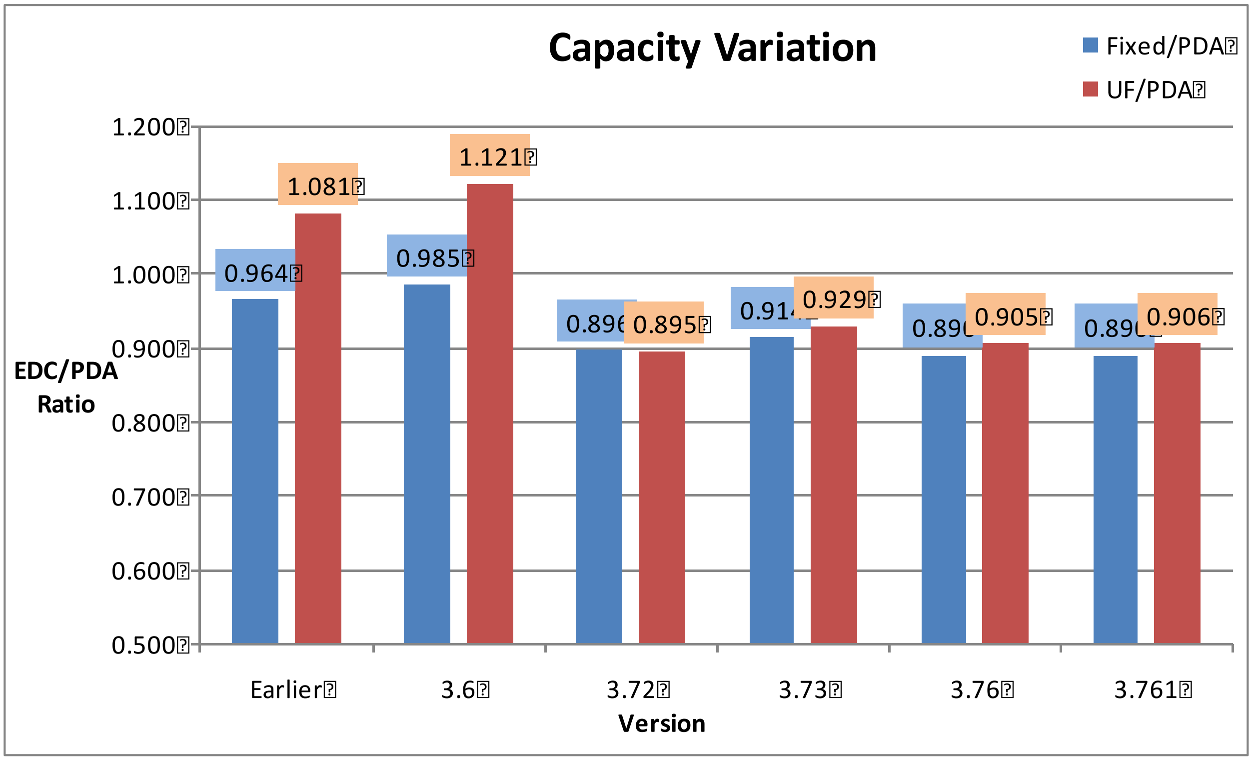

Figure 3-22 Capacity ratio variation - per pile approach

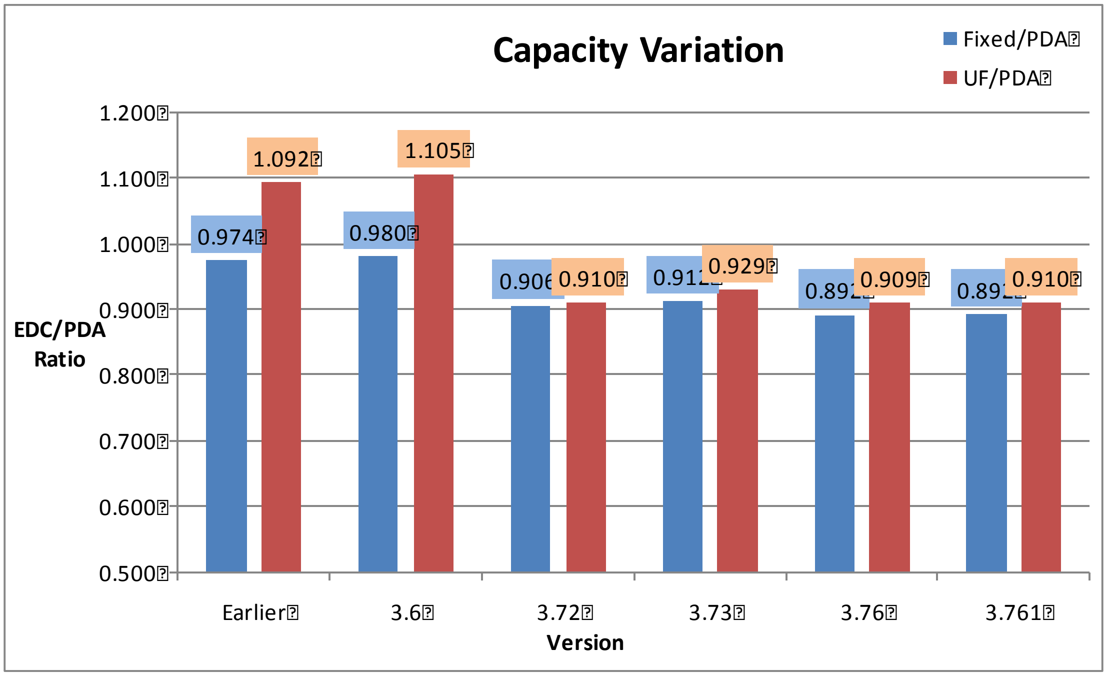

Figure 3-23 Capacity ratio variation - concurrent blow approach

Presented in Figures 3-24 and 3-25 are the maximum compression stresses based on pile and concurrent blows. As can be seen in Figure 3-25, EDC/PDA ratio for CSX is 0.92 and did not change over the change in versions. Also, the standard deviation of the mean (Table 3-8) ranges from 0.094 to approximately 0.1 with version 3.761 at 0.1.

Interestingly, the compressive stress at the bottom of the piles (CSB) measured by SmartPile are smaller than the PDA for all versions (Figs. 3-26 and 3-27). Moreover, the change appears to be reaching a plateau of 0.74 ~0.75 (i.e., PDA overpredicts the EDC measured values by 25%).

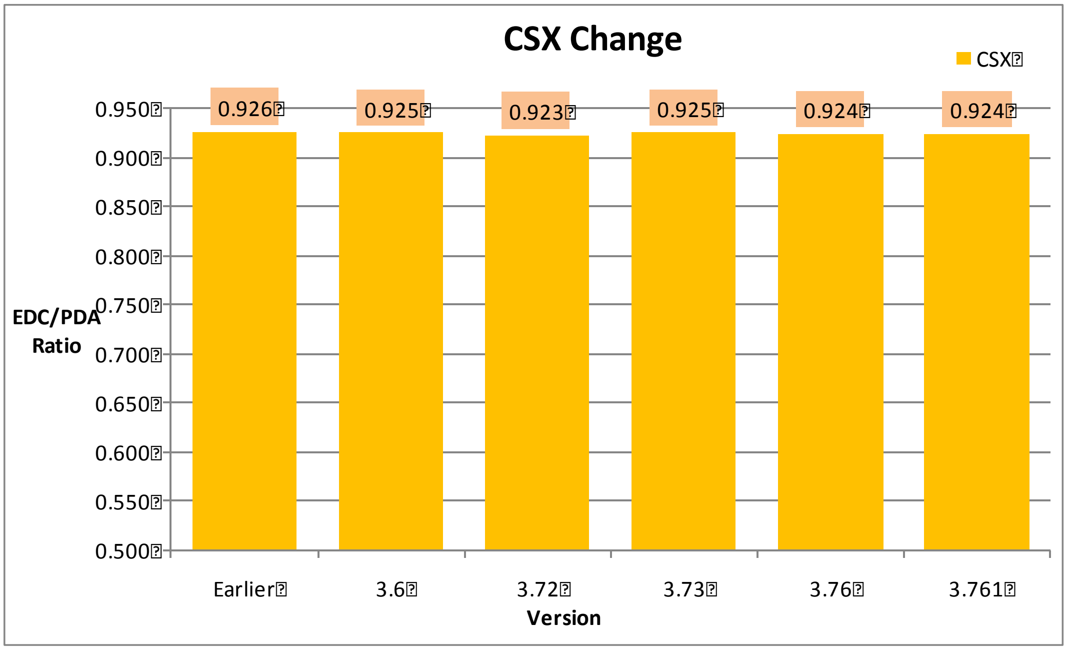

Figure 3-24 CSX ratio variation - per pile approach

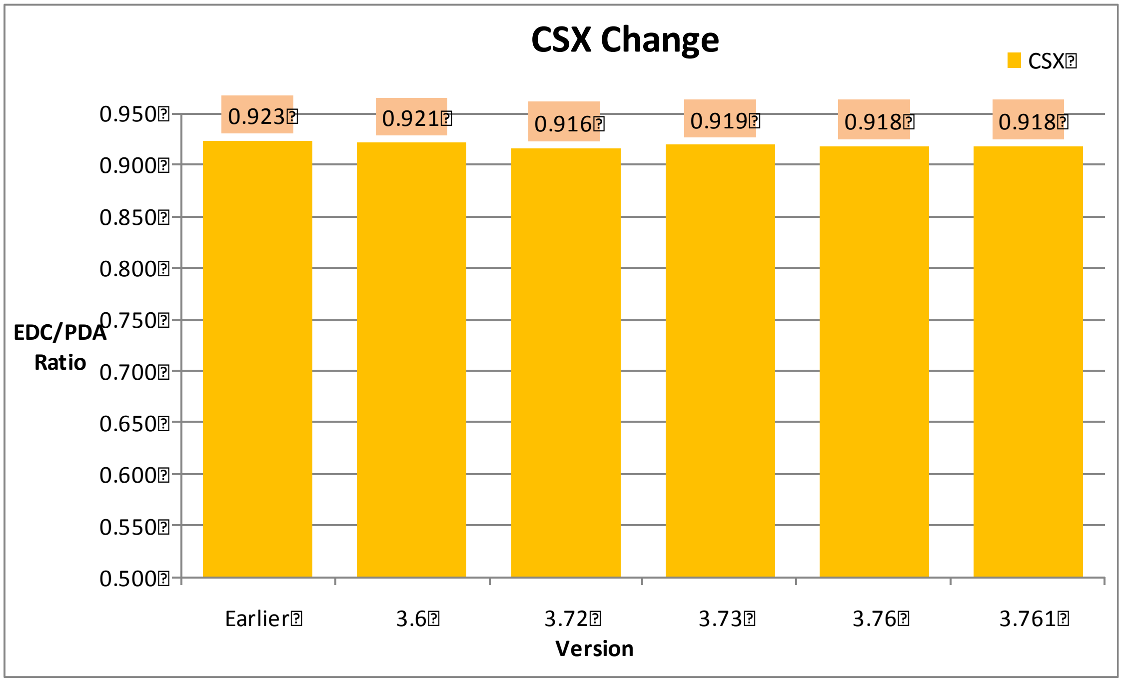

Figure 3-25 CSX ratio variation - concurrent blow approach

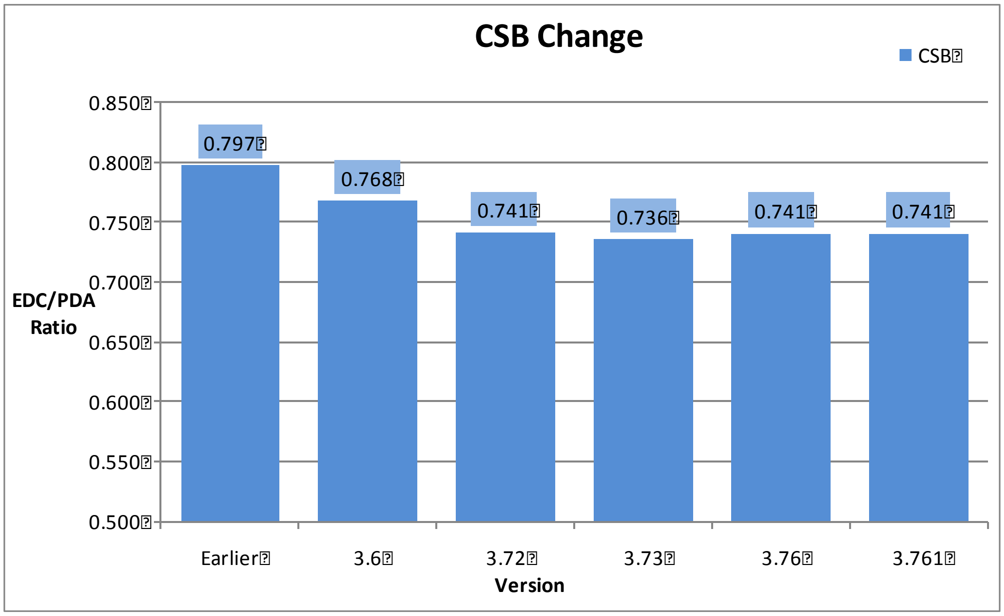

Figure 3-26 CSB ratio variation - per pile approach

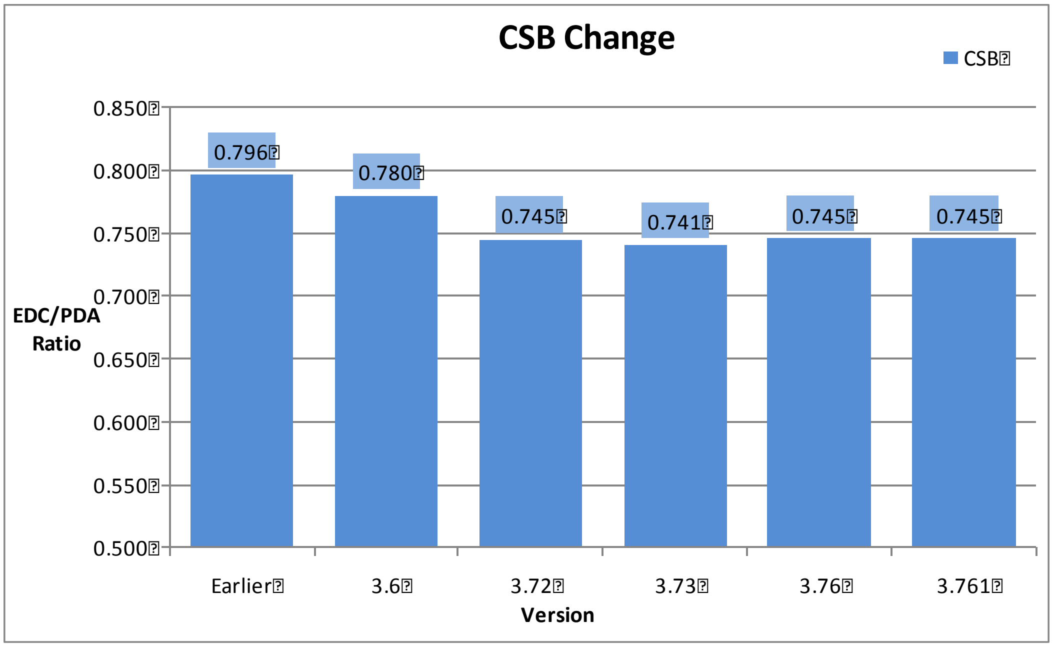

Figure 3-27 CSB ratio variation - concurrent blow approach

From discussion with SmartStructure, SmartPile Review underwent a change in tensile stress prediction (TSX) after version 3.6 (i.e., 3.7). As can be seen from Figures 3-28 and 3-29, TSX prediction are higher for EDC in early versions, but dropped in version 3.72 and 3.73, stabilizing in the range of 0.85 to 0.90 for later versions. Note there is a slight difference between piles and concurrent blows with the latter slightly higher.

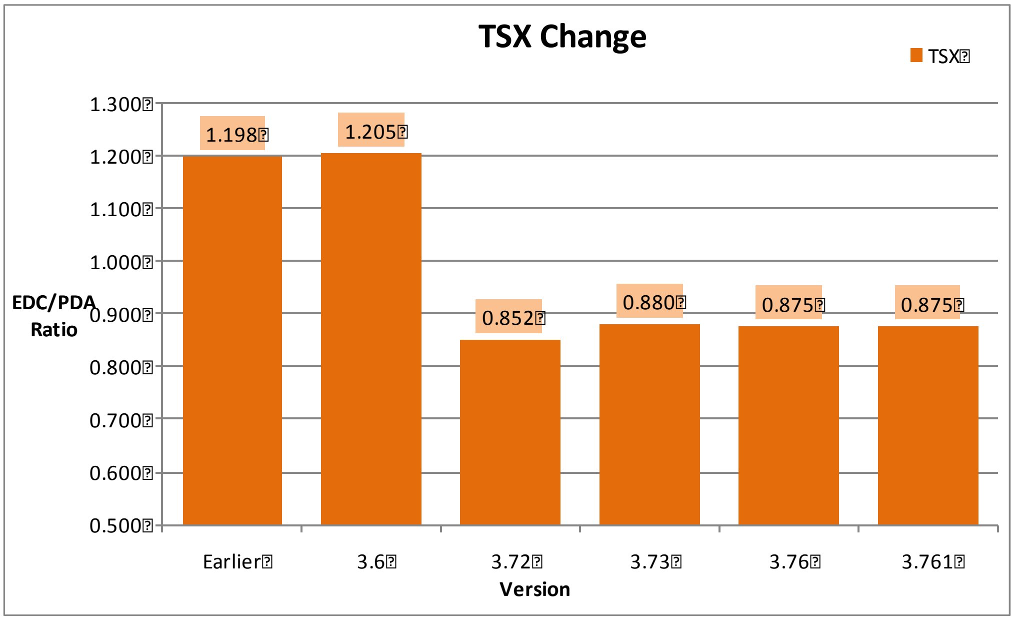

Figure 3-28 Variation in TSX ratio - rer rile approach

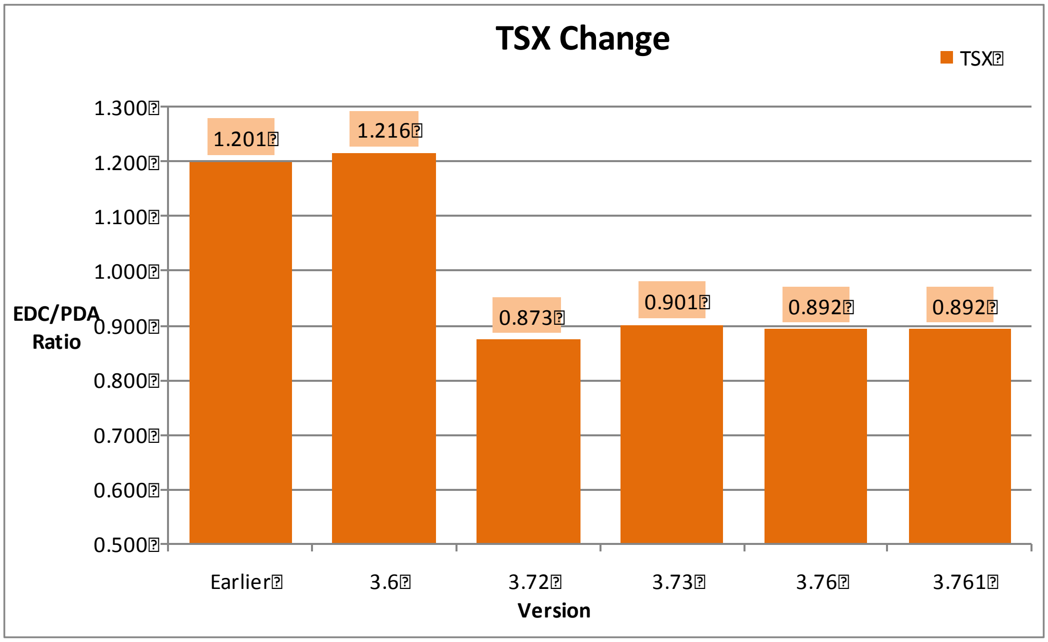

Figure 3-29 Variation in TSX ratio - concurrent blow approach

In terms of BETA (damage) and EMX (energy), very small changes were observed with changes in version. Moreover, the small changes observed in Figure 3-30 by piles are offset by the slight differences observed between pile vs. concurrent blow (Figure 3-31) results.

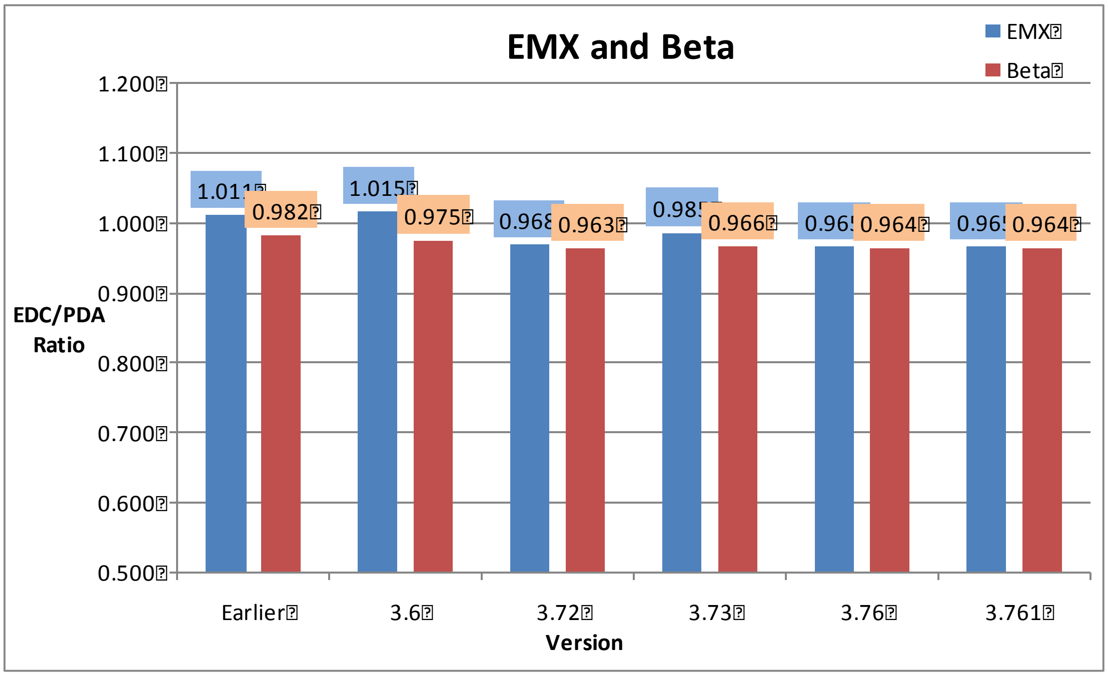

Figure 3-30 Variation in energy in pile and Beta - per pile approach

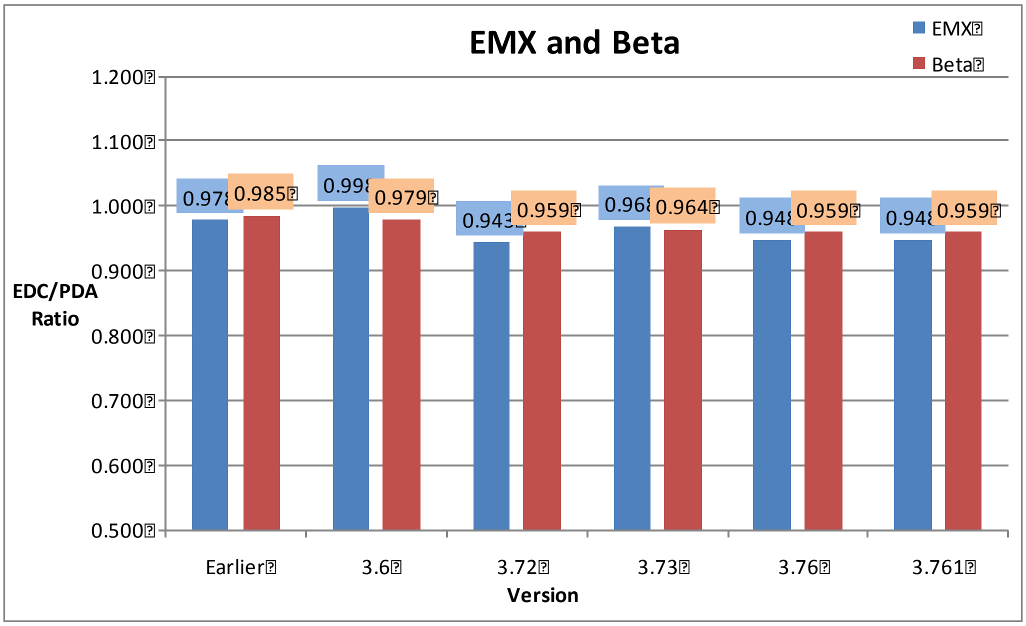

Figure 3-31 Variation in energy in pile and Beta - concurrent blow approach

Besides comparison of PDA results vs. different versions of SmartPile Review, CAPWAP predictions were compared to SmartPile Review versions as well for all applicable piles. The comparisons considered EDC Fixed total capacity, UF total capacity, as well as total side resistance and end bearing based on SmartPile version number. For instance shown in Figures 3-32 and 3-33 are SmartPile Review (3.6) results for EDC Fixed vs. CAPWAP and UF total vs. CAPWAP. The mean value (EDC/CAPWAP) is the coefficient, m, in Equation y = mx given in each figure. Below each total capacity comparison is the skin friction, Figure 3-34, and tip resistance, Figure 3-35. Other versions (3.72 -3.761) are given in Figures 3-36-3-45.

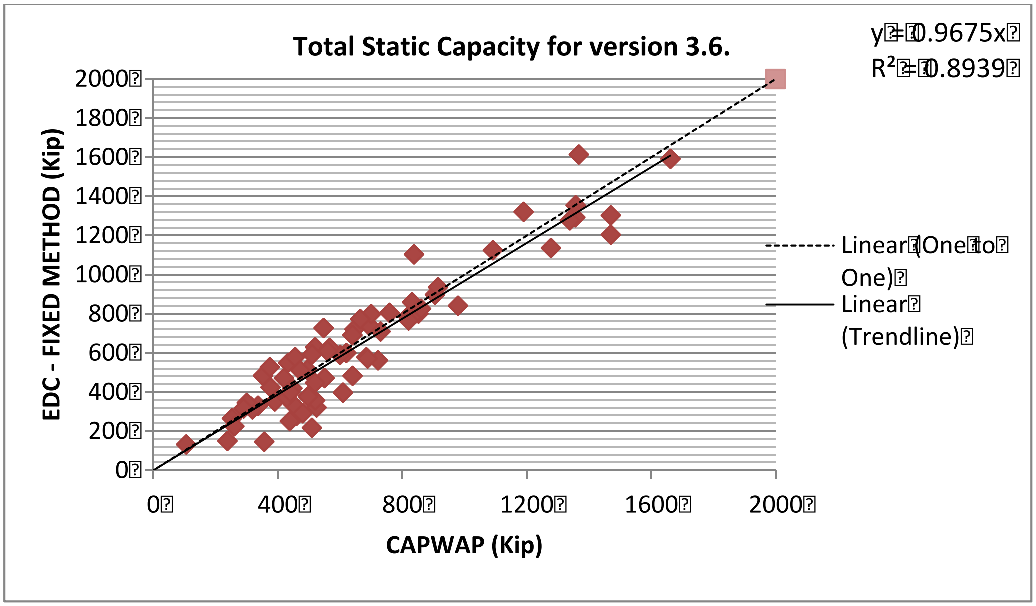

Figure 3-32 EDC 3.6 vs. CAPWAP, Fixed total capacity

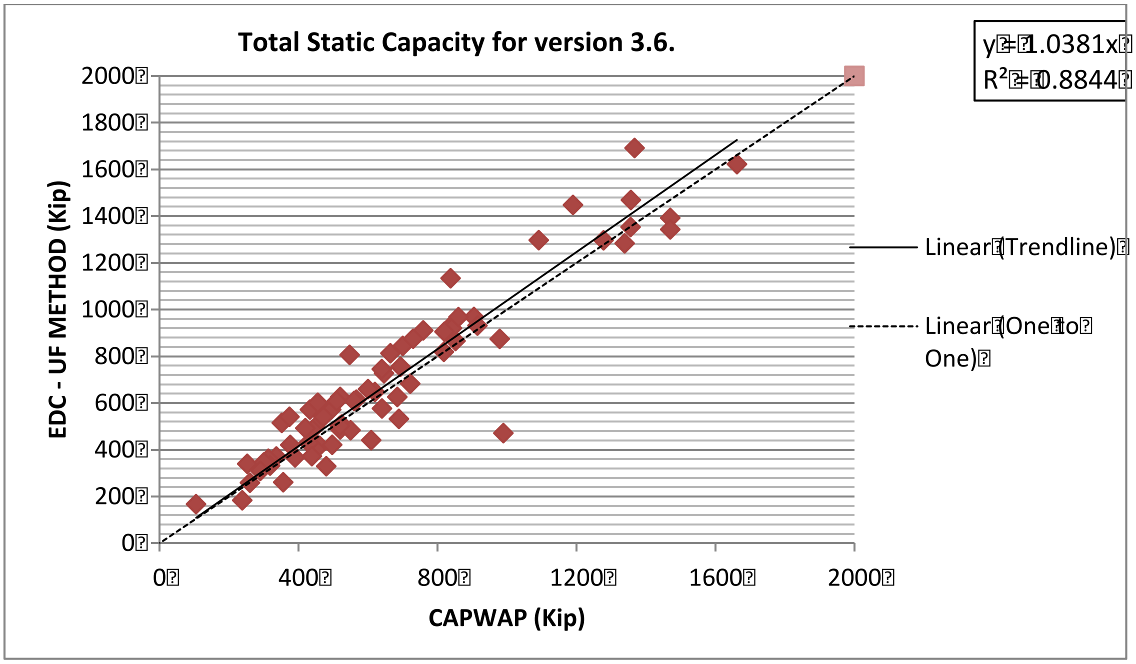

Figure 3-33 EDC 3.6 vs. CAPWAP, UF total capacity

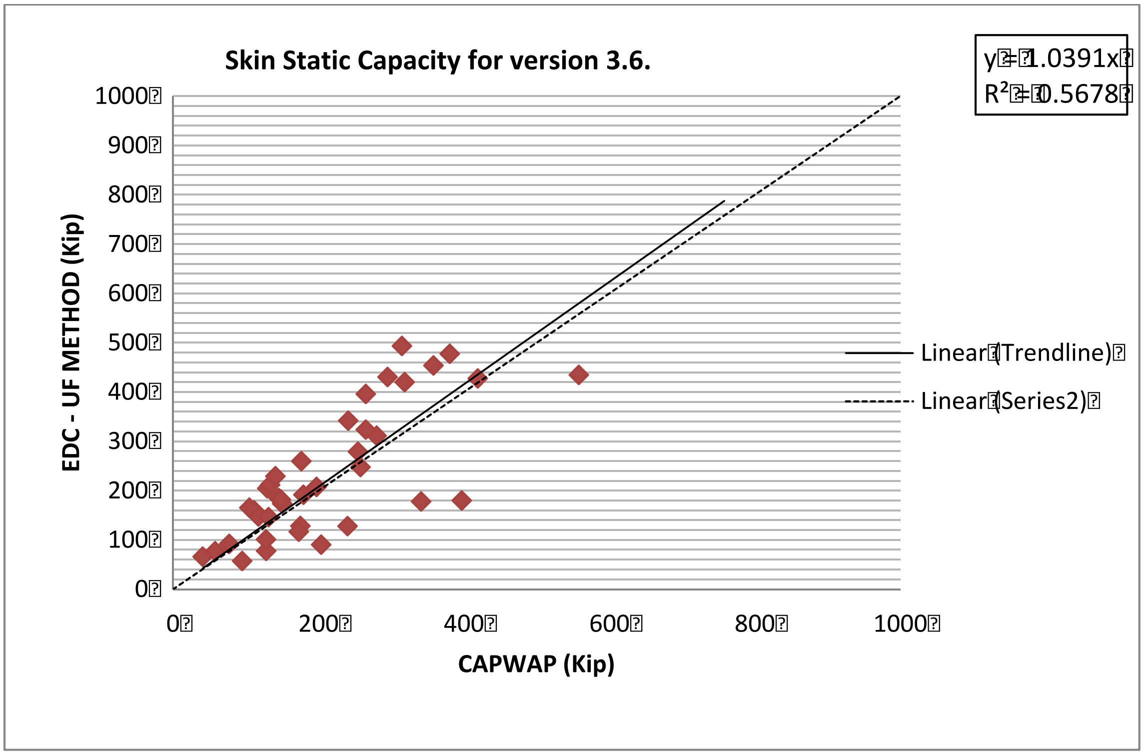

Figure 3-34 EDC 3.6 vs. CAPWAP, UF skin capacity

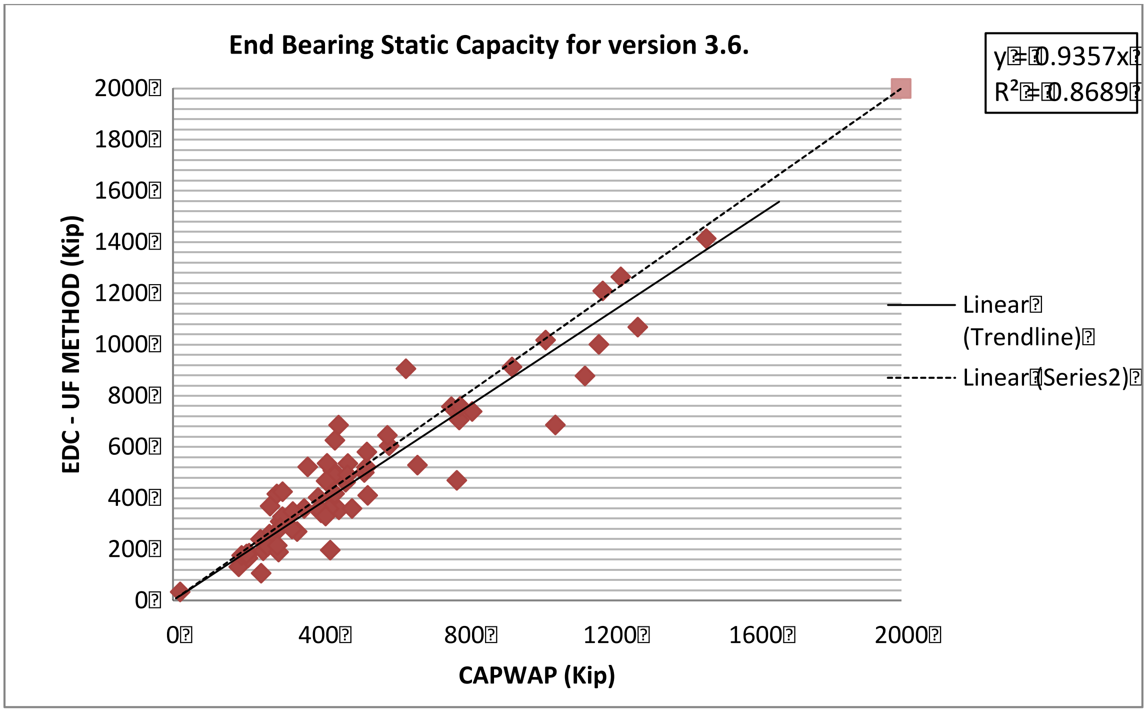

Figure 3-35 EDC 3.6 vs. CAPWAP, UF end bearing static capacity

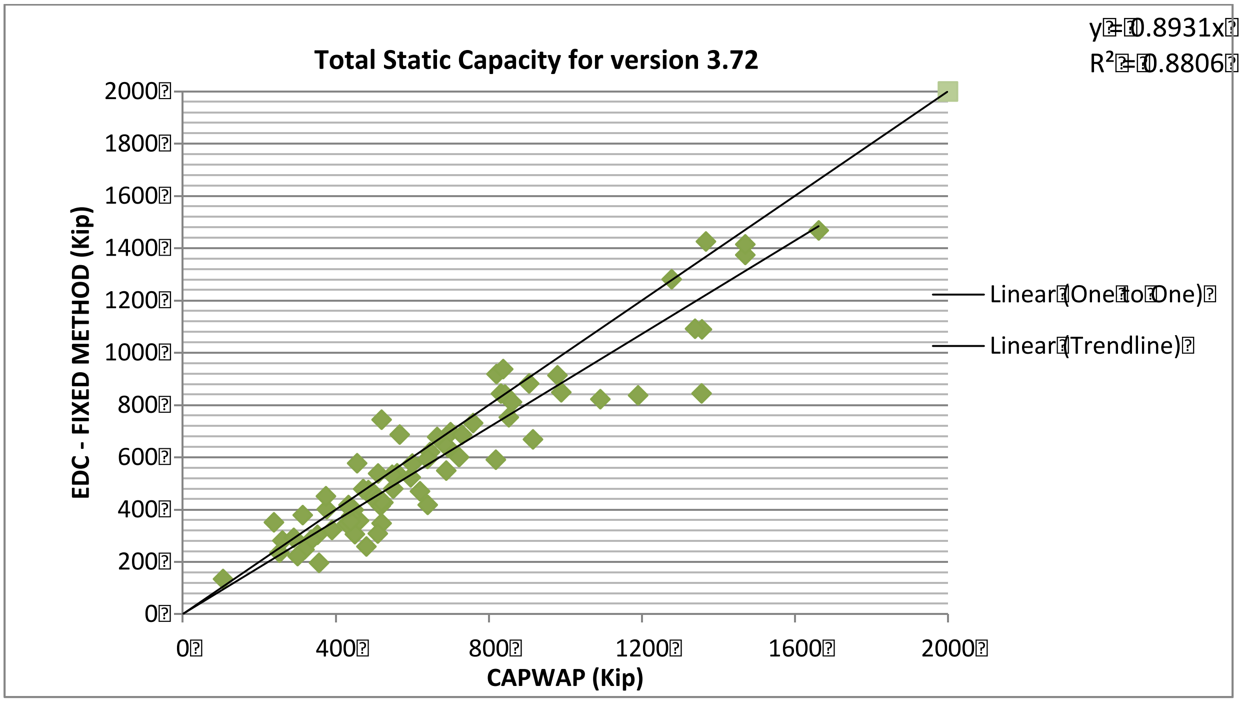

Figure 3-36 EDC 3.72 vs. CAPWAP, Fixed total capacity

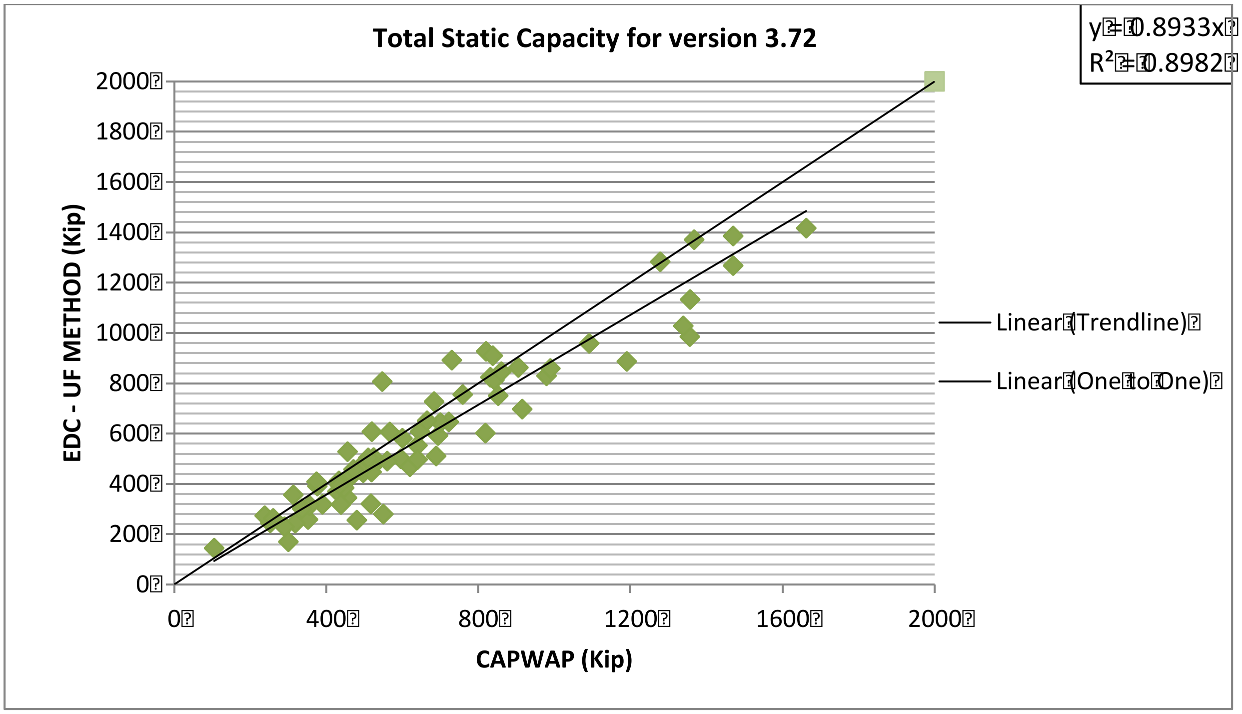

Figure 3-37 EDC 3.72 vs. CAPWAP, UF total capacity

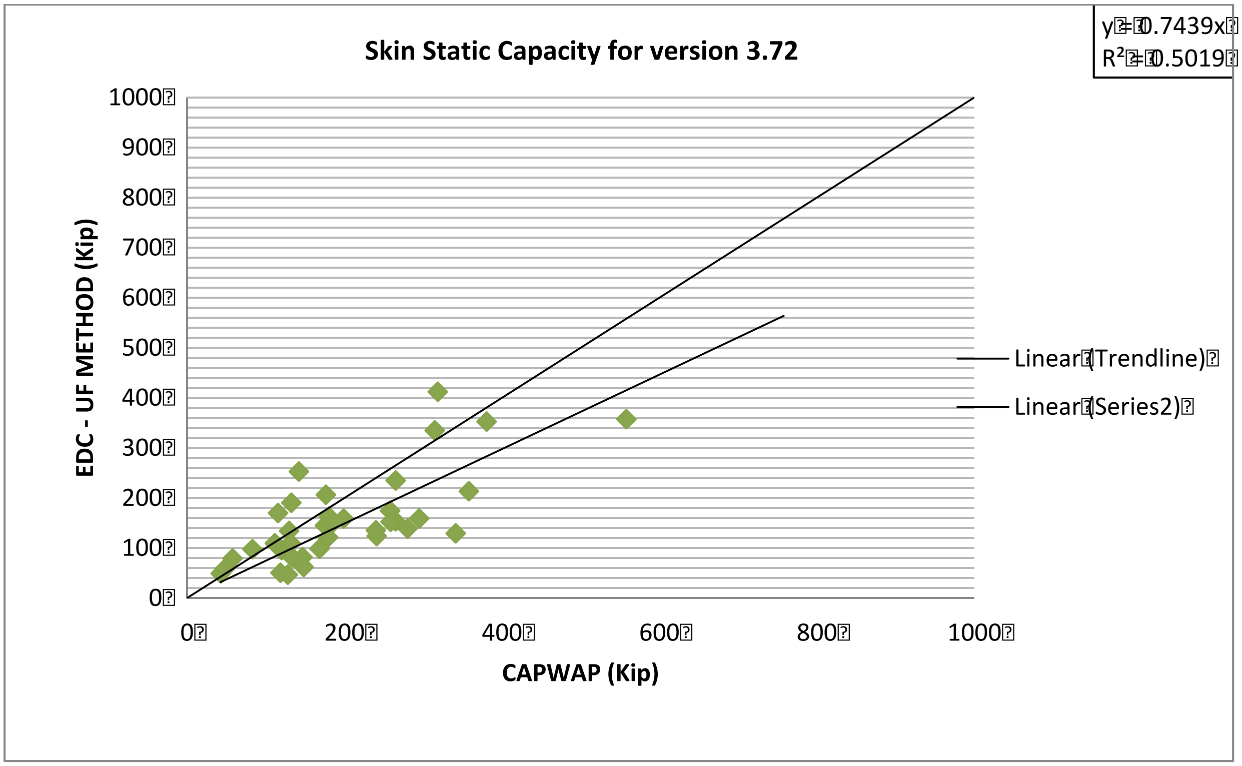

Figure 3-38 EDC 3.72 vs. CAPWAP, UF skin capacity

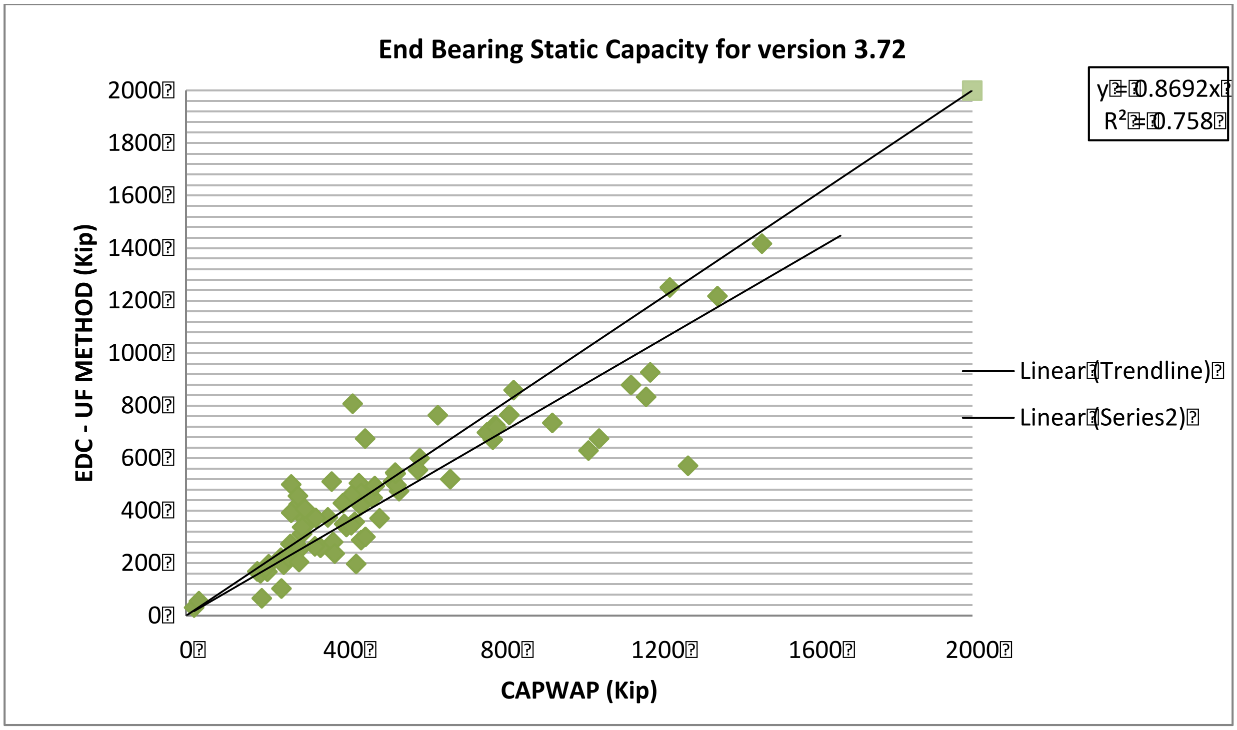

Figure 3-39 EDC 3.72 vs. CAPWAP, UF end bearing capacity

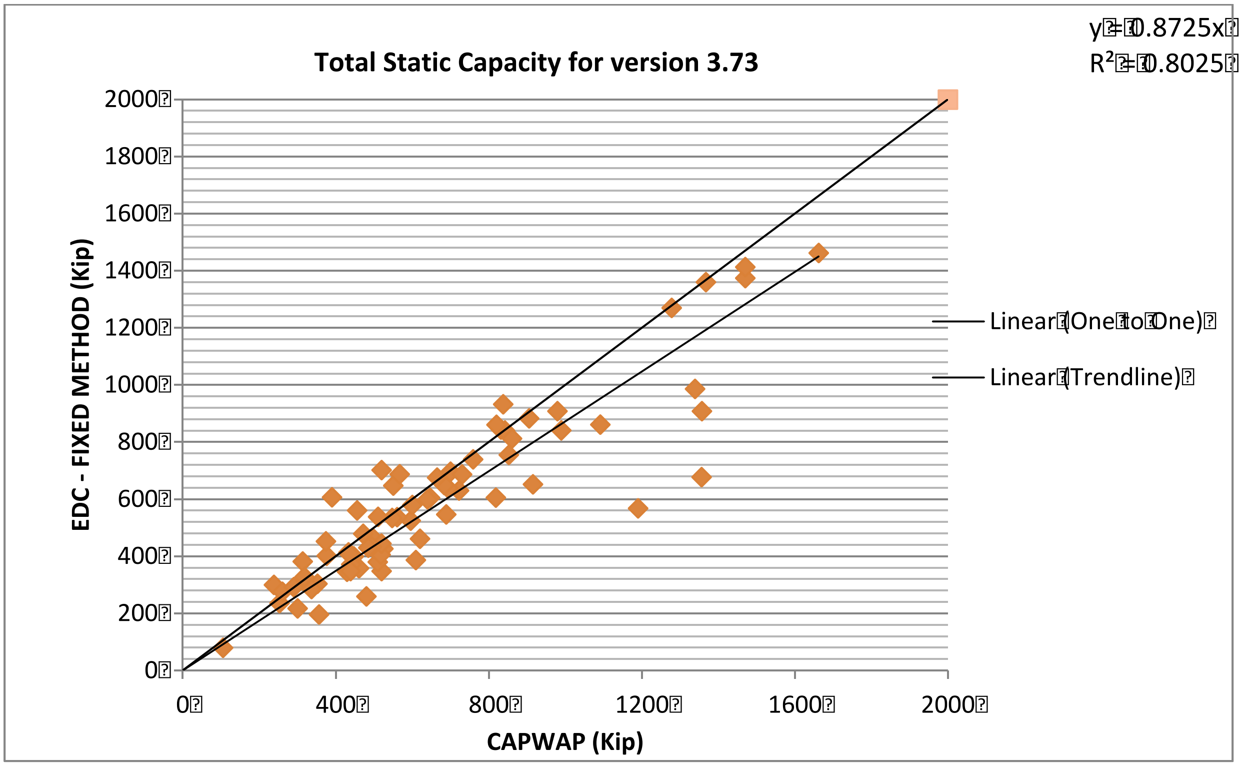

Figure 3-40 EDC 3.73 vs. CAPWAP, Fixed total capacity

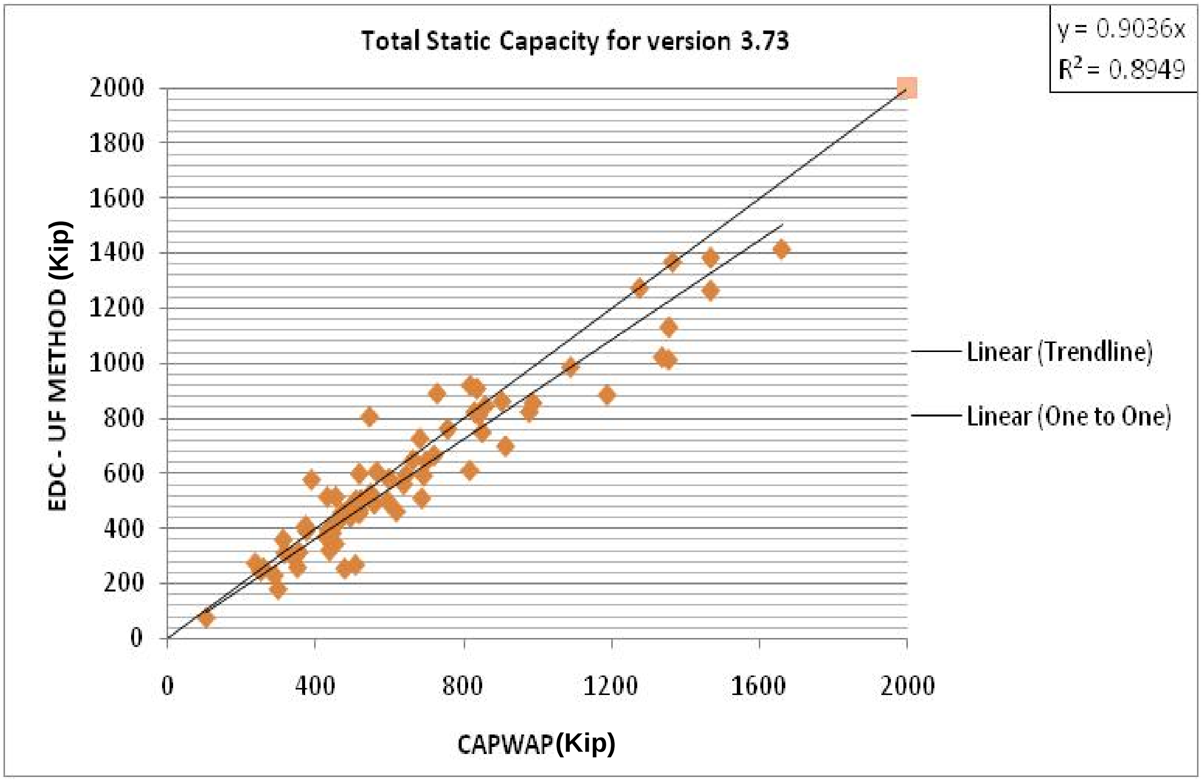

Figure 3-41 EDC 3.73 vs. CAPWAP, UF total capacity

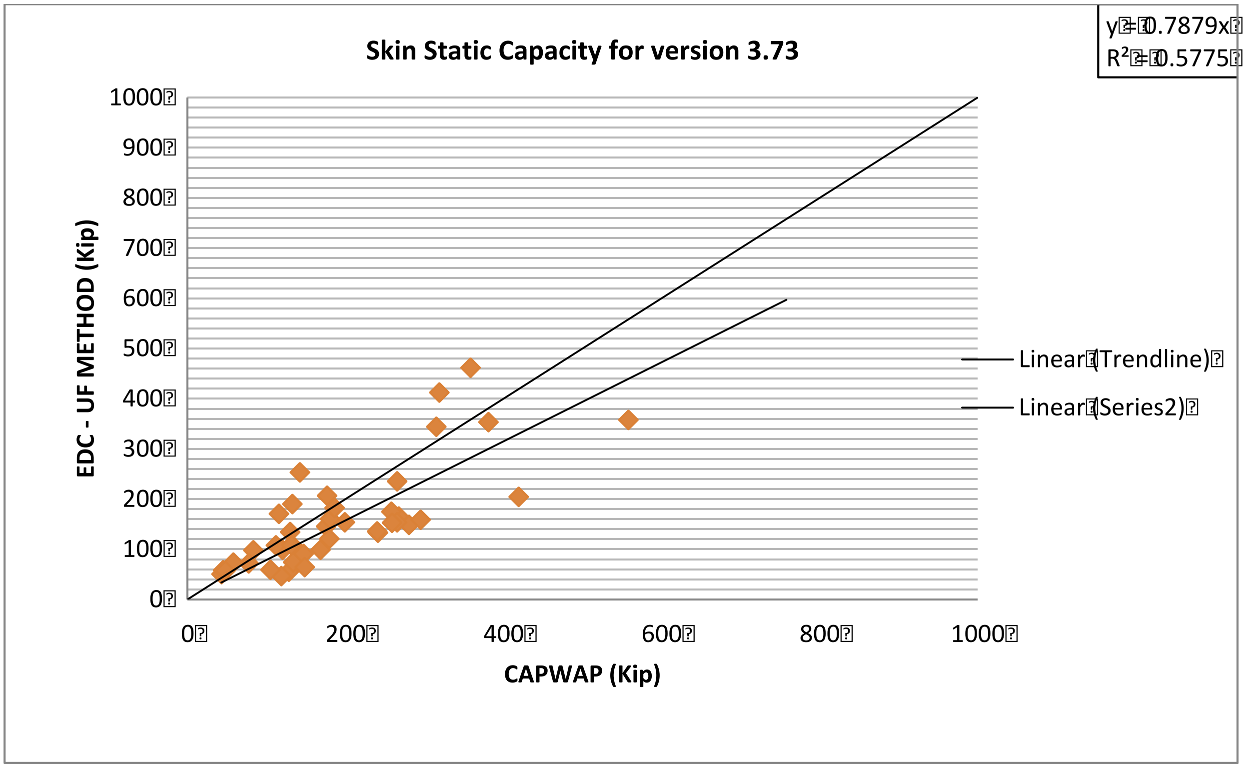

Figure 3-42 EDC 3.73 vs. CAPWAP, UF skin static capacity

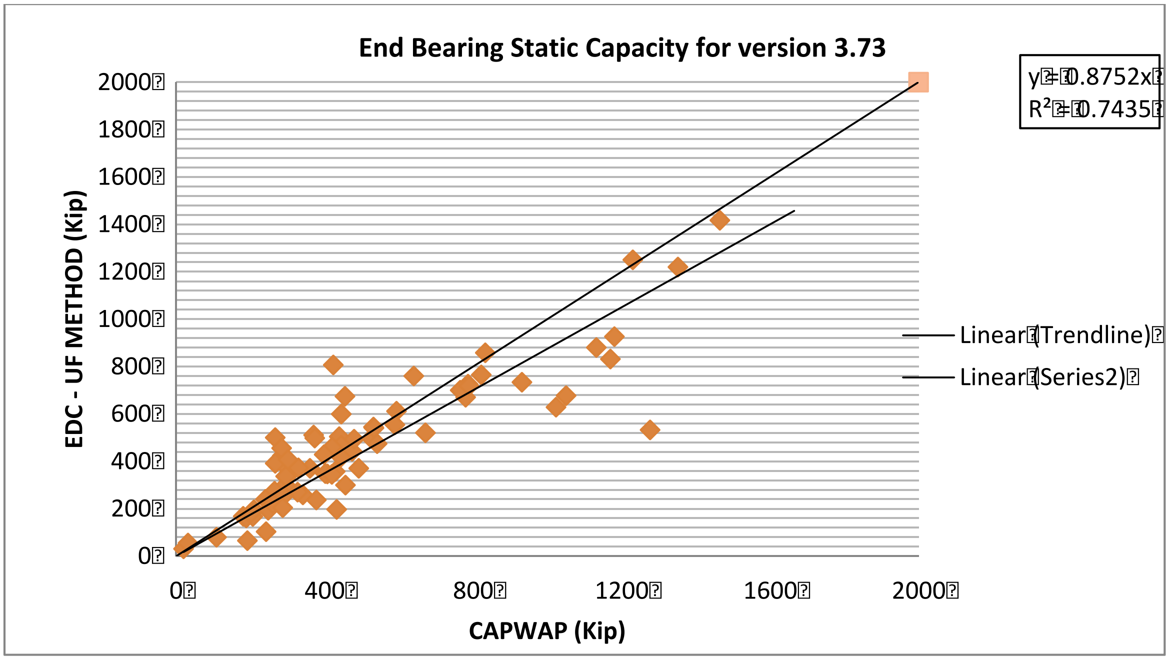

Figure 3-43 EDC 3.73 vs. CAPWAP, UF end bearing static capacity

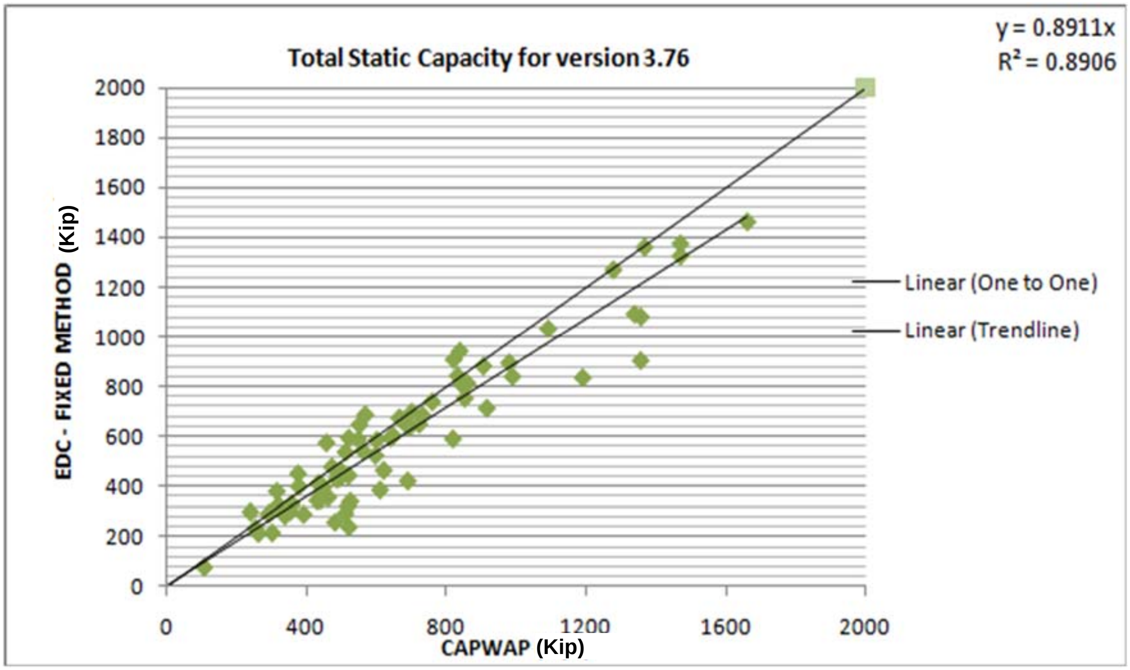

Figure 3-44 EDC 3.76 vs. CAPWAP, Fixed total capacity

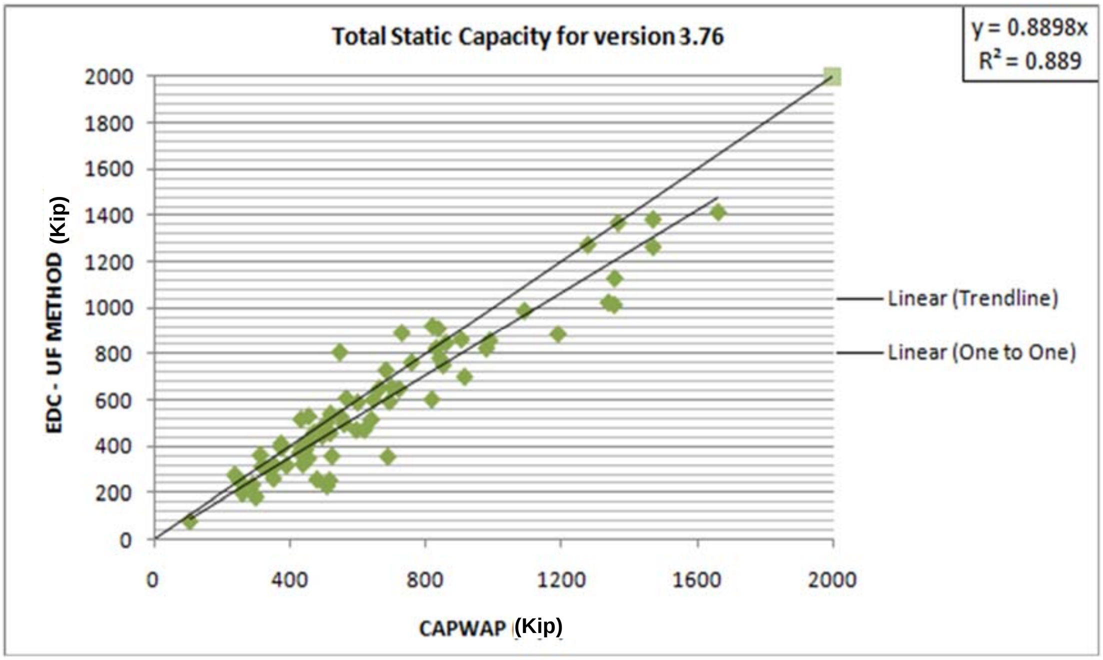

Figure 3-45 EDC 3.76 vs. CAPWAP, UF total capacity

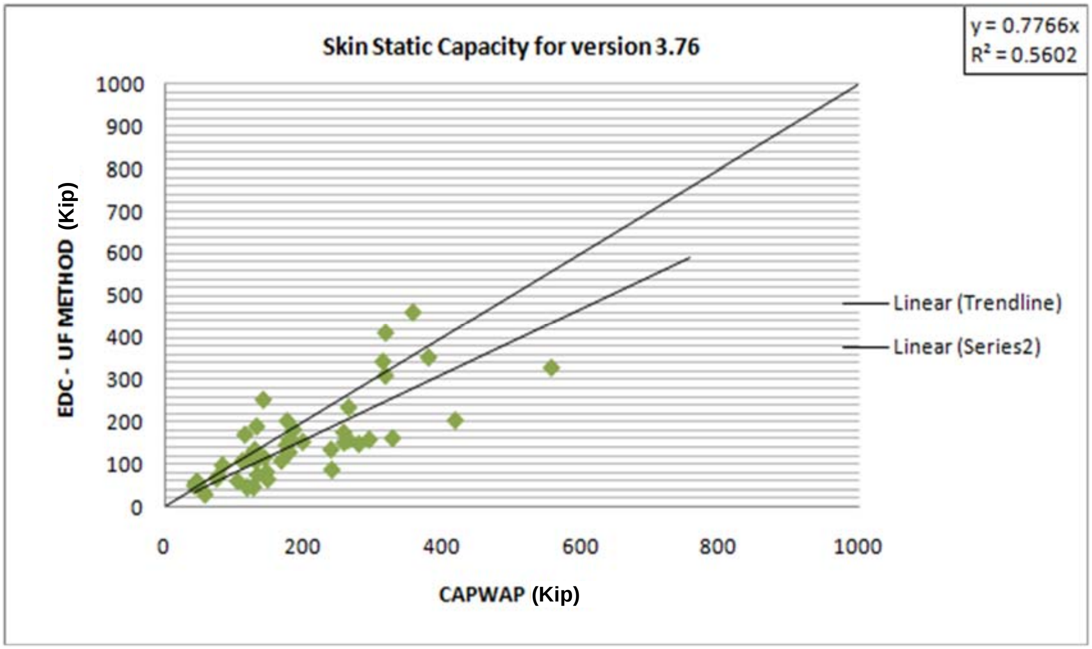

Figure 3-46 EDC 3.76 vs. CAPWAP, UF skin static capacity

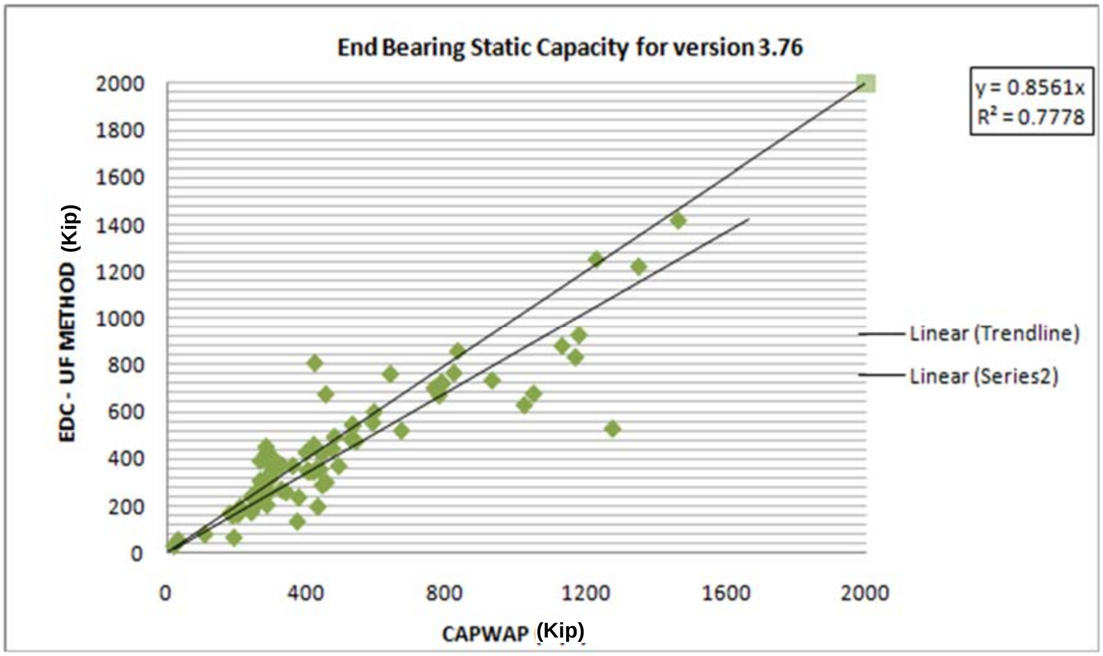

Figure 3-47 EDC 3.76 vs. CAPWAP, UF end bearing static capacity

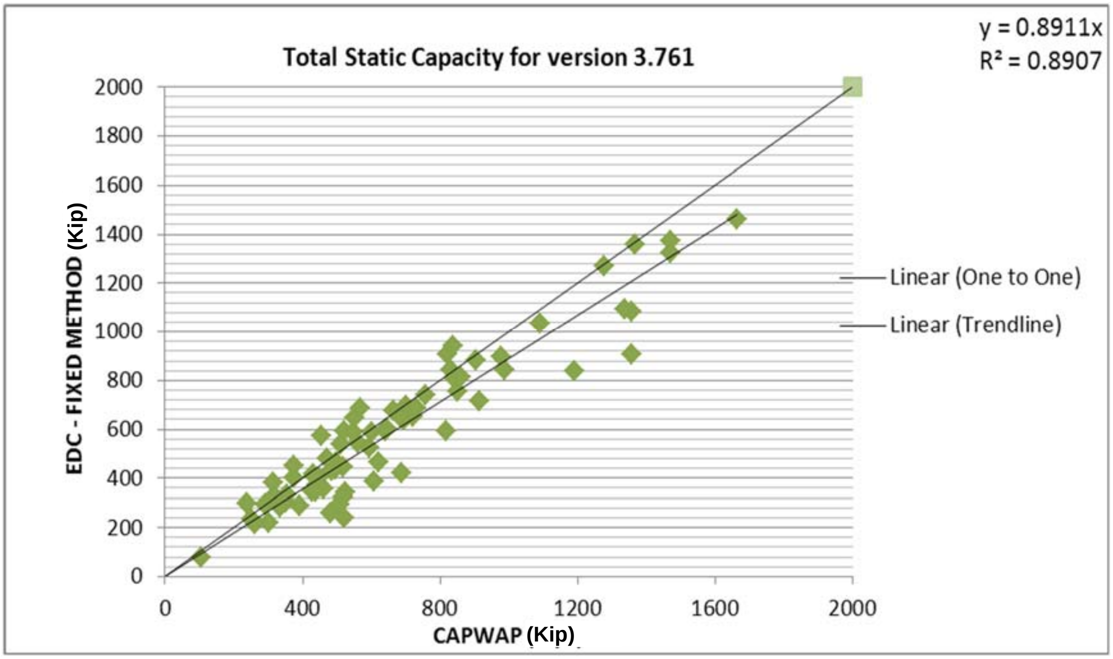

Figure 3-48 EDC 3.761 vs. CAPWAP, Fixed total capacity

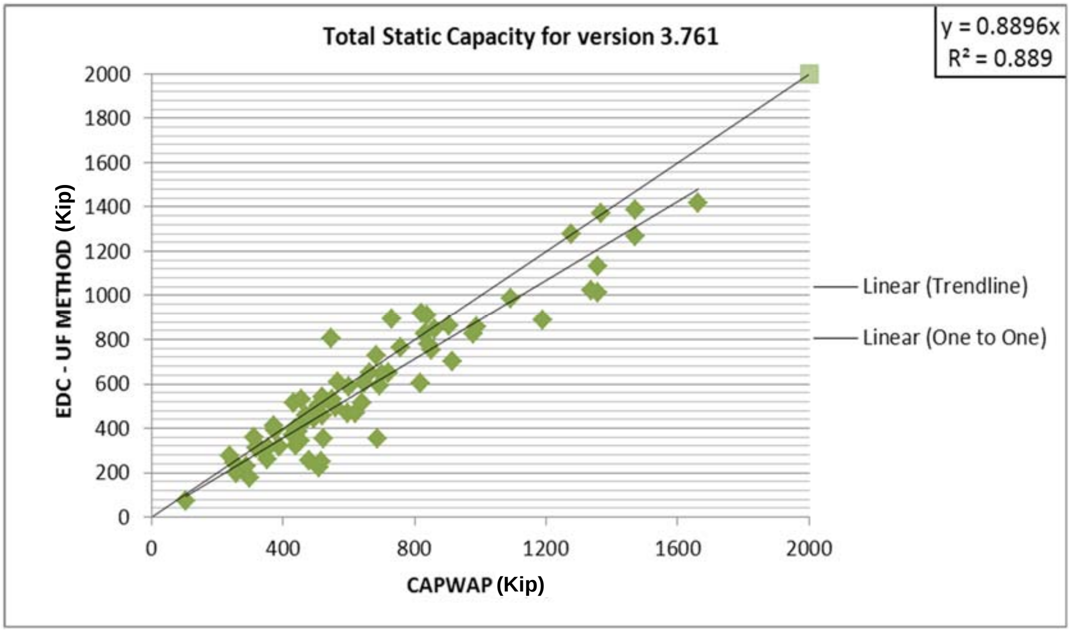

Figure 3-49 EDC 3.761 vs. CAPWAP, UF total capacity

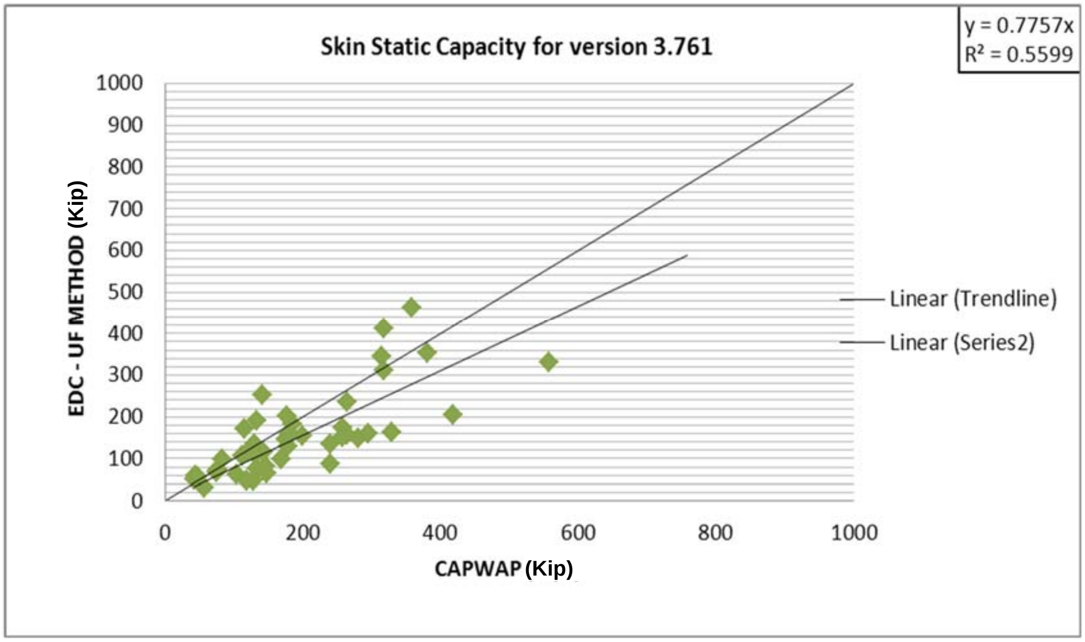

Figure 3-50 EDC 3.761 vs. CAPWAP, UF skin static capacity

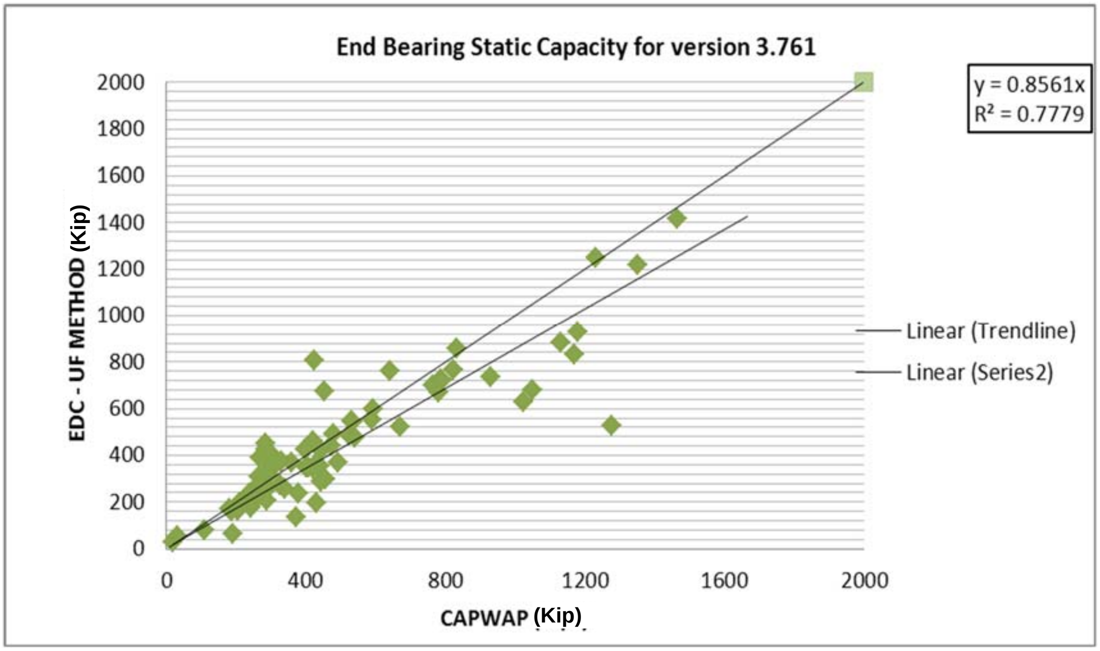

Figure 3-51 EDC 3.76 vs. CAPWAP, UF end bearing static capacity

Tables 3-9 and 3-10 show both the R^2 and Slope of the trend lines for all comparison of EDC with CAWAP (displayed on graphs). Evident from Table 3-9, the UF capacity predictions are more conservative in recent versions than previous. Also from Table 3-10, the relationship (i.e., slope) between EDC and CAPWAP are similar.

Table 3-9 Variation of R^2 from version 3.6 to version 3.761 of SmartPile Review

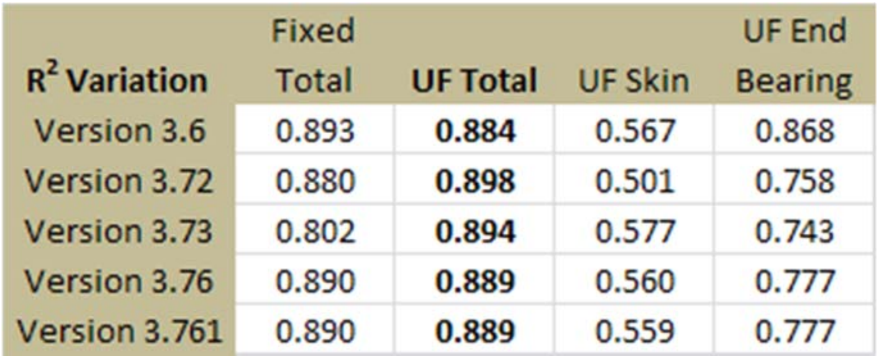

R^2 Variation	Fixed Total	UF Total	UF Skin	UF End Bearing
Version 3.6	0.893	**0.884**	0.567	0.868
Version 3.72	0.880	**0.898**	0.501	0.758
Version 3.73	0.802	**0.894**	0.577	0.743
Version 3.76	0.890	**0.889**	0.560	0.777
Version 3.761	0.890	**0.889**	0.559	0.777

Table 3-10 Variation of slope from version 3.6 to version 3.761 of SmartPile Review

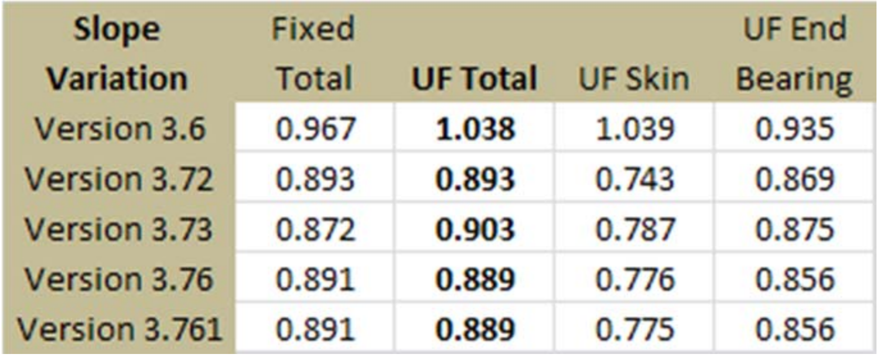

Slope Variation	Fixed Total	**UF Total**	UF Skin	UF End Bearing
Version 3.6	0.967	**1.038**	1.039	0.935
Version 3.72	0.893	**0.893**	0.743	0.869
Version 3.73	0.872	**0.903**	0.787	0.875
Version 3.76	0.891	**0.889**	0.776	0.856
Version 3.761	0.891	**0.889**	0.775	0.856

CHAPTER 4
IMPROVED ESTIMATES OF PILE SKIN FRICTION AND TIP CAPACITY

4.1 Introduction

The Florida Department of Transportation (FDOT) is in the process of implementing Embedded Data Collector (EDC) systems for driven prestressed concrete piles throughout Florida (Herrera, 2009). A goal is to achieve real time analyses of driven piles (NCHRP, 2011). Unlike the current practice (Rausche et al., 1985; Rausche et al., 2010; Smith, 1960) of using instrumentation only at the top of pile with required expertise (Kuo et al., 2007) in separating skin friction from tip resistance, techniques proposed herein allow direct assessment of skin friction and tip resistance as result of the analytical equation and boundary conditions. Note that the following sections discuss methods that are not in use by current users of SmartPile since they are either not the default method (tip resistance), or not implemented in the software (skin friction). Knowledge of skin friction and tip resistance is extremely useful when considering scour, pile freeze (Axelsson 2000, Bullock et al., 2005), or difficult pile cross-sections (e.g., large diameter cylinder piles). With regard to skin friction, Axelsson (2000) and Bullock et al. (2005) have reported skin friction increases of 20% to 100% (per log cycle) for multiple soil types with little if any change in pile tip resistance.

The following sections discuss improved assessments of skin friction and tip resistance for driven piles that could eventually be used with the EDC system. For skin friction, methods to estimate pile skin friction are presented for the linear and non-linear cases. In all three cases (linear skin, non-linear skin, tip) the pile is modeled as a single degree of freedom system, from which the mass, damping and stiffness are solved to find unique solutions. The methods are applied to four test piles at two bridge sites. A description of each site follows.

Site 1 is on SR810, Dixie Highway at Hillsboro Canal in Broward, Florida. The site consists of upper layers of approximately 15 m of medium dense sand with cemented sand zones underlain by limestone (bearing layer). The first pile analyzed (End Bent 1) was a 0.61-m-(2 ft)-square by 15.2-m-(50 ft)-long prestressed concrete pile, driven to a depth 14 m (46 ft) below the ground surface by a single acting diesel hammer. One week after installation, restrikes were conducted to investigate whether the skin friction had changed. Then the pile was load tested to failure in accordance to ASTM D1143 (quick test) three days after the restrike. The compression loads were applied using two 5000 kN (1124 kip) hydraulic jacks. The second pile of this site (Pier 8) also involved a 0.61-m-(2 ft)-square prestressed precast pile also installed approximately 15 m (46 ft) below the ground surface. Restrikes were conducted four days after installation, and the static compression load test was conducted two days after the restrikes. Similar to pile 1, data from five end of drive (EOD) blows and ten beginning of restrike (BOR) blows were analyzed.

Site 2 is at Caminada Bay, Louisiana, 70 km south of New Orleans. The site consists of 2 uppers layers: 1) 10 m (33 ft) of silty fine sand with clay (SPT N ~ 14) and, 2) 10 m (33 ft) of fine sand with silt (SPT N ~ 24); underlain by a high plasticity (40<PI<70) clay. The first pile (pile 1) presented is a 0.76-m-(2.5 ft)-square precast prestressed concrete pile installed 21 m (69 ft) below the ground surface using a single acting diesel hammer. Restrikes were conducted seven days after installation, and the static compression load test was conducted two days after the restrikes. The second pile at the Caminada Bay site (pile 2) was also a 0.76-m-(2.5 ft)-square precast prestressed concrete pile installed about 21 m (69 ft) below the ground surface. Restrikes were conducted one month after installation, and the static compression load test was conducted two days after the restrikes.

4.2 Skin Friction (Homogeneous)

4.2.1 Model Description

For any driven pile, soil static skin friction and damping forces develop on a segment, of length dx, as shown in Figure 4-1. The skin friction, *Fs* (force), is characterized as unit skin friction, *fs* (stress), times the surface area it acts on. The unit skin friction (fs) is usually characterized as a function of the pile displacement, *u(x,t)*. Using secant soil stiffness, *K*, defined as the unit skin friction per unit of displacement (Figure 4-1), the skin friction acting on segment dx is found as:

$$F_S = f_s \, A_{surf} = K \, u(x,t) \, P \, dx \, , \qquad \text{Eq. 4-1}$$

Next, assuming generalized damping, the damping force, *Fd*, is obtained as:

$$F_d = C_r \, P \, dx \, \rho_s \frac{\partial u(x,t)}{\partial t} \, , \qquad \text{Eq. 4-2}$$

Summing forces on the segment, dx, results in:

$$\downarrow \ \sum F_v = \ 0 \ = F_B - F_T - F_I - F_S \ - F_d \, ,$$

$$\left(\sigma + \frac{\partial \sigma}{\partial x} dx\right) A - \sigma \ A - \rho \, A \ dx \ \frac{\partial^2 u}{\partial t^2} - K \, P \, dx \ \ u(x,t) - C_r \ P \ dx \ \rho_s \ \frac{\partial u}{\partial t} = 0. \qquad \text{Eq. 4-3}$$

Next, cancelling plus and minus terms, and then dividing by dx and A, results in:

$$\frac{\partial \sigma}{\partial x} - \ \rho \ \frac{\partial^2 u}{\partial t^2} - \frac{K \, P}{A} \ u(x,t) - \frac{C_r \ P \ \ \rho_s}{A} \frac{\partial u}{\partial t} \ = \ 0 \, . \qquad \text{Eq. 4-4}$$

Introducing linear pile stress to pile strain and then differentiating obtain particle displacement,

$$\sigma = E \ \varepsilon = E \, \frac{\partial u}{\partial x} \quad Then \quad \frac{\partial \sigma}{\partial x} = E \, \frac{\partial^2 \, u}{\partial \, x^2} \, .$$

Substituting ∂σ/∂x and *P/A = 4/B* (typical square pile) into Eq. 4-4 and dividing by ρ, results in:

$$\frac{E}{\rho}\frac{\partial^2 u}{\partial x^2} - \frac{\partial^2 u}{\partial t^2} - \frac{4\,K}{\rho\,B}\,u(x,t) - \frac{4\,C_r\ \rho_s}{B\,\rho}\frac{\partial u}{\partial t} = 0. \qquad \text{Eq. 4-5}$$

Let: $a^2 = \frac{E}{\rho} \quad b = \frac{4\,K}{\rho\,B} \quad c = \frac{4\,C_r\ \rho_s}{B\,\rho}$

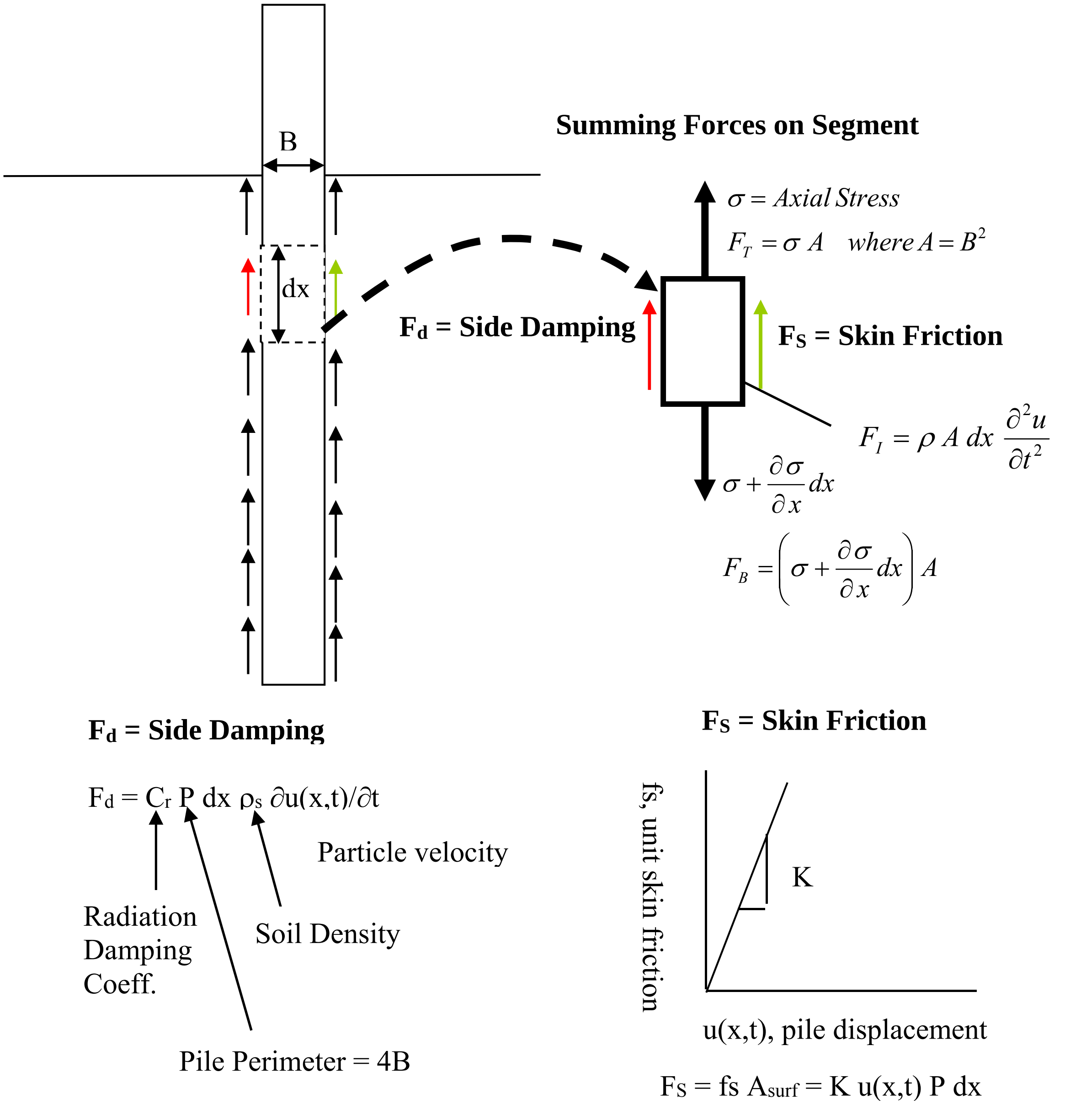

Figure 4-1 Forces acting on pile

Then, the final 1-D partial differential equation of wave propagation with skin friction, b, and damping, c, is

$$a^2 \frac{\partial^2 u}{\partial x^2} = \frac{\partial^2 u}{\partial t^2} + c \frac{\partial u}{\partial t} + b\, u(x,t). \qquad \text{Eq. 4-6}$$

In the above equations, A_{surf} is surface area where forces act over, P is pile perimeter, B is pile width, dx is segment length, C_r is viscous damping coefficient, ρ and ρ_s are pile and soil densities, E is Young's modulus of pile, and x, t are spatial and time variables, respectively.

Numerical approaches such as Newmark/Newton–Raphson algorithms (Clough and Penzien, 1993; Paz, 1997; Thomson and Dahleh, 1993) and pseudo-forces/implicit Green's function based iterations (Soares and Mansur, 2005; Strickilin and Haisler, 1977) can be used to solve Eq. 4-6 for the general case, e.g., layered soil profiles with linear or non-linear soil-pile interaction (Küçükarslan, 2002; Manna and Baidya, 2010; Novak M. and Aboul-Ella, 1978). However, all of these methods require significant computer time for solution, and may not be useful for real time global inversion. Therefore, a simple model of homogeneous soil and a linear soil-pile interaction (constant b) is employed to achieve an extremely fast analytical solution. To support the model, comparisons between the predicted and measured results are made for two case studies.

To solve Eq. 4-6 for the case of a pile with a finite length, initial and boundary conditions are required. The initial conditions are at rest, e.g., particle displacement, velocity and acceleration (u, $\partial u/\partial t$ and $\partial^2 u/\partial t^2$) are zero when t equals zero (i.e., prior to hammer impact). For the boundary conditions, strains at the top (x = 0) and bottom (x = l = pile length) of the pile are prescribed as:

$$\frac{\partial u}{\partial x} = g_1(t) \quad at\, x = 0$$
$$\frac{\partial u}{\partial x} = g_2(t) \quad at\, x = l \qquad \text{Eq. 4-7}$$

where g1(t) and g2(t) are the measured strain data (EDC) at the top and bottom of the pile as a function of time. The solution of Eq. 4-6 with the initial conditions at rest and boundary conditions of Eq. 4-7 is as follows (Polyanin, 2002):

$$\begin{aligned} u(x,t) &= -a^2 \int_0^t g_1(\tau)\, G(x,0,t-\tau)\, d\tau + a^2 \int_0^t g_2(\tau)\, G(x,l,t-\tau)\, d\tau \\ &= -a^2 \left[g_1 * G(x,0,t) - g_2 * G(x,l,t) \right] \end{aligned} \qquad \text{Eq. 4-8}$$

$$G(x,\xi,t) = \exp(-\frac{1}{2}ct) \left[\frac{\sin\left(t\sqrt{|p|}\right)}{l\sqrt{|p|}} + \frac{2}{l} \sum_{n=1}^{\infty} \cos(\mu_n x) \cos(\mu_n \xi) \frac{\sin\left(t\sqrt{a^2 \mu_n^2 - p}\right)}{\sqrt{a^2 \mu_n^2 - p}} \right],\ \mu_n = \frac{\pi n}{l} \qquad \text{Eq. 4-9}$$

where $p = b + \frac{1}{4}c^2$, * denotes the convolution operator, and $G(x,\xi,t)$ is the Green's function used to measure the response at position x caused by a unit load at position ξ.

Equation 4-8 gives particle displacements which may be inverted with the measured displacement to estimate the pile skin friction (i.e., p (b)). However, the measured displacement is usually non-zero, smooth and with few inflection points, whereas particle velocity has multiple inflection points, as well as crosses zero multiple times. Consequently, it was found with velocity, that convergence was much faster because the signals carried only one or two dominant maxima (pulses) and along with zeros, the velocity had much greater sensitivity in the inversion.

Taking the derivatives of Eqs. 4-8 and 4-9 with respect to time and using the symmetry property of the convolution operator

$$(f(t) * g(t))' = f(t)' * g(t) = f(t) * g(t)'$$

and the particle velocity may be derived as:

$$v(x,t) = u'(x,t) = -a^2\left[g_1 * G'(x,0,t) - g_2 * G'(x,l,t)\right], \qquad \text{Eq. 4-10}$$

where

$$\begin{aligned} G'(x,\xi,t) = {} & -\frac{1}{2}c\exp(-\frac{1}{2}ct)\left[\frac{\sin\left(t\sqrt{|p|}\right)}{l\sqrt{|p|}} + \frac{2}{l}\sum_{n=1}^{\infty}\cos(\mu_n x)\cos(\mu_n \xi)\frac{\sin\left(t\sqrt{a^2\mu_n^2 - p}\right)}{\sqrt{a^2\mu_n^2 - p}}\right] + \\ & + \exp(-\frac{1}{2}ct)\left[\frac{\cos\left(t\sqrt{|p|}\right)}{l} + \frac{2}{l}\sum_{n=1}^{\infty}\cos(\mu_n x)\cos(\mu_n \xi)\cos\left(t\sqrt{a^2\mu_n^2 - p}\right)\right]. \end{aligned} \qquad \text{Eq. 4-11}$$

Examination of Eqs. 4-10 and 4-11 reveal that the only unknowns are damping, c, and soil stiffness, b. The particle velocity, v(x,t), is known at both the top, v(x=0,t) and bottom, v(x =l,t) of the pile by integration of embedded pile acceleration gauges with time. Similarly, the strain at the top, g_1(x=0, t) and bottom, g_2(x=l, t) of the pile is measured directly with embedded gauges as a function of time. The unknowns, b and c were subsequently determined through an inversion scheme, which is discussed in the next section.

4.2.2 Solution Methodology

The goal of the inversion method is to estimate two unknown parameters, damping related parameter (c) and stiffness related parameter (b). From b, the static skin friction (F) can be determined as:

$$\begin{aligned} F = f_s\, A_{surf} &= K\, Max\left[u(x,t)\right] A_{surf} \\ &= \frac{b\rho\, B}{4} Max\left[u(x,t)\right]\,(4B\, l) = b\rho\, B^2 l\, Max\left[u(x,t)\right] \end{aligned} \qquad \text{Eq. 4-12}$$

where $Max\left[u(x,t)\right]$ is the mean of maximum measured displacements at the top and bottom of the pile.

The simplest way of assessing b and c is from an inversion process to match the measured data with estimated data. For instance, using particle velocity data, the estimated velocity can be calculated by assuming values of b and c, computing the time derivative of the

Green's function, G' from Eq. 4-11, and then performing the convolution, Eq. 4-10, with the measured strains (g_1, g_2). However, the analysis must be performed hundreds of thousand times to minimize the error between measured and predicted velocity as a function of time. Unfortunately, this approach can require significant computer time for the global inversion technique because of the expensive operation of the convolution in calculation of the estimated velocity data (forward modeling).

To reduce computer time, it was proposed to match the observed and predicted Green's functions through inversion directly. By doing so, the estimated Green's function is immediately obtained from Eq. 4-11. A discussion of the observed Green's function and its derivation follows.

4.2.2.1 Observed Green's Function

The observed Green's function is obtained from a deconvolution (Cartwright, 1990) of the measured data. This requires the use of the convolution theorem (Cartwright, 1990)

$$fft(f * g) = fft(f)\, fft(g)$$

where *fft(f)* denotes a Fourier transform of *f*.

First, the Fourier transform is applied to Eq. 4-10, and then with the use of the convolution theorem, the following equations are derived

$$\begin{aligned} fft(v(0,t)) &= -a^2\left[fft(g_1)\, fft(G'(0,0,t)) - fft(g_2)\, fft(G'(0,l,t))\right] \\ fft(v(l,t)) &= -a^2\left[fft(g_1)\, fft(G'(l,0,t)) - fft(g_2)\, fft(G'(l,l,t))\right] \end{aligned} \qquad \text{Eq. 4-13}$$

where *v(0,t)* and *v(l,t)* are measured velocities, and g_1 and g_2 are measured strains at the top and bottom of the pile.

Denoting $G'(0,0,t) = G'(l,l,t) = G_1$ and $G'(l,0,t) = G'(0,l,t) = G_2$, then Eq. 4-13 may be expressed in the frequency domain as

$$\begin{aligned} v(0,\omega) &= -a^2\left[g_1(\omega)\,G_1(\omega) - g_2(\omega)\,G_2(\omega)\right] \\ v(l,\omega) &= -a^2\left[g_1(\omega)\,G_2(\omega) - g_2(\omega)\,G_1(\omega)\right] \end{aligned} \qquad \text{Eq. 4-14}$$

Next, Eq. 4-14 is solved for $G_1(\omega)$ and $G_2(\omega)$

Or

$$\begin{bmatrix} G_1(\omega) \\ G_2(\omega) \end{bmatrix} = \frac{1}{a^2}\begin{bmatrix} -g_1(\omega) & g_2(\omega) \\ g_2(\omega) & -g_1(\omega) \end{bmatrix}^{-1} \begin{bmatrix} v(0,\omega) \\ v(l,\omega) \end{bmatrix} \qquad \text{Eq. 4-15}$$

where, f *(ω)* is the Fourier transform of *f (t)* at a particular frequency ω.

The Green's functions, G_1 and G_2, (Eq. 4-15) are calculated for all desired frequencies and then an inverse Fourier transform is performed in order to generate the observed Green's functions in the time domain. G_1 and G_2 in the time domain usually have very similar shapes, thus only one of them was used in the inversion process. The inversion process is presented and discussed in Appendix A.

4.2.3 Applications

4.2.3.1 Site 1

End Bent 1

The wave guide solution was applied to 12 of the end of drive (EOD) blows and 8 beginning restrike blows (BOR). The specific results of one restrike blow are presented here in detail for discussion.

Prior to running the inversion, the observed Green's function from the measured data must be found. The following three steps were completed to obtain the observed Green's functions (Figure 4-2). First, the measured strains and velocities (integrated from measured accelerations) were filtered (low-pass) to remove all signals with frequencies of 100 Hz and above (remove the high frequency noise), and a Fourier transform was performed to obtain the frequency components. Second, the transformed strain data (g_1, g_2) was also filtered (inverse filtering) to remove very low magnitudes which would result in significant magnification of

Green's functions, i.e., Eq. 4-15. The inverse filtering was bound to frequency response 1/g(ω) at the prescribed threshold γ as follows:

$$\frac{1}{g(\omega)} = \begin{cases} \dfrac{1}{g(\omega)}, & if \ \dfrac{1}{|g(\omega)|} < \gamma \\ \gamma \dfrac{|g(\omega)|}{g(\omega)}, & otherwise \end{cases} \qquad \text{Eq. 4-16}$$

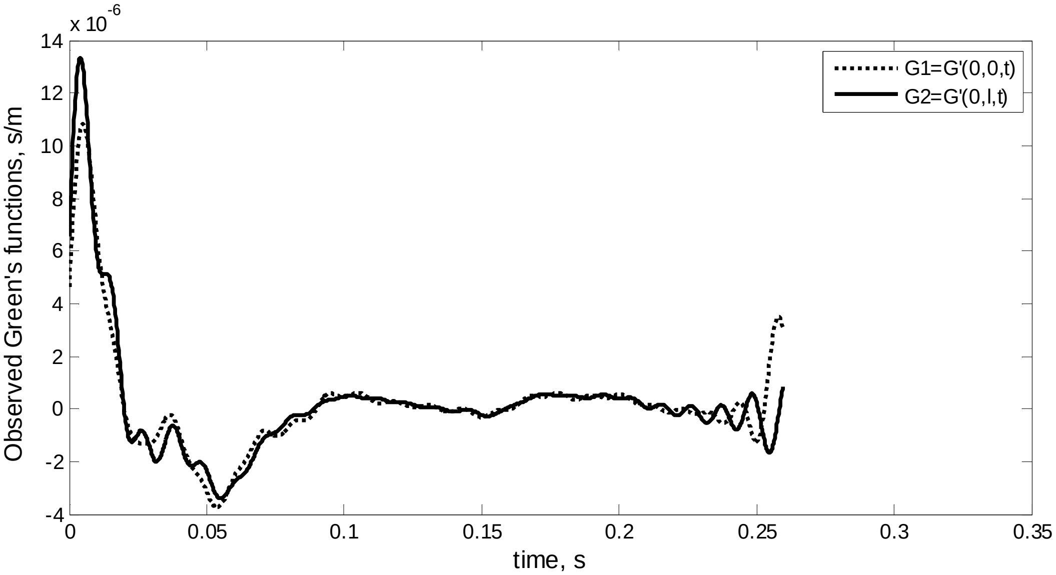

Figure 4-2 Dixie Highway End Bent 1: the observed Green's functions

In this study, the value of the threshold γ was taken such that the magnitude of filtered component g(ω) at any frequency was not less than 5% of the maximum magnitude of all components. Finally, functions G_1, G_2 were calculated for all frequencies (Eq. 4-15) and then inverse Fourier transforms were applied to generate the observed Green's functions in the time domain. Figure 4-2 presents the observed Green's functions obtained by the deconvolution of the measured data. It is observed that the two functions have similar shapes, and one of them was subsequently used in the inversion.

The inversion solution (Appendix A) is taken as the model in the final generation having the lowest least-squared error, which corresponds to b equal to 2508.6 (1/s^2) and c equal to 72.9 (1/s). The estimated Green's function (Eq. 4-11) from the inversion solution is shown together with the observed Green's function (Eq. 4-15) in Figure 4-3. It should be noted that the observed Green's function (Eq. 4-15) is computed directly from measured data without any assumption regarding the soil-pile model. The good match between the observed and estimated Green's functions suggest that the assumed homogeneous soil profile and linear relation between skin friction and displacement in the theoretical Green's function (Eq. 4-11) is acceptable. Moreover, since the maximum magnitude of the theoretical Green's function is primarily controlled by the soil stiffness (b), the inverted value of b may be inferred as a linear-equivalent secant stiffness.

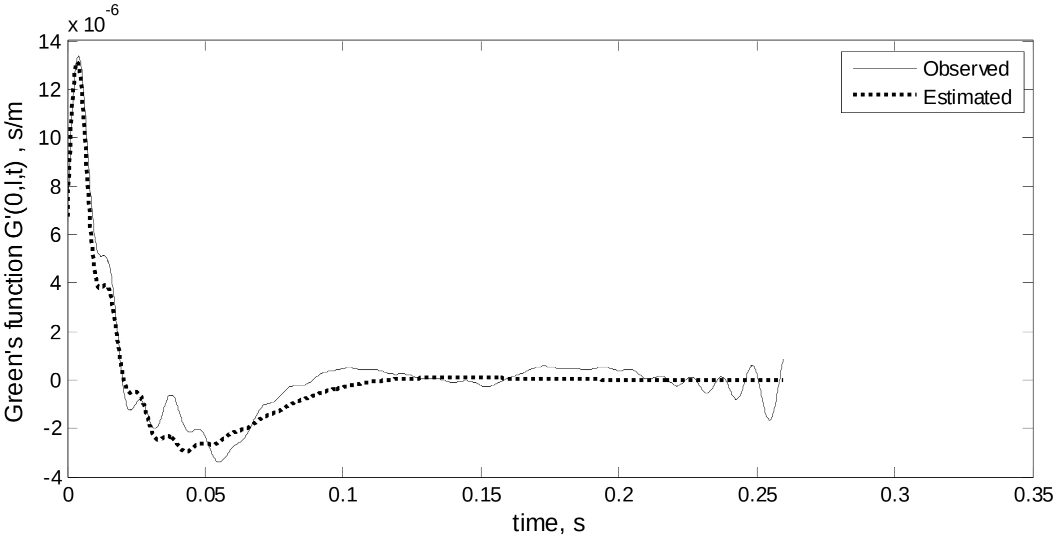

Figure 4-3 Dixie Highway End Bent 1: comparison of the observed and estimated Green's functions

The good match between the observed and estimated Green's functions subsequently leads to a good match between the observed and estimated particle velocity (Figure 4-4) from Eqs. 4-10 and 4-11. Evident from Figure 4-4, all of the dominant components are matched. It is expected that even better matches can be achieved if more complexity is accounted for into the models, e.g., dividing the soil into layers with different parameters b and c.

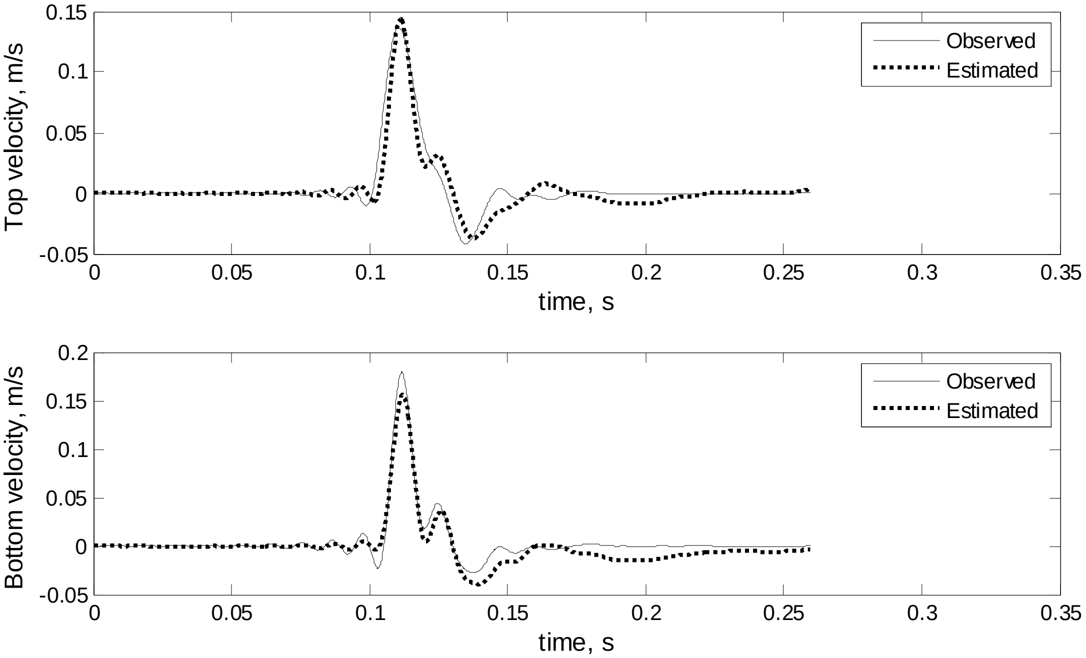

Figure 4-4 Dixie Highway End Bent 1: comparison of the observed and estimated velocities at the top and bottom of the pile

After solving for the equivalent secant stiffness b, the skin friction was calculated, Eq. 4-12, using the mean of maximum measured displacements computed from the measured accelerations at the top and bottom of the pile, or

$$F = b\rho B^2 l \, Max[u(x,t)] = 2508.6 * 2.5 * 0.61^2 * 14 * 0.020 = 653.4\,(kN)$$

The individual blow results for 12 EOD and 8 BOR are shown in Figure 4-5. For 12 EOD blows, the maximum displacements vary from 10 mm (0.4 in) to 20 mm (0.8 in), and the computed values of stiffness b varied from 4200 to 2300 ($1/s^2$) , producing similar skin frictions. In the same manner, 8 BOR blows had varying soil stiffness, b, for different displacements, but similar pile skin frictions, suggesting linear-equivalent secant stiffness. Similarly, if small displacements of the pile were to occur (i.e., insufficient hammer energy), then the mobilized skin friction would be less than the ultimate skin friction.

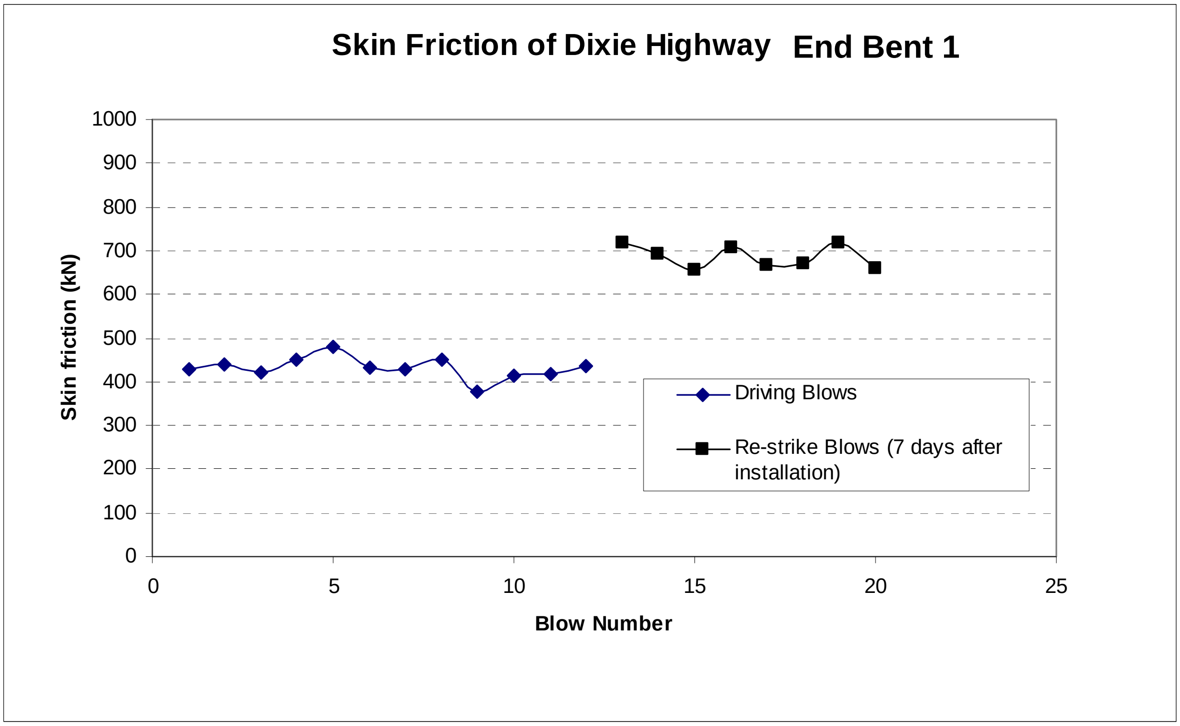

Figure 4-5 Estimated skin friction of Dixie Highway End Bent 1

Averaging, the EOD and BOR blow results separately, the skin friction increased from 430 kN (97 kips) at end of driving to 690 kN (155 kips) for restrike blows seven days later. This significant increase, 60 %, is attributed to “pile freeze”, and it is consistent with the observations of many other researchers (Bullock et al., 2005; Kuo et al., 2007; McVay et al., 1999; Titi and Wathugala, 1999). The phenomenon of “pile freeze” not only occurs in clays but also in dense to very dense sands, as well as cemented sands. Increases in skin friction of 10 to 100 % after driving may be due pore pressure dissipation, or total stress changes. Bullock et al. (2005) have shown that freeze generally occurs linearly with log cycles in time.

For comparison, the result of static compression load test for end bent 1 is shown in Figure 4-6. Based on the load test, the ultimate skin friction was achieved at a small displacement of about 5 mm (0.2 in), which is less than the observed displacement from 10 mm

(0.4 in) to 20 mm (0.8 in) measured for each blow during installation. Thus, the ultimate skin friction can be inferred from dynamic responses because the pile mobilized sufficient displacements. In the displacement range from 10 mm (0.4 in) to 20 mm (0.8 in), the skin friction from the static load test (Figure 4-6) is from 750 kN (169 kips) to 800 kN (180 kips), and it compares favorably to the estimated 690 kN (155 kips) from dynamic data. The difference of about 10 percent may be explained as: 1) the load test was conducted 3 days after the restrike blows, and skin friction would be higher from ”pile freeze”; or 2) the difference may be due to the layered subsurface profile, which may not be completely modeled by two average parameters b and c.

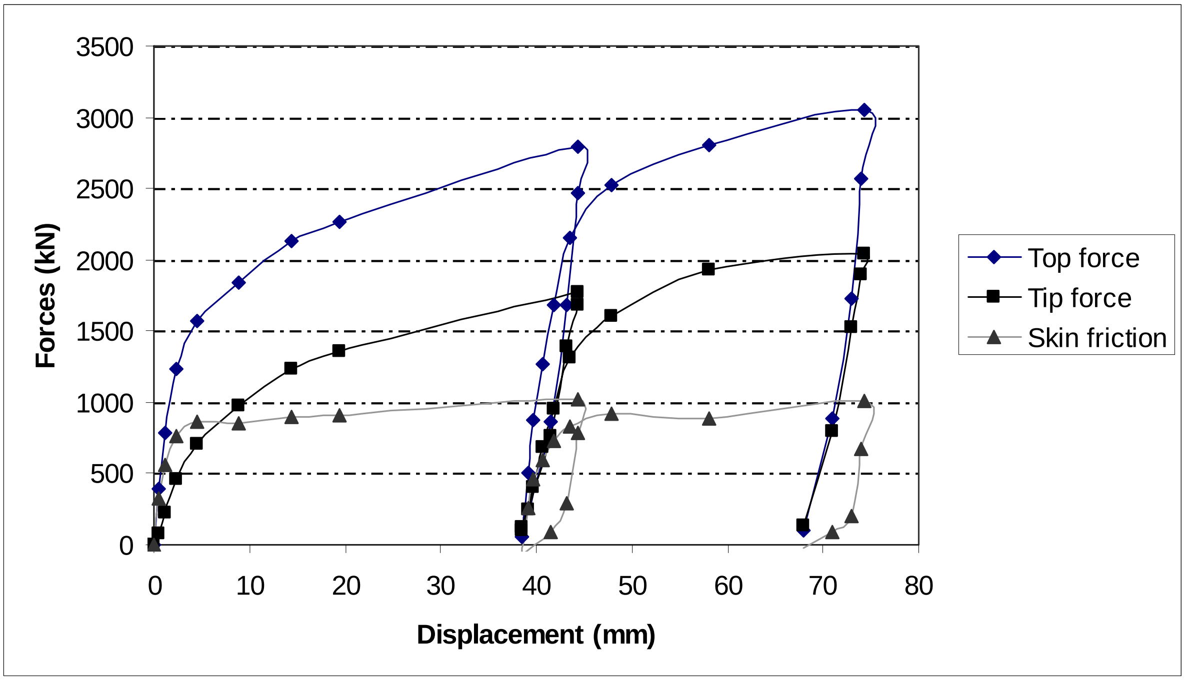

Figure 4-6 Static compression load test of Dixie Highway End Bent 1

Pier 8

Figure 4-7 shows both the EOD and BOR estimated ultimate skin frictions. Again, a significant increase of skin friction, 64%, was observed from the end of drive estimate, i.e., 500 kN (112 kips) to the beginning of restrike estimate, 820 kN (184 kips), after four days.

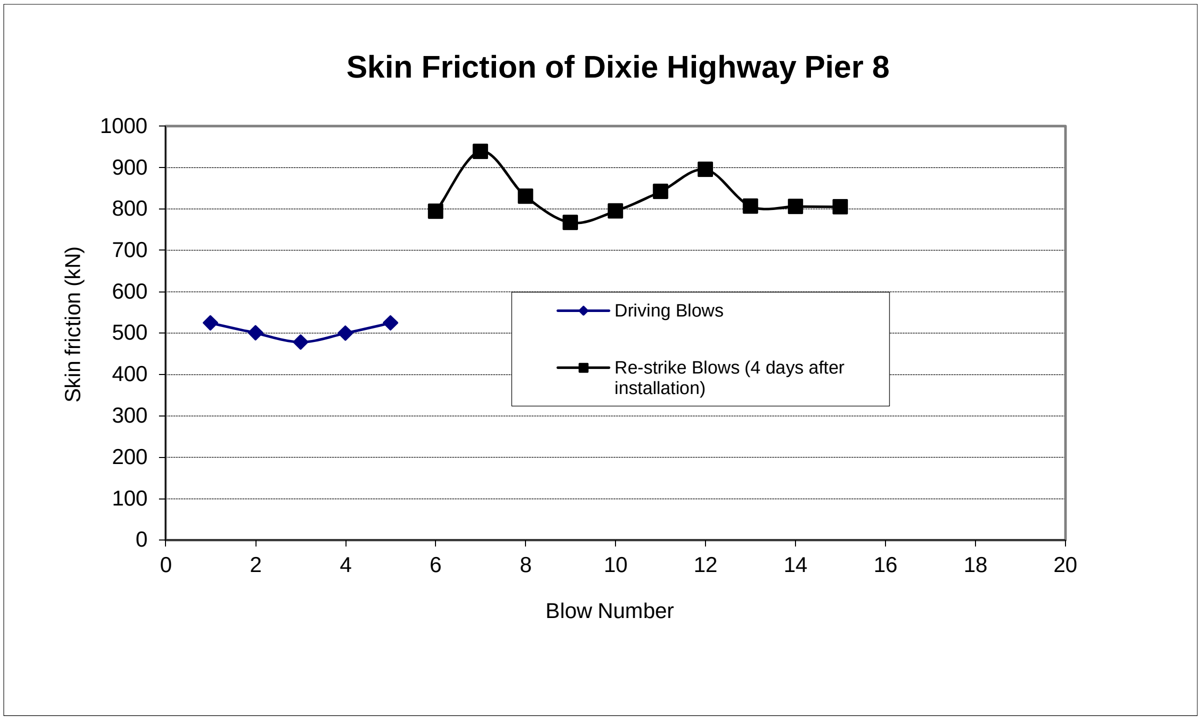

Figure 4-7 Estimated skin friction of Dixie Highway Pier 8

Figure 4-8 presents the result of static compression load test for pier 8, which occurred two days after the restrike. From the figure, the ultimate static skin friction is mobilized at small displacement, approximately 5 mm (0.2 in). At 10 mm (0.4 in) to 20 mm (0.8 in) of displacements (i.e., displacements/blow), the skin frictions were 900 kN (202 kips) to 950 kN (214 kips), respectively. Again, the results are consistent with end bent 1, skin friction from the load test was about ten percent higher than the dynamic results.

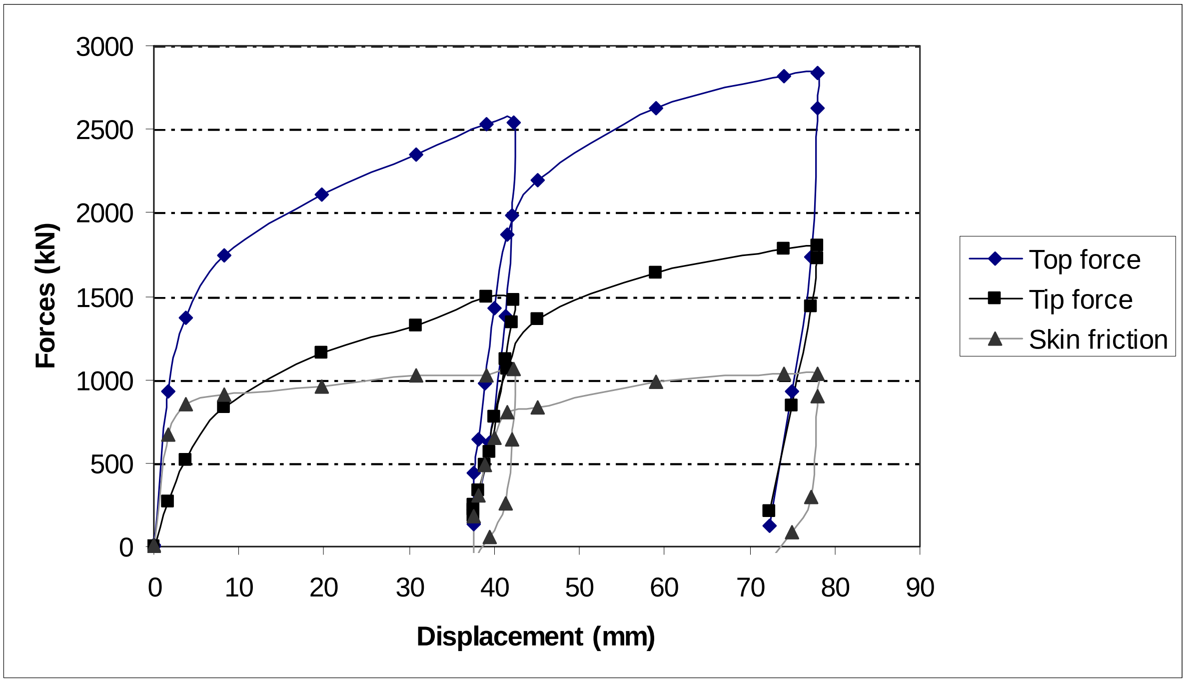

Figure 4-8 Static compression load test of Dixie Highway Pier 8

4.2.3.2 Site 2

Bent 1

The proposed solution technique was applied to seven of the end of drive (EOD) blows and eight of the beginning of restrike (BOR) blows. In a similar fashion to site 1, inversion results of one EOD blow is presented to validate the model assumptions. The estimated Green's function (Eq. 4-11) from the inversion solution is shown together with the observed Green's function (Eq. 4-15) in Figure 4-9. Again, the generally good matching between observed and estimated Green's functions shows that the model can simulate relatively well the actual performance of the soil-pile system. However, some mismatch (i.e., at time from 0.05 to 0.1 s or from 0.15 to 0.20 s) also indicates that the layered soil profile cannot be completely modeled by a homogeneous soil profile. The mismatch is mostly associated with high frequency components (short wave lengths), which are sensitive to the non-uniform soil profile, and a better match can be achieved if using only low frequency (i.e., < 50 Hz) components (long wave lengths) for inversion. This can be considered as a limitation of the proposed technique that may not account properly properties of anomalies (very weak or strong embedded zones, voids) around the pile.

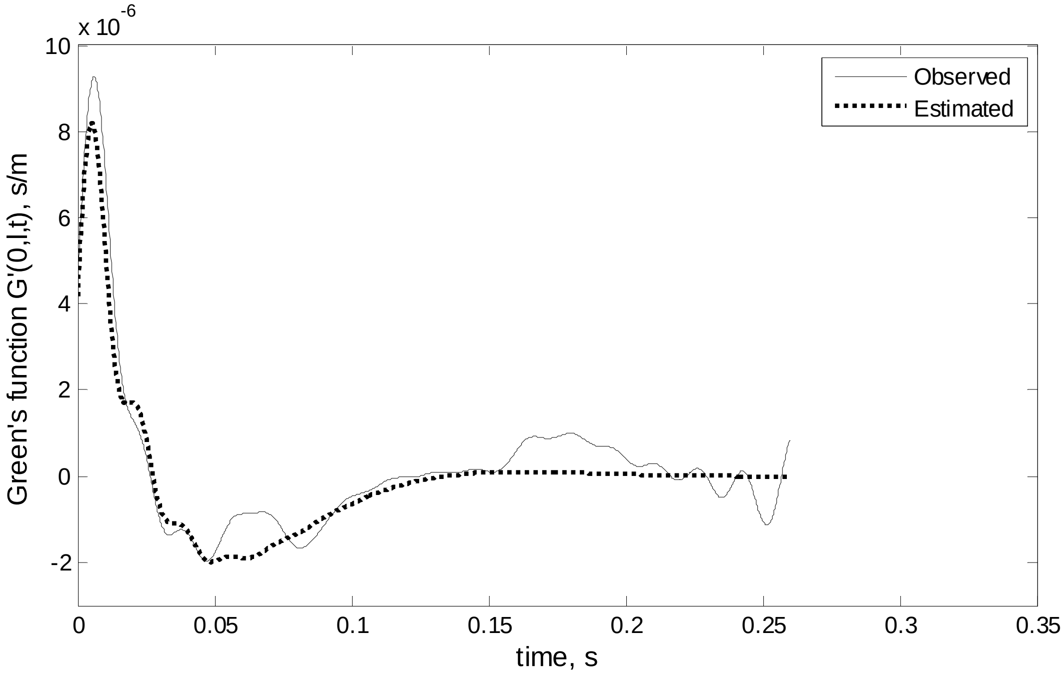

Figure 4-9 Caminada Bay Bent 1: comparison of the observed and estimated Green’s functions

Presented in Figure 4-10 is the velocity comparison. Again, from the convolution of Eq. 4-10, the relatively good match between the observed and estimated Green’s functions leads to a relatively good match between the observed and estimated particle velocities at the top and bottom of the pile.

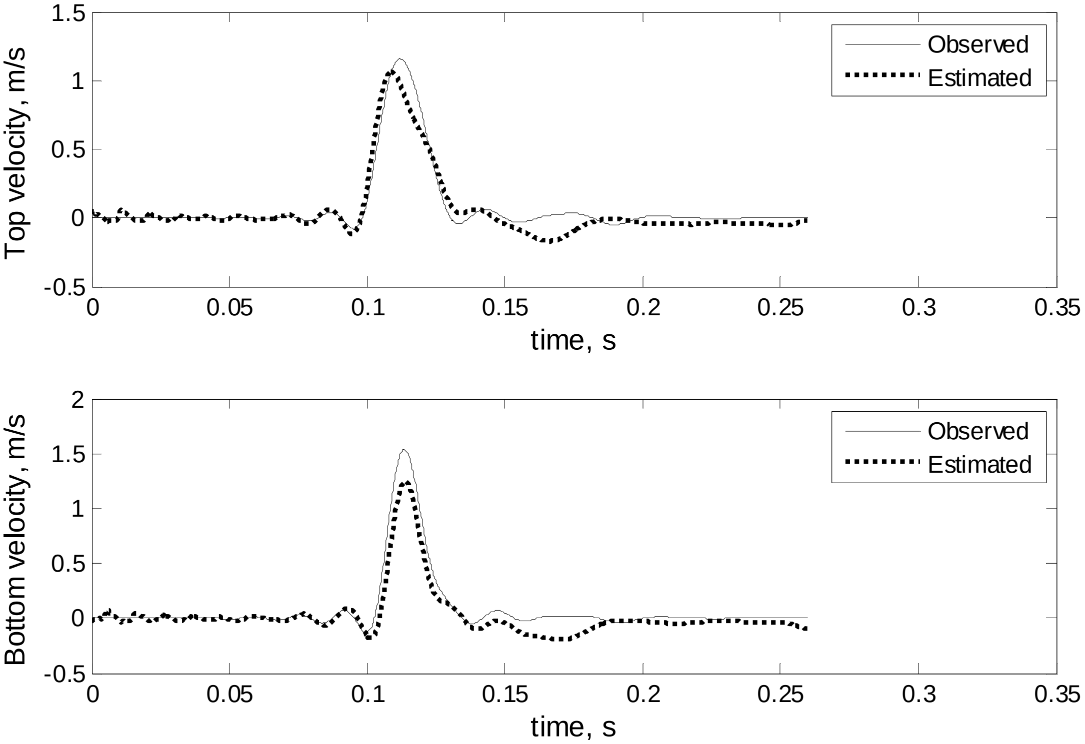

Figure 4-10 Caminada Bay Bent 1: comparison of the observed and estimated velocities at the top and bottom of the pile

The estimated skin frictions for the EOD blows and the BOR blows are shown in Figure 4-11. Again, inverted values of stiffness (b) changed accordingly to the maximum displacements to produce similar skin frictions for both EOD and BOR blows. As expected with the soil profile, i.e., fine sand with silt and clay, "pile freeze" phenomenon was also observed on the site. The skin friction increased by 50% from 1200 kN (270 kips) at EOD to 1800 kN (405 kips) at BOR.

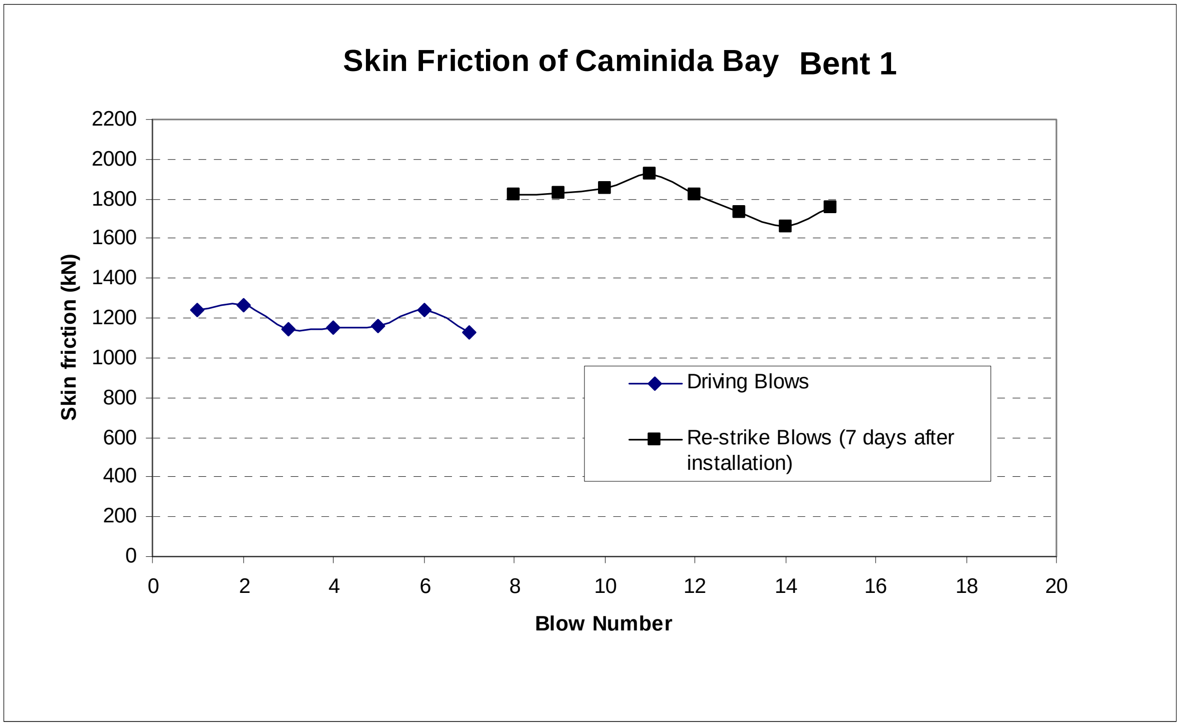

Figure 4-11 Estimated skin friction of Caminada Bay Bent 1

A top down load test was also performed on Caminada Bay bent 1. Shown in Figure 4-12 is the measured top force, as well as skin and tip resistance as a function of displacement. The skin friction was separated from the tip resistance based on strain gauges cast at the tip of the pile. From the load test, the ultimate skin friction was found at a displacement of approximately 10 mm (0.4 in), which was less than the maximum observed displacement for each EOD and BOR blow, i.e., 10 mm (0.4 in) to 20 mm (0.8 in). Therefore, the values computed from the EOD and BOR blows may be considered the ultimate skin friction. In the displacement range of 10 mm (0.4 in) to 20 mm (0.8 in), the skin friction measured from the static load test (Figure 4-12) was approximately 1750 kN (393 kips) to 1800 kN (405 kips). The latter agrees very favorably with the predicted average BOR skin friction of 1800 kN (405 kips).

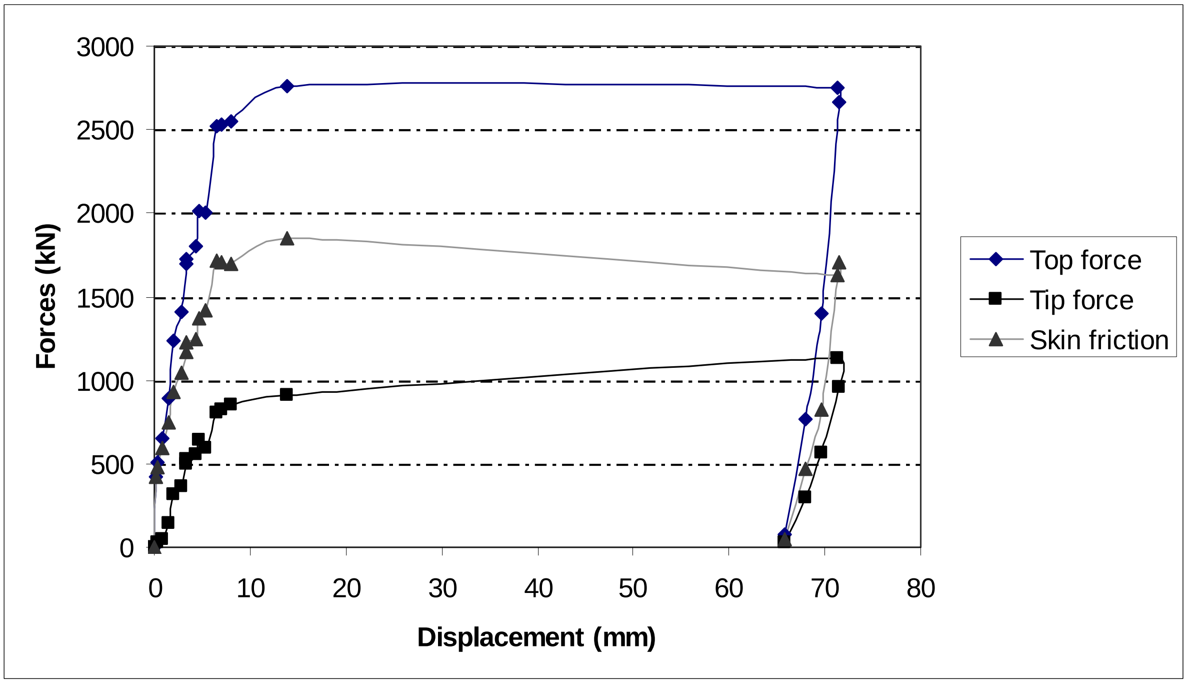

Figure 4-12 Static compression load test of Caminada Bay Bent 1

Bent 7

The estimated skin frictions for five blows at EOD, and eight blows at BOR, are shown in Figure 4-13. It was found that the skin friction increased 25% after installation from 1600 kN (360 kips) at EOD, to 2000 kN (450 kips) at BOR.

Again a load test was performed on Caminada Bay bent 7 with results presented in Figure 4-14. For the same range of displacement, i.e., 10 mm (0.4 in) to 20 mm (0.8 in), observed in the dynamic measurements, the skin friction from the load test varied from 2000 kN (450 kips) to 2700 kN 607 kips), which compares favorably to that of 2000 kN (450 kips) estimated from the dynamic data at BOR.

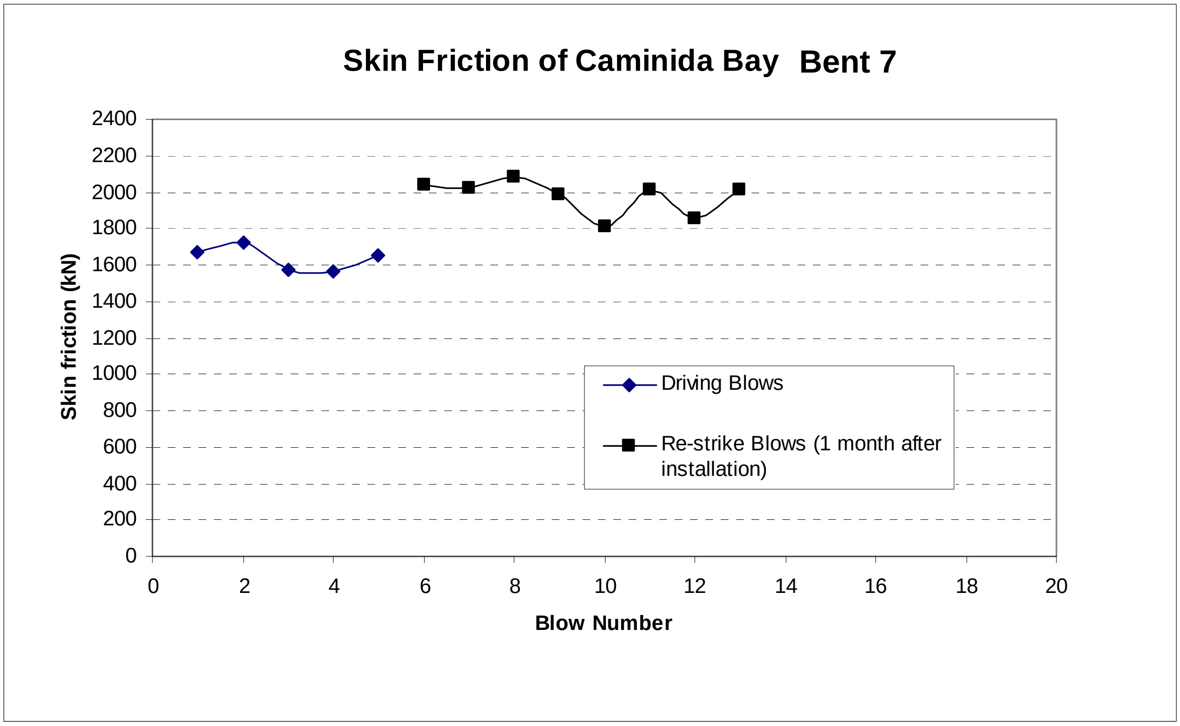

Figure 4-13 Estimated skin friction of Caminada Bay Bent 7

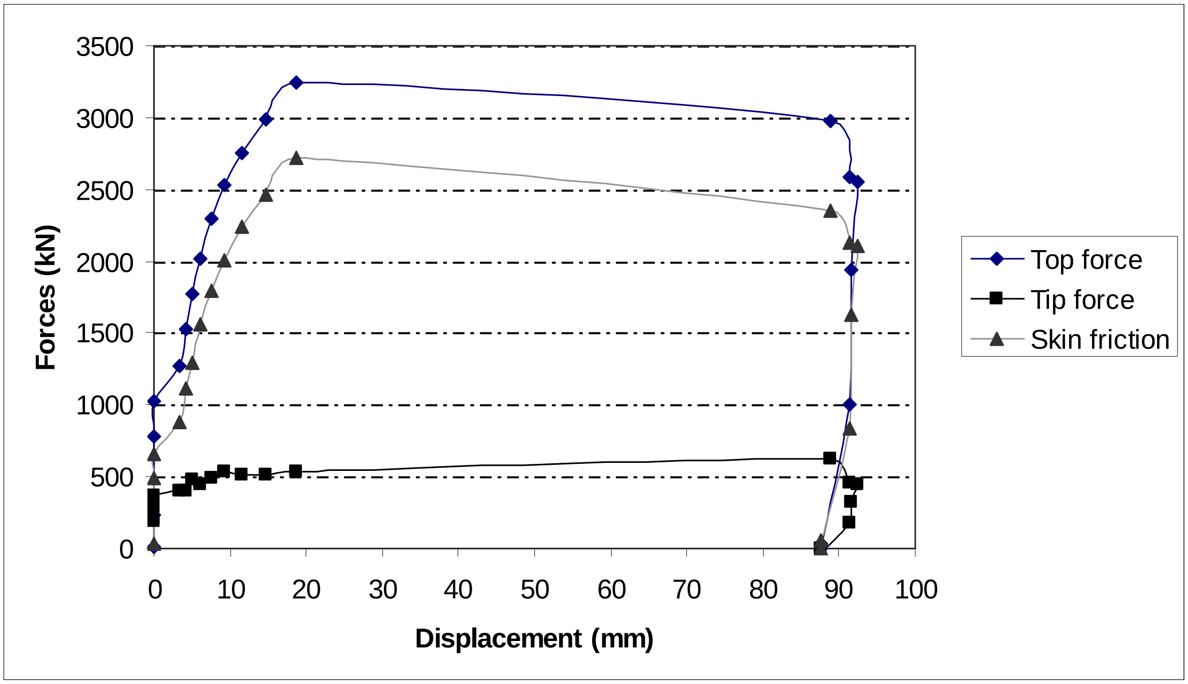

Figure 4-14 Static compression load test of Caminada Bay Bent 7

4.3 Skin Friction (Non-Homogenous)

4.3.1 Model Description

The soil-pile system is modeled as a combination of pile segments with nonlinear skin friction and damping acting on each one, as illustrated in Figure 4-15. Wave propagation in the pile subject to identified soil resistance forces may be modeled with a 1-D partial differential equation (Tran et al., 2011a) as,

$$a^2 \frac{\partial^2 u}{\partial x^2} = \frac{\partial^2 u}{\partial t^2} + c\,\frac{\partial u}{\partial t} + \bar{b},$$
$$\textit{where}$$
$$a^2 = \frac{E}{\rho} \quad \bar{b} = \frac{4\,f_s}{\rho\,B} \quad c = \frac{4\,C_r\ \rho_s}{B\,\rho} \qquad \text{Eq. 4-17}$$

In this equation, the parameter $\bar{b}$ is the static skin friction, and estimation of its value as a function of displacement is the main focus of this paper.

As shown in Figure 4-15, the unit static skin friction of each segment, f_s, can be characterized as a function of the pile displacement, $u(x,t)$

$$f_s = \begin{cases} K \cdot u(x,t) & \textit{for loading with } u(x,t) \le q \\ f_u & \textit{for loading with } u(x,t) > q \\ f_u - \bar{K} \cdot [\max(u) - u(x,t)] & \textit{for unloading} \end{cases}$$
$$\textit{and} \qquad \text{Eq. 4-18}$$
$$f_u = K \cdot q$$

In the above equations, K and $\bar{K}$ are the loading and unloading stiffness (kN/m^3), q is the displacement (quake), f_u is the mobilized ultimate unit skin friction, C_r is the viscous damping coefficient, ρ and ρ_s are the pile and soil densities, and E is the pile's Young's modulus for each segment of the pile. Max(u) is the maximum displacement at spatial location x, B is the pile width (assuming it is square), and x and t are spatial and time variables, respectively. Both K and $\bar{K}$ have been correlated with the soil's shear modulus, G (El Naggar and Novak, 1994) and the

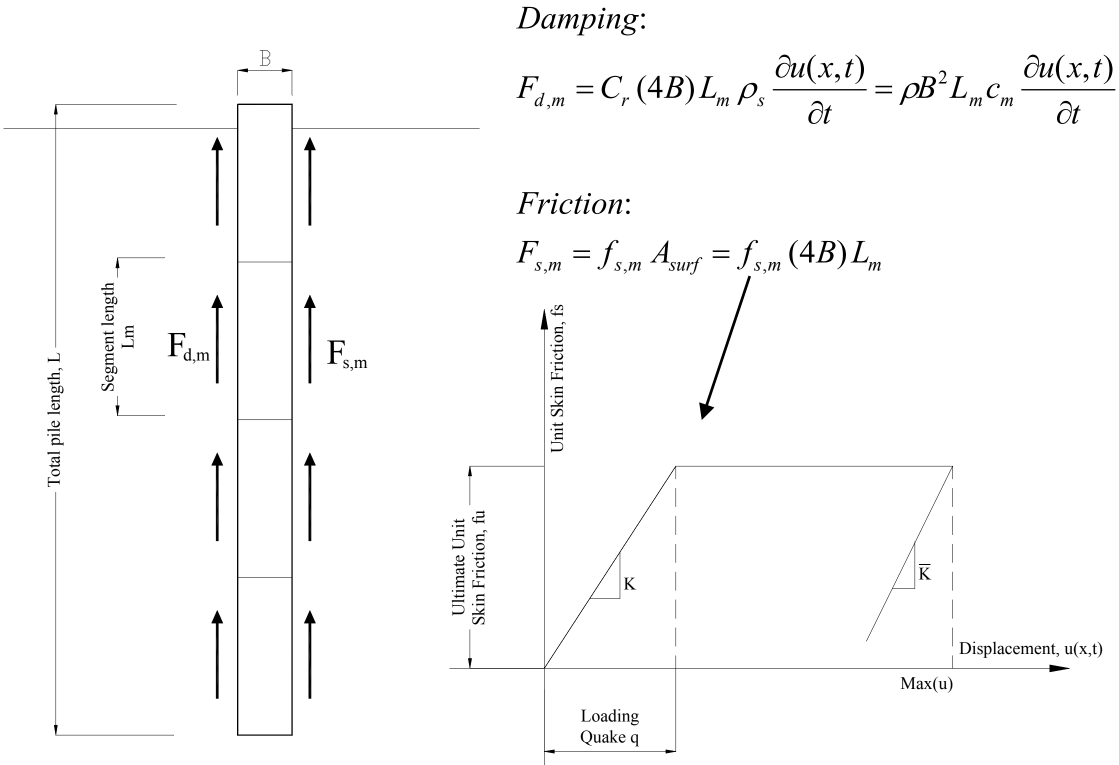

Damping:

$$F_{d,m} = C_r\,(4B)\,L_m\,\rho_s\,\frac{\partial u(x,t)}{\partial t} = \rho B^2 L_m c_m \frac{\partial u(x,t)}{\partial t}$$

Friction:

$$F_{s,m} = f_{s,m}\,A_{surf} = f_{s,m}\,(4B)\,L_m$$

Figure 4-15 Forces acting on pile

ultimate unit skin friction, f_u, have been associated with in situ standard penetration test (SPT) (Kelly, 2004; Meyerhof, 1976) and cone penetration test (CPT) (Bustamante and Gianeselli, 1982) data.

For a pile of finite length, initial and boundary conditions are required to solve Eq. 4-17. The initial conditions at rest, prior to hammer impact, are such that the particle displacement, velocity and acceleration (u, $\partial u/\partial t$ and $\partial^2 u/\partial t^2$) are zero when t equals zero. The prescribed boundary conditions are the spatial derivatives at the top ($x = 0$) and bottom ($x = L$ = pile length) of the pile,

$$\begin{aligned} \frac{\partial u}{\partial x} &= g_1(t) \quad at\, x = 0 \\ \frac{\partial u}{\partial x} &= g_2(t) \quad at\, x = L \end{aligned} \qquad \text{Eq. 4-19}$$

where $g_1(t)$ and $g_2(t)$ are the measured strain data (EDC) at the top and bottom of the pile as a function of time. It is noted that the measured strain at the bottom of the pile [$g_2(t)$] is the dynamic base resistance acting on the pile tip, and thus the stiffnesses of the pile tip and the soil below the tip are not required for solving Eqs. 4-17, 4-18 and 4-19. In other words, using the top and bottom gauges, the skin friction can be estimated separately from the tip resistance.

Equations 4-17, 4-18 and 4-19 are solved numerically at nodes along the pile, as shown Figure 4-16, using a central finite difference approach for a quadratic rate of convergence. The derivatives in space and time are expressed as follows:

$$\begin{aligned}
\left.\frac{\partial^2 u}{\partial x^2}\right|_{i,j} &= \frac{U_{i+1,j} - 2U_{i,j} + U_{i-1,j}}{\Delta x^2}, \\
\left.\frac{\partial^2 u}{\partial t^2}\right|_{i,j} &= \frac{U_{i,j+1} - 2U_{i,j} + U_{i,j-1}}{\Delta t^2}, \\
\left.\frac{\partial u}{\partial t}\right|_{i,j} &= \frac{U_{i,j+1} - U_{i,j-1}}{2\Delta t}, \\
\left.\frac{\partial u}{\partial x}\right|_{i,j} &= \frac{U_{i+1,j} - U_{i-1,j}}{2\Delta x}, \qquad i = 1,2,..N; \;\; j = 2,3,..n
\end{aligned} \qquad \text{Eq. 4-20}$$

Introducing stiffness-related parameters $k = \frac{4\,K}{\rho\,B}$ and $\bar{k} = \frac{4\,\bar{K}}{\rho\,B}$ and applying Eq. 4-20 to Eq. 4-17, one may solve for the vertical displacement, U, of node i at time step (j+1) explicitly as

$$U_{i,j+1} = \frac{a^2 \dfrac{U_{i+1,j} - 2U_{i,j} + U_{i-1,j}}{\Delta x^2} - \dfrac{U_{i,j-1} - 2U_{i,j}}{\Delta t^2} + c_i \dfrac{U_{i,j-1}}{2\Delta t} - \bar{b}_{i,j}}{\dfrac{1}{\Delta t^2} + \dfrac{c_i}{2\Delta t}},$$

where

$$\bar{b}_{i,j} = \begin{cases} k_i U_{i,j} & \textit{for loading with } U_{i,j} \le q_i \\ k_i q_i & \textit{for loading with } U_{i,j} > q_i \\ k_i q_i - \bar{k}_i[\max(U_{i,1\ldots j}) - U_{i,j}] & \textit{for unloading} \end{cases} \qquad \text{Eq. 4-21}$$

In these equations, i and j are the indices for space and time discretization, N and n are the numbers of the spatial nodes and the time steps, Δx and Δt are intervals for space and time, c_i and q_i are the damping and loading quake at spatial node i, k_i and $\bar{k}_i$ are numerical values of the stiffness parameters k and $\bar{k}$ at spatial node i, and $U_{i,j}$ and $\bar{b}_{i,j}$ are the numerical displacement and skin friction at spatial node i and time step j.

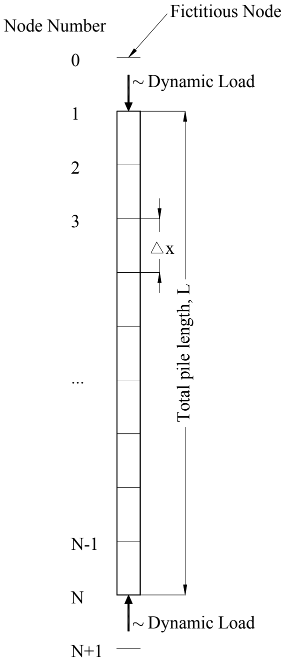

Figure 4-16 Pile discretization

The pile is initially at rest (i.e., displacement = 0 at time steps j = 1 and 2), and then it is perturbed by applying the boundary conditions (prescribed strains, Eq. 4-19) at the top and bottom of the pile. To guarantee second order accuracy for every spatial node, two fictitious nodes (0 and N+1) were added above the top and below the tip of the pile, and their particle displacements are calculated from measured strains and displacements of internal nodes (Eq. 4-20) as

$$U_{0,j} = U_{2,j} - 2(\Delta x)g_{1,j} \ ,$$
$$U_{N+1,j} = U_{N-1,j} + 2(\Delta x)g_{2,j} \ , \qquad \text{Eq. 4-22}$$

where $g_{1,j}$ and $g_{2,j}$ are the measured strains at the top and tip of the pile at time step j. Knowing the displacements at two time steps (j-1 and j), the displacement at the next time step (j+1) can be calculated with Eq. 4-21 for nodes 1 through N.

To maintain the stability and accuracy of the solution (i.e., avoid numerical dispersion), at least 10 spatial nodes per wavelength of particle motion and a time step less than the travel time in each element (two adjacent nodes) are recommended (Virieux, 1986)

$$\Delta t \leq \frac{\Delta x}{a} \qquad \text{Eq. 4-23}$$

For example, a prestressed concrete pile with a wave speed, a (Eq. 4-17), of 5000 m/s (16,400 ft/s) and a measured particle motion of 500 Hz should have a nodal spacing, Δx, of 1 m (3.28 ft) (minimum wavelength / 10 nodes = wave speed / maximum frequency / 10 = 5000 / 500 / 10 =1 m), and a time increment, Δt, of less than 0.0002 s (Eq. 4-23).

Equation 4-21 gives particle displacements, which may be compared with the measured displacement to estimate the pile skin friction. However, the pile top and bottom displacements are usually nonzero and smooth with few inflection points, whereas the particle velocity data generally have multiple maxima, minima, and zero values, which generally result in faster conversion of unknowns in the inversion. Therefore, the particle velocity, with central derivatives of displacement with respect to time was again used.

To verify the accuracy of the proposed approach, a numerical analysis of a 0.61-m (2 ft)-square by 14 m (46 ft) long concrete pile embedded in a homogeneous soil profile with a linear skin friction vs. the displacement relationship (k =3000 1/s^2, Eq. 4-21) and constant viscous damping, c (120 1/s, Eq. 4-17) was compared with the analytical solution (Tran et al., 2011a).

Note, the skin friction varies along the length of the pile, x, as a function of time, t, through the unit skin friction stiffness (k) times the particle displacement [$u(x,t)$]. Using the measured top and bottom strains (g_1 and g_2, Figure 4-17(a)) from one of the Florida test pile blows, the analytical and numerical solutions of particle velocity at the top and bottom [$v(0,t)$, $v(L,t)$] of the pile are shown in Figure 4-17(b) as a function of time. Evidently, the two solutions are almost identical.

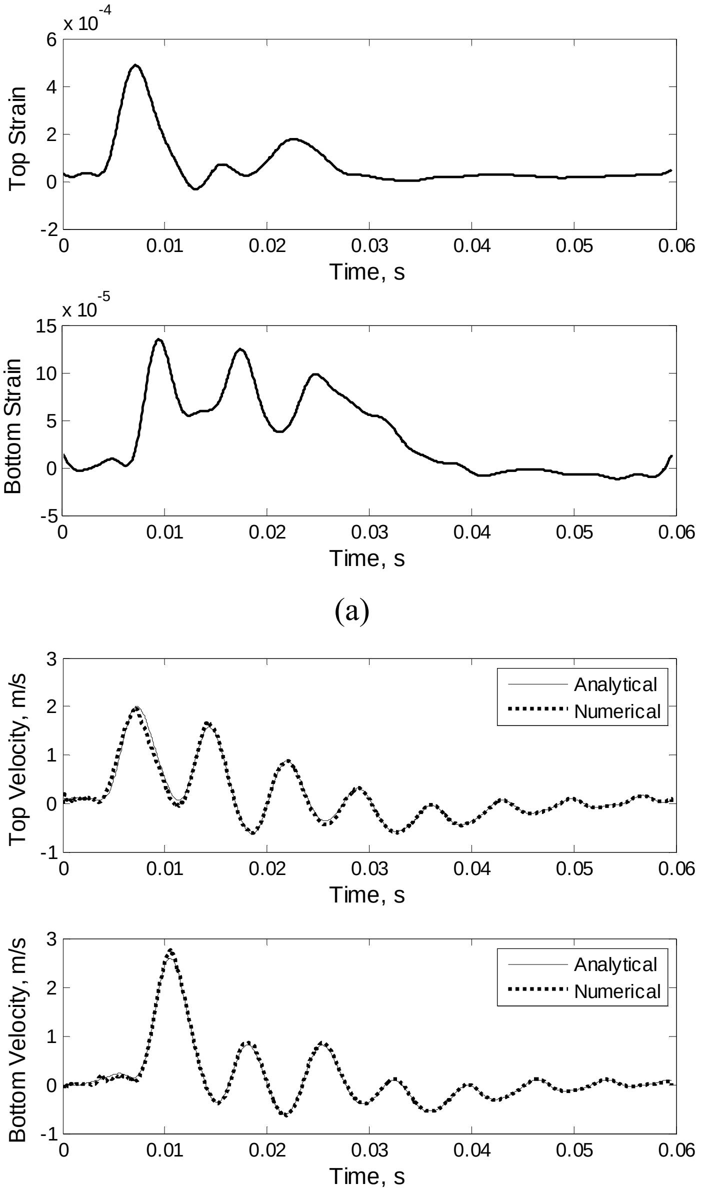

(a)

(b)

Figure 4-17 Verification of the numerical scheme: (a) measured strains at the top and bottom of the pile and (b) a comparison of the analytical and numerical solutions

4.3.2 Solving for Unknown Pile-Soil Resistance along the Pile

It is of great interest to estimate unknown pile-soil resistance parameters, i.e., stiffness-related parameters (q, k, and $\bar{k}$, Figure 4-15) and damping (c) for multiple segments along the pile. Knowing the latter, the total static skin friction, F_s, on the pile can be estimated as

$$F_S = \frac{\rho B}{4} \sum_{l=1}^{n_s} A_m k_m q_m , \qquad \text{Eq. 4-24}$$

where A_m, k_m, and q_m are the pile side area, loading stiffness, and loading quake of the m^{th} segment, respectively, and n_s is the number of segments.

The simplest way of assessing the unknowns is to use an inversion to match the predicted particle velocities (top and bottom) with the measured values. Generally, each pile-soil segment can be characterized with four unknowns: damping c_m, loading quake q_m, loading stiffness k_m, and unloading stiffness $\bar{k}_m$. In doing so, the number of unknowns will become large (i.e., four times the number of segments), requiring significant computation time for the inversion as well as the possibility of inconsistent segment parameters. To limit the number of unknowns and ensure consistent segment parameter values, the following assumptions were made.

First, a single loading quake (q) is used for all segments. Typically, the variation in the loading quakes between segments is small, and by using one quake with a different loading stiffness, k_m (Eq. 4-24), the variation in the ultimate skin frictions, $f_{u,m}$ (Figure 4-15), is represented, and it may be readily compared with traditional in situ testing data (e.g., SPT, CPT, etc.) as a function of depth. Similarly, the unloading stiffness, $\bar{k}_m$, for any segment was assumed to be proportional to the segment's loading stiffness, k_m, through the proportional parameter, α,

$$\bar{k}_m = \alpha \cdot k_m \qquad \text{Eq. 4-25}$$

Here, the proportional parameter, α (unknown), is assumed to be the same for all segments.

One of the dynamic forces in Eq. 4-17 acting on the pile-soil interface is damping. It is characterized with a viscous damping coefficient, c_m, for each segment along the pile. Early work, by Smith (1960) and later work by El Naggar and Novak (1994), assumed that the damping force was proportional to the static skin friction. For verification, an analytical approach (Tran et al., 2011a) was used to estimate the average viscous damping (c, Eq. 4-17) and the ultimate static skin friction ($\bar{b}$, Eq. 1) for one of the statically load-tested piles. Five end-of-drive and five restrike blows were analyzed, and the average damping (c) vs. the average ultimate static skin friction ($\bar{b}$) is shown in Figure 4-18 for all ten blows. Note, the parameters $\bar{b}$ and c were inverted independently to one another, with no assumption of any relationship between the damping and the skin friction. From Figure 4-18, a linear relationship is shown to exist between the ultimate skin friction and damping parameters, as suggested by Goble et al. (1975). Moreover, even though the values of $\bar{b}$ and c in Figure 4-18 characterize the average over the whole pile length, it is reasonable to assume a linear relationship between damping and ultimate skin friction exists for individual segments. Thus, the damping parameter of the m^{th} segment, c_m, is characterized by

$$c_m = \beta\,(k_m \cdot q) \qquad \text{Eq. 4-26}$$

In the above equation, β is assumed to be the same for all segments of the pile. For the case of a homogeneous deposit, the parameter β would be the slope of a linear line fitted to predicted points (pairs of $\bar{b}$ and c) in Figure 4-18.

Using the model proposed in Eqs. 4-21, 4-25, and 4-26, the number of unknowns to be solved is equal to the number of segment stiffnesses ($k_1, k_2 \ldots k_m$) plus three additional parameters: quake, unloading, and damping parameters (q, α and β).

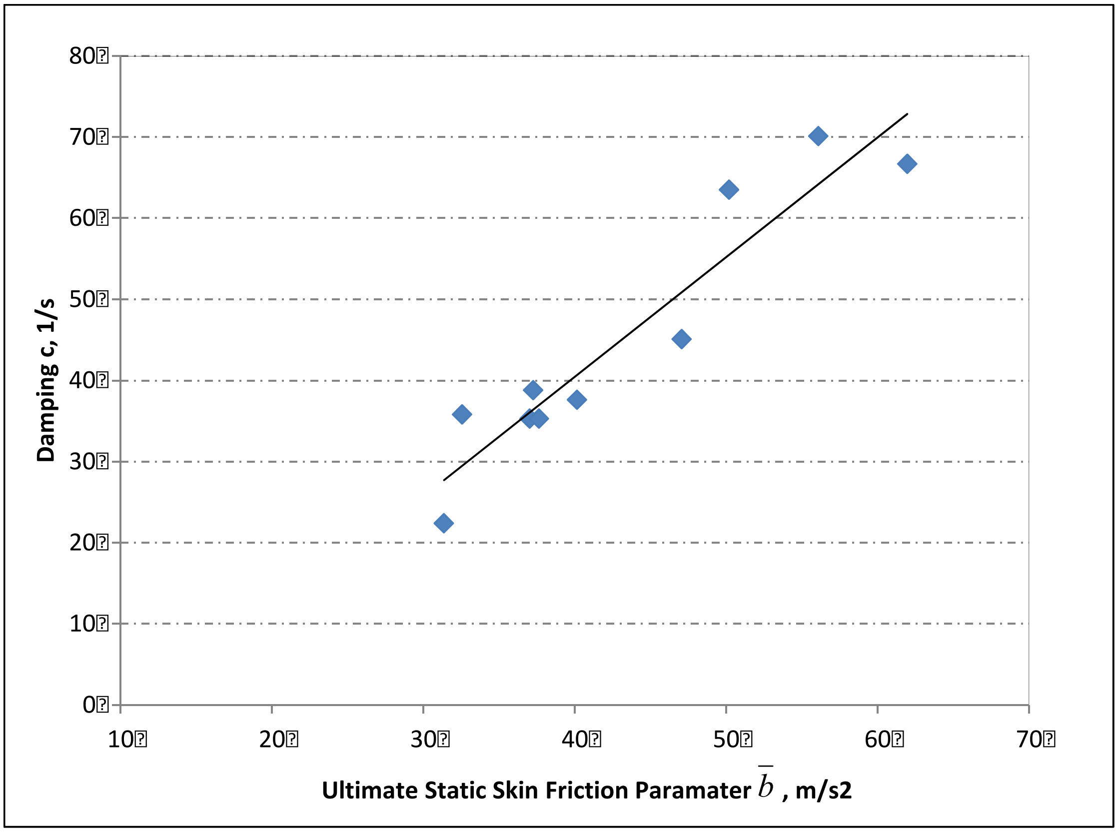

Figure 4-18 Relationship between damping and ultimate static friction for 10 blows

In addition, because of the limited sensitivity of the measured signals with respect to soil resistance forces (damping and skin friction), segment lengths should be no smaller than 1/5 to 1/4 of the wavelengths of the dominant measured velocity data to ensure consistent resistance forces for each segment. For instance, a short pile usually has one dominant wave component with a wavelength comparable to the pile length. Thus, the pile should be divided into no more than 4 or 5 segments. For long piles, there may be a few dominant wave components with wavelengths of 1, 1/2, or 1/3 of the pile length, and thus, the number of segments may be increased. For all of the cases presented here, the total number of unknowns per pile was less than 10. The inversion process is presented and discussed in Appendix A.

4.3.3 Applications

4.3.3.1 Site 1

End Bent 1

The proposed solution was applied to 5 of the Beginning of Restrike (BOR) blows. The specific results of one blow are presented here in detail for discussion. The 14 m (46 ft) length pile was divided into four equal segments (based on SPT N values, Figure 9a) with a total number of unknowns of 4-19. Also specified were the constraints of the unknowns used in the inversion process. The following constraints were applied: the unloading coefficient, α , was allowed to vary from 1 to 10 (dimensionless); the damping coefficient, β , ranged from 0 to 1 (s/m); the loading quake, q, varied from 0 to the maximum measured displacements; and the loading stiffness parameters, k_m, could vary from 0 to 20000 ($1/s^2$).

The inversion solution (Appendix A) is taken as the model in the final generation with the lowest least-squares error (Eq. A-1). The estimated particle velocities from the inversion solution are shown, together with the observed pile top and bottom velocities, in Figure 4-19. Agreement between estimated and observed data was found, with most of the dominant components well matched. It is expected that even better matches can be achieved if more complexity is accounted for in the models, e.g., using different loading quakes and damping and unloading stiffness coefficients for individual segments or increasing the number of pile segments. However, by doing so, the computation time will increase, and the uncertainty of the estimated parameters may increase (e.g., the sensitivity of the added parameter is small).

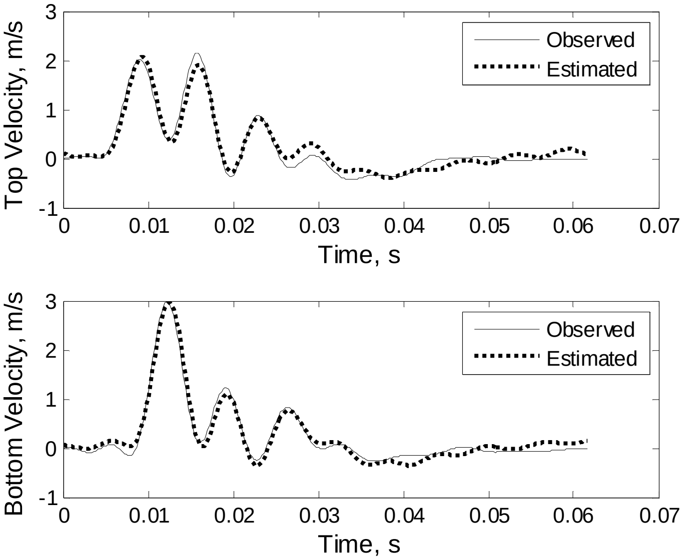

Figure 4-19 Dixie Highway End Bent 1: comparison of the observed and estimated velocities at the top and bottom of the pile

Figure 4-20 presents the final mobilized skin friction as functions of the pile displacement on four equally spaced pile segments. Segment 1 is the top and 4 is the bottom of the pile, and the total (Figure 4-20) is their summation. Generally, the skin friction increased with depth (sands), with the exception of segment 2, which was in a loose zone. The converged loading quake, q, was 5.42 mm, which is less than the maximum pile displacement of 20 mm for the blow, suggesting that the ultimate skin friction was achieved. Using the loading quake (q = 5.42 mm) and the segment stiffness parameters (k_1= 8000, k_2 = 3843, k_3=13333, and k_4 = 16706 1/s^2), the ultimate skin friction can be calculated (Figure 4-15) as

$$F_S = \rho B^2 q \frac{L}{4} \sum_{i=1}^{4} k_i = 2.5 \times 0.61^2 \times 0.00542 \times \frac{14}{4} \times (8000 + 3843 + 13333 + 16706) = 739.23\,(kN)(166 kips)$$

The estimated values of all parameters of the 5 BOR blows for end bent 1 are given in Table 4-1. Shown in Figure 21(a) are the ultimate unit skin frictions vs. the mean SPT ‘N’ values along the pile segments, plotted with the depth for the centers of each segment. The estimated ultimate unit skin frictions (q*kᵢ) for the individual pile segments are consistent between blows and are correlated with the mean SPT 'N' values.

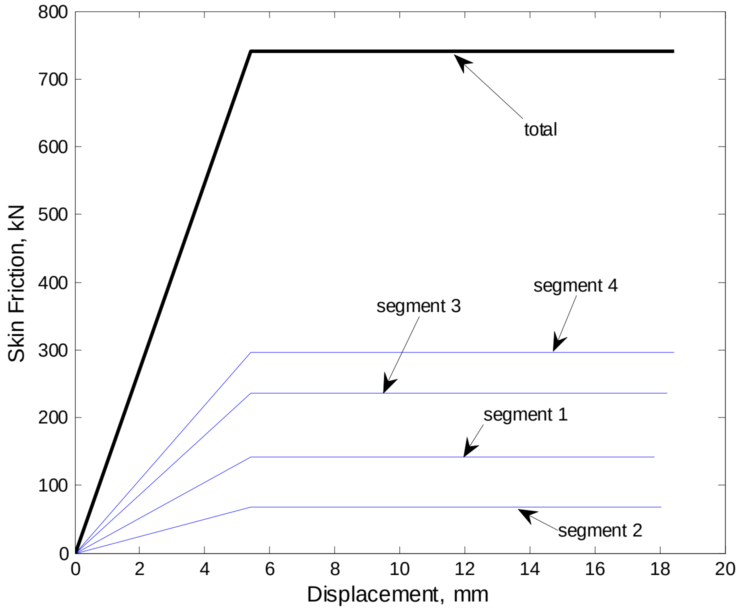

Figure 4-20 Estimated skin friction of Dixie Highway End Bent 1 for one blow

Table 4-1 Estimated parameters of Dixie Highway End Bent 1

Blow #	Loading stiffness parameter k (1/s^2)				Loading quake, q (mm)	Damping Coefficient, β (s/m)	Unloading Coefficient, α (dimensionless)
	Seg #1	Seg #2	Seg #3	Seg #4			
1	7922	6431	9647	14549	6.64	0.62	1.88
2	8000	3843	13333	16706	5.42	0.51	2.99
3	6739	5668	11435	16414	5.35	0.41	2.27
4	7814	4133	7381	10909	7.13	0.40	2.01
5	7352	4384	9325	13890	6.30	0.38	2.00

The results for the total skin friction vs. the displacement for the individual blows for end bent 1 are presented in Figure 4-22. It is observed that estimated loading quakes of the blows vary only in a small range from 5 mm (0.2 in) to 7 mm (0.28 in). In addition, the estimated ultimate skin friction of blow 1,830 kN (411 kips), was approximately 15 % higher than the predicted values for the four subsequent blows (700 - 740 kN (157 – 166 kips)). A possible explanation of the reduction is the loss of particle interlock (i.e., friction) due to pore pressure increase from particle rearrangement from blow 1 to the later blows.

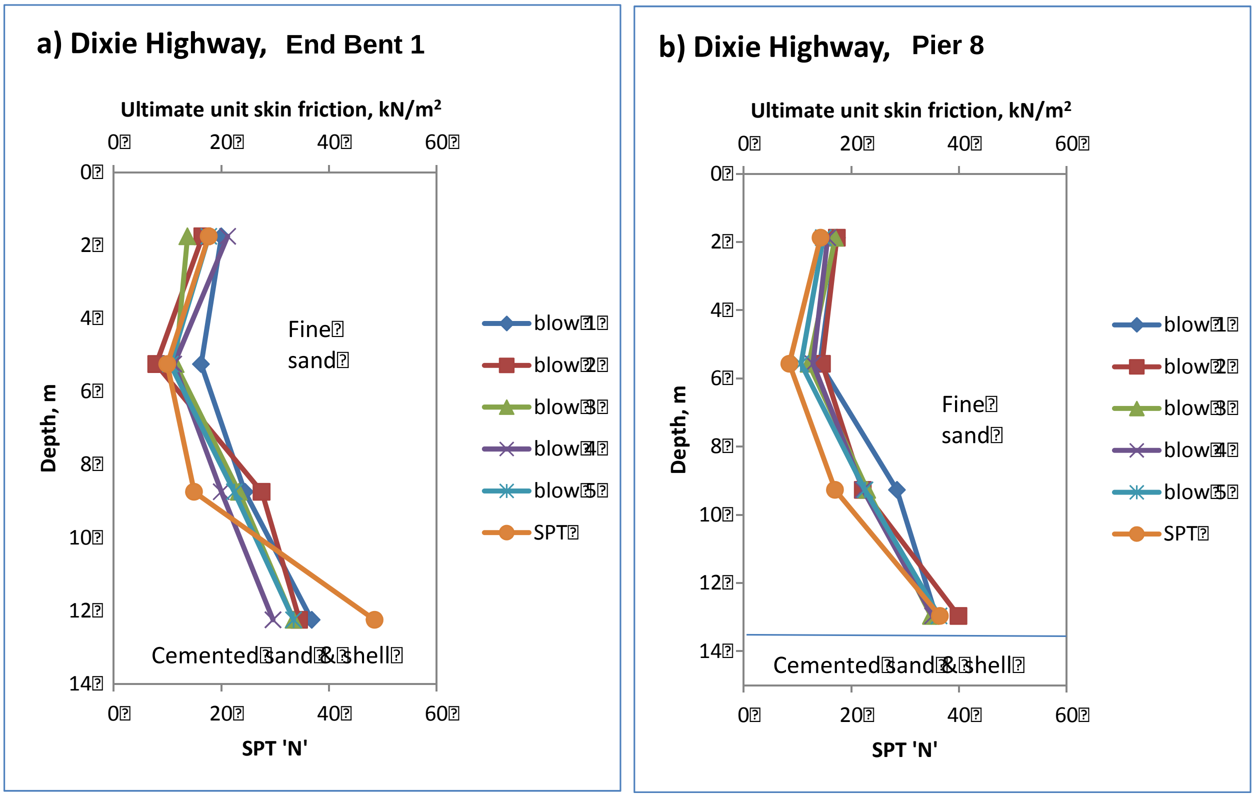

Figure 4-21 Ultimate unit skin friction on pile segments and SPT ‘N’ values at Dixie Highway

For comparison, the measured skin friction from the static load test on end bent 1 is shown in Figure 4-22 vs. the predicted responses of the 5 BOR blows. Evidently from the load test, the ultimate skin friction was achieved at a quake displacement of approximately 5 mm, which compares favorably with the predicted loading quakes (5 - 7 mm (0.2 – 0.28 in) for 5 blows). Because the estimated quakes were less than the observed total pile displacements (10 mm (0.4 in) to 20 mm (0.8 in)), the magnitude of the mobilized pile skin friction is displacement dependent. In the displacement range of 5 to 20 mm (0.2 to 0.8 in), the skin friction from the static load test varied from 870 kN (196 kips) to 900 kN (202 kips), and the average (5 BOR blows) estimated ultimate value was 740 kN (166 kips), i.e., approximately 15 % lower than the measured value.

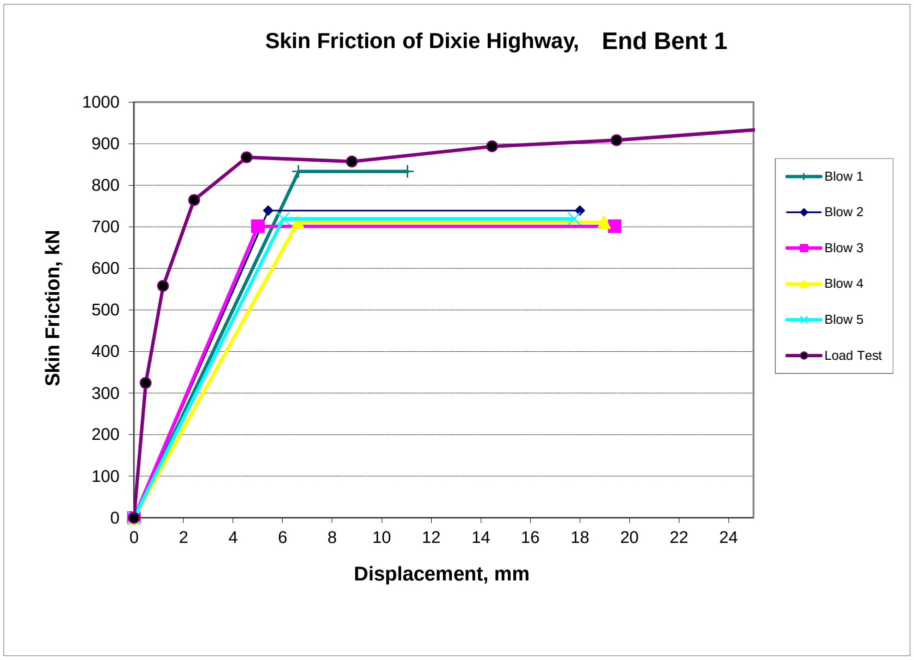

Figure 4-22 Skin friction of Dixie Highway End Bent 1

Pier 8

Similar to end bent 1, data from 5 Beginning of Restrike (BOR) blows were analyzed, and the estimated values of all parameters are given in Table 4-2. The ultimate unit skin frictions and the mean SPT ‘N’ values along the pile segments are shown in Figure 21(b). Again, the estimated ultimate unit skin frictions on the individual pile segments are similar between blows and are consistent with the SPT ‘N’ values.

Table 4-2 Estimated parameters of Dixie Highway Pier 8

Blow #	Loading stiffness parameter k ($1/s^2$)				Loading quake, q (mm)	Damping Coefficient, β (s/m)	Unloading Coefficient, α (dimensionless)
	Seg #1	Seg #2	Seg #3	Seg #4			
1	8890	7264	14604	18319	5.12	0.64	6.93
2	7659	6435	9788	17647	5.64	0.42	4.95
3	8533	6067	11533	17467	5.23	0.28	5.97
4	7267	6000	10333	16333	5.64	0.25	6.11
5	5600	4021	8533	13733	6.94	0.26	6.65

The results for the total side friction for pier 8 blows are shown, together with the static load test results, in Figure 4-23. Again, the estimated loading quakes from all blows varied from 5 to 7 mm (0.2 to 0.28 in), which compares favorably with the approximate 5 mm (0.2 in) from the load test. The estimated ultimate skin friction of the first restrike was 875 kN (197 kips), which was 10 % higher than the average of 5 consecutive BOR values. For 5 to 20 mm (0.2 to 0.8 in) displacements, the skin frictions from the load test were 850 kN (191 kips) to 950 kN (214 kips), respectively. The predicted skin friction from the first blow was within the measured load test range, and the average of 5 successive blows was approximately 10 % lower than the measured value.

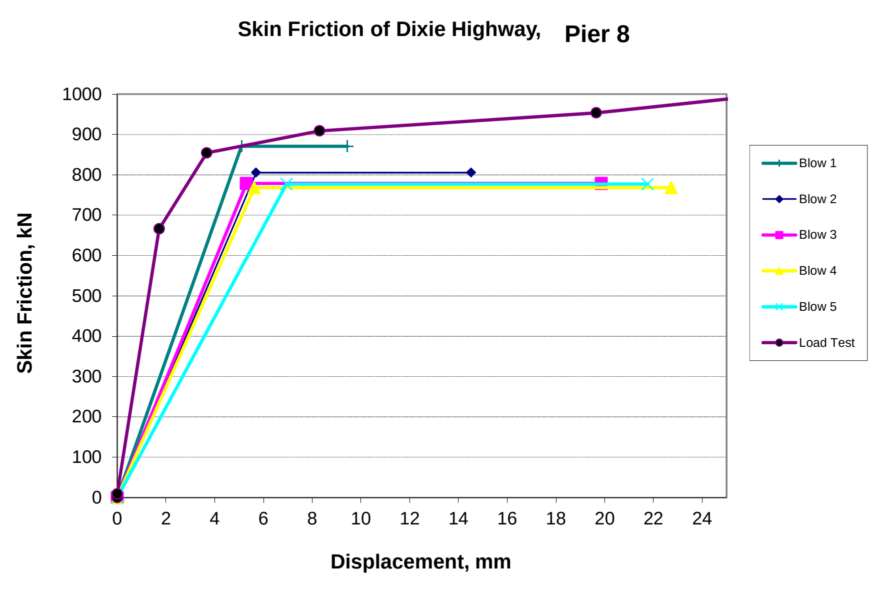

Figure 4-23 Skin friction of Dixie Highway Pier 8

4.3.3.2 Site 2

Bent 1

The new algorithm was applied to the 5 Beginning of Restrike (BOR) blows. In a similar fashion to site 1, inversion results of one blow are presented for discussion of the pile-soil model assumptions/results. Because the pile was 21 m (69 ft) long and the frequency content of the signal was 200 Hz, the pile was divided into 5 equal segments for a total of 8 unknowns ($k_1 \ldots k_5$, q, α and β). The inversion began with the generation of 200 random values for each parameter, followed by fifty generations of offspring with selection controlled by signal matching (Eq. A-1) until a converged solution was achieved (approximately one minute on a 3.4 GHz desktop computer). The final parameters were selected from the inversion's final generation with the lowest least-squares error.

The predicted response (i.e., forward modeling), using the back-solved parameters and the prescribed strains at the top and bottom of the pile, is presented in Figure 4-24. The measured and predicted velocities at the top and bottom of the pile are shown in the figure. Based on the quality of the match (top and bottom of the pile), the assumptions about the number of segments, the multilinear skin friction-displacement relationship and damping appear acceptable.

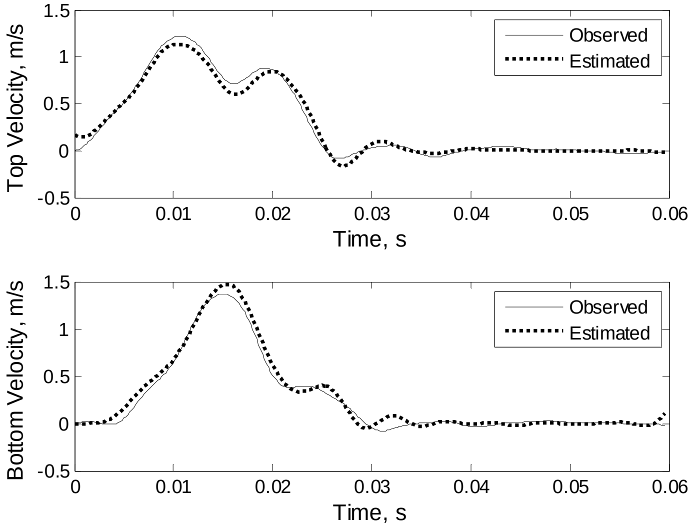

Figure 4-24 Caminada Bay Bent 1: comparison of the observed and estimated velocities at the top and bottom of the pile

The estimated values of all unknown parameters are given in Table 4-3, and the estimated ultimate skin frictions $(q*k_i)$ on the segments with the mean SPT ‘N’ values are shown in Figure 4-25(a). The estimated ultimate skin frictions on the pile segments are consistent for the different blows, and they correlate with the mean SPT ‘N’ values, which are only available down to a depth of 15 m (49 ft).

Table 4-3 Estimated parameters of Caminada Bay Bent 1

Blow #	Loading stiffness parameter k $(1/s^2)$					Loading quake, q (mm)	Damping Coefficient β (s/m)	Unloading Coefficient, α (dimensionless)
	Seg #1	Seg #2	Seg. #3	Seg. #4	Seg. #5			
1	9608	12941	24510	30980	35686	3.84	0.37	10.12
2	6961	10882	16863	23431	30686	5.03	0.41	15.23
3	6667	8039	15980	21569	35784	5.43	0.37	16.87
4	8392	12941	15490	19020	38471	4.85	0.34	19.25
5	11212	16001	25627	27373	36690	4.29	0.34	18.43

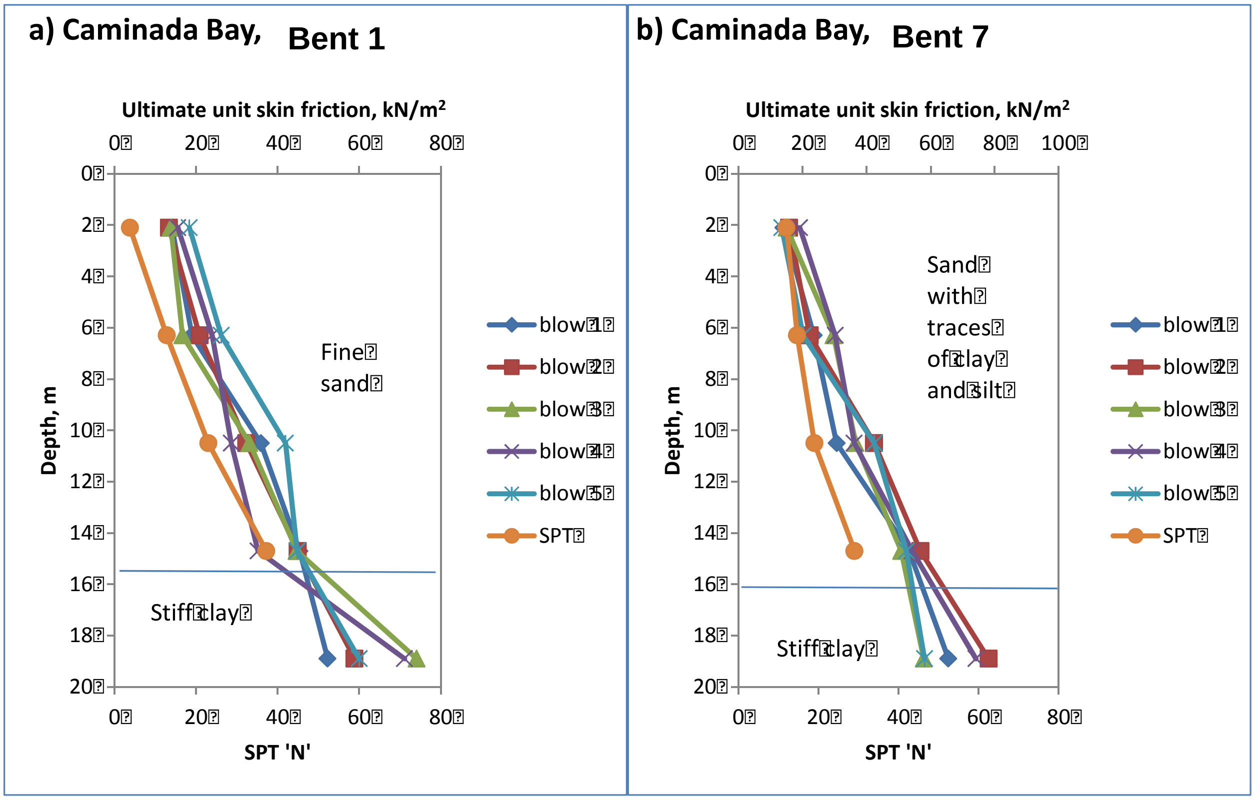

Figure 4-25 Ultimate unit skin friction on pile segments and SPT ‘N’ values at Caminada Bay (a) Bent 1 and (b) Bent 7

The individual blow results for 5 BOR blows for bent 1 along with the static load test results are shown together in Figure 4-26. For the pile, predicted loading quakes from the 5 blows varied from 4 to 6 mm (0.16 to 0.24 in), which compares favorably with the measured 6 mm (0.24 in) from the static load test. The ultimate skin friction measured from the static load test was 1800 kN (405 kips) at 13 mm (0.5 in) of displacement, which diminished to 1650 kN (371 kips) at 70 mm (2.8 in) of displacement. The average (5 blows) predicted ultimate resistance was 1700 kN (382 kips) at 18 mm (0.7 in) of displacement.

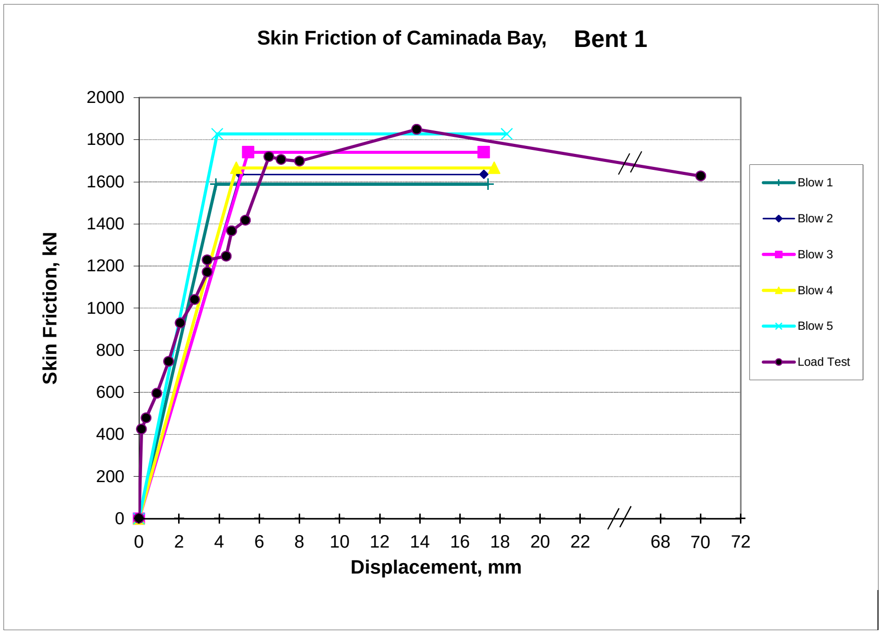

Figure 4-26 Skin friction of Caminada Bay Bent 1

<u>Bent 7</u>

The estimated values of all unknown parameters obtained from the genetic inversion are given in Table 4-4. Shown in Figure 4-25(b) are the estimated ultimate skin frictions (k_i*q) for the various segments for each blow, along with the mean SPT 'N' values for each segment. Again, the estimated ultimate skin frictions on the pile segments are consistent for the different blows, and they are correlated with the mean SPT 'N' values.

Table 4-4 Estimated parameters of Caminada Bay Bent 7

Blow #	Loading stiffness parameter k ($1/s^2$)					Loading quake, q (mm)	Damping Coefficient β (s/m)	Unloading Coefficient, α (dimensionless)
	Seg. #1	Seg. #2	Seg. #3	Seg. #4	Seg. #5			
1	3569	5940	7745	13451	16549	10.01	0.37	25.10
2	3941	5529	10529	14118	19412	10.56	0.24	21.92
3	5051	9984	12289	17078	19442	7.81	0.31	25.32
4	6118	9667	11569	17353	23725	8.20	0.22	23.47
5	4403	6568	13777	17014	18870	8.08	0.38	20.40

The estimated total bent 7 skin frictions for 5 blows at BOR are shown, together with the load test result, in Figure 4-27. It is observed that the estimated skin friction vs. axial pile displacement agrees well with the measured static load test response up to 12 mm (0.47 in) of displacement, after which point the predicted resistance was constant at 2150 kN (483 kips). The measured static friction peaked at 2700 kN (607 kips) (20% higher) and dropped to 2300 kN (517 kips) (7% higher) at 90 mm (3.5 in) of displacement. The static load test suggests that the soil may be undergoing remolding (i.e., loss of stiffness/strength with movement).

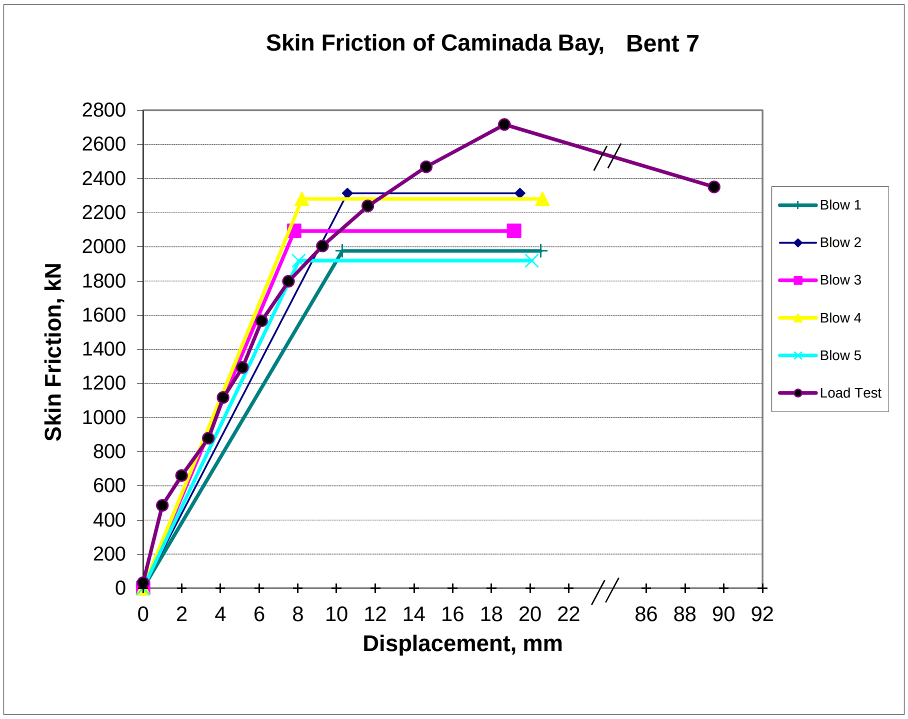

Figure 4-27 Skin friction of Caminada Bay Bent 7

4.4 Tip Resistance

4.4.1 Solution Methodology

The pile tip is modeled as a single degree of freedom (SDOF) system

$$m\ddot{x} + c\dot{x} + kx = P(t) \qquad \text{Eq. 4-27}$$

where x is displacement and dots denote derivatives of the displacement with respect to time. *P(t)* is the dynamic force measured at the tip and *m*, *c*, and *k* are the mass, viscous damping, and stiffness of the system, respectively.

For an individual hammer blow, the input energy arriving at the pile tip may be determined directly from the tip strain and accelerometer gauges. The input energy must be balanced by the inertia, damping and static energy from the soil-structure interaction at the pile tip

$$\int (m\ddot{x} + c\dot{x} + kx)dx = \int P(t)dx \qquad \text{Eq. 4-28}$$

To assist with the implementation of the integration, the integration variable can be changed to time (Liang and Feeny, 2006) as

$$\int_t^{t+T} (m\ddot{x} + c\dot{x} + kx)\dot{x}dt = \int_t^{t+T} P(t)\dot{x}dt \qquad \text{Eq. 4-29}$$

where T indicates a finite time interval.

In Eq. 4-29 the only unknowns at the pile tip are *m*, *c*, and *k*. Generally, *m* is the mass of pile and soil below the tip gauges which is moving with the tip, and the damping, *c* is the viscous damping coefficient related to frequency of particle velocity, soil type, and magnitude of strain (Zhang et al., 2001). However, the stiffness, *k*, is not a constant and is a function of displacement (i.e., nonlinear). To limit the number of unknowns for a quick and consistent inversion, the pile's static tip force vs. displacement (Q-Z curve) response is modeled as a function of a three loading segments (l_1, l_2, l_3) and one unloading segment as shown in Figure 4-28. Intersection points A and B fall within ranges 1 and 2 which are set as the maximum displacement, Max(u)/2. Thus, segment lengths can be searched as

$$0 \le l_1 \le Max(u)/2,$$
$$0 \le l_3 \le Max(u)/2,$$
$$and \;\; l_2 = Max(u) - l_1 - l_3.$$

note that the number of the loading segments can be reduced if l_1 and/or l_3 are close to zero.

The simplest way of assessing unknowns (m, c, l_1, k_1, k_2, l_3, k_3 and k_4) is from an inversion process to match the measured input energy (right side of Eq. 4-29) with the computed inertia, damping, and stiffness energies (left side of Eq. 4-29). The estimated energies can be calculated by assuming values of the unknowns and computing the left hand side of the Eq. 4-29 using the acceleration, velocity, and displacement from measured tip data, which may be compared to the measured energy.

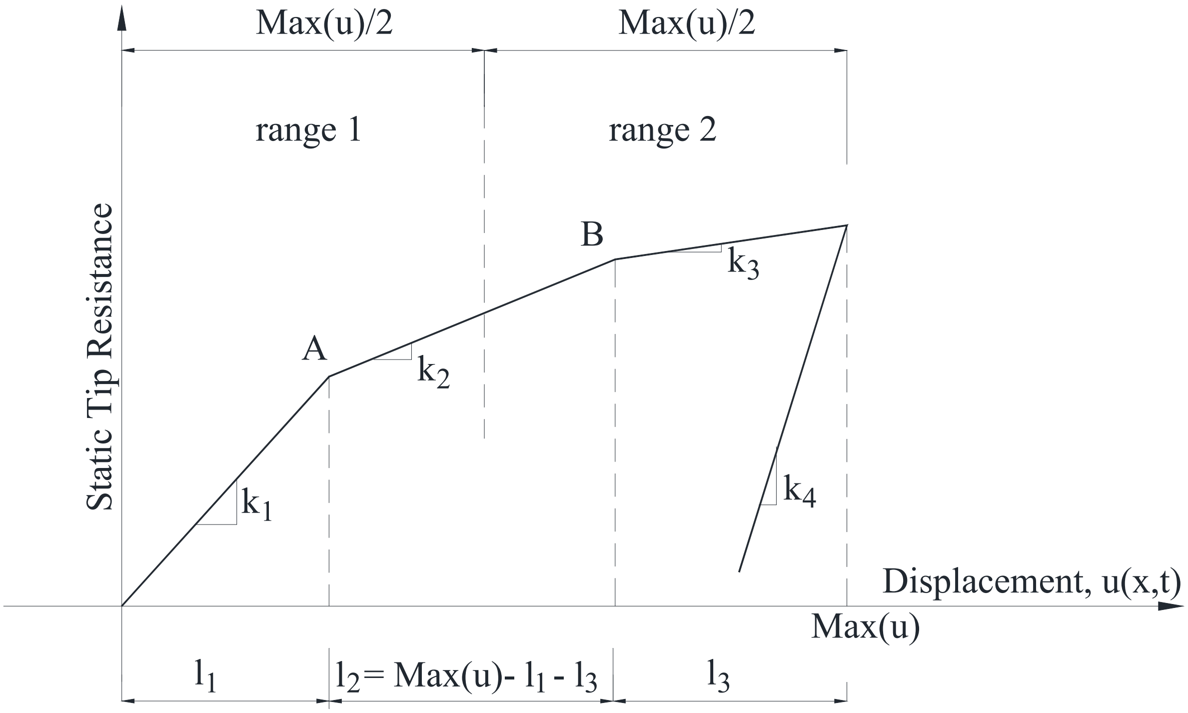

Figure 4-28 Static tip resistance vs. displacement

Also of great interest are the times, T_i, where the velocity ($\dot{x}$) goes to zero. Here, the incremental energy change is zero, i.e., both sides of Eq. 4-29; but, the force equilibrium applied at the pile tip, Eq. 4-27, readily reveals that the static resistance, kx is equal to dynamic force, $P(t)$ minus the inertia force, $m\ddot{x}$. Moreover for many of the zero velocity times (i.e., zero damping force), the inertia force is also zero (acceleration), resulting in a direct assessment of static resistance. Consequently, it was decided to use both energy and force equilibrium at the pile tip in the inversion to increase accuracy and robustness of the solution.

4.4.2 Algorithm Evaluation

4.4.2.1 Synthetic Data

Synthetic data (total force) was generated for single degree of freedom model with known nonlinear stiffness, viscous damping, and mass for an applied motion as a function of time. Next, the synthetic data (particle motion and force vs. time) was input to the inversion program and the algorithm was used to solve for nonlinear stiffness, damping and mass from the synthetic data. Theoretically, the interpreted model should be the same as the model assumed at the start. By conducting model studies in which the "answer" is known, a protocol was developed to systematically and consistently analyze the error associated with the inverted values of model parameters.

For this evaluation, the measured acceleration ($\ddot{x}$), velocity ($\dot{x}$) and displacement (x) from one of the field test piles, was used to generate the synthetic total force ($P(t)$) from Eq. 4-27 and shown in Figure 4-29 as free noise data. Here, the mass (m) and damping (c) were assumed as 1000 (kg) and 750 (kN·s/m) (51 kips·s/ft), respectively. The stiffness (k) was assumed to be a combination of four linear segments as shown in Figure 4-28. The loading stiffness k_1, k_2, k_3 and unloading stiffness k_4 were equal 100, 50, 10 and 1000 (kN/mm) (571, 285, 57 and 5710 (kips/in)), and the segment lengths $l_1 = l_2 = l_3 = \text{Max}(u)/3 = 6.8$ mm (0.27 in), respectively.

Next, the synthetic force ($P(t)$) and motion ($\ddot{x}$, $\dot{x}$, and x) was input into the inversion program to invert for unknown parameters (k_i, l_i, c, and m). During inversion, the algorithm allowed the mass (m) to vary from 0 to 2000 (kg), the damping (c) to vary from 0 to 2000 (kN.s/m) (137 kips·s/ft), the loading stiffness (k_1, k_2, k_3) to vary from 0 to 150 (kN/mm) (0 to 857 kips/in), the unloading loading (k_4) to vary from 0 to 2000 (kN/mm) (0 to 11,420 kips/in), and the segment lengths (l_1 and l_3) to vary from 0 to Max(u)/2 =10 mm (0.4 in). The inversion convergence process is discussed in Appendix A.

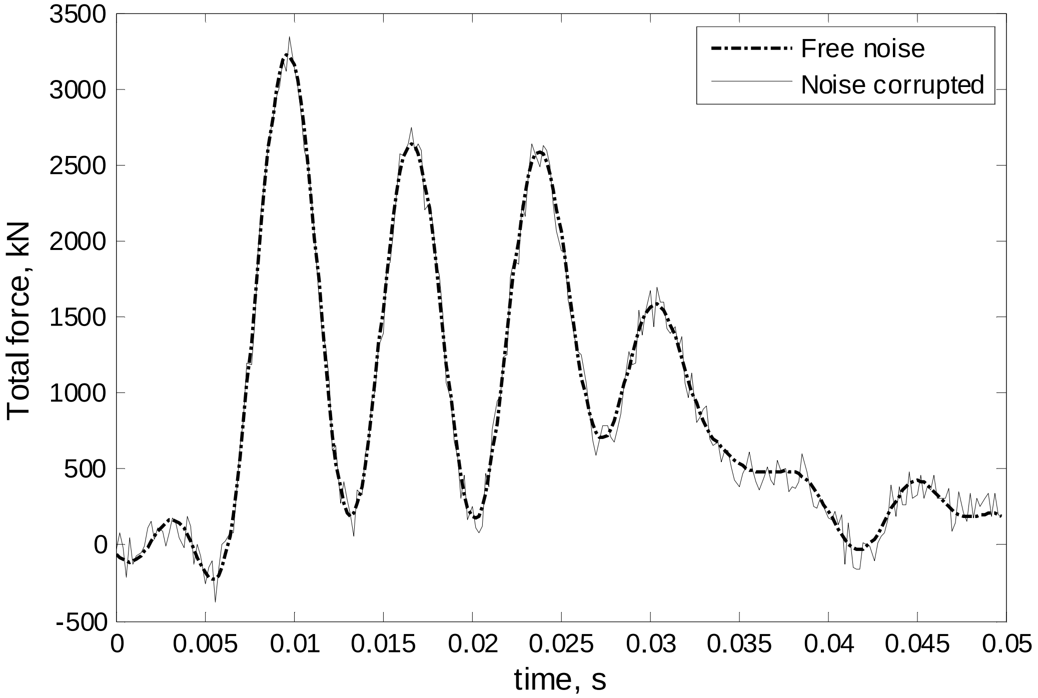

Figure 4-29 Synthetic data with and without noise

To investigate the consistency of the inversion algorithm, 10 consecutive inversion runs on the synthetic data were conducted, and the inverted results of the static resistance and the minimum least-squared errors of each generation are shown in Figure 4-30. It is observed that the predicted results are very similar to the true model (Figure 4-30(a)), suggesting good repeatability of the algorithm. The minimum least-squared error reduces from 300 in the first generation to less than 20 in the final generation (Figure 4-30(b)).

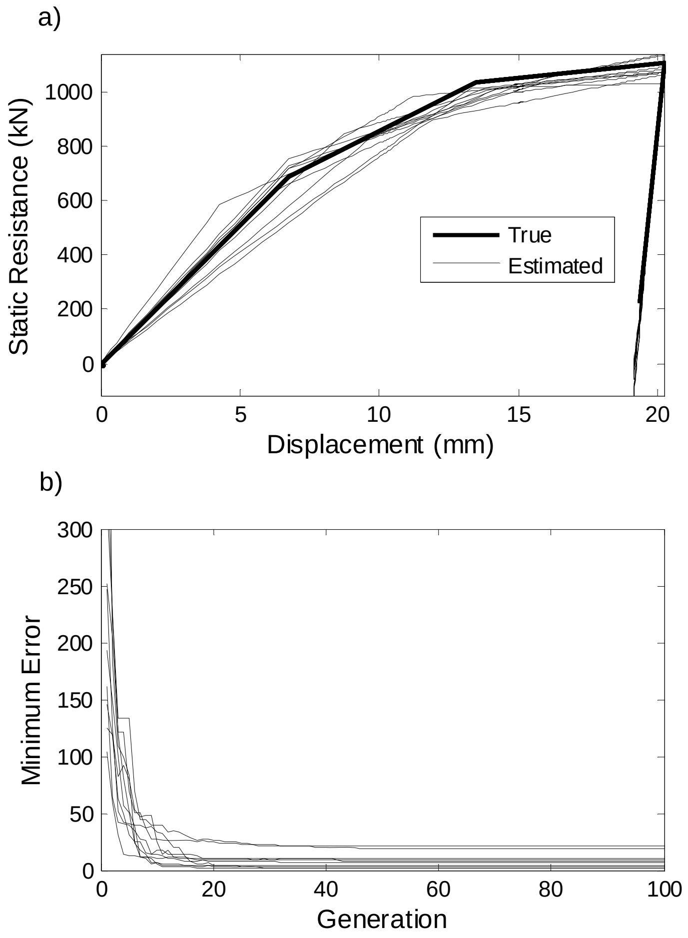

Figure 4-30 Free noise synthetic data: a) inverted results of 10 runs, and b) the minimum least-squared errors of 10 runs

To investigate the influence of noise in the measured signal, random noise with frequency between 20 Hz and 2500 Hz (1/signal length and 1/2 Nyquist frequency) and amplitude of 5% the peak synthetic force was added, Figure 4-29 as noise corruption. In a similar fashion to the free noise analysis, 10 inversion runs were performed on the noise corrupted data. All the parameter constraints and inversion criteria were the same as the noise free analysis. The inverted results of static resistance and the minimum least-squared errors of each generation are shown in Figure 4-31. Evident, even with 5% noise, the inverted results are consistently about the mean (i.e., true value) (Figure 4-31(a)), showing the robustness of the technique. The minimum least-squared error reduces from 500 in the first generation to about 150 in the final generation (Figure 4-31(b)).

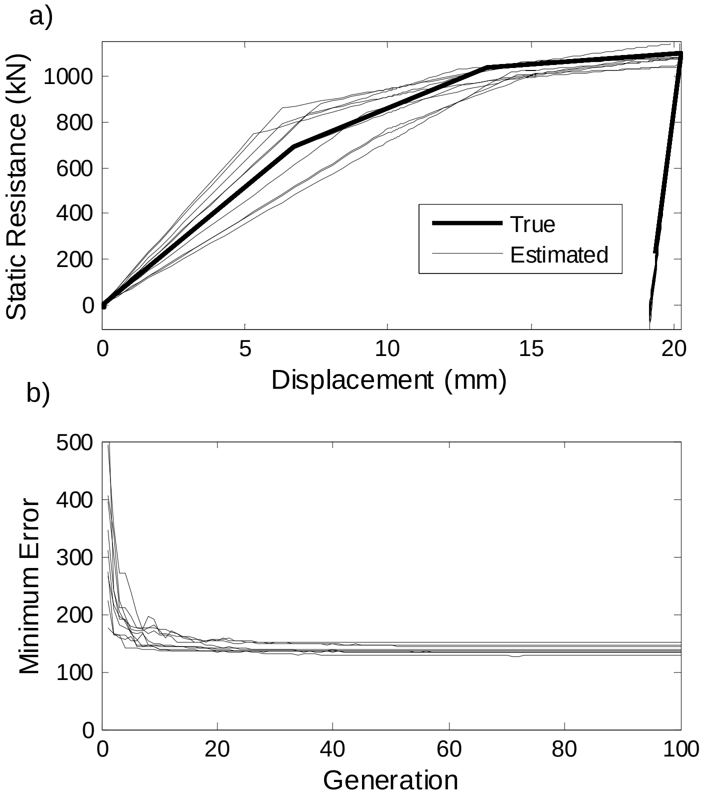

Figure 4-31 Noise corrupted synthetic data: a) inverted results of 10 runs, and b) the minimum least-squared errors of 10 runs

In general, inversion results from synthetic data sets with and without noise shows that the proposed algorithm consistently inverts the static resistance to within 20% of the true model. Evidently, it would be better if one can run inversion 10 times for each data set and get the average of the inverted results. However, by doing so, the requirement of a real time solution may be violated. Alternatively, it proposed that the average of 5 or 10 consecutive blows be used to represent the tip resistance of a pile at a specified depth. Specifically in pile driving, typical blow counts varying from 40 to 150 blows per 0.3 m (0.98 ft), the latter will represent a small change in tip movement (<75 mm (2.95 in)).

4.4.2.2 Measured Data

The developed algorithm has been shown to work well on the synthetic data. However, in the end, for acceptance and possible implementation, the predicted results must compare favorably with measured response (i.e., static load tests). Recently, the Florida Department of Transportation (FDOT) with the support of the Federal Highway Administration (FHWA) paid for the monitoring (top and bottom) of two 0.61-m-square piles at a site in South Florida, as well as static top down load testing of the piles. Similarly, the Louisiana Department of Transportation monitored (top and bottom) two 0.76-m-(2.5 ft)-square piles driven into silty sands, restruck up to one month later to assess pile freeze, and then static load tests were conducted on the piles. The tip resistance for all four piles at end of initial drive (EOID), and restrike were computed with the proposed approach and compared with the measured tip resistance from the static load tests.

4.4.2.2.1 Site 1

End Bent 1

The developed algorithm was used to model 10 restrike blows for comparison with one another and the measured tip resistance from the static load test. The specific results of one of the restrike blow are presented here in detail for discussion.

Prior to running the inversion, both the measured strain and acceleration at the tip of the pile were low-pass filtered to remove all components of frequencies higher than 200 Hz. By doing so, high frequency noise was removed, reducing the number of local maxima and minima in the data, resulting in quick and consistent inversion. Also, the relationship of static tip resistance and displacement (Q-Z curve) was modeled by a multilinear curve having three loading segments (l_1, k_1, k_2, l_3, k_3) and one unloading segment (k_4). Consequently, the total number of unknowns was eight: mass, damping, four different stiffness, and two segment lengths.

The inversion began with the first generation of 200 random models. During inversion, the algorithm allowed the mass (m) to vary from 0 to 3000 (kg), the damping (k) to vary from 0 to 2000 (kN·s/m) (0 to 137 kips·s/ft) , the loading stiffness (k_1, k_2, k_3) to vary from 0 to 300 (kN/mm) (0 to 1,710 kips/in), the unloading loading (k_4) to vary from 0 to 2000 (kN/mm) (0 to 11,420 kips/in), and the segment lengths (l_1 and l_3) to vary from 0 to Max(u)/2.

Figure 4-32 presents the total energy arriving at the pile tip, as well as the predicted components due to inertia, damping, and static resistance, and the error (difference between measured total energy, $\int_t^{t+T} P(t)\dot{x}\,dt$ and sum of predicted components). The nearly zero error shows an excellent energy balance with time, especially for later points in the plot (i.e., total energy). Shown in Figure 4-33 are the individual forces: inertia, damping, static, as well as their sum vs. the measured total force with time. Apparent from the figure, the total estimated and measured forces match well for most of the points along the time axis. Interestingly, from Figure 4-32, for typical tip accelerations (i.e., both positive and negative values, Figure 4-33), inertia energies at the pile tip are small (positive and negative areas cancel); however, a significant portion of the input energy is consumed by damping and the nonlinear soil stiffness (i.e., movement of soil below the pile tip). Also evident from Figure 4-33 are a number of discrete times (e.g., 0.014 sec, 0.022 sec, 0.027 sec, etc.) where damping and inertia force are negligible, and the static resistance just equals the measured total force. Figure 4-34 shows the estimated static force, damping force, predicted total force and measured total forces as a function of the pile tip displacement. Since the inertia energy is small, the sum of the areas under the damping force and static force curves must equal the area under the total measured force vs. displacement (Figure 4-34). Also, since the damping coefficient *c* is fixed for the whole displacement or time trace, changing the pile soil-stiffness in the later displacement segments must balance the changes in damping energy in each of the latter segments. Note, similar force and energy balance from sensor data may be validated through a spreadsheet using the ideas just discussed.

In the case of the genetic algorithm, it should be evident that the quality of the match between the predicted and measured total forces and energies (Figs. 4-32, 4-33, and 4-34) is a function of the complexity of models considered, e.g., number of segments in the Q-Z curve, unloading stiffness, etc. Adding more segments will not only increase CPU time, but also increase the uncertainty of estimated parameters which may violate the requirement of a fast and unique solution.

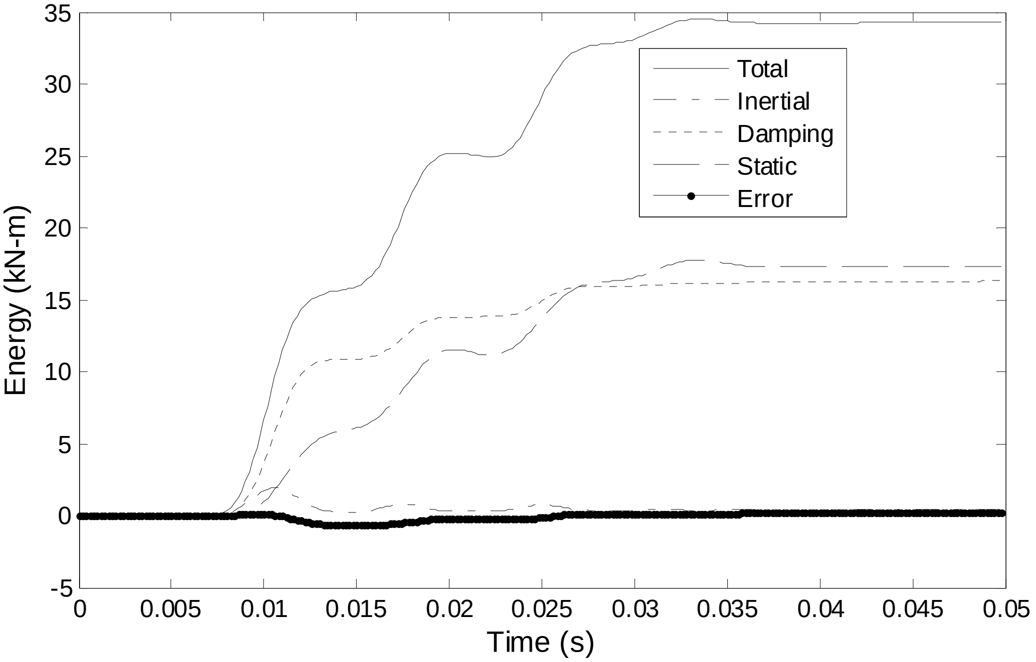

Figure 4-32 Dixie Highway End Bent 1: energy balancing

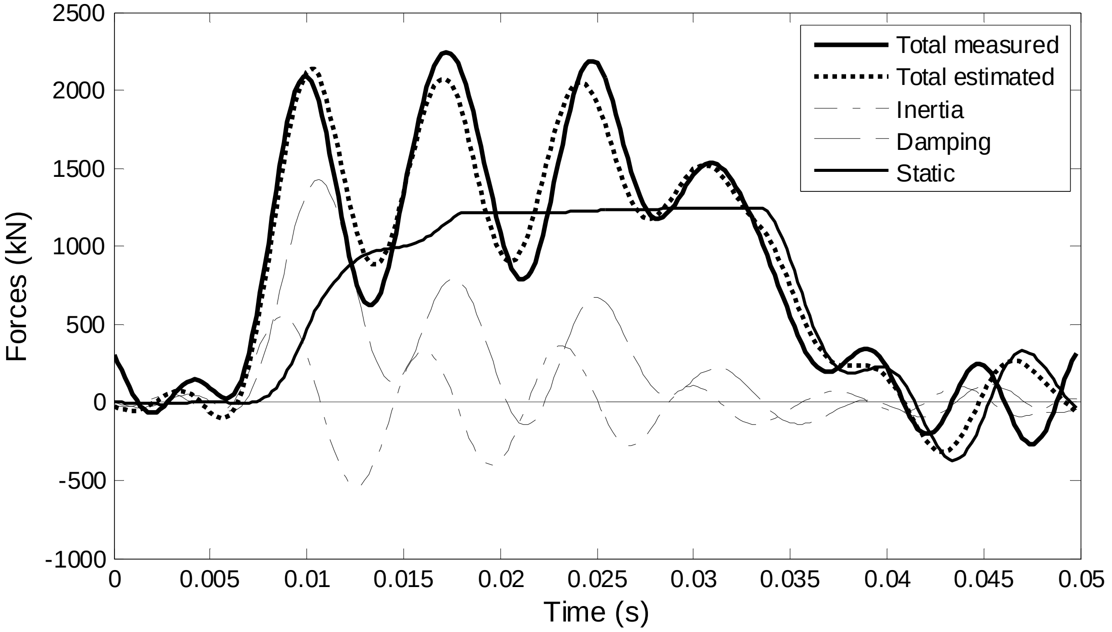

Figure 4-33 Dixie Highway End Bent 1: forces in time domain

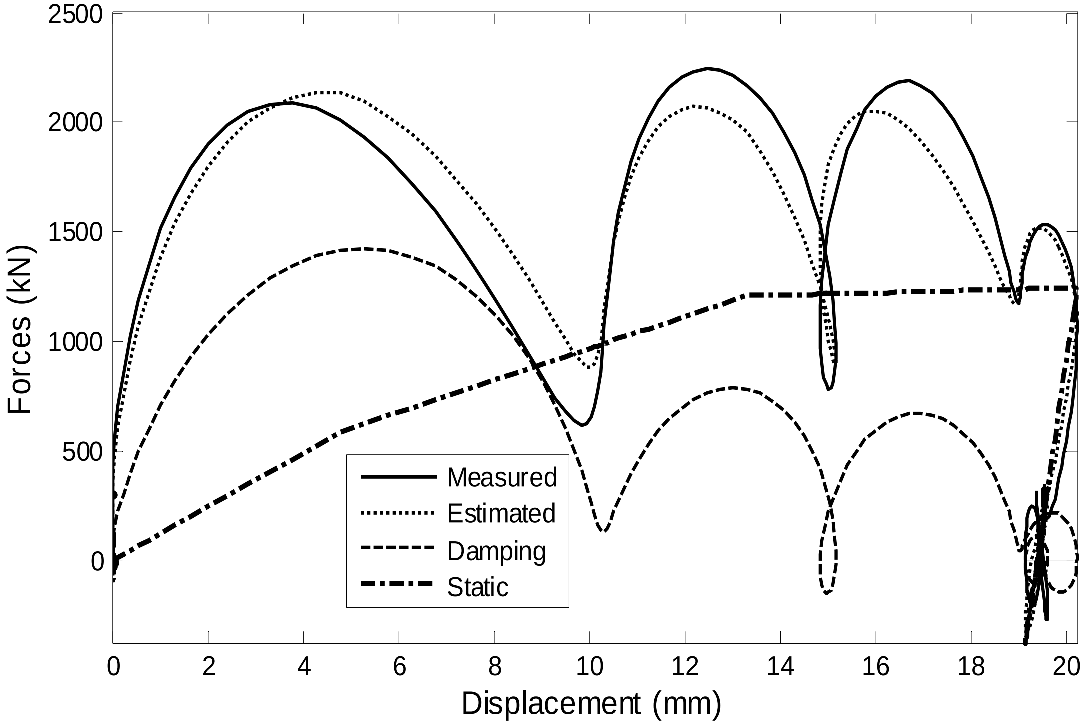

Figure 4-34 Dixie Highway End Bent 1: forces versus displacement

Inversion results of static tip resistance for five restrike blows before the load test are presented together with the result of the static compression load test in Figure 4-35(a). The five estimated tip resistance curves are similar and compare favorably to measured static tip response, especially at large displacement. Similarly, the results of five restrike blows after the load test are presented together with the result of the load test in Figure 4-35(b). The excellent agreement between the estimated resistances and that of the load test was again found. In addition, comparing the results in Figure 4-35(a) against those in Figure 4-35(b), the differences of the estimated results of blows before and after the load test are small, suggesting little if any pile tip freeze.

Also of importance is mobilized tip resistance at displacements other than specified blow count values, i.e. service loads. For instance, from Fig. 4-35, considering Davisson capacity at the top of the pile, the mobilized tip resistance is approximately 900 to 1000 kN (202 to 225 kips) and occurs at 8 to 12 mm (0.3 to 0.47 in) of tip displacement. The latter is less than the observed dynamic tip displacements, i.e., 15 to 25 mm (0.6 to 0.98 in) and its associated higher tip resistance, i.e., 1000 kN (225 kips) to 1400 kN (315 kips). Knowing the static load vs. displacement response of the tip is very useful for predicting the load transfer for other service or strength load cases in design.

Pier 8

Shown in Figure 4-36 is the estimated static tip resistance vs. displacements for 5 blows before (3 days prior to static load test) and 5 blows after (4 days) the static load test. Evident is the repeatability of the results for multiple blows and the favorable comparison to the static load test result, especially at large displacement.

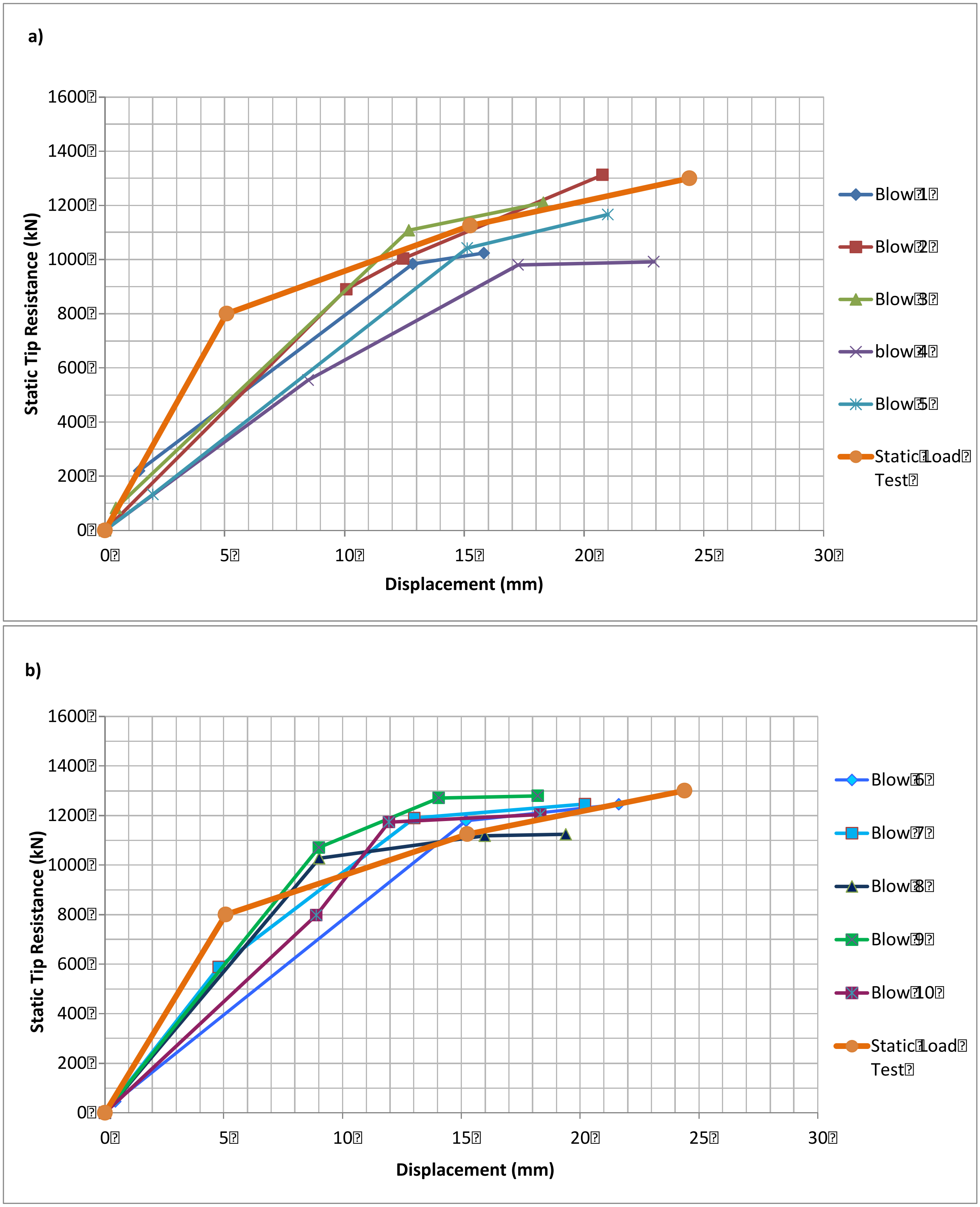

Figure 4-35 Estimated tip resistance of Dixie Highway End Bent 1: a) blows before the load test, and b) blows after the load test and b) blows after the load test

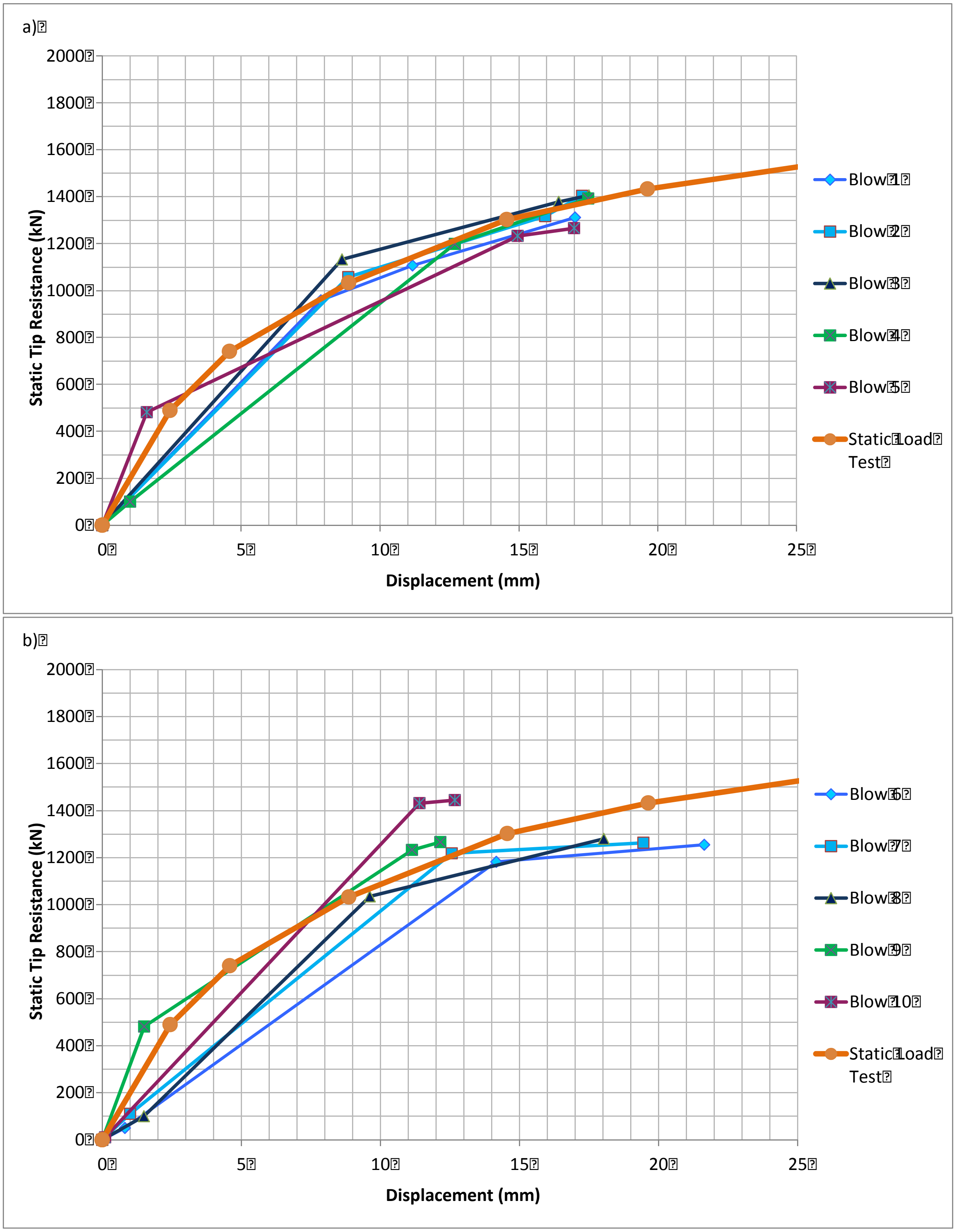

Figure 4-36 Estimated tip resistance of Dixie Highway Pier 8: a) blows before the load test, and b) blows after the load test

4.4.2.2.2 Site 2

Bent 1

The developed algorithm was used on 5 of the end of initial drive (EOID) blows as well as 5 of the beginning of restrike (BOR) blows to investigate changes of the tip resistance after a week (i.e., EOID vs. BOR) due to pile freeze. Similar to the Dixie Highway site, the energy balancing and force matching for one blow are presented in Figs. 4-37 and 4-38. In the case of the energy (Figure 4-37), the small residual error represents a good match between the input energy and the energies associated with inertia, damping and static resistance. Similarly, the total estimated and measured forces (strain data) at the pile tip (Figure 4-38), match well for most of the points along the time axis. Some interesting observations from the results: the total measured or predicted energy at the pile tip (inertia + damping + static) was three times smaller for the Caminada pile than that for the Dixie Highway piles, even though the pile was larger (D = 0.76 m (2.5 ft) vs. 0.61 m (2 ft)) and moved equal to or greater than the Dixie Highway pile tip displacements for any blow. The inertia energy at the beginning of the blow is greater for the Caminada Bay pile than that for Dixie pile due to the added soil mass moving with the pile tip; however, after 0.028 sec the total inertia energy was zero (again positive and negative contribution), and the total tip energy was balanced by damping and static tip resistance. Again, at discrete times (e.g., 0.28 sec and 0.38 sec) the velocity is zero, and static resistance must equal total tip resistance, and the sum of the damping and static energy after 0.28 sec must balance the total supplied energy at the tip. Evident from the latter restraints, both the damping and static resistance may be readily found.

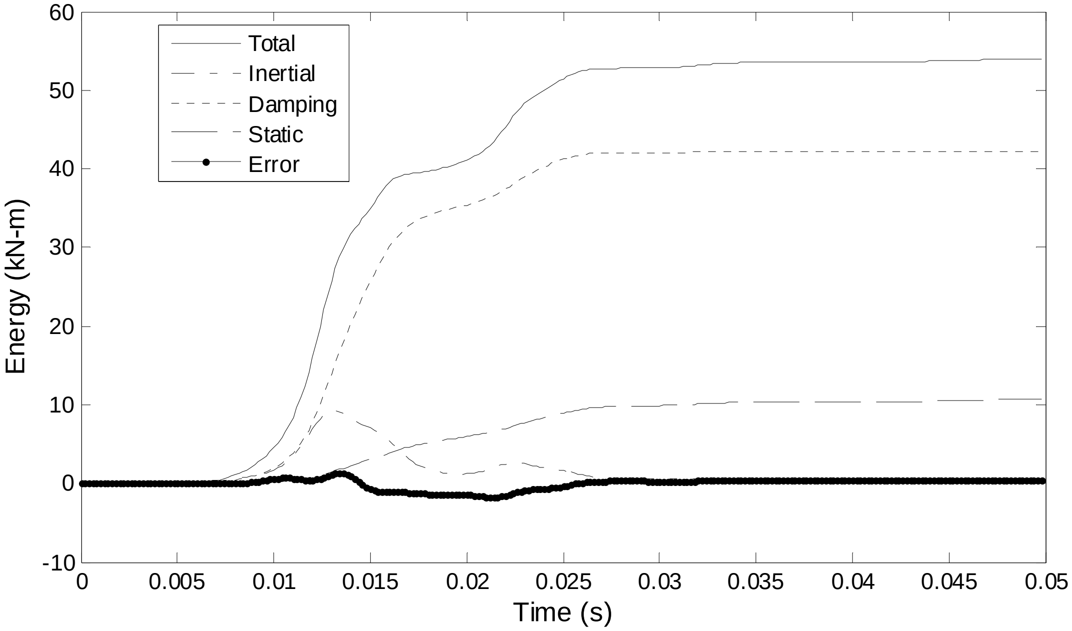

Figure 4-37 Caminada Bay Bent 1: energy balancing

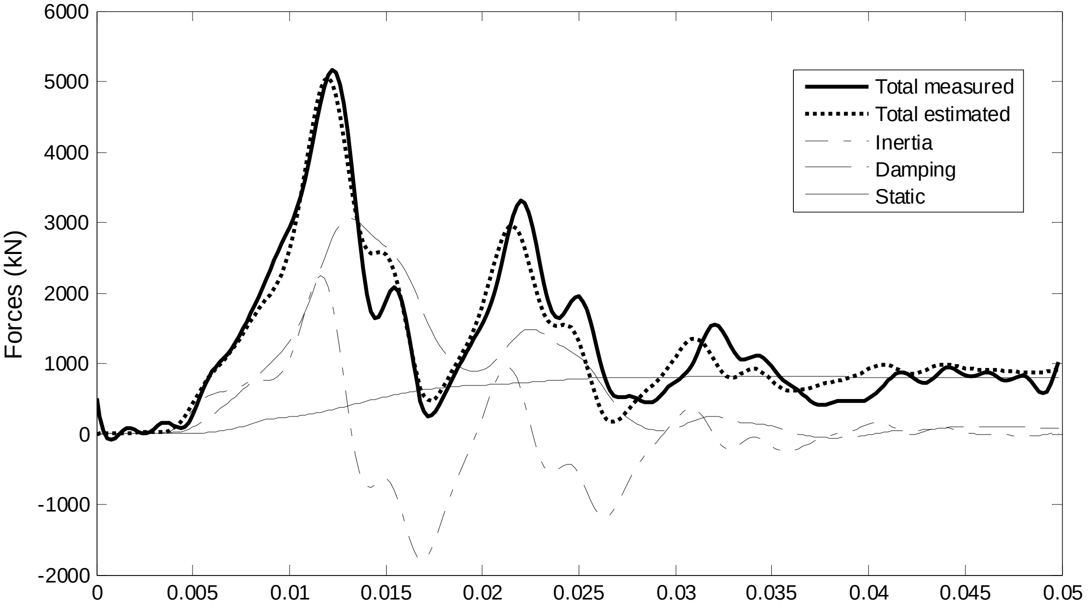

Figure 4-38 Caminada Bay Bent 1: forces in the time domain

The predicted static tip resistance for 5 blows, at EOID, and 5 restrike blows (BOR), 7 days after EOID, are shown in Figure 4-39. A comparison of the predicted static EOID response vs. BOR resistance shows an approximate 15% increase in the tip resistance after one week. The latter is consistent with other observations (Titi and Wathugala 1999, McVay et al. 1999, Axelsson 2000, Bullock et al. 2005, and Kuo et al. 2007) which identified possible skin friction increases of 100 percent due to pore pressure or total stress changes, but increases in tip resistance of less than 20 percent.

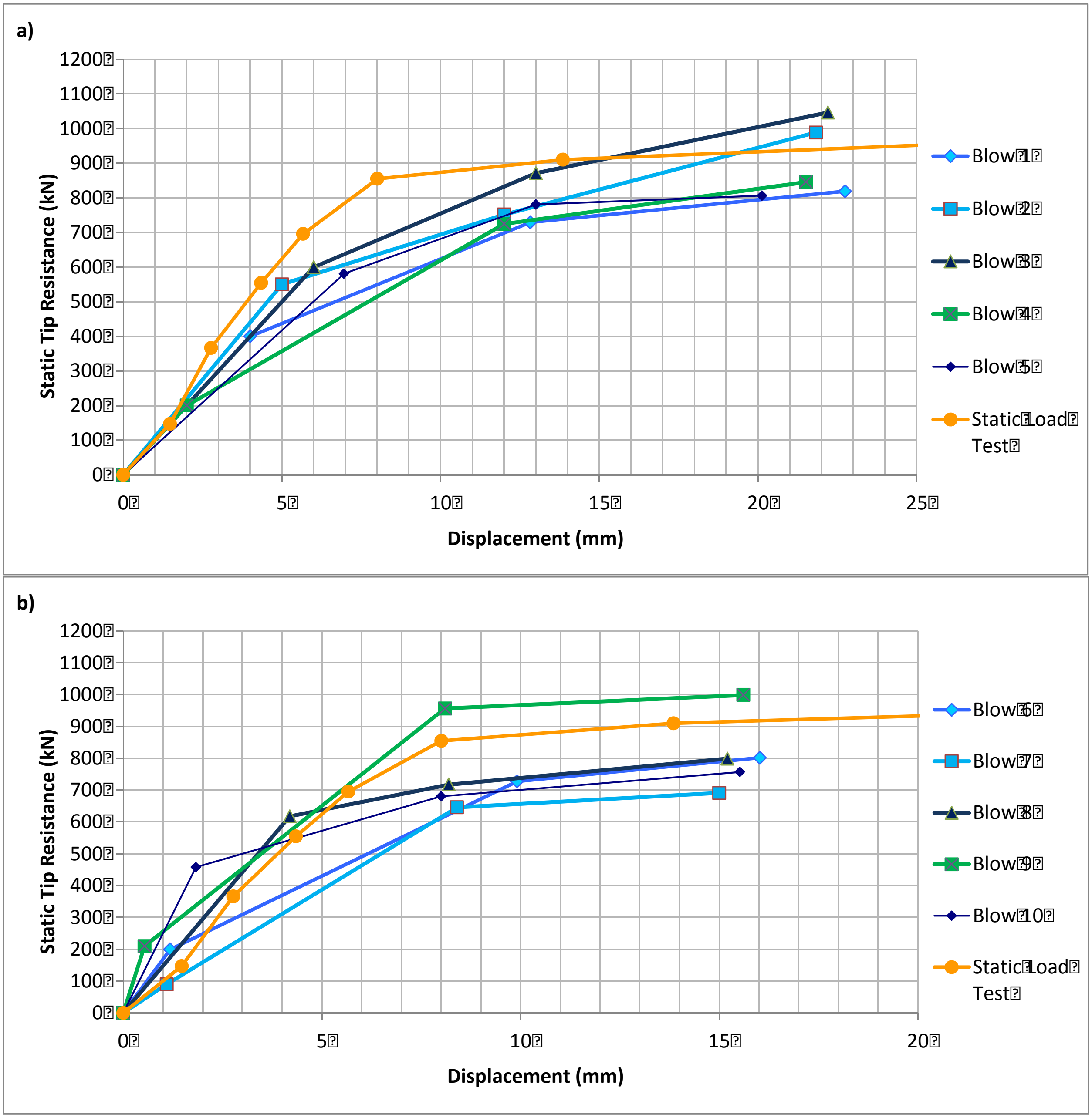

Figure 4-39 Estimated tip resistance of Caminada Bay Bent 1: a) blows at the end of driving (EOD), and b) blows at the beginning of restrike (BOR).

For comparison, the measured static tip response from a top down load test (9 days after EOID) is also shown in Figure 4-39. It is observed that the estimated tip resistances compare very favorable to the load test response. Assessing Davisson capacity on the static load test, the pile tip displaced 10 to 15 mm (0.4 to 0.6 in), which is less than the maximum observed displacements (15 mm (0.6 in) to 25 mm (0.98 in)) of the EOID and BOR blows. In the displacement range of 10 mm (0.4 in) to 15 mm(0.6 in), the pile capacity measured from the static load test was approximately 900 kN (202 kips), which compared very favorably to the predicted 800 kN (180 kips) from the average of the 10 blows analyzed.

Bent 7

The estimated tip resistance for 5 blows at EOID, and 5 blows at BOR, are shown in Figure 4-40.

Evident from a comparison of the results, the ultimate tip resistance increased by 18%, one month after installation, i.e., from 340 kN (76 kips) (average of 5 blows) at EOID to 400 kN (90 kips) (average of 5 blows) at BOR. A load test was performed on the 2nd pile and the static tip resistance vs. displacement is also presented in Figure 4-40. The predicted static resistance for all blows at BOR compares favorably with the measured static tip resistance.

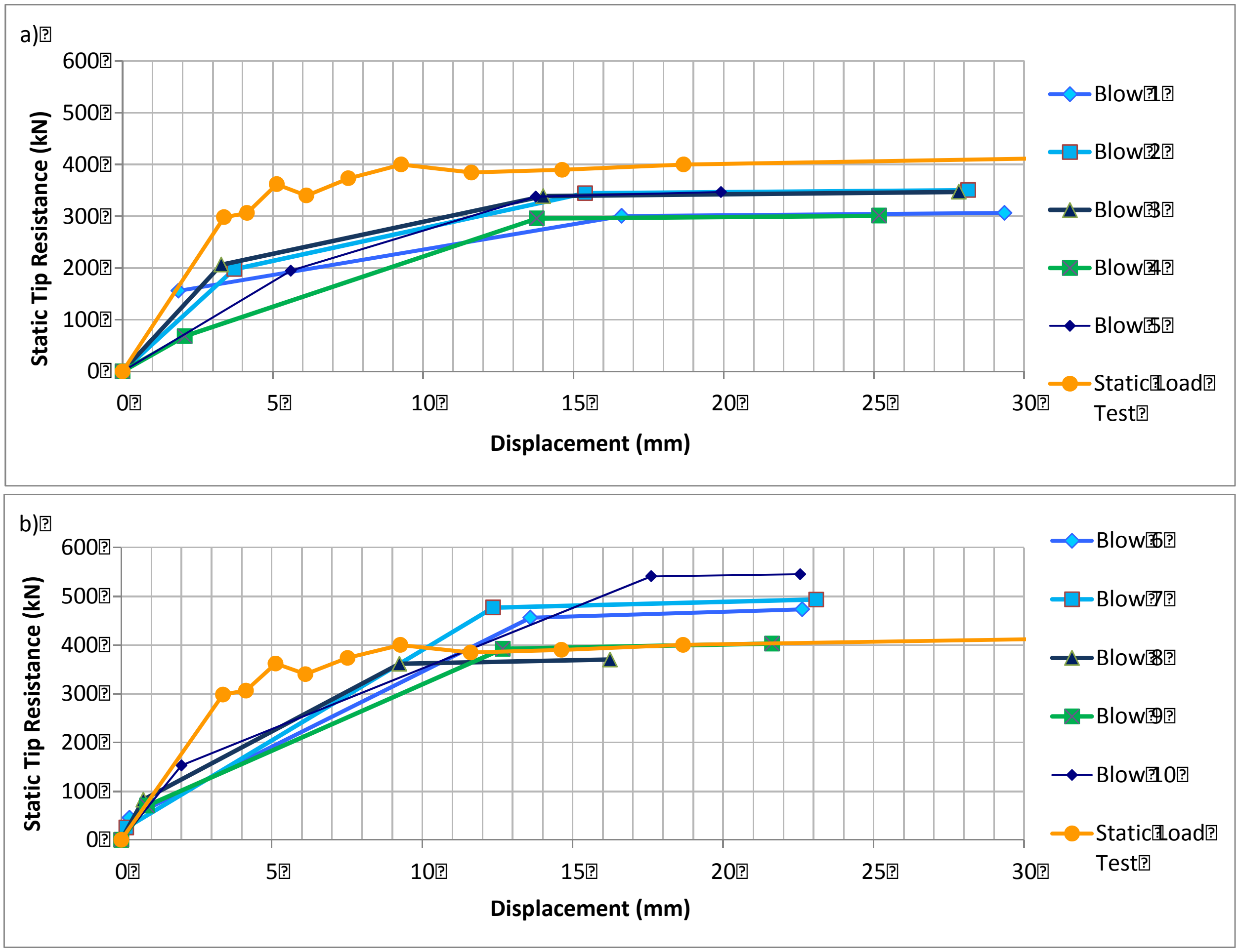

Figure 4-40 Estimated tip resistance of Caminada Bay Bent 7: a) blows at the end of driving (EOD), and b) blows at the beginning of restrike (BOR).

4.5 Conclusions

New solution strategies are presented for estimating skin friction and tip resistance in "real time" from hammer blow information (strain and velocity) measured at the top and bottom of the pile. For skin friction, the strategy involves a solution of the 1-D wave propagation problem for skin friction and damping subject to known initial and boundary conditions. Methods for both linear and non-linear skin friction, developed from the solution strategy, are presented. For tip resistance, the strategy uses a nonlinear single degree of freedom to characterize the bottom 1D section of pile (below the gauges) and soil. A global optimization scheme using a genetic algorithm is employed to solve for soil stiffness (b) and damping (c) by matching predicted and observed velocity and strain traces in the skin friction problem and minimize error in the energy and force equilibrium balance. A significant improvement over current practice is each strategy provides unique solutions for the soil stiffness, k, and damping, c, along the pile length (homogenous), on segments of the pile (homogenous segments representing a non-homogenous case) and at the tip of the pile (pile and soil below pile tip). Furthermore, the analysis shows that the damping is proportional to the stiffness.

Each solution strategy was used on four driven piles for which conventional static load tests were performed. Significant observations for each follow:

- For the four piles investigated under the soil conditions encountered (sand, silts and clays), the homogeneous or average material property approach was shown to give reasonable comparisons between the measured and estimated skin frictions.
- Each of the four piles was divided into 4 to 5 segments with 8 to 10 unknowns. The genetic global optimization converged within 50 iterations, requiring approximately one minute on a PC desktop computer with a 3.4 GHz CPU. For the four piles investigated under the soil conditions encountered (sand, silts and clays), the approach was shown to give consistent and reasonable comparisons between the estimated and measured skin frictions (less than 20 % difference).
- For tip resistance, the strategy involves dividing the response into 3 loading and one unloading segments where the static tip stiffness is assumed constant. Within any segment, if the velocity and acceleration is zero, then the static force (i.e., stiffness) is known (equal to total tip force). In addition, due to the dynamic nature of the pile (i.e., positive and negative inertia forces), after approximately half the trace, inertia energy is negligible and damping energy (function of *c* value) plus static energy (function of

stiffness, *k*) must balance the applied tip energy. The solution (force and energy) may be done with an Excel spreadsheet within a few minutes or with the genetic algorithm in about 5 seconds on a 3.4 GHz CPU computer.

- For tip resistance, the solution strategy was used on each of the four piles, which conventional static load tests were performed. The piles varied in width, length, and embedded soil types (sands to silty-sands, tipped in clay and limestone). Analyses were performed both at EOID and BOR after various times (one week up to a month). Good comparisons between the estimated static tip force vs. displacement and the measured response from load tests were found.

CHAPTER 5
OBSERVED AND PREDICTED PILE FREEZE

5.1 Background

This chapter discusses mostly predictions made by the newly developed tip and skin resistance prediction methods that are either not used as the default method in SmartPile Review (tip), or have not been implemented in the software's algorithm (skin friction). Pile freeze effects have been documented by many researchers. Bullock et al. (2005) investigated five fully instrumented piles driven into a variety of soils (sand, clay, mixed soils) at four different FDOT bridge sites. After 16 to 1727 days elapsed time, and Osterberg load testing to separate side shear from end bearing, side shear increases of 12% to 32% per log cycle of time were recorded.

Chen et al. (1999) presented two case histories where the changes in pile capacity were observed with time. Both showed increase in pile capacity, but one driven into clayey sand showed 70% increase in pile shaft friction. Similarly, Kehoe (1989) investigated two Florida mixed cohesive soil sites with driven square prestressed concrete piles. Static and dynamic tests showed that the total pile capacities increased on average from 58% to 200% within 11 days after driving.

Chow et al. (1998), McVay et al. (1999), Axelsson (2000), Bullock et al. (2005), and Kuo et al. (2007) concluded that the pile set-up occurs primarily as a result of side shear increase, not due to end bearing. Penetration of the pile, displaces soil both downward, outward and upward from the pile as the pile tip passes a point in space. The process not only shears the soil, it remolds (i.e., clay) and repacks (sand – void ratio) both near and outward from the wall of the pile. The process not only generates excess pore pressure (i.e., below water table) which dissipate, but changes in total stress (hoop stresses) which change in time (Bullock et al., 2005).

Recently, NCHRP Synthesis Report 418, suggests that total pile capacity be assessed from dynamic pile monitoring at both EOID and BOR. In the case of EOID, the full tip resistance is assumed to be mobilized, but the skin friction may be under predicted due to loss of lateral effective stress during driving. Nevertheless, after days, during initial restrike blows (i.e., BOR) the pile may exhibit full pile skin friction due to excess pore pressure dissipation. Of concern in the report (NCHRP 418) is that the total pile capacity at BOR may not be fully mobilized, i.e., full skin but only portion of the tip resistance due to limited movement of pile tip. Consequently, there is a great interest in predicting both skin friction and tip resistance at both EOID and BOR, as well as quantifying their level of accuracy. Also of interest is identification of the level of mobilized tip movement (vs. resistance) at EOID vs. BOR.

5.2 SR 810, Dixie Highway at Hillsboro Canal in Broward Florida

The site consists of upper layers of approximately 49 ft of medium dense sand with cemented sand zones underlain by limestone. Three piles (Pier 4, Bent 1 and Pier 8) piles were load tested. The first pile (Pier 4) was uplift and the last two piles were top down compression tests with measured skin and tip (Chapter 2). A discussion of each follows.

5.2.1 Pier 4, Dixie Highway

The pile was 24” x 72 ft driven with a diesel hammer with measurements made at EOID and 3 days (BOR) after initial driving. Shown in Figure 5-1 are predicted skin friction at (a) EOID and (b) three days later, BOR using skin friction model from Chapter 4. SmartPile Review ver 3.73 reports a value of 171kips (760 kN) for BOR (three days) which compares favorably with the load test 212 kips (950 kN) at Davisson. Evident from Figure 5-1 the skin friction of the pile has increased by 30% in three days.

Also of interest is the end bearing behavior of the pile at EOID and at same BOR (3 days) to distinguish differences in tip mobilization. Shown in Figure 5-2 is the predicted tip

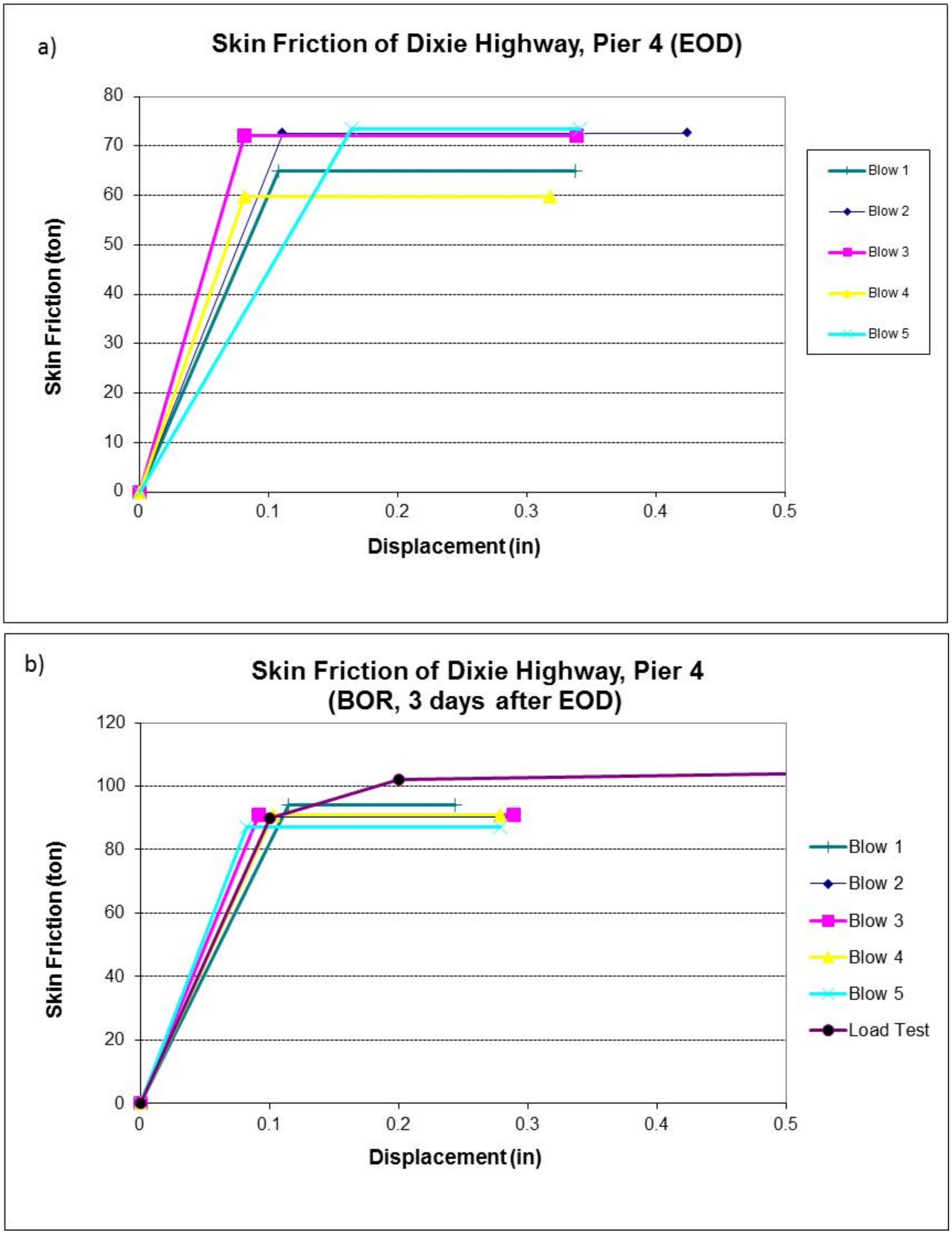

Figure 5-1 Estimated skin friction of Dixie Highway, Pier 4: a) blows at the end of driving (EOD), and b) blows at the beginning of restrike (BOR)

tip resistance for Pier 4 pile at (a) End of initial Drive, EOID and (b) BOR, three days after EOID. The predictions for all five blows are based on the energy tip approach (Chapter 4). In the case

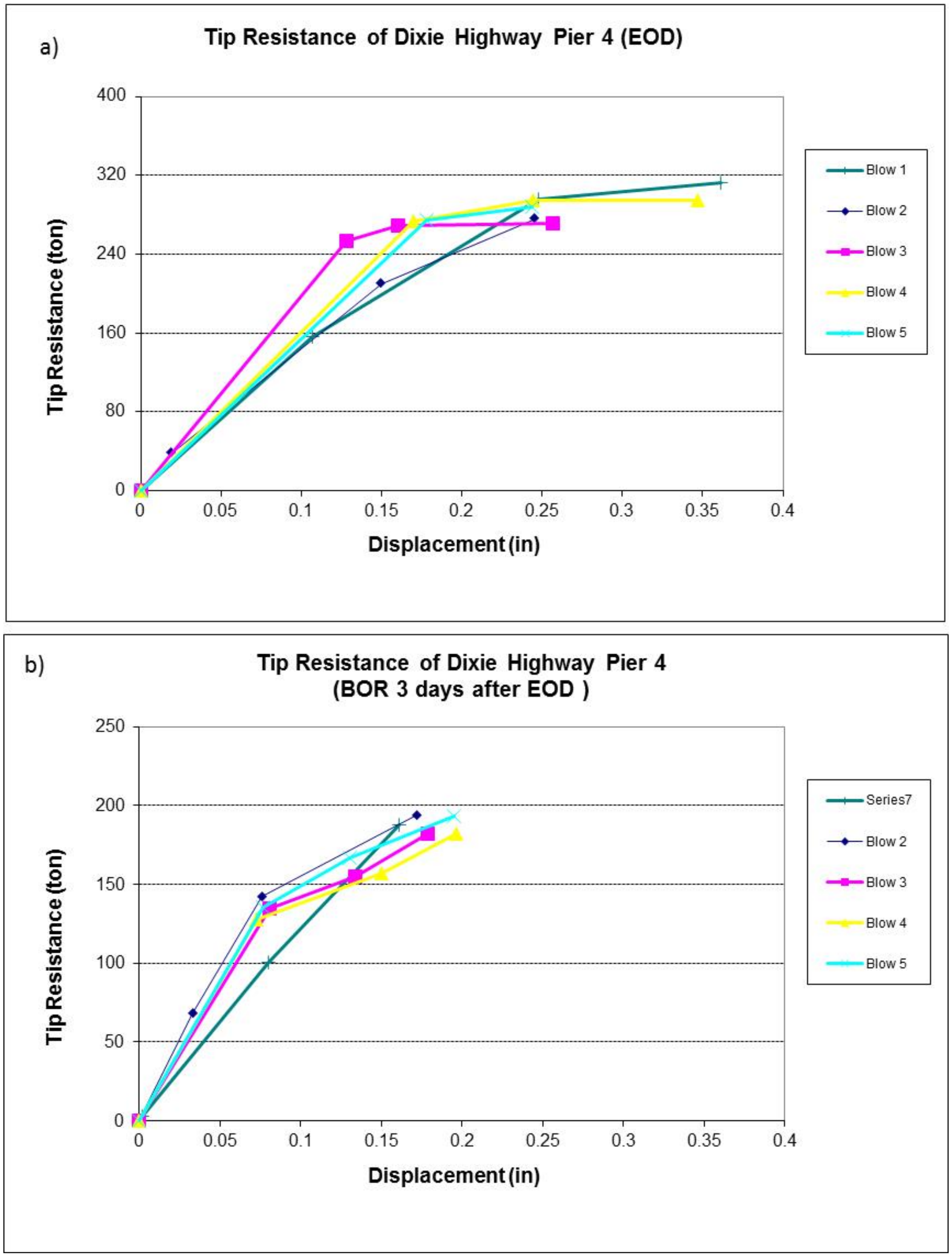

Figure 5-2 Estimated tip resistance of Dixie Highway, Pier 4: a) blows at the end of driving (EOD), and b) blows at the beginning of restrike (BOR).

of SmartPile Review 3.73, the estimated ultimate tip at EOID was 800 kips (3500 kN). A comparison of EOID vs. BOR tip resistance shows a decrease of resistance with time. However, the decrease may be associated with amount of tip displacement mobilized with the hammer. In the case of BOR only 4 mm (0.16") of tip movement occurred, whereas in the case of EOID, 9 mm (0.35") of movement occurred. The latter agrees with NCHRP 418 discussion of mobilized skin and tip resistance.

5.2.2 End Bent 1, Dixie Highway

The pile was a 24-in-square by 50-ft-long (22 ft shorter than Pier 4) prestressed concrete pile, driven to a depth 46 ft below the ground surface by a single acting diesel hammer. Restrikes were conducted approximately one week after installation to investigate the changes of pile capacity. Shown in Figure 5-3 is the estimated skin friction using the skin friction model from Chapter 4. SmartPile Review 3.73 reports a value of 50 tons for BOR which compares favorably with the load test 67 tons at Davisson. Evident from Figure 5-3, the skin friction of the pile has increased by 75% in one week.

Shown in Figure 5-4 is the predicted BOR and measured static tip resistance of End Bent 1 Pile. The predicted tip was computed from the energy tip approach (alternative approach in SmartPile Review), Chapter 4. The unloading point approach in SmartPile review 3.72 reported a value of 349 kips (1550 kN), slightly higher than the Davisson reported load test value of 296 kips (1320 kN). Of interest was the small change between the EOID and BOR because the mobilized tip displacement, 25 mm, (Figure 5-3) was sufficient to mobilize the full tip resistance.

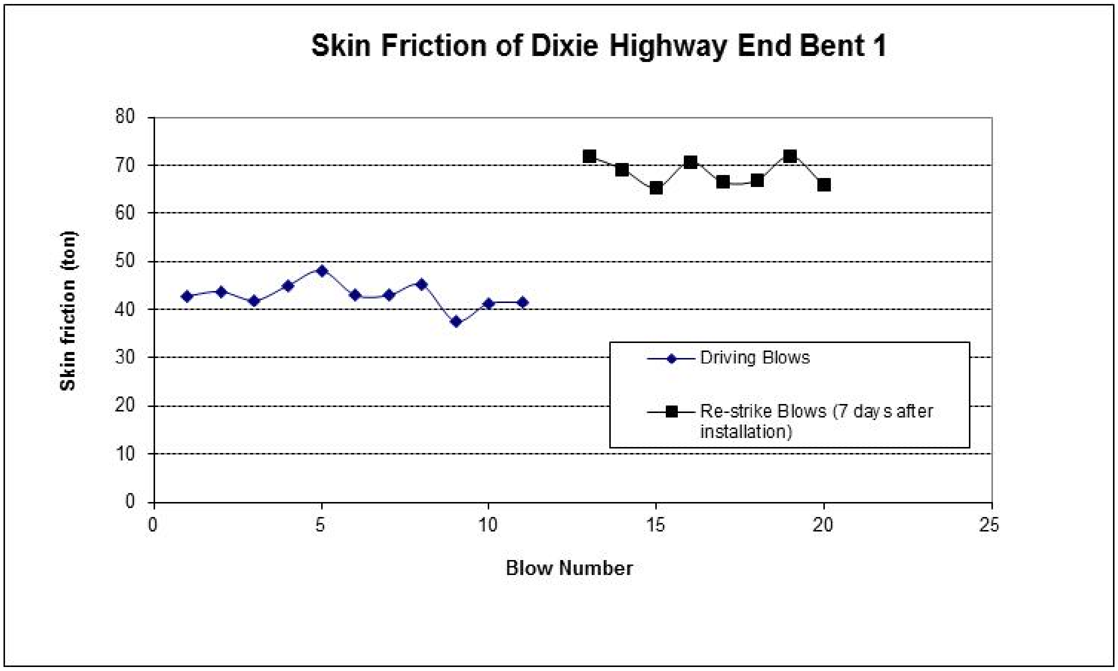

Figure 5-3 Estimated skin friction of Dixie Highway End Bent 1at EOID and BOR

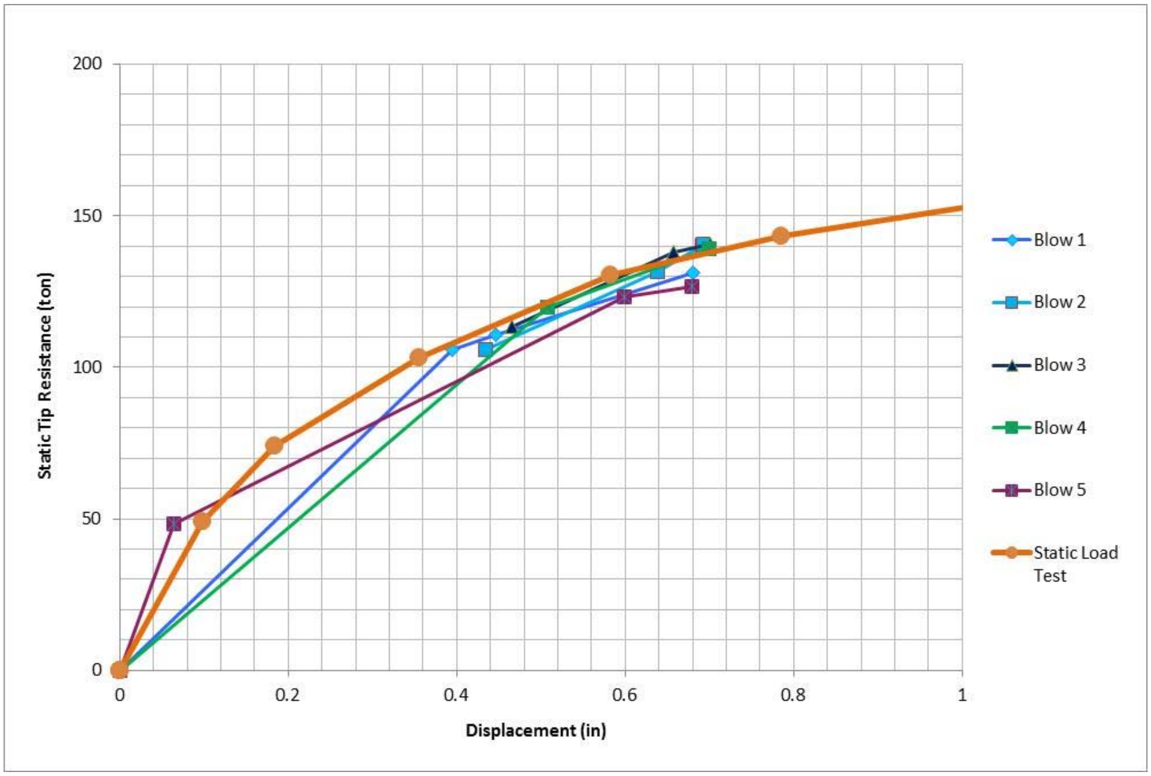

Figure 5-4 Estimated and predicted tip resistance for End Bent 1 at BOR

5.2.3 Pier 8, Dixie Highway

The pile was a 24-in-square by 50-ft-long (22 ft shorter than Pier 4) prestressed concrete pile, driven to a depth 46 ft below the ground surface by a single acting diesel hammer. Restrikes were conducted approximately four days after installation to investigate the changes of pile capacity. Shown in Figure 5-5 is the estimated skin friction using the skin friction model from Chapter 4. SmartPile Review 3.73 reports a value of 110 tons for BOR which is slightly larger than the load test value, 90 tons at Davisson capacity. Evident from Figure 5-5, the skin friction of the pile has increased by 75% in four days.

Shown in Figure 5-6 is the predicted BOR and measured static tip resistance of the Pier 8 Pile. The predicted tip was computed from the energy tip approach (alternative approach in SmartPile Review), Chapter 4. The unloading point approach in SmartPile Review 3.72 reported a value of 250 kips (1100 kN), slightly higher than the Davisson reported load test value of 200 kips (900 kN). Note, there was little change between the EOID and BOR because the mobilized tip displacement, 20 mm, (Figure 5-6) was sufficient to mobilize the full tip resistance.

5.3 Caminada Bay, Louisiana

Caminada Bay, Louisiana, is 42 miles (70 km) south of New Orleans. The site consists of either uppers layers: 1) 49 ft (15 m) of silty fine sand or, 2) 53 ft (16 m) of fine sand with traces of silt and clay, underlain by a high plasticity (40<PI<70) clay deposit. Two piles were driven on this site with a diesel hammer and monitored with EDC gauges at the top and bottom of the pile. Discussion of each follows.

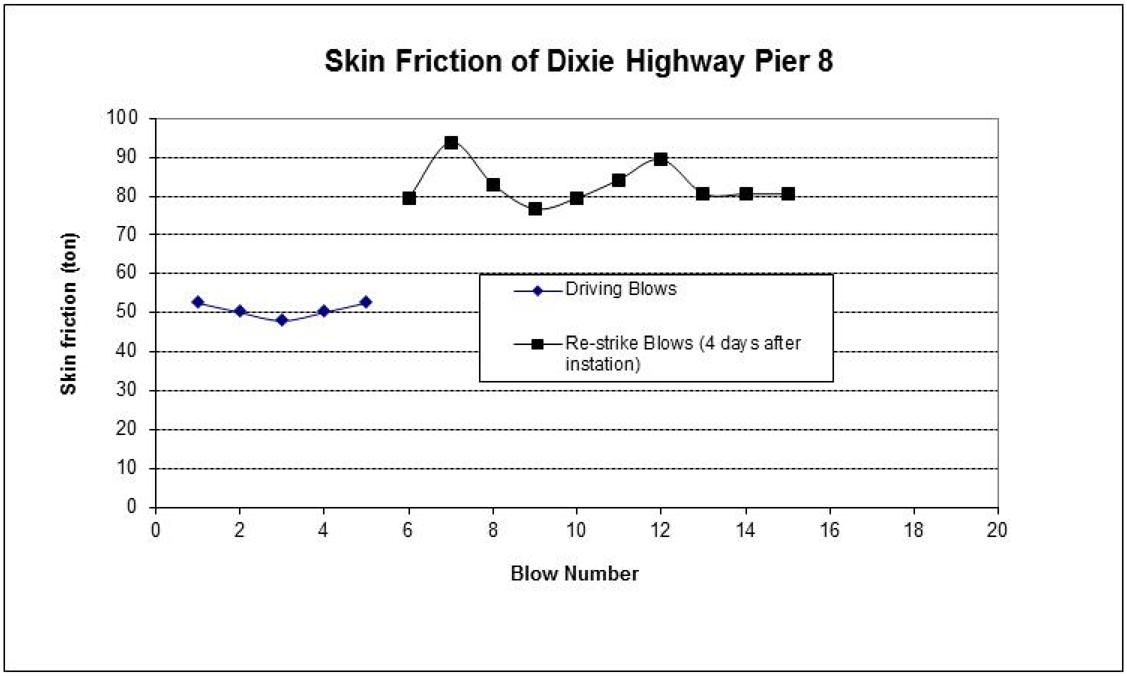

Figure 5-5 Estimated skin friction of Dixie Highway Pier 8 at EOID and BOR

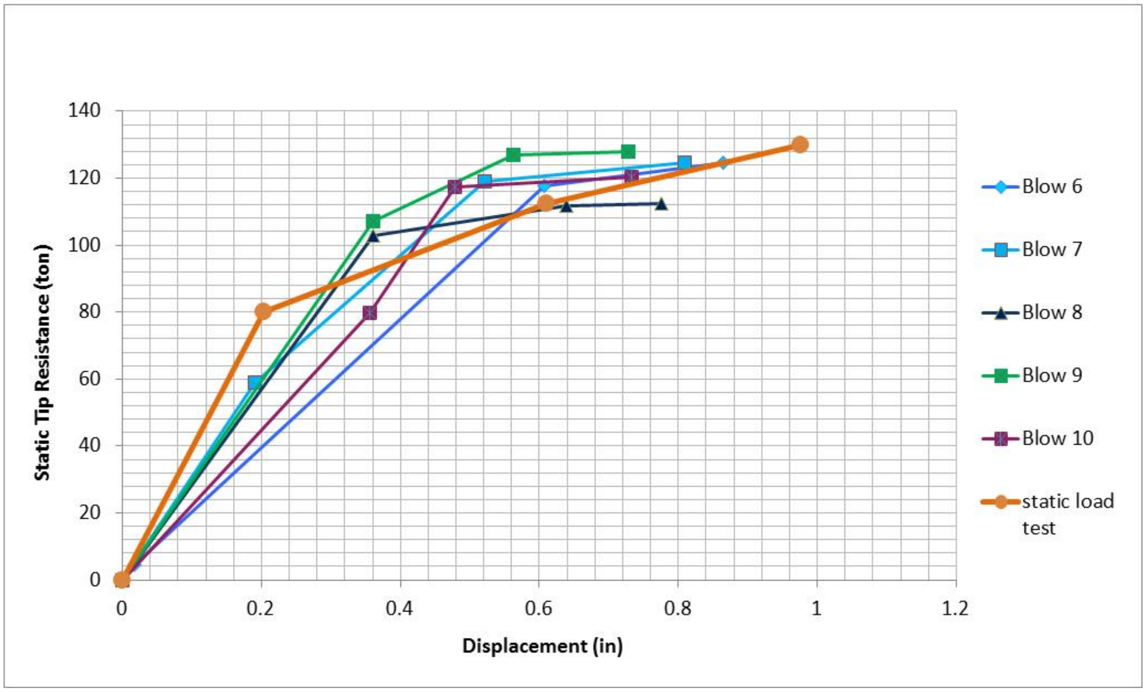

Figure 5-6 Estimated and predicted tip resistance for Pier 8 Pile at BOR

5.3.1 Caminada Bay Bent 1

The first test pile was a 30-in-square precast prestressed concrete pile driven 69 ft (21 m) below the ground surface using a single acting diesel hammer. Restrikes were conducted seven days after installation, and the static compression load test was conducted two days after the restrikes.

Shown in Figure 5-7 is the estimated skin friction using the skin friction model from Chapter 4. SmartPile Review 3.73 reports a value of 480 kips (2135 kN) for BOR which is larger than the load test value, 395 kips (1757 kN) at Ultimate Capacity. Evident from Figure 5-7, the skin friction of the pile has increased by 50% in one week.

Shown in Figure 5-8 is the predicted BOR and measured static tip resistance of the Bent 1 Pile. The predicted tip was computed from the energy tip approach (alternative approach in SmartPile Review), Chapter 4. The unloading point approach in SmartPile Review 3.72 reported a value of 94 kips (440 kN), lower than the Davisson reported load test value of 145 kips (700 kN). Of interest was the small change between the EOID and BOR because the mobilized tip displacement, 0.63 in (16 mm), (Figure 5-8) was sufficient to mobilize the full tip resistance.

5.3.2 Caminada Bay Bent 7

The second test pile was a 30-in-square precast prestressed concrete pile driven 69 ft (21 m) below the ground surface using a single acting diesel hammer. Restrikes were conducted one month after installation, and the static compression load test was conducted two days after the restrikes.

Shown in Figure 5-9 is the estimated skin friction using the skin friction model from Chapter 4. SmartPile Review 3.73 reports a value of 520 kips (2313 kN) for BOR which is slightly smaller

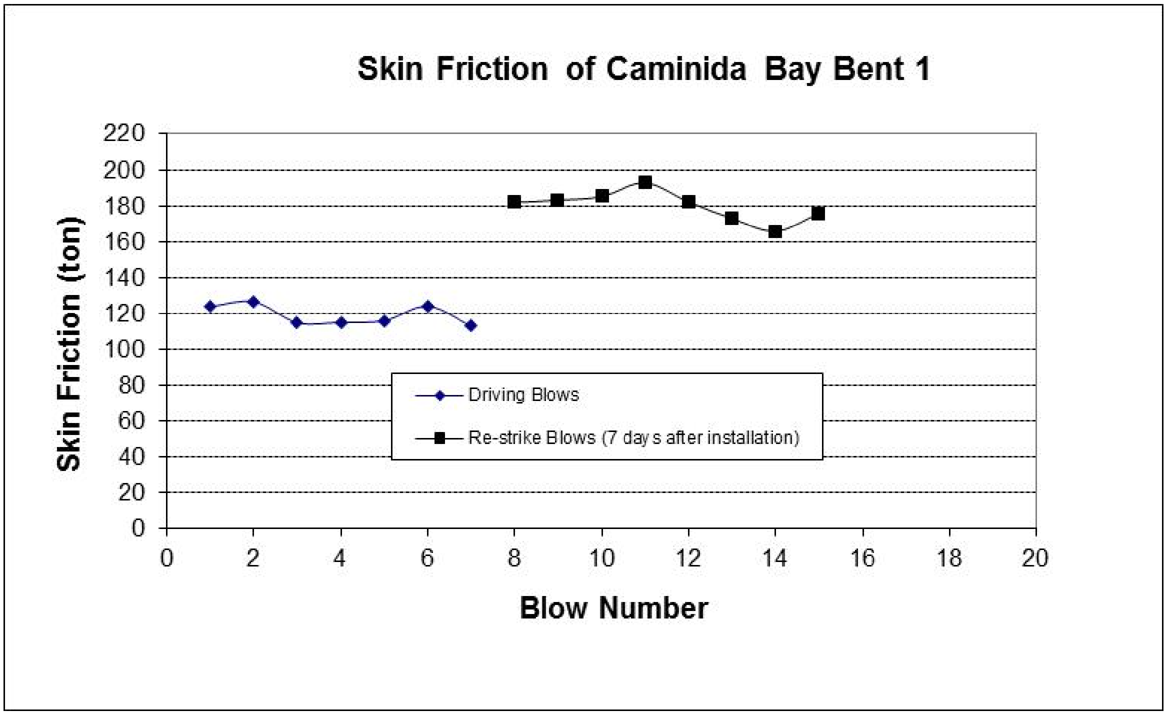

Figure 5-7 Estimated skin friction of Caminada Bay Bent 1 at EOID and BOR

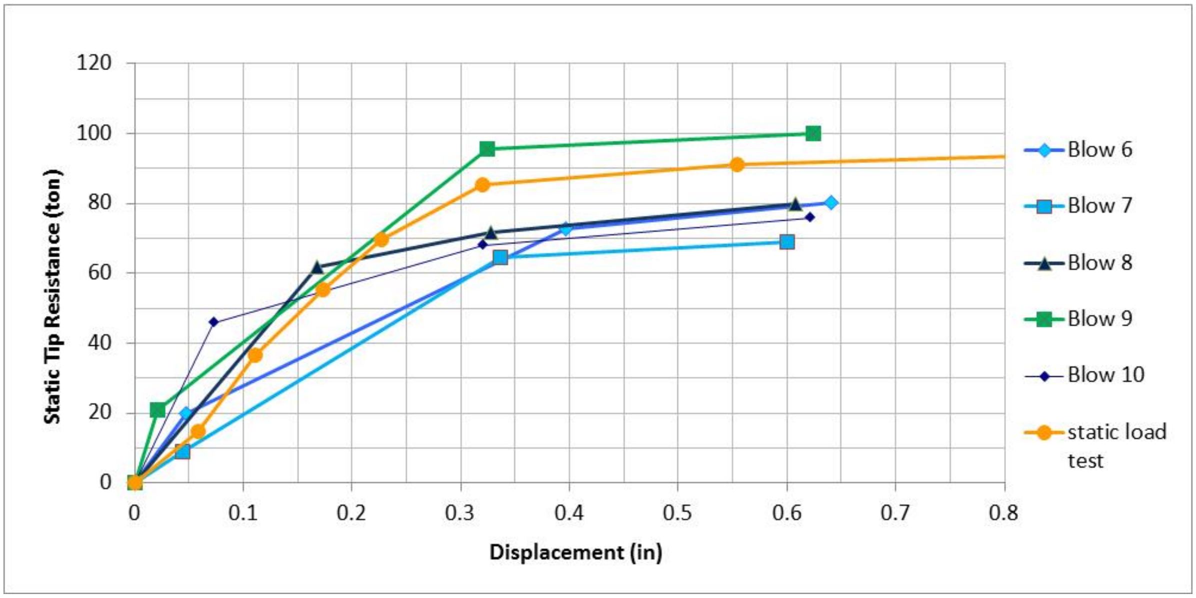

Figure 5-8 Estimated and predicted tip resistance for Caminada Bay Bent 1 Pile at BOR

than the load test value, 545 kips (2424 kN) at Ultimate Capacity. Evident from Figure 5-9, the skin friction of the pile has increased by 25% in one month.

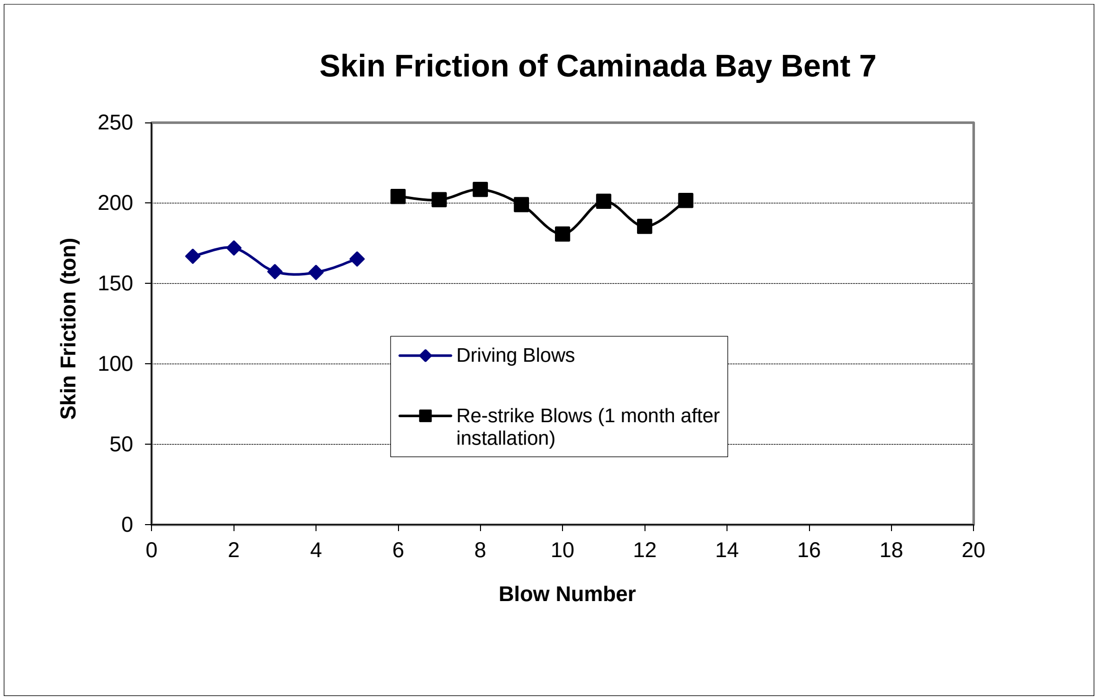

Figure 5-9 Estimated skin friction of Caminada Bay Bent 7 at EOID and BOR

Shown in Figure 5-10 is the predicted BOR and measured static tip resistance of the Bent 7 Pile. The predicted tip was computed from the energy tip approach (alternative approach in SmartPile Review), Chapter 4. The unloading point approach in SmartPile Review 3.72 reported a value of 67 kips (300 kN), slightly lower than the Davisson reported load test value of 80 kips (350 kN). Again, there was little change between the EOID and BOR because the mobilized tip displacement, 1 in (25 mm), (Figure 5-10) was sufficient to mobilize the full tip resistance.

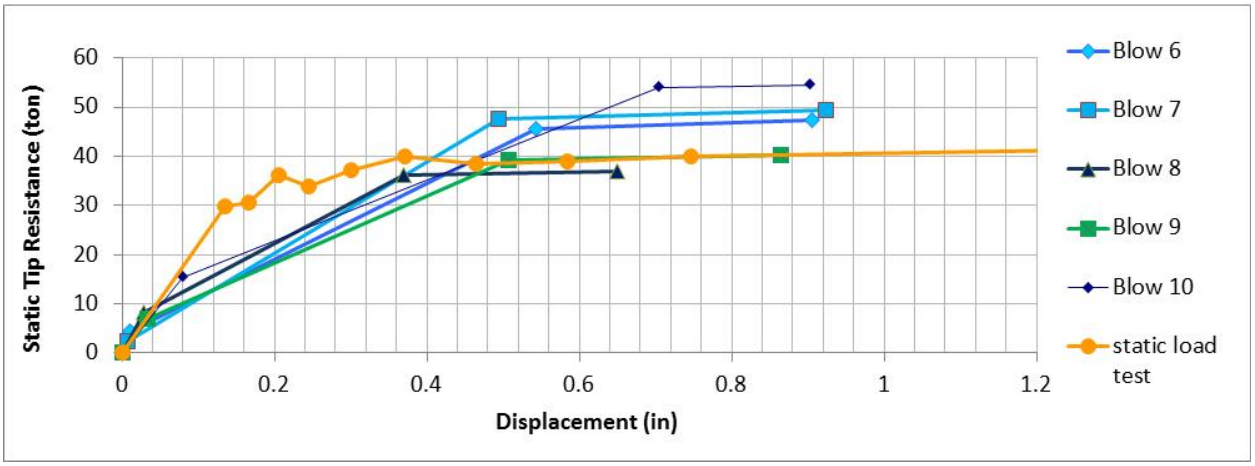

Figure 5-10 Estimated and predicted tip for Caminada Bay Bent 7 Pile at BOR

5.4 Bayou Lacassine, Louisiana Piles

The monitored piles, 30-in-square and 75-ft-long, were driven with an ICE I-62 diesel hammer, into a multiple layered clay deposit with a few silt seams. Bent 1, Pile 3 was driven on 9/18/2012 to a depth of 70.5 ft, and Bent, 1 Pile 1 was driven on 10/04/2012 to a depth of 69.6 ft. Both piles had restrike information recorded (EDC) ten minutes and one day after EOID. Approximately two weeks after each pile was driven, a static top down compression test was performed to failure.

Unfortunately, even though the piles were instrumented with EDC gauges at the top and bottom of pile, they were only monitored at EOID and BOR, i.e., not when the static load test was performed. Therefore, only the total capacity change with time is presented. Shown in Figures 5-11 and 5-12 are CEI (Applied Foundation) and SmartPile Review (ver 3.761) average (five EOID and three BOR) blows from the session reports for Piles 1 and 3. Evident the results are similar, with both piles experiencing pile freeze. The percentage increase in total capacity was higher for pile 1 (80%) vs. pile 3 (33%); however the absolute change (200 kips) are similar for both piles.

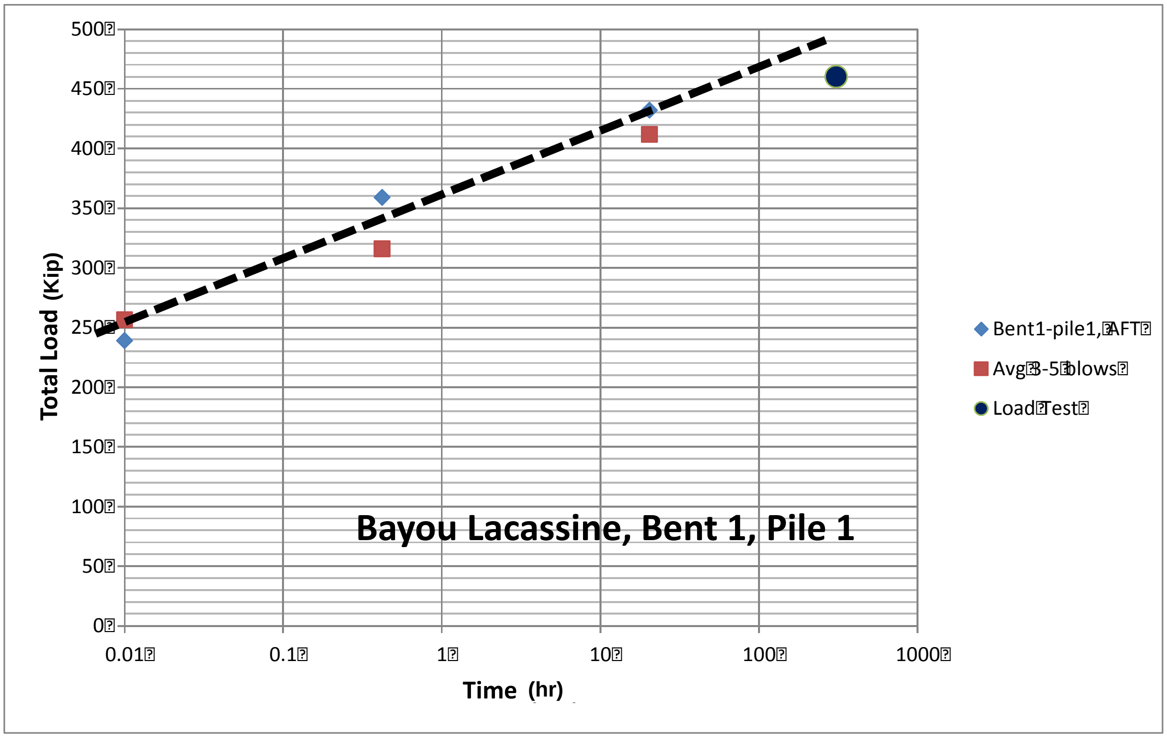

Figure 5-11 Bayou Lacassine Bent 1, Pile 1: SmartPile's total static resistance vs. time and static load test

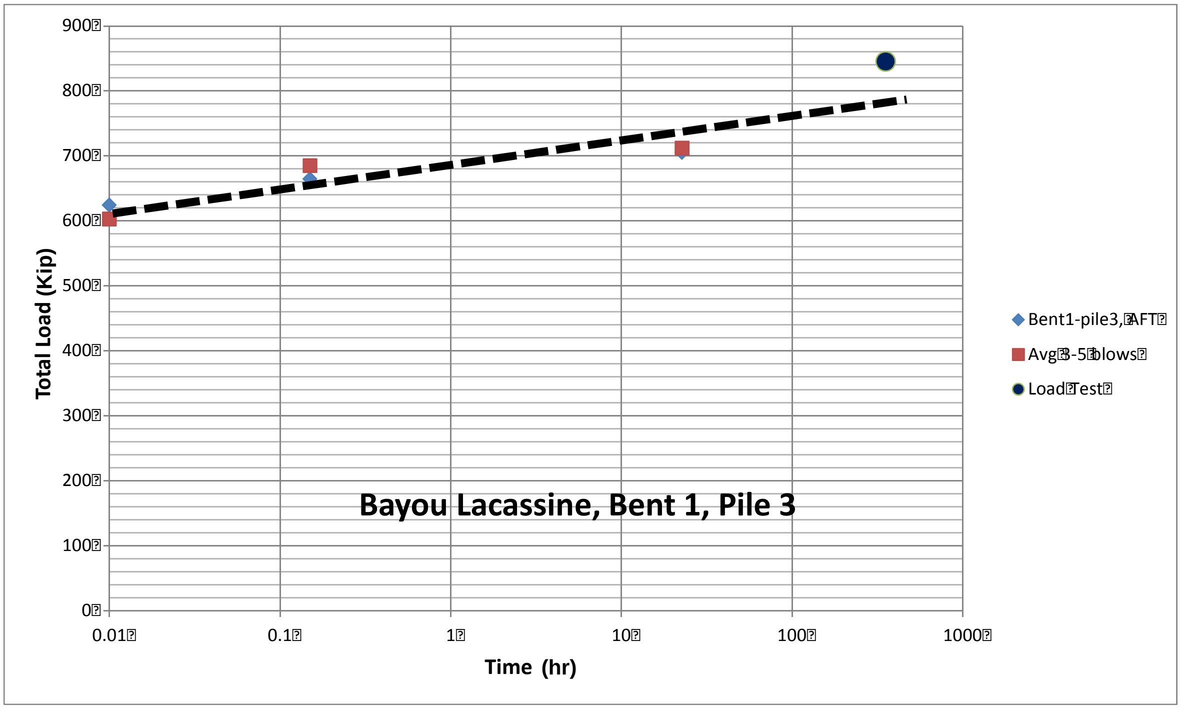

Figure 5-12 Bayou Lacassine Bent 1, Pile 3: SmartPile's total static resistance vs. time and static load test

Also shown in Figures 5-11 and 5-12 are the measured Davisson capacity, plotted 336 hours (two weeks) after EOID. The predicted response (dashed line) was within 8% of the measured static response for both piles. Since the LRFD Φ assessment (Task 2) is for SmartPile predictions, the last recorded BOR predicted capacities, which were one day after EOID, was used to assess Φ in Chapter 6.

5.5 I-95 US 192 Bent 3, Pile 5

The last pile presented for freeze discussion is for US 192, Bent 3, Pile 5, in Florida. This pile had no reported load test information; however the pile was long (24-in-square and 105-ft-long, embedded 100 ft) and driven into sand and weathered rock, with the possibility of skin friction freeze and reduced mobilized tip resistance due to tip displacements.

Shown in Figure 5-13 is the estimated skin friction using the skin friction model from Chapter 4 for EOID (a) and after two days (b). Evident the pile skin friction at end of drive was very small (50 kips) given the length of the pile; however at restrike (two days later), the skin friction was four times larger (200 kips).

In the case of tip resistance, Figure 5-14 shows five EOID blows predicted from the energy tip approach (alternative approach in SmartPile Review), Chapter 4. From the figure, EOID shows 400 kips of tip resistance at tip movement of 0.04 ft (0.48 in or 12mm). Subsequently, after two days the pile was restruck, and Figure 5-15 shows the measured BOR response for five blows. The restrike analysis shows a mobilized tip resistance of only 300 kips but at tip displacement of 0.025 ft (0.3 in or 7.6 mm). A comparison of the mean EOID vs. mean BOR tip resistance is given in Figure 5-16. Evident of from the figure, the EOD and BOR stiffness are quite similar, but the difference in tip resistance is due to the mobilized tip displacements (0.48 in vs. 0.3 in).

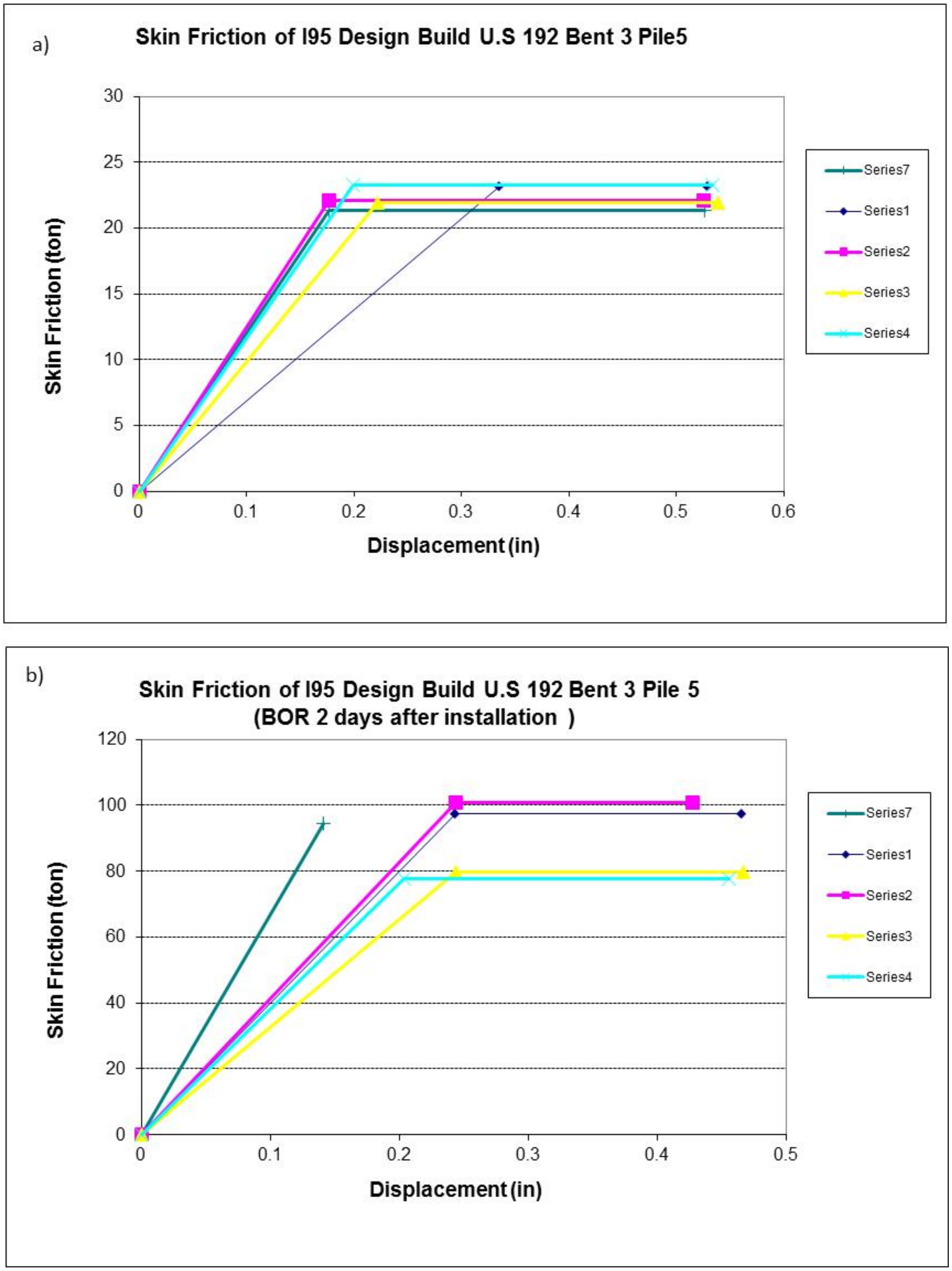

Figure 5-13 I-95 U.S 192 Bent 3, Pile5: a) blows at the end of driving (EOID), and b) blows at the beginning of restrike (BOR)

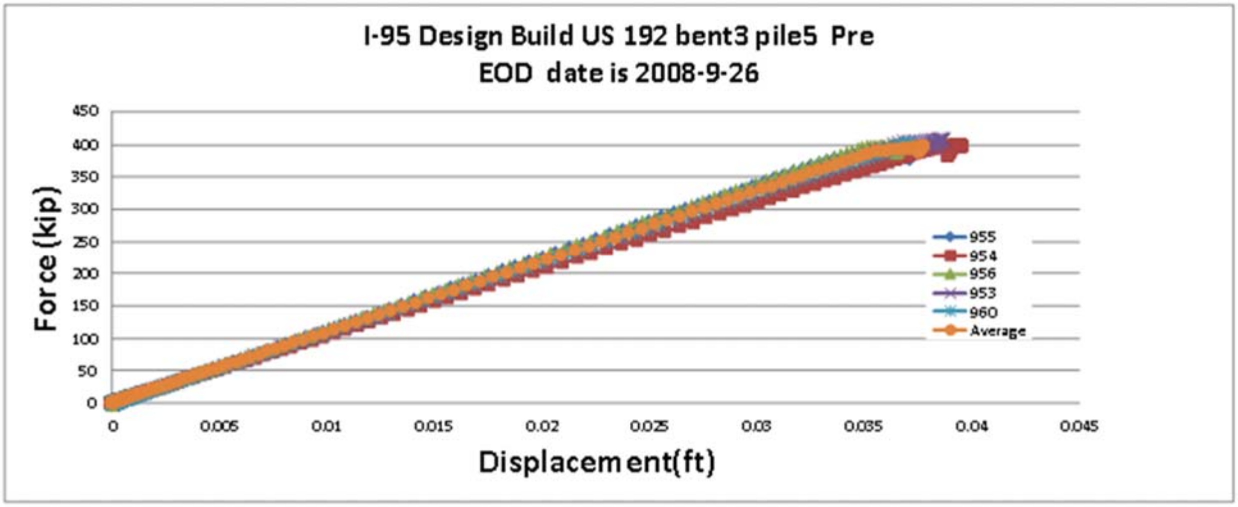

Figure 5-14 I-95 U.S 192 Bent 3, Pile 5: tip resistance at EOID

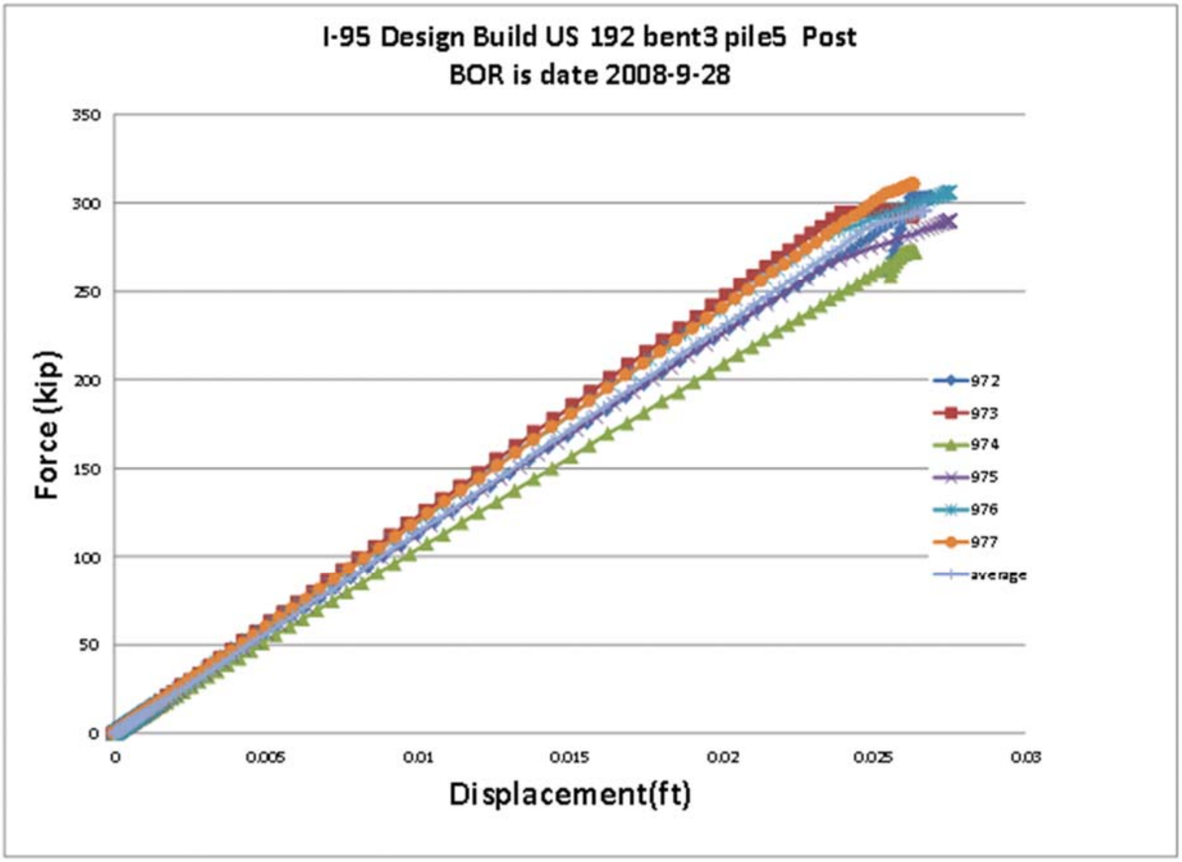

Figure 5-15 I-95 U.S 192 Bent 3, Pile 5: tip resistance at 2 day BOR

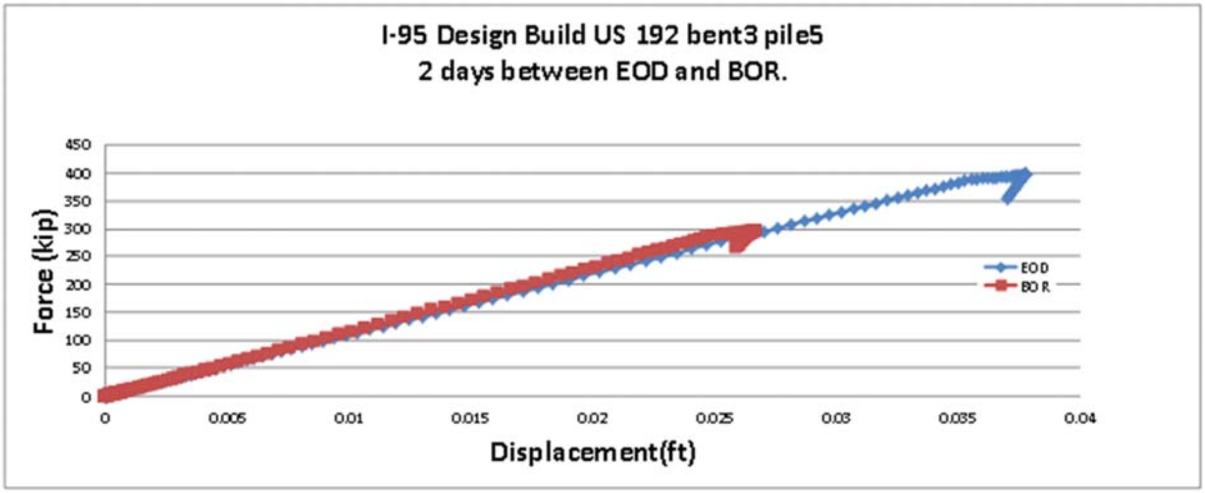

Figure 5-16 I-95 U.S 192 Bent 3, Pile 5: tip resistance at EOID vs. BOR

If pile capacity was assessed as suggested by NCHRP 418, the pile would have total capacity of 600 kips, i.e., 400 kips tip (EOID) plus 200 kips (BOR) skin, vs. 500 kips (skin: 200 kips BOR + tip: 300kips BOR). This represents a 20% increase in estimated pile capacity, attributed to changes in mobilized tip resistances due to pile tip displacements during driving (i.e., EOID vs. BOR). Clearly, there is interest in estimating separately the skin and tip resistance of a pile. Chapter 6 presents the EDC assessment of LRFD resistance factors for total, tip and skin separately of one another.

CHAPTER 6
LRFD RESISTANCE FACTORS FOR EDC MONITORED PILES

6.1 Introduction

For implementation of any new technology, LRFD resistance factors should be determined specifically for the methods used to assess pile capacity. Such assessments may be performed on total pile capacity (NCHRP 507) or individual resistances (skin and tip resistance) as well. For instance, uplift piles are designed only for skin friction and consider no tip resistance. Generally, for any LRFD resistance valuation, 20 to 30 high quality static resistances (e.g., total, skin or tip) measured from pile load testing: top down compression testing, static uplift or bottom-up Osterberg Testing in various soil/rock conditions are required.

For this work, a total of 12 static pile test results were collected along with EDC, PDA and CAPWAP results. For the 12 piles, a total of 17 independent measurements (i.e., total, skin, and tip capacities) were recorded. Note, independent values were identified as total and tip capacities for top down tests, and skin friction for uplift tests. Given the number of piles, and independent measurements, it was decided to assess only one LRFD Φ for combined total, tip and skin (uplift) for EDC SmartPile Review. Since only 17 values were recorded (not 20 to 30), a discussion of LRFD Φ ranges is also included.

6.2 Assessment and Discussion of LRFD Resistance Factors

Shown in Table 6-1 is all of the collected data to date. The database consists of 12 piles (8-Florida, and 4-Louisiana), eight are top down compression and four are uplift or tension piles. A plot of measured and predicted (EDC/SmartPile) skin, tip and total resistance from Table 6-1 is shown in Figure 6-1. Note, the EDC/SmartPile vs. Measured include both skin and tip resistance. Since, the current version of SmartPile software independently computes only tip and total capacity (skin is the difference), skin friction data should be removed with the exception of

5th Street Bascule Bridge. In the latter case, the load tests are uplift, i.e., skin friction; since no tip or static top down data is compared, then measured and predicted (Total – Tip) skin friction, i.e., uplift, may be compared since there is no duplication of predictions.

Table 6-1 Collected measured and predicted (SmartPile and CAPWAP) pile response

	MEASURED			**PREDICTED**			**PREDICTEC**		
Site & Pile	Davisson Capacity	Tip Capacity	Skin Resistance	SmartPile Total Capacity	SmartPile Tip Capacity	SmartPile Skin Resistance	CAPWAP Davisson	CAPWAP Tip Cap	CAPWAP Skin Cap
	(Kip)	(Kip)	(Kip)	(Kip)	(Kip)	(Kip)	(Kip)	(Kip)	(Kip)
Dixie Highway End Bent 1	430	296	134	448	349	99	420	315	105
Dixie Highway Pier 8	380	200	180	470	250	220	430	144	286
Caminida Bay Bent 1, LADOT	540	144.8	395.2	574	94	480	600	194	406
Caminida Bay Bent 7 LADOT	625	80	545	587	67	520	540	143	397
Bayou Lacassine LADOT, Bent 1 Pile 1	460			432					
Bayou Lacassine LADOT, Bent 1 Pile 3	845			712					
I-95 Jax	380	200	180	369	263	106	356	137	219
Dixie Highway Pier 4			212			171			290
5th St Bascule Pier 2 Pile 37			185			220			198
5th St Bascule Pier 2 Pile 53			180			200			235
5th St Bascule Pier 3 Pile 9			68			150			135
5th St Bascule Pier 3 Pile 42			153			215			270

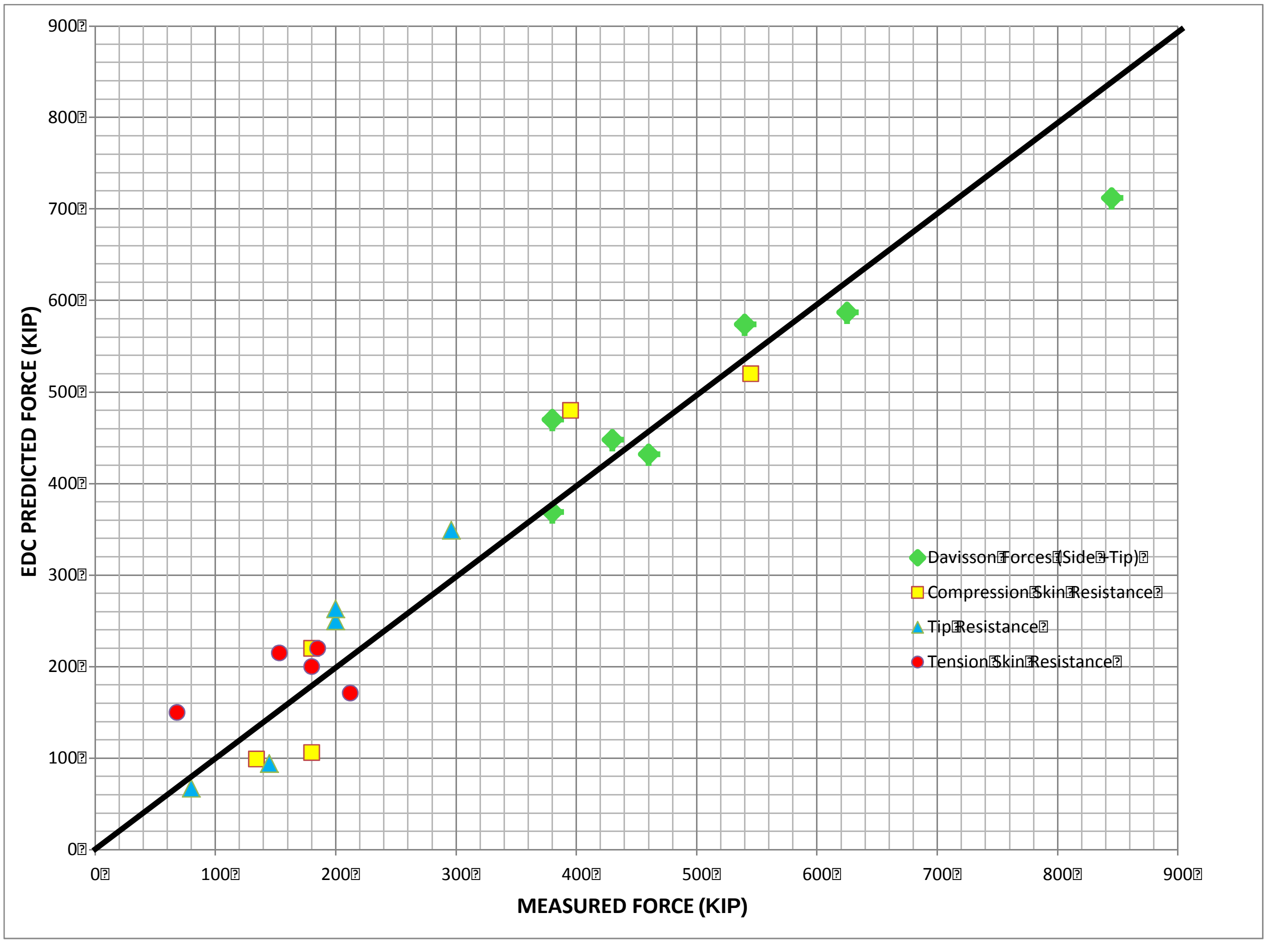

Figure 6-1 EDC/SmartPile vs. measured skin, tip and Davisson total resistance

A total of 17 values are compared in Figure 6-2, representing **independent** SmartPile predictions. For this data set, the bias or λ (ratio of measured/predicted) was 0.96, and standard deviation, σ, was 0.248, and their ratio, the coefficient of variation, CV_R, was 0.258. Using Eq. 6-1 (AASHTO, 2012), with the λ and CV_R, Φ was determined to be 0.65, for a reliability, β, of 2.33.

Note, in Equation 6-1, the LRFD Φ equation by FHWA (2001), the representation for CV_Q presented by Styler (2006) was used. The CV_Q can be represented in terms of its dead and live load CV components as shown in Equation 6-2. Also, in FHWA's Eq. 6-1, $\lambda_R = \lambda$, i.e., the bias that was presented.

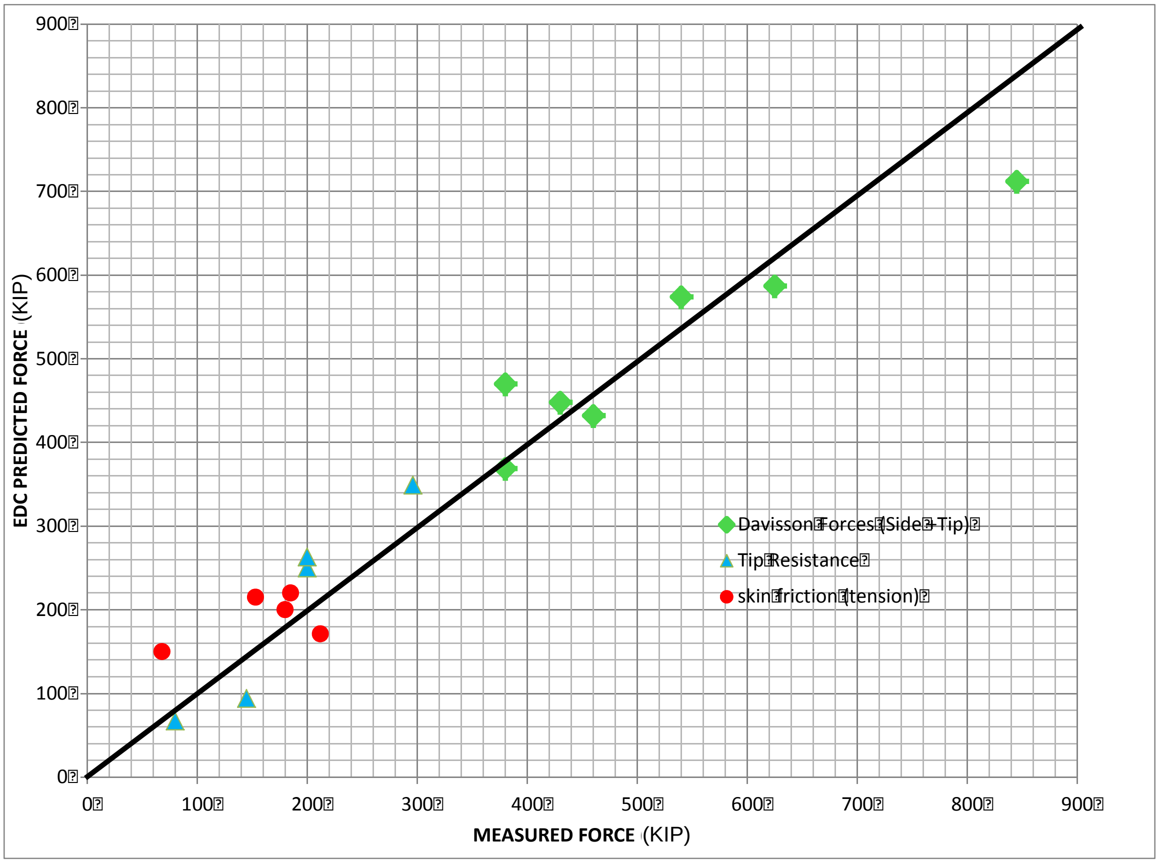

Figure 6-2 EDC/SmartPile vs. measured skin-uplift, tip and Davisson total resistance

$$\Phi = \frac{\lambda_R \cdot \left(\gamma_D \cdot \frac{q_D}{q_L} + \gamma_L\right) \cdot \sqrt{\frac{\left(1 + CV_Q^2\right)}{\left(1 + CV_R^2\right)}}}{\left(\lambda_D \cdot \frac{q_D}{q_L} + \lambda_L\right) \cdot e^{\sqrt{\ln\left[\left(1+CV_R^2\right)\left(1+CV_Q^2\right)\right]}}} \qquad \text{Eq. 6-1}$$

$$CV_Q^2 = \frac{\left(\frac{q_D}{q_L}\lambda_D CV_D\right)^2 + \left(\lambda_L CV_L\right)^2}{\left(\frac{q_D}{q_L}\lambda_D\right)^2 + 2\frac{q_D}{q_L}\lambda_D\lambda_L + {\lambda_L}^2} \qquad \text{Eq. 6-2}$$

where the parameters besides λ_R, CV_R and β are selected according to the AASHTO (2012) recommendation for load cases, I, II, and IV: dead to live load ratio $q_D/q_L = 2$, dead load factor γ_D 1.25, live load factor $\gamma_L = 1.75$, dead load bias factor $\lambda_D = 1.08$, live load bias factor $\lambda_L = 1.15$, dead load coefficient of variation $CV_D = 0.128$, and live load coefficient of variation $CV_L = 0.18$.

The latter compares favorably with NCHRP 507-Table 20, Figure 6-3 (below) showing, $\Phi = 0.65$ for CAPWAP for BOR blows, with $\beta = 2.33$. The latter was adopted by AASHTO and FDOT for high strain rate dynamic pile monitoring.

Also shown in Figure 6-3 is Φ/λ ratio of 0.56. The latter is obtained from the LRFD design equation,

$$R_{design} = \Phi\ R_N \qquad \text{Eq. 6-3}$$

where R_N is the predicted CAPWAP capacity. Solving for R_N from the bias, $\lambda = R_{measured}/R_N$ and substituting it into Eq. 6-3, gives

$$R_{design} = (\Phi/\lambda)\ R_{measured} \qquad \text{Eq. 6-4}$$

which represents the % of measured response (e.g., load test) that may be used for design. SmartPile EDC has a Φ/λ ratio of 0.67 (i.e., 0.65/0.96) or 67% of measured (static load test) is available for design vs. 57% for CAPWAP.

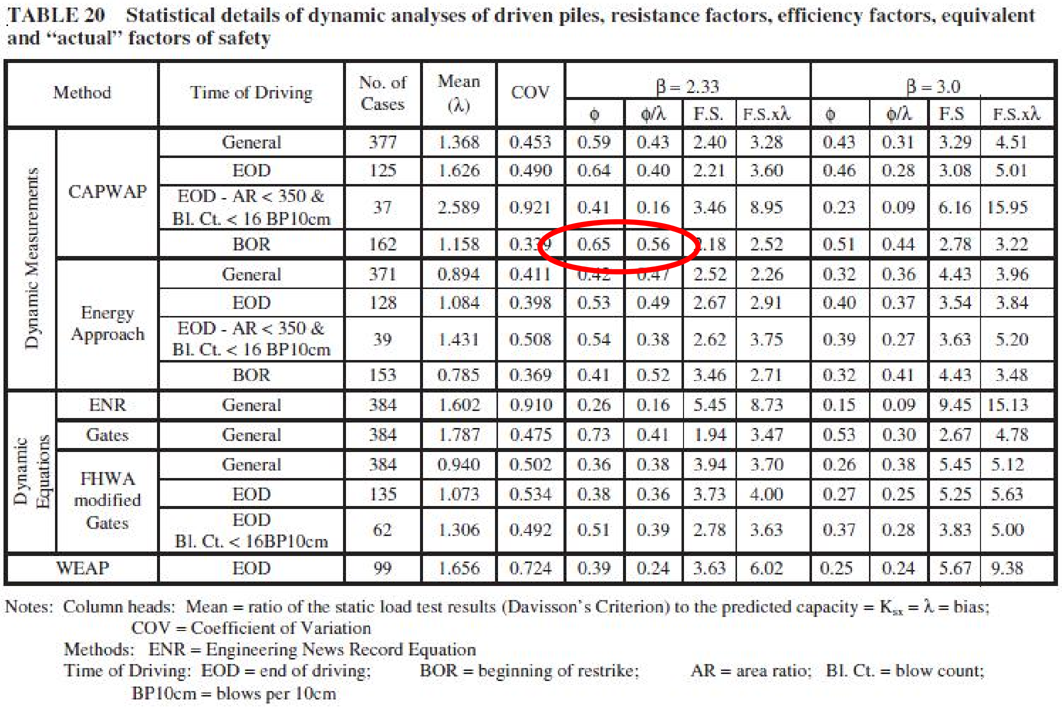

TABLE 20 Statistical details of dynamic analyses of driven piles, resistance factors, efficiency factors, equivalent and "actual" factors of safety

Method		Time of Driving	No. of Cases	Mean (λ)	COV	β = 2.33				β = 3.0			
						φ	φ/λ	F.S.	F.S.xλ	φ	φ/λ	F.S	F.S.xλ
Dynamic Measurements	CAPWAP	General	377	1.368	0.453	0.59	0.43	2.40	3.28	0.43	0.31	3.29	4.51
		EOD	125	1.626	0.490	0.64	0.40	2.21	3.60	0.46	0.28	3.08	5.01
		EOD - AR < 350 & Bl. Ct. < 16 BP10cm	37	2.589	0.921	0.41	0.16	3.46	8.95	0.23	0.09	6.16	15.95
		BOR	162	1.158	0.339	0.65	0.56	.18	2.52	0.51	0.44	2.78	3.22
	Energy Approach	General	371	0.894	0.411	0.42	0.47	2.52	2.26	0.32	0.36	4.43	3.96
		EOD	128	1.084	0.398	0.53	0.49	2.67	2.91	0.40	0.37	3.54	3.84
		EOD - AR < 350 & Bl. Ct. < 16 BP10cm	39	1.431	0.508	0.54	0.38	2.62	3.75	0.39	0.27	3.63	5.20
		BOR	153	0.785	0.369	0.41	0.52	3.46	2.71	0.32	0.41	4.43	3.48
Dynamic Equations	ENR	General	384	1.602	0.910	0.26	0.16	5.45	8.73	0.15	0.09	9.45	15.13
	Gates	General	384	1.787	0.475	0.73	0.41	1.94	3.47	0.53	0.30	2.67	4.78
	FHWA modified Gates	General	384	0.940	0.502	0.36	0.38	3.94	3.70	0.26	0.38	5.45	5.12
		EOD	135	1.073	0.534	0.38	0.36	3.73	4.00	0.27	0.25	5.25	5.63
		EOD Bl. Ct. < 16BP10cm	62	1.306	0.492	0.51	0.39	2.78	3.63	0.37	0.28	3.83	5.00
WEAP		EOD	99	1.656	0.724	0.39	0.24	3.63	6.02	0.25	0.24	5.67	9.38

Notes: Column heads: Mean = ratio of the static load test results (Davisson's Criterion) to the predicted capacity = K_{sx} = λ = bias;
COV = Coefficient of Variation
Methods: ENR = Engineering News Record Equation
Time of Driving: EOD = end of driving; BOR = beginning of restrike; AR = area ratio; Bl. Ct. = blow count;
BP10cm = blows per 10cm

Figure 6-3 NCHRP 507 LRFD resistance factors for dynamic measurements

For additional comparison with SmartPile's EDC, CAPWAP's reported predictions (Table 6-1) for the same piles are shown in Figure 6-4. Fifteen predictions [Bayou Lacassine – results were not available] are shown. Evident, total predictions are closer to the 45° line, i.e., predicted similar to measured; however a greater difference is observed when predicting skin or tip resistance. This observation agrees with results given by Alvarez et al. [Dynamic Pile Analysis Using CAPWAP and Multiple Sensors], who showed that the skin and tip resistance changed from 20 to 31% with the use of tip sensors. The data in Figure 6-3 (skin, tip and total CAPWAP) has a bias, λ, of 0.91, $CV_R = 0.311$, and LRFD $\Phi = 0.54$ for $\beta=2.33$. Note, the Φ is lower than the NCHRP 507 value (0.65) due to the larger variability with the inclusion of skin and tip resistance.

Finally, the question exists if sufficient measured and predicted SmartPile EDC data has been collected to use $\Phi = 0.65$ [bias, $\lambda= 0.96$, $\sigma = 0.248$, $CV_R = 0.258$] as suggested from Figure 6-2. Impacting the LRFD Φ is both the bias, λ, and CV_R (or σ, i.e., $CV_R = \sigma/\lambda$) uncertainty. For independent data, the variance of mean (i.e., bias) is given by σ^2/N where N total number of data samples (i.e., 17). Therefore the expected range of the bias is between $\lambda - \sigma/\sqrt{N}$ and $\lambda + \sigma/\sqrt{N}$ or $0.9 < \lambda < 1.02$. Similarly, the variance of the variance is given by $\frac{\boldsymbol{2\sigma^4}}{\boldsymbol{N-1}}$. Consequently, the expected range in standard deviation is given as $\sigma \pm \frac{\sqrt{2}\sigma^2}{\sqrt{N-1}}$ or $0.24 < \sigma < 0.27$. Using the minimum bias (0.9) and standard deviation (0.24), $\Phi = 0.59$; in the case of the maximum bias (1.02) and standard deviation (0.27), $\Phi = 0.68$. Evident the difference between two cases is not significant (<15%). Note, however these cases do not necessarily represent the worse and best LRFD Φ values. The worst case has $\Phi = 0.55$ [$\lambda=0.9$, $\sigma=0.27$] and best case, $\Phi = 0.73$ [$\lambda=1.02$, $\sigma=0.24$], i.e., opposite combination of limits. It should be noted that a bias of 0.9 is not expected, since a comparison of 140 piles (Chapter 4) showed ratio of EDC/CAPWAP near one, and Figure 6-3 shows a bias of 1.15 between measured and CAPWAP.

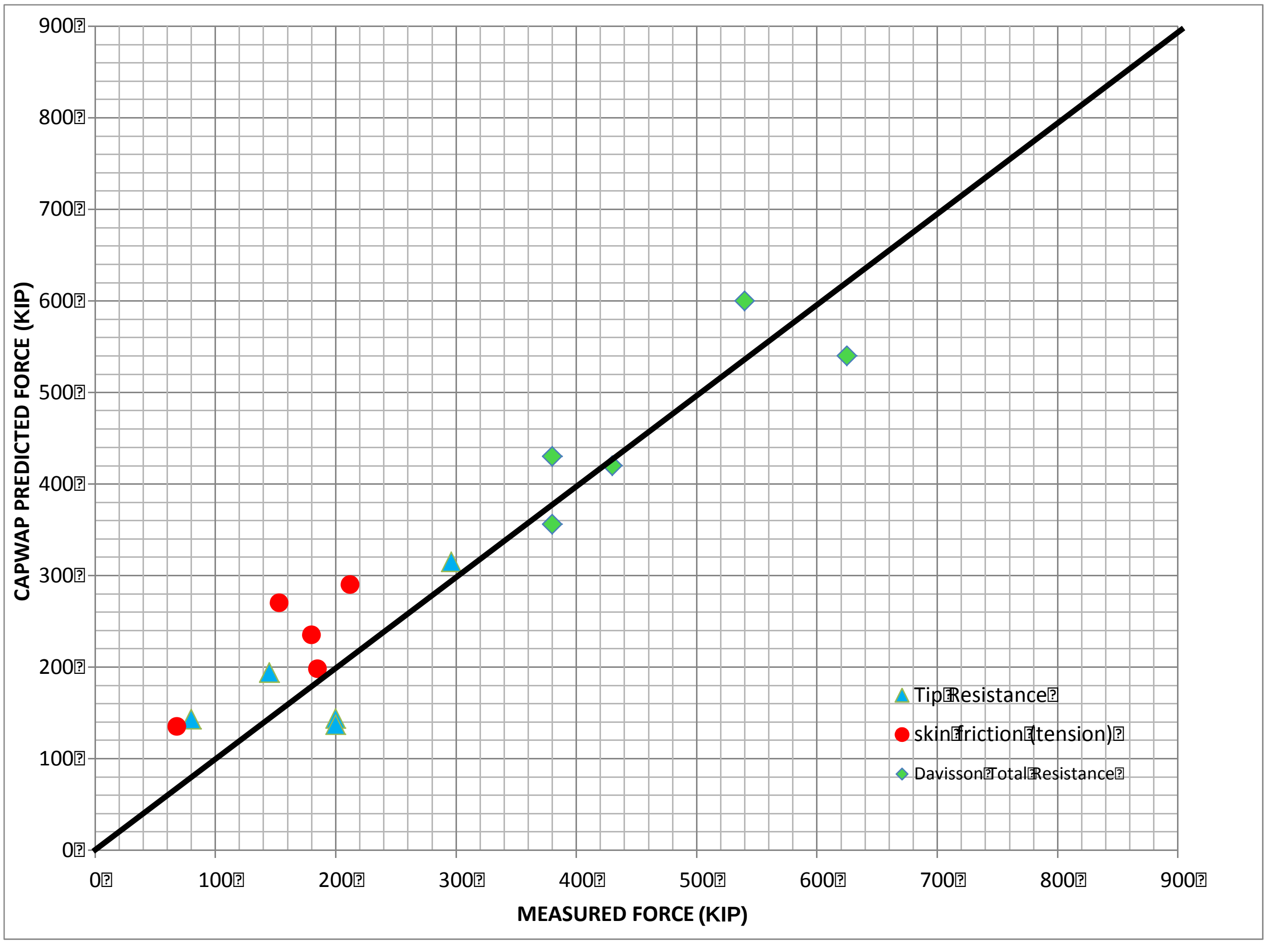

Figure 6-4 CAPWAP vs. measured skin-uplift, tip and Davisson total resistance

Of greater significance is increasing the size of the database (e.g., 17 to 30) which would reduce the uncertainty in the mean, $\sigma/\sqrt{N}$, and the standard deviation, $\pm\frac{\sqrt{2}\sigma^2}{\sqrt{N-1}}$ by 25%. However, since it is not known if Smart Structures or any DOTs have load tests planned with EDC, the computed LRFD λ, CV_R, and Φ are considered best estimates at this time.

CHAPTER 7
SUMMARY, CONCLUSIONS, AND RECOMMENDATIONS

7.1 Background

Monitoring the installation of driven pile foundations is of critical importance for ensuring adequate safety of pile-supported structures (e.g., bridges). Dynamic load testing of driven test piles is currently the preferred alternative used by industry on the grounds that it is a cost effective and a reliable method for assessing total capacity. EDC is a new system developed to monitor piles during driving that employs pile top and tip instrumentation that provides direct measurements of stresses and motions at both the top and bottom of the pile. Using both sets of gauges, the EDC software assess stresses (top and bottom), total pile capacity, as well as end bearing and skin friction "real time" for every blow of the hammer.

In an effort to evaluate the effectiveness of the EDC system the FDOT engaged in an evaluation program (Phase I) of comparison with *dynamic load testing methods* and wave matching software (i.e., CAPWAP), which is used by industry. Phase I yielded promising results, prompting the Central Office's Geotechnical team to pursue the implementation of EDC as well as evaluating its reliability by comparing the recorded results with static load tests, i.e., Phase II. To adopt the EDC technology as an alternate to current pile driving monitoring practice, the FDOT requires LRFD resistance factors for the technology which should be established from a sufficiently large database of instrumented *static load test* results. This report details the effort to collect the static load tests, along with EDC and CAPWAP data for developing resistance factors for LRFD design. Since the EDC gauges are located at both the top and bottom of the pile, most load tests identified skin friction and end bearing capacity. In all, 17 tests are reported on, five of which have only skin friction capacity reported. With these capacities, the bias, λ, and CV of resistance are reported for the EDC method. This is followed by LRFD Φ for skin friction, end bearing and total static capacity.

7.2 Summary of Comparisons of EDC to PDA and CAPWAP Results

For the dynamic load testing comparisons, a total of 139 instrumented piles including EDC, PDA, and CAPWAP at EOID, and BOR were considered. The monitored piles were located in all FDOT districts, as well as the Florida Turnpike. A total of 213,000 hammer blows were monitored and evaluated. Five progressive versions of SmartPile Review software was analyzed (3.6, 3.72, 3.73, 3.76 and 3.76.1) with the following observations/summaries

- Fixed method EDC/PDA ratio was consistent (0.89 to 0.97) for all version numbers, with little variability (max CV = 0.17);
- UF method EDC/PDA ratio was slightly unconservative (1.12) for earlier versions (3.6), but conservative (0.89 to 0.93) for later releases, with little variability (max CV = 0.18);
- Top pile compressive stresses, CSX (EDC/PDA), were consistent (0.91 to 0.93) for all versions, with little variability (max CV = 0.09);
- Bottom pile compressive stresses, CSB (EDC/PDA), ranged from 0.77 for earlier version (3.6), but quickly stabilized at 0.74 for all subsequent versions (3.72-3.761), with maximum variability (CV = 0.25);
- Pile tension stress, TSX (EDC/PDA), was slightly unconservative (1.2) for earlier versions (3.6), but was conservative (0.87 to 0.90) for all later releases, with max variability (CV = 0.29);
- UF EDC/CAPWAP total capacity ratio varied from 1.0 (ver 3.6) to 0.89 (ver 3.761), with $R^2 = 0.89$;
- UF EDC/CAPWAP skin friction ratio varied from 0.78 to 1.04, with $R^2 = 0.57$;
- UF EDC/CAPWAP tip resistance ratio varied from 0.85 to 0.93, with $R^2 = 0.76$.

7.3 Summary of Estimates of Pile Skin Friction and Tip Resistance with EDC Measurements

New solution strategies are presented for estimating skin friction and tip resistance in “real time” from hammer blow information (strain and velocity) measured at the top and bottom of the pile. For skin friction, the strategy involves a solution of the 1-D wave propagation problem for skin friction and damping subject to known initial and boundary conditions. Methods for both linear and non-linear skin friction, developed from the solution strategy, are presented. For tip resistance, the strategy uses a nonlinear single degree of freedom to characterize the bottom 1D section of pile (below the gauges) and soil. A significant improvement over current practice is each strategy provides unique solutions in estimating skin friction and tip resistance capacity.

Each solution strategy was used on four driven piles which had the EDC system installed and which conventional static load tests were performed. Significant observations for each follow:

- For the four piles investigated under the soil conditions encountered (sand, silts and clays), the homogeneous or average material property approach was shown to give reasonable comparisons between the measured and estimated skin frictions.
- Each of the four piles was divided into four to five segments with eight to ten unknowns. The genetic global optimization converged within 50 iterations, requiring approximately one minute on a PC desktop computer with a 3.4 GHz CPU. For the four piles investigated under the soil conditions encountered (sand, silts and clays), the approach was shown to give consistent and reasonable comparisons between the estimated and measured skin frictions (less than 20 % difference).
- For tip resistance, the strategy involves dividing the response into three loading and one unloading segments where the static tip stiffness is assumed constant. Within any segment, if the velocity and acceleration is zero, then the static force (i.e., stiffness) is known (equal to total tip force). In addition, due to the dynamic nature of the pile (i.e., positive and negative inertia forces), after approximately half the trace, inertia energy is negligible and damping energy (function of c value) plus static energy (function of stiffness, k) must balance the applied tip energy. The solution (force and energy) may be

done with an Excel spreadsheet within a few minutes or with the genetic algorithm in about five seconds on a 3.4 GHz CPU computer.

- For tip resistance, the solution strategy was used on each of the four piles, which conventional static load tests were performed. The piles varied in width, length, and embedded soil types (sands to silty-sands, tipped in clay and limestone). Analyses were performed both at EOID and BOR after various times (one week up to a month). Good comparisons between the estimated static tip force vs. displacement and the measured response from load tests were found.

7.4 Summary of Observed and Estimated Pile Freeze

Pile freeze has been shown to significantly increase pile capacity (Chow et al. (1998), McVay et al. (1999), Axelsson (2000), Bullock et al. (2005), and Kuo et al. (2007)). NCHRP Synthesis Report 418 (2011), suggests that total pile capacity be assessed from dynamic pile monitoring at both EOID and BOR. In the case of EOID, the full tip resistance is assumed to be mobilized, but the skin friction may be under predicted due to loss of lateral effective stress during driving. Nevertheless, after days, during initial restrike blows (i.e., BOR) the pile may exhibit full pile skin friction due to excess pore pressure dissipation. Of concern in the report (NCHRP 418) is that the total pile capacity at BOR may not be fully mobilized, i.e., full skin but only portion of the tip resistance due to limited movement of pile tip. Consequently, there is a great interest in predicting both skin friction and tip resistance at both EOID and BOR, as well as quantifying their level of accuracy. Also of interest is identification of the level of mobilized tip movement (vs. resistance) at EOID vs. BOR.

To address this, the skin friction and end bearing at EOID and BOR for seven piles was predicted with the improved methods presented in Chapter 4. There was load test information from six of the piles and four had their EDC monitored during the test. The estimates of skin and tip capacities were in good agreement with the observed test results. For two piles where their EDC was not monitored during the load test, the estimated total load was in good agreement with the observed test result. Estimates of skin friction showed increases of 30% three days after EOID, 75% one week after EOID, 75% four days after EOID, 50% one week after EOID, 25% one month after EOID, and 400% two days after EOID. Estimates of tip resistance were computed based on an energy approach and compared with that from the load tests. With the exception of one pile, there was little to no change of the resistance with time. However, one pile showed a decrease in tip resistance between EOID and BOR. This was attributed to the amount of tip displacement mobilized by the hammer. In the case of BOR only 4 mm (0.16 in) of tip movement occurred, whereas in the case of EOID, 9 mm (0.35 in) of movement occurred. The latter agrees with NCHRP 418 discussion of mobilized skin and tip resistance.

7.5 Summary of LRFD Resistance Factors for Piles with EDC

Shown in Table 7-1 is the all of the collected data to date. The database consists of 12 piles (8-Florida, and 4-Louisiana), eight are top down compression and four are uplift or tension piles. For the 12 piles, a total of 17 independent measurements (i.e., total, skin, and tip capacities) were recorded. Note, independent values were identified as total and tip capacities for top down tests, and skin friction for uplift tests. Given the number of piles, and independent measurements, it was decided to assess only one LRFD Φ for combined total, tip and skin (uplift) for EDC SmartPile Review.

A total of 17 values are compared in Figure 7-1, representing independent SmartPile predictions. For this data set, the bias or λ (ratio of measured/predicted) was 0.96, and standard deviation, σ, was 0.248, and their ratio, the coefficient of variation, CV_R, was 0.258. Using

AASHTO’s recommended equation for LRFD Φ, 0.65 was determined for a reliability, β, of 2.33.

Table 7-1 Collected measured and predicted (SmartPile and CAPWAP) pile response

	MEASURED			PREDICTED			PREDICTEC		
Site & Pile	Davisson Capacity	Tip Capacity	Skin Resistance	SmartPile Total Capacity	SmartPile Tip Capacity	SmartPile Skin Resistance	CAPWAP Davisson	CAPWAP Tip Cap	CAPWAP Skin Cap
	(Kip)	(Kip)	(Kip)	(Kip)	(Kip)	(Kip)	(Kip)	(Kip)	(Kip)
Dixie Highway End Bent 1	430	296	134	448	349	99	420	315	105
Dixie Highway Pier 8	380	200	180	470	250	220	430	144	286
Caminida Bay Bent 1, LADOT	540	144.8	395.2	574	94	480	600	194	406
Caminida Bay Bent 7 LADOT	625	80	545	587	67	520	540	143	397
Bayou Lacassine LADOT, Bent 1 Pile 1	460			432					
Bayou Lacassine LADOT, Bent 1 Pile 3	845			712					
I-95 Jax	380	200	180	369	263	106	356	137	219
Dixie Highway Pier 4			212			171			290
5th St Bascule Pier 2 Pile 37			185			220			198
5th St Bascule Pier 2 Pile 53			180			200			235
5th St Bascule Pier 3 Pile 9			68			150			135
5th St Bascule Pier 3 Pile 42			153			215			270

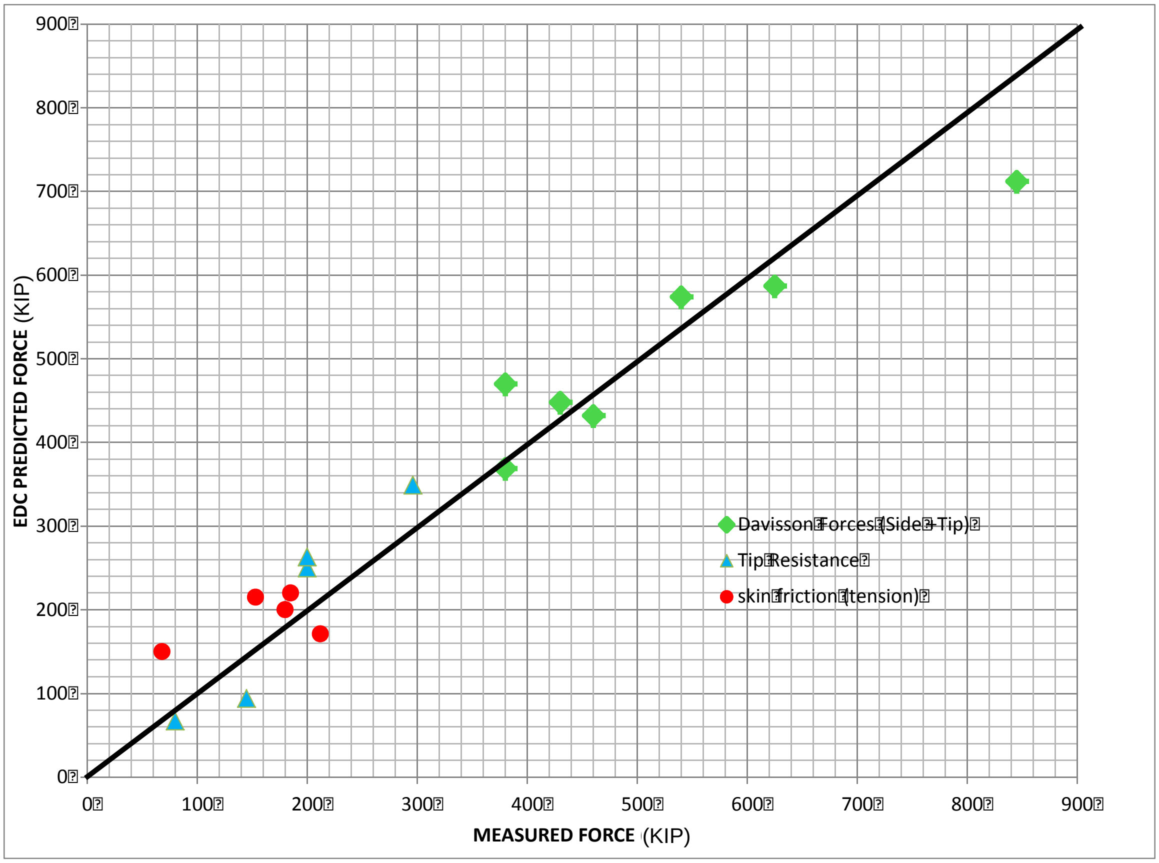

Figure 7-1 EDC/SmartPile vs. measured skin-uplift, tip and Davisson total resistance

The latter compares favorably with NCHRP 507-Table 20, which shows $\Phi = 0.65$ for CAPWAP for BOR blows, with $\beta = 2.33$. The latter was adopted by AASHTO and FDOT for high strain rate dynamic pile monitoring.

Furthermore, NCHRP 507-Table 20 shows Φ/λ ratio of 0.56. The latter is obtained from the LRFD design equation

$$R_{design} = \Phi \, R_N \qquad \text{Eq. 7-1}$$

where R_N is the predicted CAPWAP capacity. Solving for R_N from the bias, $\lambda = R_{measured}/R_N$ and substituting it into Eq. 7-1, gives

$$R_{design} = (\Phi/\lambda) \, R_{measured} \qquad \text{Eq. 7-2}$$

which represents the % of measured response (e.g., load test) that may be used for design.

SmartPile EDC has a Φ/λ ratio of 0.67 (i.e., 0.65/0.96) or 67% of measured (static load test) is available for design vs. 57% for CAPWAP.

Finally, the question of sufficient measured and predicted SmartPile EDC data was addressed. Impacting the LRFD Φ is both the bias, λ, and CV_R (or σ, i.e., $CV_R = \sigma/\lambda$) uncertainty. For independent data, the variance of mean (i.e., bias) is given by σ^2/N where N total number of data samples (i.e., 17). Therefore the expected range of the bias is between $\lambda - \sigma/\sqrt{N}$ and $\lambda + \sigma/\sqrt{N}$ or $0.9 < \lambda < 1.02$. Similarly, the variance of the variance is given by $\frac{2\sigma^4}{N-1}$. For the data collected, the expected range in standard deviation is given as $\sigma \pm \frac{\sqrt{2}\sigma^2}{\sqrt{N-1}}$ or $0.24 < \sigma < 0.27$. Using the minimum bias (0.9) and standard deviation (0.24), Φ = 0.59; in the case of the maximum bias (1.02) and standard deviation (0.27), Φ = 0.68. The difference between two cases is not significant (<15%). Note, however these cases do not necessarily represent the worse and best LRFD Φ values. The worst case has Φ = 0.55 [λ=0.9, σ=0.27] and best case, Φ = 0.73 [λ=1.02, σ=0.24], i.e., opposite combination of limits. It should be noted that a bias of 0.9 is not expected, since a comparison of 140 piles (Chapter 4) showed ratio of EDC/CAPWAP near one, and Figure 6-3 shows a bias of 1.15 between measured and CAPWAP.

7.6 Recommendations

It is recommend to increase the size of the database (e.g., 17 to 30) as this would reduce the uncertainty in the mean, $\sigma/\sqrt{N}$, and the standard deviation, $\pm \frac{\sqrt{2}\sigma^2}{\sqrt{N-1}}$ by 25%. However, at the current time, it is not known if Smart Structures or any DOTs have load tests planned with EDC. It is therefore recommended, based on the findings of the work discussed herein, that the computed LRFD λ, CV_R, and Φ are considered best estimates at this time.

REFERENCES

AASHTO (2012). *AASHTO LRFD Bridge Design Specifications (US Customary Units), Fourth Edition*, AASHTO, Washington, D.C.

Ardalan, H., Eslami, A., Nariman-Zadeh, N. (2009). Piles Shaft Capacity from CPT and CPTu Data by Polynomial Neural Networks and Genetic Algorithms, *Computers and Geotechnics*, No. 36, pp. 616–625.

Axelsson, G. (2000). *Long-Term Set-up of Driven Piles in Sands*, PhD. Dissertation, Royal Institute of Technology, Sweden.

Brown, D.A. (1994). Evaluation of Static Capacity of Deep Foundations from Statnamic Testing, *Geotechnical Testing Journal*, Vol. 17, No. 4, pp. 403-414.

Bullock, P.J., Schmertmann, J., McVay, M.C., and Townsend, F. (2005). Side shear setup II: Results from Florida Test Piles, *Journal of Geotechnical and Geoenvironmental Engineering*, Vol. 131, No. 3, pp. 301-310.

Bustamante, M., and Gianeselli, L. (1982). Pile Bearing Capacity Predictions by Means of Static Penetrometer, CPT, Vol. 2, *Proc., 2nd European Symposium on penetration Testing, ESOPT-II*, Amsterdam, The Netherlands, pp. 493-500.

Cartwright, M. (1990). *Fourier Methods for Mathematicians, Scientists, and Engineers*, Ellis Horwood Limited, Division of Simon and Schuster International Group, West Sussex, England.

Chen, C.S., Liew, S.S., and Tan, Y.C. (1999). Time Effects on the Bearing Capacity on Driven Pile, *11th Asian Regional Conf on Soil Mechanics and Geotechnical Eng*, Balkema, Rotterdam.

Chow, F.C., Jardine, R.J., Brucy, F., and Nauroy, J.F. (1998). Effects of Time On the Capacity of Pipe Piles in Dense Marine Sand, *Journal of Geotechnical and Geoenvironmental Engineering*, Vol. 24, No. 3, pp. 254-264.

Clough, R.W. and Penzien, J. (1993). *Dynamics of Structures*, 2nd edition, McGraw-Hill, New York.

Deeks, A. (1992). *Numerical Analysis of Pile Driving Dynamics*, PhD Dissertation, University of Western Australia.

El Naggar, M.H. and Novak, M. (1994). Nonlinear Model for Dynamic Axial Pile Response, *Journal of Geotechnical Engineering*, Vol. 120, No. 2, pp. 308–329.

FHWA (2001). *Load and Resistance Factor Design (LRFD) for Highway Bridge Substructures*, FHWA Publication No. HI-98-032, Federal Highway Administration, Washington, D.C.

Gallagher, K., and Sambridge, M. (1994). Genetic Algorithms: A Powerful Tool for Large-Scale Non-Linear Optimization Problems, *Comput. Geosci.*, Vol. 20, No. 7, pp. 1229–1236.

Goble, G., Likins, G, and Rausche, F. (1975). *Bearing Capacity of Piles from Dynamic Measurements*, Final Report for Ohio Department of Transportation, Dept. of Civil Engineering, Case Western Reserve.

Goldberg, D. (1989). *Genetic Algorithms in Search, Optimization and Machine Learning*, Addison Wesley Publishing Company, Boston, MA..

Herrera, R. Jones, L., Lai, P. (2009). Driven Concrete Pile Foundation Monitoring with Embedded Data Collector System, *ASCE Geotechnical Special Publication 185*, pp. 621-628.

Kehoe, S.P. (1989). *An Analysis of Time Effect On the Bearing Capacity of Driven Piles*, Master Thesis, Department of Civil Engineering, University of Florida, Gainesville, FL.

Kelly, S. (2004). Unit Skin Friction from the Standard Penetration Test Supplemented with the Measurement of Torque, *Journal of Geotechnical and Geoenvironmental Engineering*, Vol. 130, No. 5, pp. 540-543.

Kuo C., Cao G., Guisinger, A. L., and Passe, P. 2007. A Case History of Pile Freeze Effects in Dense Florida Sands. TRB Annual Meeting, Washington, D.C.

Koper, K. D., Wysession, M. E., and Wiens, D. A. (1999). Multimodal Function Optimization with Niching Genetic Algorithm: A Seismological Example, *Bull. Seismol. Soc. Am.*, No. 89, pp. 978–988.

Küçükarslan, S. (2002). Time Domain Dynamic Analysis of Piles under Impact Loading, *Soil Dynamics and Earthquake Engineering*, Vol. 22, No. 2, pp. 97-104.

Lai, P., McVay, M., Bloomquist, D. and Badri, D. (2008). Axial Pile Capacity of Large Diameter Cylinder Piles*, ASCE Geotechnical Special Publication STP 180*, Geo- Institute, pp. 366-384.

Lewis, C.L. (1999). *Analysis of Axial Statnamic Testing by the Segmental Unloading Point Method*, Master Thesis, University of South Florida, Tampa, Fl.

Liang, J.W. and Feeny, B. F. (2006). Balancing Energy to Estimate Damping Parameters in Forced Oscillators, *Journal of Sound and Vibration*, No. 295, pp. 988–998.

Manna, B. and Baidya, D.K. (2010). Dynamic Nonlinear Response of Pile Foundations Under Vertical Vibration—Theory Versus Experiment, *Soil Dynamics and Earthquake Engineering*, Vol. 30, No. 6, pp. 456-469.

McVay, M.C., Schmertmann, J., Townsend, F., and Bullock, P.J. (1999). Pile Friction Freeze: A Field and Laboratory Study, Final report, Florida Department of Transportation, *Contract No.99700-7584-119, FHWA No. 0510632*, 1312 pages.

Meyerhof, G. (1976). Bearing Capacity and Settlement of Pile Foundation, *ASCE Geotechnical Engineering Division*, Vol. 102, No. GT3, pp. 195-228.

Meyers and Chawla (1999). *Mechanical Behavior of Materials*, Prentice Hall, Inc.

Middendorp, P., Bermingham, P., Kuiper, B. (1992). Statnamic Load testing of Foundation Pile, *Proceedings of the 4th International Conference on Application of Stress-Wave Theory to Piles*, Hague, Netherlands, pp. 581-588.

Mullins, G., Lewis, C., and Justason, M. (2002). Advancements in Statnamic Data Regression Techniques, *ASCE Proceedings of International Deep Foundations Congress GSP116*, Orlando, Florida, pp. 430-438.

NCHRP (2011). Developing Production Pile Driving Criteria from Test Pile Data, *Synthesis Report 418*, Transportation Research Board of National Academies, 503 pages.

Novak, M. and Aboul-Ella, F. (1978). Impedance Function of Piles in Layered Media, *Journal of the Engineering Mechanics Division*, No. EM3, pp. 643-660.

Pasdarpour, M., Ghazavi, M., Teshnehlab, M., Sadrnejad, S. A. (2009). Optimal Design of Soil Dynamic Compaction Using Genetic Algorithm and Fuzzy System, *Soil Dynamics and Earthquake Engineering*, Vol. 29, No. 7, pp. 1103-1112.

Paz, M. (1997). *Structural Dynamics—Theory and Computation,* 4th edition, Chapman and Hall, New York.

Pedroso, D. M. and Williams, D. J. (2011). Automatic Calibration of Soil–Water Characteristic Curves Using Genetic Algorithms, *Computers and Geotechnics*, Vol. 38, pp. 330–340.

Polyanin, A. D. (2002). *Handbook ofLlinear Partial Differential Equations for Engineers and Scientists*, Chapman and Hall/CRC, Boca Raton, FL.

Pullammanappallil, S.K. and Louie, J.N. (1994). A Generalized Simulated Annealing Optimization for Inversion of First Arrival Time, *Bulletin of the Seismological Society of America*, Vol. 84, No. 5, pp. 1397-1409.

Randolph, M.F., Simons, H.A., (1986). An Improved Soil Model for One Dimensional Pile Driving Analysis, *Proceedings of the 3rd International Conference on Numerical Methods in Offshore Piling*, Nantes, France, pp. 3-17.

Rausche, F., Goble, G., and Likins, G. (1985). Dynamic Determination of Pile Capacity, *Journal of Geotechnical Engineering*, Vol. 111, No. 3, pp. 367-383.

Rausche, F., Likins, G., and Hussein, M. (2008). Analysis of Post-Installation Dynamic Load Test Data for Capacity Evaluation of Deep Foundation, *Geotechnical Publication No. 180: From Research to Practice in Geotechnical Engineering*, ASCE, Reston, Virginia, pp. 312-330.

Rausche, F., Likins, G., Liang, L., and Hussein, M. (2010). Static and Dynamic Models for CAPWAP Signal Matching, *Geotechnical Special Publication No. 198: The Art of Foundation Engineering Practice*, ASCE, Reston, VA, pp. 534-553.

Rodríguez-Zúñiga, J. L., Ortiz-Alemán, C., Padilla, G., and Gaulon, R. (1997). Application of genetic algorithms to constrain shallow elastic parameters using in situ ground inclination measurements, *Soil Dynamics and Earthquake Engineering,* Vol. 16, No. 3, pp. 223-234.

Sambridge, M. and Mosegaard, K. (2002). Monte Carlo Methods in Geophysical Inverse Problems, *Reviews of Geophysics*, 3.

Sen, M.K. and Stoffa, P.L. (1991). Nonlinear Multiparameter Optimization Using Genetic Algorithms: Inversion of Plane-Wave Seismograms, *Geophysics*, Vol. 56, No. 11, pp. 1794-1810.

Sen, M.K. and Stoffa, P.L. (1995). Global Optimization Methods in Geophysical Inversion, *Adv. Explor. Geophysics*, Vol. 4.

Sharma, S.P. and Kaikkonen, P. (1998). Two-Dimensional Non-Linear Inversion of VLF-R Data Using Simulated Annealing: *Geophysics J. Int.*, Vol. 133, pp. 649-668.

Skov, R and Denver, H (1988). Time-Dependence of Bearing Capacity of Piles, *Proc. 3rd Int. Conf. on Application of Stress-wave Theory to Piles*, Ottawa, Canada, pp. 879-888.

Smith, E.A.L. (1960). Pile Driving Analysis by the Wave Equation, *Journal of the Soil Mechanics and Foundations Division*, ASCE, Vol. 86, No. 4.

Soares, D. and Mansur, W. J. (2005). A Time Domain FEM Approach Based on Implicit Green's Functions for Non-Linear Dynamic Analysis, *Int. J. Numer. Meth. Engng*, Vol. 62, pp. 664–681.

Strickilin, J.A. and Haisler,, W.E. (1977). Formulations and Solution Procedures for Nonlinear Structural Analysis, *Computers and Structures*, Vol. 7, pp. 125–136.

Styler, M. A. (2006). *Development and implementation of the Diggs format to perform LRFD resistance factor calibration of driven concrete piles in Florida*, Master Thesis, Department of Civil and Coastal Engineering, University of Florida.

Tarantola, A. (2005). *Inverse problem theory and methods for model parameter estimation*, Society for Industrial and Applied Mathematics, Philadelphia.

Thomson, W.T. and Dahleh, M.D. (1993). *Theory of Vibration with Applications*, 5th edition, Prentice-Hall, Englewood Cliffs, NJ.

Titi, H. H. and Wathugala, G. W. (1999). Numerical Procedure for Predicting Pile Capacity-Setup/Freeze, *Transportation Research Record*, No. 1663, pp. 25-32.

Tran, K. T. and Hiltunen, D.R. (2011). Inversion of First-Arrival Time Using Simulated Annealing, *Journal of Environmental and Engineering Geophysics*, Vol. 16, pp. 25-35.

Tran, K. T, McVay, M., Herrera, R., and Lai, P. (2011a). A New Method for Estimating Driven Pile Static Skin Friction with Instrumentation at the Top and Bottom of the Pile, *Soil Dynamics and Earthquake Engineering*, Vol. 31, pp. 1285-1205.

Tran, K. T, McVay, M., Herrera, R., and Lai, P. (2011b). Estimating Static Tip Resistance of Driven Piles with Bottom Pile Instrumentation, *Canadian Journal of Geotechnical Engineering*, Vol. 49, pp. 381-393.

Virieux, J. (1986). P-SV Wave Propagation in Heterogeneous Media: Velocity-Stress Finite-Difference Method, *Geophysics*, Vol. 51, No. 4, pp. 889-901.

Zhang, L., McVay, M., and Ng, W. (2001). A Possible Physical Meaning of Case Damping in Pile Dynamics, *Canadian Geotechnical Journal*, Vol. 38, pp. 83-94.

APPENDIX
INVERSION METHOD

Skin Friction

Inversion involves minimizing a least-squared error, *E(m)*, which measures the difference between observed data and estimated data associated with model *m* (a pair of assumed values of b and c), or

$$E(m) = \frac{1}{N}\sum_{k=1}^{N}\left[d_k - g_k(m)\right]^2 \qquad \text{Eq. A-1}$$

where d_k and g_k are the *kth* observed and estimated Green's function values, respectively, and N is the number of observation points. A least squared error equal of 0 is obtained when a perfect match between the observed and estimated data is found.

Genetic algorithm has recently been applied in evaluation of various dynamic data sets. Rather than discussing the analogy of genetic algorithm that has been well described by authors (Goldberg, 1989; Sen and Stoffa, 1991, 1995, Sambridge and Mosegaard, 2000), a brief description of the process used in this study is presented herein.

For this application, the algorithm requires a binary code (Figure A-1(a)), e.g., 8 bits, of 0 or 1, to represent each model parameter, i.e., b and c. For a code of *nb* bits: $\{a_{nb}, a_{nb-1}, a_{nb-2} \ldots a_1\}$ representing the parameter m_{ij}, the resolution of the parameter is determined as:

$$\Delta m_{ij} = \frac{\max_{ij} - \min_{ij}}{2^{nb} - 1}, \qquad \text{Eq. A-2}$$

and the parameter may be determined by,

$$m_{ij} = \min_{ij} + \Delta m_{ij}\sum_{n=1}^{nb} a_n \cdot 2^{n-1} \qquad \text{Eq. A-3}$$

Generally, the number of bits, *nb*, selected should be based on the expected range of the parameter and its desired resolution.

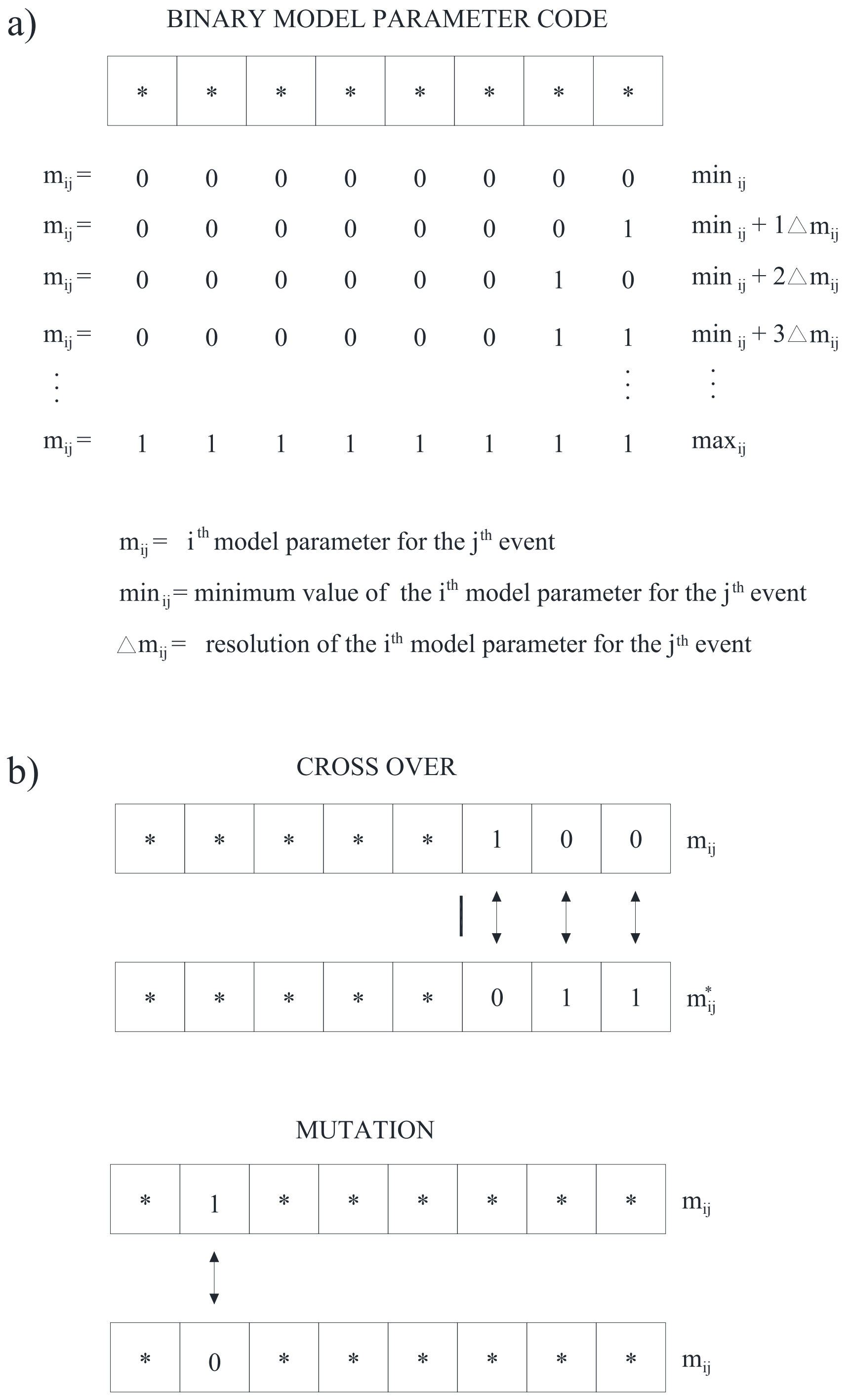

Figure A-1 Genetic algorithm: a) parameter coding, and b) crossover and mutation

The Genetic algorithm begins with a suite of random (the first generation with a population number of *Np*) model pairs (e.g., b (stiffness) and c (damping)). Each parameter in a pair (a or b) in the first generation is found by randomly selecting a code of bits (0 and 1) and then calculating the parameter value from Eq. A-3. After that, the least-squared error of each model pair of the first generation is determined from Eq. A-1.

The algorithm then generates offspring from the current parents by reproduction, which essentially consists of three operations: selection, crossover, and mutation, and are updated as follows:

1) Select a pair of models from the current generation for reproduction. The probability of parent selection is based on the ratio of each model's inverse error to the sum of all inverse errors:

$$P_s(m) = \frac{\frac{1}{E(m)}}{\sum_A \frac{1}{E(m)}}, \qquad \text{Eq. A-4}$$

where A denotes all models in the current generation. Again, two different pairs (b or c) are selected as parents.

2) Conduct the processes of crossover and mutation for the selected 2 pair sets in step 1. Only one parameter is randomly selected for the crossover and mutation, Figure A-1(b) between each parent (i.e., b parent 1 to b parent 2). The coded parameter selected is subjected to the possibility of bit crossover with parents with a specified probability p_x. If crossover is to occur, randomly pick a cross position and exchange all the bits to the right of the position (Figure A-1(b)). A mutation follows the crossover, and it is simply the alteration of a random selected bit in the parameter code based on a specified probability p_m (Figure A-1(b)). After the processes of crossover and mutation, least-squared errors, Eq. A-1 is performed on the conceived children.

3) The two new pairs (i.e., model) generated in step 2 are copied to the new generation. Then, each new model's error is compared to error of a model in the current generation selected under a uniform random selection and used only once. If the new model's error is smaller, the

new model is kept in the new generation. If it is more, the randomly selected model replaces the new model in the new generation with a probability p_u.

4) Repeat steps 1, 2, and 3 until a new generation is found with *Np* models. All fitness of models in the new generation are stored and used for generating of the next generation.

Generations will be generated by repeating steps 1, 2, 3, and 4 until a specified number of generations are completed. Then, the inversion result is taken as the model of the final generation having the lowest least-squared error.

The selection of a reasonable population number *Np* is important. Selecting a large value leads to unnecessary computations, whereas using a small value leads to a local solution. In this study, Np values of 20, 50, 100, and 200 pairs were evaluated, with the 100 pair population recommended. With a population of 100, the model parameters usually begin to localize after 10 generations and converge after 50 generations. For piles studied, 50 generations was sufficient to obtain reproducible b and c values.

The probabilities of crossover p_x, mutation p_m, and update p_u are the other important parameters in the global optimization in the genetic algorithm. This work strictly follows the suggested guidelines by Sen and Stoffa (1991), which uses a low value of mutation probability (= 0.01), a moderate value of crossover probability (= 0.6) and a high value of update probability (= 0.9).

Inversion Convergence Process for Linear Skin Friction

The inversion began by first generating 100 random models (Figure A-2). Next, fifty generations of genetic alterations were performed to find the final solution. The analyses (i.e., fifty generations) took about 3 seconds on a 3.4 GHz laptop, i.e., “real time”. Figure A-2 illustrates how the process converges. The paired parameters (b and c) for all generations: 1, 10, 20, 30, 40 and 50 are presented. Note in the first generation, the models are randomly distributed over all of the parameter space. By generation 10, models start localizing, and by generation 50, most model parameters cluster around the global solution values. It is also observed that the dots representing model pairs (b,c), horizontally align very quickly, indicating the damping, c of the pair converges much faster than the stiffness, b.

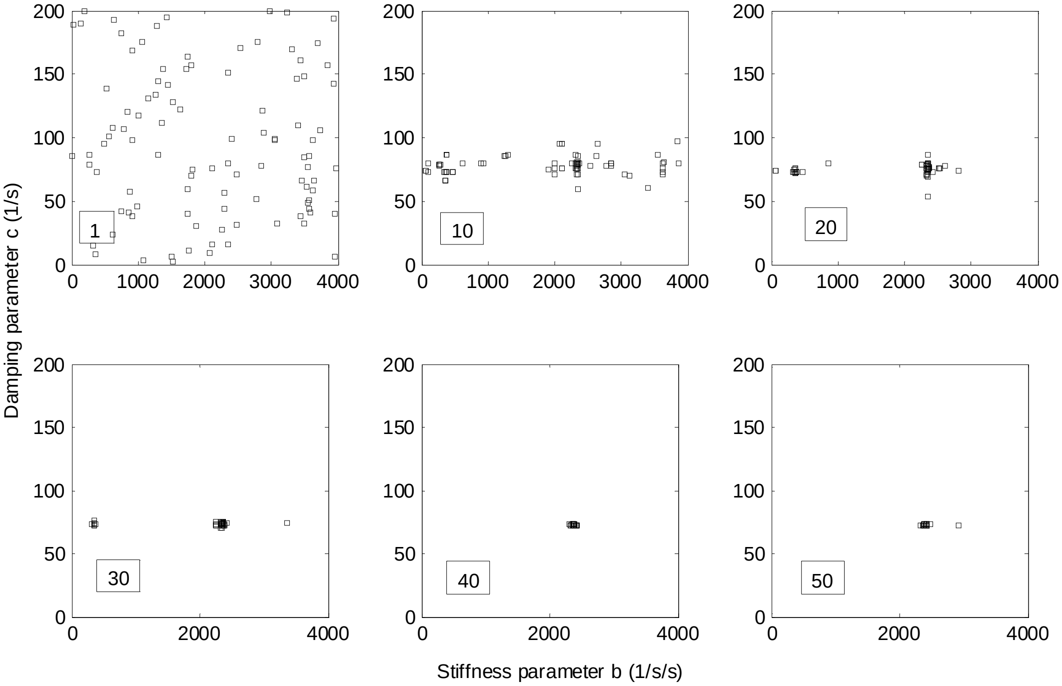

Figure A-2 Dixie Highway Pile 1: distribution of 100 models at the end of generations: 1, 10, 20, 30, 40, and 50

Inversion Convergence Process for Non-Linear Skin Friction

For the inversion process, it began by first generating 200 random models (top row of Figure A-3). Next, fifty generations were performed to find the converged solution (approximately one minute on a 3.4 GHz desktop computer). The inversion process shows that the dots representing model parameters (k_m and q) horizontally align very quickly, indicating that the loading quake (q) converges much faster than the stiffness (k_m). This suggests that the average loading quake for all segments has more of an influence on particle velocities than the individual loading stiffness of any one segment.

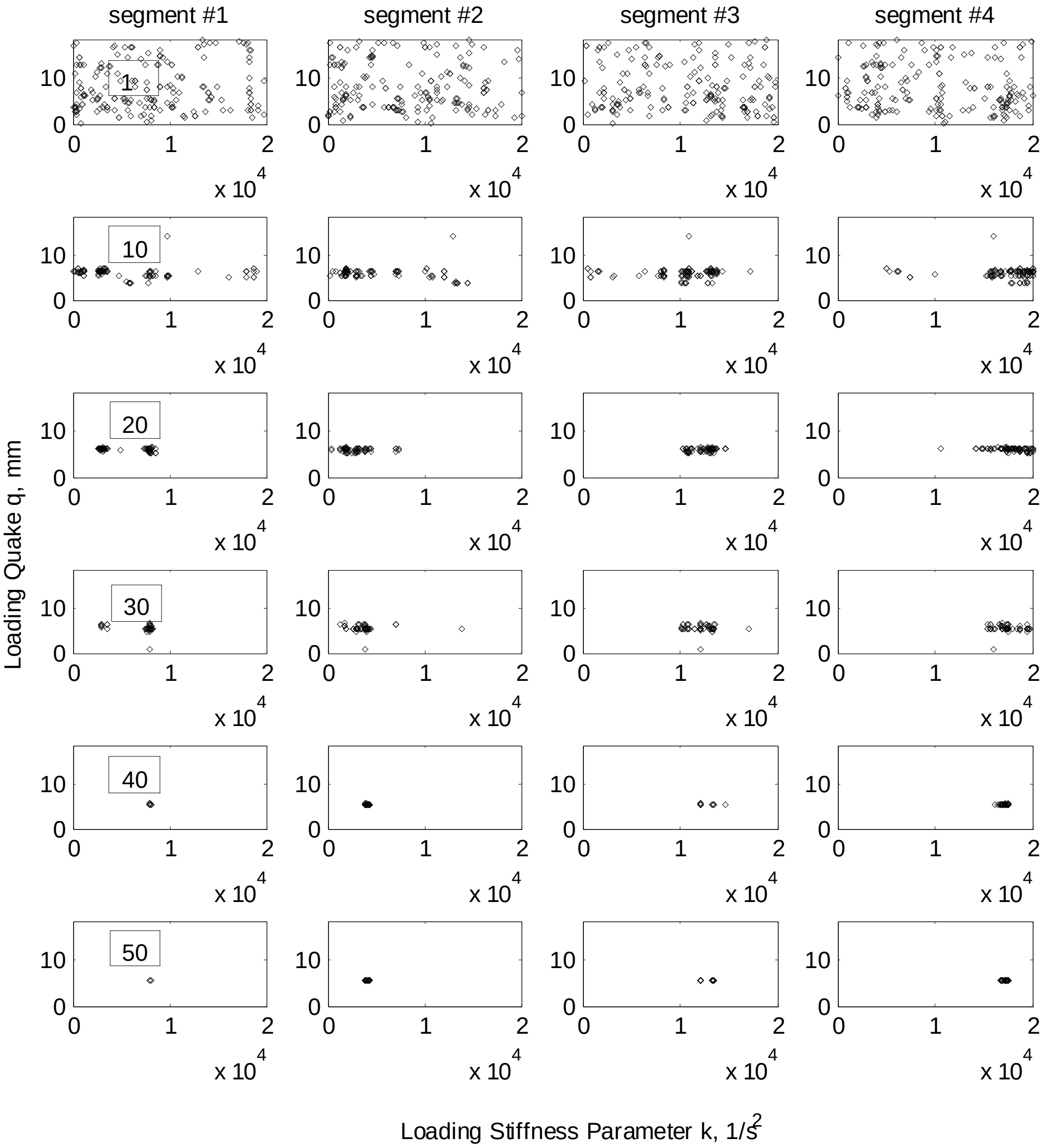

Figure A-3 Dixie Highway Pile 1: distribution of 200 models at the end of generations 1, 10, 20, 30, 40, and 50

Tip inversion

Inversion involves minimizing a least-squared error (Tarantola, 2005), *E(M)*, which measures the difference between measured data and estimated data associated with model *M* (a set of assumed values of the unknowns: m, c, l_1, k_1, k_2, l_3, k_3 and k_4):

$$E(M) = \frac{1}{N}\sum_{k=1}^{N}\left[d_k - g_k(M)\right]^2 + \frac{1}{N}\sum_{k=1}^{N}\left[D_k - G_k(M)\right]^2 \qquad \text{Eq. A-5}$$

where d_k and g_k are respectively the *k-th* measured and estimated energy, D_k and G_k are respectively the *k-th* measured and estimated normalized total forces. Note, the magnitude of force may be twenty times the magnitude of energy, and "equal" goodness of fit are required for both energy and force, thus a normalizing coefficient (e.g., proportional to peak displacement) was applied to the total forces to ensure the same magnitude as the maximum observed energy. In Eq. A-5, N is the number of measured values, and *E(M)* is the least squared error (value of 0 occurs for perfect match between the measured data and estimated data).

To overcome the need for reasonable initial model and prior information, a genetic algorithm was applied to Eq. A-5 to obtain a global minimum. Genetic algorithms have recently been applied in evaluation of various dynamic data sets (Sen and Stoffa 1991, 1995; Gallagher and Sambridge 1994; Koper et al. 1999). General discussion of genetic algorithms has been well described by Goldberg (1989).

For this application, the algorithm requires a binary code (Figure A-1), e.g., 8 bits, of 0 or 1, to represent each model parameter. For a code of *nb* bits: $\{a_{nb}, a_{nb-1}, a_{nb-2} \ldots a_1\}$and user selected minimum, $\min_{ij}$, and maximum, $\max_{ij}$, values, the parameter, m_{ij} ,of the model M, has the following resolution:

$$\Delta m_{ij} = \frac{\max_{ij} - \min_{ij}}{2^{nb} - 1}, \qquad \text{Eq. A-6}$$

and the parameter's value may be determined by,

$$m_{ij} = \min_{ij} + \Delta m_{ij} \sum_{n=1}^{nb} a_n \cdot 2^{n-1} \qquad \text{Eq. A-7}$$

Generally, the number of bits, *nb,* selected should be based on the expected range of the parameter and its desired resolution.

The genetic algorithm begins with a suite of random models (the first generation with a population number of *Np*). Each parameter of a model in the first generation is found by randomly selecting a code of bits (0 and 1) and then calculating the parameter value from Eq. A-7. After that, the least-squared error of each model of the first generation is determined from Eq. A-5.

The algorithm then generates offspring from the current parents by reproduction, which essentially consists of three operations: selection, crossover, and mutation, and by update as follows:

1) Select a pair of models from the current generation for reproduction. The probability of parent selection is based on the ratio of each model's inverse error to the sum of all inverse errors:

$$P_s(M) = \frac{\frac{1}{E(M)}}{\sum_A \frac{1}{E(M)}}, \qquad \text{Eq. A-8}$$

where *A* denotes all models in the current generation. Two different models are selected as parents.

2) Conduct the processes of crossover and mutation for parameters of the selected two models in step 1. Only one parameter is randomly selected for the crossover and mutation (Figure 1b) between each parent (i.e., parent 1 to parent 2). The coded parameter selected is subjected to the possibility of bit crossover with parents with a specified probability p_x. If crossover is to occur, randomly pick a cross position and exchange all the bits to the right of the position (Figure A-1(b)). A mutation follows the crossover, and it is simply the alteration of a random selected bit (Figure A-1(b)) in the parameter code based on a specified probability p_m. After the processes of crossover and mutation, least-squared errors (Eq. A-5) are performed on the conceived children.

3) The two new models generated in step 2 are copied to the new generation. Then, each new model's error is compared to error of a model in the current generation selected under a uniform random selection and used only once. If the new model's error is smaller, the new model is kept in the new generation. If it is larger, the randomly selected model replaces the new model in the new generation with a probability p_u.

4) Repeat steps 1, 2, and 3 until a new generation is found with Np models. All least-squared errors of models in the new generation are stored and used for generating of the next generation.

Generations will be generated by repeating steps 1, 2, 3, and 4 until a specified number of generations are completed. Then, the inversion result is taken as the model of the final generation having the lowest least-squared error.

The selection of a reasonable population number Np is important. Selecting a large value leads to unnecessary computations, whereas using a small value leads to a local solution. In this study with problems of about 10 unknowns, many values of Np, i.e., 100, 200, 300, and 400 have been evaluated, with 200 being recommended. With the population number of 200, the model parameters usually begin to localize after 40 generations and converge after 100 generations. As expected, the mass and damping converged the fastest (constant for all segments) with stiffness localizing the last (highest change over the trace); however the ultimate static resistance, i.e., at peak displacement was found to insensitive to number of segments, initial stiffness, etc.

The probabilities of crossover p_x, mutation p_m, and update p_u are the other important parameters in the global optimization in the genetic algorithm. This work strictly follows the suggested guidelines by Sen and Stoffa (1991), which uses a low value of mutation probability (= 0.01), a moderate value of crossover probability (= 0.6) and a high value of update probability (= 0.9).

Inversion Convergence Process for Tip Resistance

Figure A-4 illustrates how the process converges for the loading segments, whose estimated values are the focus of this work. The lengths and stiffness of the three loading segments from all models of generations 1, 20, 40, 60, 80, and 100 are presented. The true model parameters are indicated by large square dots in each subplot. Note, the first generation models were randomly distributed over the parameter space. By generation 20, models start localizing, and by generation 100, most model parameters cluster around the true values. Concurrently, the mass, damping, and unloading stiffness were also well inverted to their true values (not shown here).

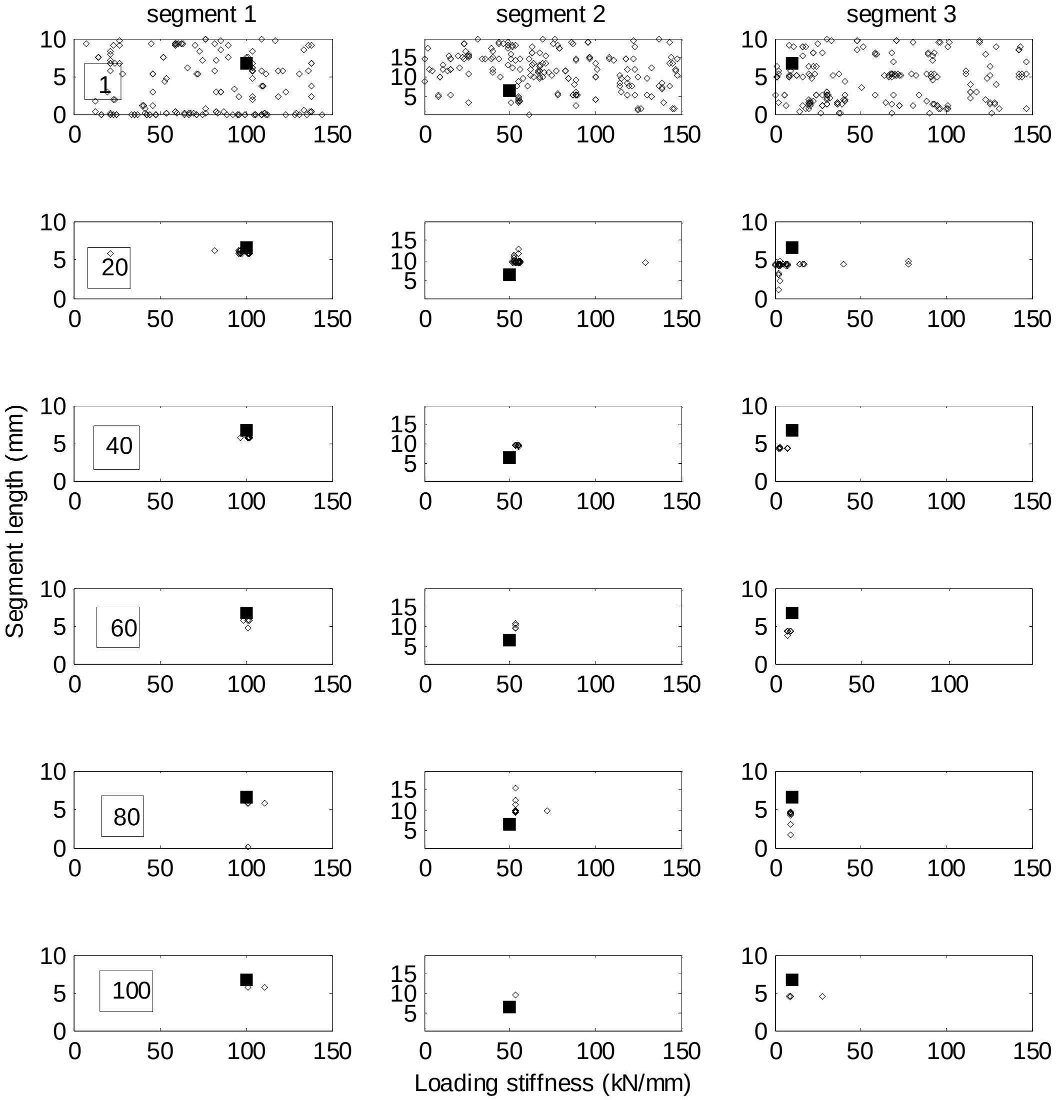

Figure A-4 Synthetic model: distribution of loading segments from 200 models of generations 1, 20, 40, 60, 80, and 100. The square dot in each plot presents the true stiffness and lengths of the loading segments